



AUTHOR:

TITLE:

YEAR:

OpenAIR citation:

This work was submitted to- and approved by Robert Gordon University in partial fulfilment of the following degree:

OpenAIR takedown statement:

Section 6 of the “Repository policy for OpenAIR @ RGU” (available from <http://www.rgu.ac.uk/staff-and-current-students/library/library-policies/repository-policies>) provides guidance on the criteria under which RGU will consider withdrawing material from OpenAIR. If you believe that this item is subject to any of these criteria, or for any other reason should not be held on OpenAIR, then please contact openair-help@rgu.ac.uk with the details of the item and the nature of your complaint.

This is distributed under a CC _____ license.



ROBERT GORDON
UNIVERSITY ABERDEEN

PhD 2015

**Development of Formation Damage Models
for Oilfield Polymers**

IDAHOSA, Patrick Egbe Goddey
The Robert Gordon University
PhD 2015



Development of Formation Damage Models for Oilfield Polymers

IDAHOSA, Patrick Egbe Goddey

The Robert Gordon University, 2015

Development of Formation Damage Models for Oilfield Polymers

IDAHOSA, Patrick Egbe Goddey

A Thesis Submitted in Partial Fulfilment of the Requirements of the
Robert Gordon University, Aberdeen, United Kingdom for the Award
of the degree of Doctor of Philosophy.

October, 2015





Development of Formation Damage Models for Oilfield Polymers

IDAHOSA, Patrick Egbe Goddey

Supervisors:

Dr. G. F. Oluyemi, CEng.

Dr. Radharkrishna Prabhu

Prof. Babs M. Oyeneyin, CEng.

Funding:

This PhD research was funded by the Federal Government of Nigeria through the Petroleum Technology Development Fund (PTDF).

DECLARATION

I hereby declare that this thesis is my work and submitted to the Robert Gordon University, IDEAS Research Institute/School of Engineering, Aberdeen, the United Kingdom in fulfilment of the requirements for the award of the degree of Doctor of Philosophy (PhD) in Petroleum Engineering. I also confirm that in accordance with the academic rules and research ethical conduct of the University, this work has not been submitted in any form for another degree or qualification at any other academic institution, and that all materials that are not original to this work have been fully cited and acknowledged.

ACKNOWLEDGMENTS

I would like to thank Dr. Gbenga F. Oluyemi, Dr. Radharkrishna Prabhu, and Prof. Babs M. Oyeneyin for their supervision. I would like to thank all the members who serve in the committee for my PhD defence (Dr Carlos A. Grattoni as external examiner, Dr James Njuguna as internal examiner, and Dr Nirmalie Wiratunga as internal converner). To my colleagues in the RGU Well Engineering Research Group (WERG), I say thank you to you all. This research is funded by the Federal Government of Nigeria through the Petroleum Technology Development Fund (PTDF)-thank you. I would like to thank my employer, the Petroleum Training Institute (PTI), Nigeria for their contribution in granting me study leave to enable me embark on this PhD research program.

I am indeed grateful to SNF Floerger, ZAC de Milieux, 42163 Andrezieux, France. This company manufactured and kindly provided (in powder form) all the commercial grade partially Hydrolysed Polyacrylamide (HPAM) polymers used in the experiments; while the Xanthan Gum polymers was manufactured and supplied by CP Kelco Shandong Biological Co., Ltd, 140 Yanhe Road, Wulian County, Rizhao City, Shandong, Peoples Republic of China-thank you.

I would like to thank Dr. Matthew Kerr, Dr. Graeme Kay, Dr. Kyari Yates, Laurie Smith, John Woods, Kirsty Enright and other technical staff of the School of Pharmacy and Life Sciences for the opportunity to conduct numerous and several important measurements in their facilities. I would also like to thank Alan Mclean and the technical staff of the School of Engineering for their support. I thank many others whose names are not mentioned but have contributed to this work in one way or another. I came across many others, though did not contribute to this work, I thank them all as well, because my meeting with them was a source of learning for me.

Finally, I would like to thank my family (my wife, Mrs Bukola Deji Idahosa and my lovely children – Williams, Maris, Peter and Paul) for the long

time I kept away from them while in School. I thank my mother in-law (Mrs Comfort Remilekun Iwalaiye) for her continuous prayers for me. As for you my dear Bukola, I thank you in a very special way for all your love, patience, standing by me in endless fasting and prayers and moral support throughout this academic journey; this work, after all, also belongs to you.

DEDICATION

To my GOD who made it possible; *thank you* LORD JESUS.

NOMENCLATURE

k_1	Adjustable equilibrium or affinity constant for adsorption
v	Frontal velocity
A_{pr}	Percentage activity of polymer product
ΔP_w	Pressure drop during brine flow after polymer adsorption at a certain flow rate, Q_s .
A	Avogadro's number, 7.023×10^{23} molecules/mol
F_{r_bf}	Brine flushed resistance factors
K	Consistency index in power-law equation
A	Core cross-sectional area
C_{tr}	Effluent tracer concentration
C_{ads}	Equilibrium adsorbed for a particular concentration
C_f	Final equilibrium concentration of polymer solution
C_i	Initial concentration of polymer solution
k_0	Initial permeability
C_{p0}	Injected-polymer concentration
C_{tr0}	Injected-tracer concentration
k_d	Instantaneous or damaged permeability
n_d	Number of data points
k_d/k_0	Permeability damage ratio
C_p	Polymer concentration in effluent

M_w	Polymer molecular weight
F_{r-p}	Polymer resistance factors
ΔPV	Pore volume increment
ΔP_{w0}	Pressure drop during brine flow before polymer injection at flow rate q_s .
ΔP_{pol}	Pressure drop during polymer solution flow at flow rate q_s .
R_g	Radius of gyration
r_M	Radius of molecular coil in dilute solution
A_s	Rock surface area
Ad_{max}	Theoretical maximum adsorption capacity for the system
q	Volumetric flow rate
W_p	Weight of polymer solution
W_s	Weight of solid
K, a	Empirical constants in the Mark-Houwink equation
a, b, c, d	Fitting parameters in rheological models
A, B	Empirical fitting coefficients in equation 7.11.
API	American Petroleum Institute
BPD	Barrels of Oil Per Day
CaCl ₂	Calcium chloride anhydrous
CFD	Computational Fluid Dynamics
CMC	Carboxymethylcellulose

EDXA	Energy Dispersive X-ray Analysis
EHT	Equivalent Hydrodynamic Thickness
EOR	Enhanced Oil Recovery
FEM	Finite Element Method
HCl	Hydrochloric acid
HEC	Hydroxyethylcellulose
HPAM	Hydrolysed Polyacrylamide
HSE	Health, Safety and Environment
IAPV	Inaccessible Pore Volume
IOR	Improved Oil Recovery
KCl	Potassium chloride
K_{rw}	Water relative permeability
$MgCl_2 \cdot 6H_2O$	Magnesium chloride hexahydrate
MICP	Mercury Injection Capillary Pressure
Na_2CO_3	Sodium hydrogen carbonate
NaCl	Sodium chloride
NaOH	Sodium hydroxide
OGI	Oil and Gas Industry
PAAD	Percent average arithmetic deviation
PAM	Polyacrylamide
PDF	Permeability Distribution Function
PEO	Polyethylene Oxide
ppm	Parts per million

PSD	Pore-Size Distribution
PV	Pore Volume
R_k	Permeability reduction
R_m	Mobility reduction
R_p	Hydrodynamic or effective pore radius
RRF	Residual Resistance Factor
SEM	Scanning Electron Microscopy
SFB	Synthetically Formulated Brines
SI	Polymer screening index
S_{iw}	Irreducible water saturation
TDS	Total dissolved solids (TDS1, 3.0 % brine; TDS2, 13.5 % brine; TDS3, 3.2 % brine)
UK	United Kingdom
XRD	X-ray Diffraction Analysis

Greek symbols

\check{p}	Axisymmetric scalar functions
\check{u}	Axisymmetric vector fields
r, θ, z	Cylindrical coordinates
ϕ	Porosity
\dot{Q}	Energy dissipation rate
n	Flow behaviour index in the power-law equation
$\check{\Omega}$	Half section of axisymmetric 3-D domain

k'	Huggins parameter which describes solvent quality
ϕ_0	Initial porosity
ϕ_d	Instantaneous or damaged porosity
α_i	Non-dimensional textural factor
Γ_{PV}	Polymer fractional pore volume (PV) retained
$[\mu]_0$	Polymer intrinsic viscosity
Γ_p	Polymer mass retained
μ	Polymer viscosity
μ_∞	Polymer viscosity at infinite shear rate
μ_p^0	Polymer viscosity at zero shear rate
α_s	Pore structure geometrical factor
μ_{sol}	Solvent viscosity
λ	Time constant (i.e. relaxation time for realignment of polymer rods in a shear flow field)
Φ	Universal constant= 2.1×10^{21}
ρ_{g_rock}	Rock grain density
μm	Micrometer
u_r, u_θ, u_z	Radial, angular and axial components of a vector field
ϵ_H	Adsorbed layer thickness
λ	mobility ratio, md/cp.

Subscripts and superscripts

i	Index
∞	Infinite
0	initial, base, or reference value
d	damage or instantaneous
e	equilibrium or effective
f	final
g	gyration
i	initial
p	polymer
pr	product
s	solid
sol	solvent
w	water, weight

Table of Contents

Table of Contents

DECLARATION	v
ACKNOWLEDGMENTS	vi
DEDICATION	viii
NOMENCLATURE	ix
Table of Contents.....	xv
Table of Figures	xxii
Table of Tables	xxxiii
Abstract.....	xxxv
1. Chapter 1 – Introduction	1
1.1 General	1
1.2 Polymer Applications in Petroleum Engineering.	5
1.3 Research Aims and Objectives	8
1.3.1 Aims.....	8
1.3.2 Objectives	9
1.4 Methodology	9
1.5 Contributions to knowledge	11
1.5.1 Polymer-induced formation damage prediction models.....	11
1.5.2 HPAM rheological behaviour prediction models	11
1.5.3 Limitation of the Langmuir isotherm	11
1.5.4 Unique experimental approach.....	12
1.5.5 Polymer Selection Model	13
1.6 Description of Chapters	13
2. Chapter 2 – Theory and Mechanisms of Formation Damage	15
2.1 General	15
2.2 Formation Damage Mechanism	18

3. Chapter 3 – Literature Review	22
3.1 Introduction	22
3.2 Overview of EOR polymers	24
3.2.1 Xanthan gum	25
3.2.2 Hydrolysed polyacrylamide (HPAM).....	26
3.3 Previous Work on Polymer-Induced Formation Damage.	27
4. Chapter Four – Rheological Characterization of Polymer Solutions	36
4.1 Introduction	36
4.2 Polymer Viscosification Mechanism	36
4.3 Polymer Bulk Viscosity Theory	37
4.4 Polymer Molecular Radius	39
4.5 Non-Newtonian Viscosity-Shear Rate Relationships	40
4.5.1 The Power-law (Ostwald-de Waele) Model	40
4.5.2 The Four Parameter Carreau Model.....	40
4.6 Rheological Characterization and Measurements of Field Parameters Affecting Polymer Solutions	43
4.6.1 Overview of Laboratory Tests.....	43
4.6.2 Experimental – Materials and Methods	43
4.6.2.1 Materials and Procedures for Preparation of Synthetic Formation Brines	43
4.6.2.2 Polymers used for the research	45
4.6.2.3 Laboratory Procedure for Preparation of Polymer Solutions from Dry Polyacrylamide Products.	45
4.6.2.4 Materials and Methods for Polymer Solution Preparations ...	47
4.6.2.5 Determination of Activity of Polymer Product (A_{pr}) by the oven method.....	47
4.6.2.6 Calculations for Preparing a Stock Solution Using Dry Polyacrylamide Products.	48

4.6.2.7 Calculations for Dilution of Stock Solution.....	49
4.7 Rheological measurements and characterization of polymer Solutions.....	50
4.7.1 Temperature Control - <i>The Peltier Plate</i>	52
4.7.2 Samples preparation for rheological measurements	52
4.7.3 Methodologies.....	53
4.7.3.1 Steady state flow/ stepped flow.....	53
4.7.3.2 Temperature ramp.....	54
4.7.3.3 Continuous ramp	54
4.7.3.4 Peak Hold	54
4.8 Results and Discussion	54
4.8.1 Dependence of Viscosity on Shear Rate.....	54
4.9 Flow data modelling	58
4.10 Relationship of Polymer Concentration and Viscosity	60
4.12 Effect of Temperature on Viscosity	62
4.13 Effect of molecular weight.....	65
4.14 Effects of Salinity and Hardness on Viscosity	66
4.15 Peak Hold Procedure	69
4.16 Continuous Ramp Test.....	70
4.17 Modelling rheological behaviour of polymer solutions under shear and concentration	74
4.18 Conclusion	78
5. Chapter 5 – Simulation of Shear-Thinning Fluid Rheology in Porous Media.	80
5.1 Introduction	80
5.1.1 Objective.....	82
5.2 Mathematical and Numerical Framework.....	83
5.2.1 Model Definition	83

5.2.2	Model Geometrical Domain	85
5.2.3	Constriction (Pore Throat) Geometry used for the Simulation. .	86
5.3	Boundary Condition Settings	86
5.3.1	Pressure outlet.....	86
5.3.2	Slip or Axial Symmetry Boundary Condition	87
5.3.3	Wall Boundary Condition	87
5.4	Numerical Solution of Axisymmetric flow	88
5.5	Results and Discussion	89
5.5.1	Comparative Analysis of the Effects of Different Constrictions and Inlet Pressures on Viscosity.	89
5.6	Conclusions.....	92
6.	Chapter 6 – Polymer Core Flooding: Equipment, Material Preparation, and Methods	94
6.1	Introduction	94
6.2	Equipment, Materials and Methods.....	95
6.2.1	Synthetic Brine Formulation.....	95
6.2.2	Polymers used for core flooding	96
6.2.3	Polymer Solutions Preparation for core flooding.....	96
6.3	Porous Media Description, Preparation and Characterization	97
6.3.1	Clashach Cores	97
6.3.1.1	Petrophysical Properties Determination for Clashach Cores .	98
6.3.1.2	Calculation of Mercury Injection Data	98
6.3.2	Commercial Silica Sand	107
6.4	Sand pack porosity and pore volume measurements	113
6.5	Clashachs and Sand pack permeability measurements.....	113
6.6	Core flooding Experimental Setup	116
6.6.1	Flow rig leakage test and Transducer calibration	120

6.7	Flow rate determination and in-situ estimation of shear rates in cores/sandpacks.	121
6.8	Conclusion	126
7.	Chapter 7 – Experimental Procedures, Results, and Discussion for Polymer Core Flooding	127
7.1	Introduction	127
7.1.1	Experimental	127
7.2	Experiment A: Effect of concentration on polymer retention	127
7.2.1	Experiment AI: Static (or batch) adsorption test	129
7.2.1.1	Procedures for Static (or batch) Adsorption Experiment AI.	130
7.2.1.2	Calculation of Static (or batch) Adsorption from Experimental Data.	134
7.2.2	Static Desorption Experiment.....	135
7.2.3	Static Re-adsorption Experiment	135
7.3	Static Adsorption Experiment II - Influence of Polymer Concentration	136
7.4	Results and Discussion of Static Experiments	137
7.5	Polymer Dynamic (or flow) adsorption experiments.....	145
7.5.1	Dynamic Retention Experiments in Sandpacks and Soft Clashach Cores	149
7.5.2	Experiment A2: Polymer Dynamic Retention in Sandpacks: Effect of Concentration.....	149
7.5.2.1	Polymer injection procedure.....	150
7.5.3	Experiment B: Effect of flow-rate on polymer retention	151
7.5.3.1	Method to detect flowrate-dependent retention	153
7.5.4.1	Mechanism of inaccessible pore volume (IAPV).....	154
7.5.4.2	IAPV and Polymer Retention Calculations from Experimental Data	158

7.5.5	Experiment D: Effect of salinity and polymer type on polymer retention.....	158
7.6	Polymer dynamic (flow) adsorption experiment with Clashach Cores.....	160
7.6.1	Experiment E: Effect of permeability and pore size distributions.....	160
7.6.2	Determination of mobility reductions and residual resistance factors	163
7.7	Results and Discussion of Dynamic Experiments	166
7.7.1	Experiments A2: Effect of concentration.....	166
7.7.2	Experiment B: Effect of flow-rate on polymer retention	167
7.7.3	Experiment C: Effect of inaccessible pore volume (IAPV).....	172
7.7.3.1	Retention and IAPV Calculation method.....	174
7.7.4	Experiment D: Effect of salinity and polymer type on adsorption.....	176
7.7.5	Experiment E: Effect of permeability and pore size distributions.....	179
7.8	Permeability Reduction Mechanism.....	181
7.8.1	Impact of Polymer Retention	183
7.8.2	Polymer-Induced Formation Damage	184
7.9	Polymer-induced Formation Damage Modelling	186
7.9.1	Model Validation using different Initial Polymer Concentration and Adsorption Datasets	191
7.10	Polymer Selection model for Flood Design	193
Chapter 8	– Conclusions and Recommendations for Future Work.....	196
8.1	Conclusion	196
8.2	Recommendations for future work	199
References	201
Appendices	227

Appendix A: Experimental High Mercury Injection Capillary Pressure (MICP).....	227
Appendix B: Procedure for Experimental X-ray diffraction (XRD) and Analysis.....	233
Appendix C: Porosity and Grain Density Determination Procedure	235
Appendix D: Procedure for the Determination of Sand Particle Size	237
Appendix E: Procedure for Gas Permeability Determination	238
Appendix F: Procedure for the Turbidity (Bleach) Method for Polymer Concentration Determination	240
Appendix G: Photographs Showing Construction Stages of the Set-up used for the Implementation of the Polymer Dynamic Core flood Experiments.....	243
Appendix H: Publications.....	246

Table of Figures

Figure 1.1: Mobility control for chemical flood.....	2
Figure 1.2 - Polymer adsorption on rock surface. The picture shows the adherence of polymer molecules (forming network) on pore surface by physical adsorption (provoked by the forces of van der Waal's and hydrogen bonding). In the case of chemisorption, full chemical bonds are formed between the the polymer molecules and the solid surface.	3
Figure 1.3 - Report of number of world polymer projects in selected countries	4
Figure 1.4 - Polymer-flooding project evaluation	5
Figure 1.5 - Frequency of lithology for polymer-flooding application	5
Figure 1.6 - Role of Polymer in Enhanced Oil Recovery.	7
Figure 1.7 - Pictorial view of a typical polymer flood.....	7
Figure 2.1 - Flow Chart of Common Formation Damage Mechanism.....	19
Figure 2.2 - Common Formation Damage Mechanisms.....	20
Figure 3.1 - Chemical structure of xanthan gum.	26
Figure 3.2 - Chemical structure of partially hydrolysed polyacrylamide	27
Figure 4.1 - Effect of concentration on polymer viscosity.....	38
Figure 4.2 - Shear-thinning behaviour of polymers: (a) Xanthan gum, (b) HPAM	41
Figure 4.3 - Comparison of Power-law and Carreau Model for polymer solution.	42
Figure 4.4 - Millipore™ filter pumping/deionizing unit	44
Figure 4.5 - Pictorial views of the AR1000 Rheometer: (a) front view, (b) rear view	50

Figure 4.6 – Picture of TA Instruments advanced rheometer (model AR1000) used for the polymer characterisation.....	51
Figure 4.7 – Picture of a Jenway 3505 digital pH/ion-meter used for measuring pH of samples.....	51
Figure 4.8 - The Cone and Plate geometry schemes: (a) shows variety of geometry for different viscosity conditions, (b) shows truncation gap or height.....	52
Figure 4.9 - Explanation for the effect of shear on the shape of general flow curve.....	55
Figure 4.10 - Dependence of viscosity on shear rate for FP3630 S: (a) 500ppm, (b) 750ppm, (c) 1000ppm, (d) 2000ppm in 0.1% NaCl, pH=8.2 and 25 °C.....	56
Figure 4.11 - Effect of shear rate on viscosity of FP3630 S solution at different concentrations in 0.1% NaCl, pH=8.2 and 25 °C	56
Figure 4.12 - Dependence of viscosity on shear rate for FloComb C3525: (a) 500ppm, (b) 750ppm, (c) 1000ppm, (d) 2000ppm in 0.1% NaCl, pH=8.2 and 25 °C.....	57
Figure 4.13 - Effects of shear rate on viscosity of C3525 solution at different concentrations in 0.1% NaCl, pH=8.2 and 25 °C	57
Figure 4.14 - Data fit to Carreau model for concentrations of FP3630 S in 0.1% NaCl, pH=8.2 and 25 °C	58
Figure 4.15 - Data fit to Carreau model for concentrations of FloComb C3525 in 0.1% NaCl, pH=8.2 and 25 °C.....	59
Figure 4.16 - Shear stress vs. Shear rate of 500 ppm solution of sample FP3330 S in 0.1% NaCl, pH=8.2 and 25 °C	60
Figure 4.17 - Viscosity vs. time of 500 ppm solution of sample FP3330 S in 0.1% NaCl, pH=8.2 and 25 °C.....	60

Figure 4.18 - Dependence of viscosity on shear rate of 500 ppm solution of sample FP3330 S in 0.1% NaCl, pH=8.2 and 25 °C.....	60
Figure 4.19 - Plot of polymer concentration vs. viscosity @ shear rates of 6 s ⁻¹ and 10 s ⁻¹ : (a) FP3630 S (b) FloComb C3525 in 0.1% NaCl, pH=8.2 and 25 °C.....	61
Figure 4.20 - Effects of pH on viscosity of 750 ppm of sample FP3330 S in 0.1% NaCl measured at 25 °C and pH=8.2.....	62
Figure 4.21 - Viscosity as function of temperature for 1000 ppm of FP3630 S at pH=8.2 and at constant shear rate of	64
Figure 4.22 - Viscosity as function of temperature for 1000 ppm of FloComb C3525 at pH=8.2 and at constant shear rate of 1 s ⁻¹ from 10 °C to 70 °C	64
Figure 4.23 - Viscosity as function of temperature for 1000 ppm of FP3330 S at pH=8.2 and at constant shear rate of	65
Figure 4.24 - Effect of temperature on viscosity for 1000 ppm of three samples at pH=8.2. The temperature ramp test was performed over a range of 10 °C to 70 °C at constant shear rate of 1 s ⁻¹	65
Figure 4.25 - Effect of molecular weight on viscosity for three samples (750 ppm each) in 0.1% NaCl brine, pH of 8.2 and test temperature of 25 °C. Shear rate range of 0.1-100 s ⁻¹ typical of field project was applied to the samples.....	66
Figure 4.26 - Effect of salinity and hardness on viscosity of 750 ppm of FloComb C3525 solution of pH=8.2 measured at constant shear rate (7.3 s ⁻¹) and 25 °C.....	67
Figure 4.27 - Effect of salinity and hardness on viscosity of 750 ppm of FP3630 S solution of pH=8.2 measured at constant shear rate (7.3 s ⁻¹) and 25 °C.....	68

Figure 4.28 - Effect of salinity and hardness on viscosity of 750 ppm of FP3330 S solution of pH=8.2 measured at constant shear rate (7.3 s^{-1}) and $25 \text{ }^{\circ}\text{C}$ 68

Figure 4.29 - Effect of salinity and hardness on viscosity of 750 ppm for the three samples solutions of pH=8.2 measured at constant shear rate (7.3 s^{-1}) and $25 \text{ }^{\circ}\text{C}$. This result confirms the manufacturer’s claim that FloComb C3525 is calcium tolerant as it has lower viscosity loss as calcium ion concentration increases..... 69

Figure 4.30 - Peak hold procedure showing time-based viscosity stability for 750 ppm solution (pH=8.2) of FP3630 S in 0.4% NaCl measured at @ 10 s^{-1} and $25 \text{ }^{\circ}\text{C}$ 69

Figure 4.31 - Peak hold procedure showing time-based viscosity stability for 750 ppm solution (pH=8.2) of FloComb C3525 solution in 0.4% NaCl measured at @ 10 s^{-1} and $25 \text{ }^{\circ}\text{C}$ 70

Figure 4.32 - Peak hold comparison showing time-based viscosity stability for 750 ppm solutions (pH=8.2) of FP3630 S and FloComb C3525 @ 10 s^{-1} in 0.4% NaCl..... 70

Figure 4.33 - Continuous ramp results for sample FP3630 S in 0.1% NaCl: open cycles (o) is experimental data and dash (—) is Herschel-Bulkley model fit to experimental data. The sample has a yield stress of about 0.06452 Pa 71

Figure 4.34 - Continuous ramp step results for sample FloComb C3525 in 0.1% NaCl: open cycles (o) is experimental data and dash (—) is Herschel-Bulkley model fit to experimental data. The sample has a yield stress of about 0.06399 Pa..... 72

Figure 4.35 - Data fit to Herschel-Bulkley model for samples FP3630 S and FloComb C3525: open cycles (\circ) is experimental data for FloComb C3525, closed cycles (\bullet) is experimental data for sample FP3630 S; and dash (—) is Herschel-Bulkley model fit to experimental data for both samples. The figure shows similarity in yield stress for both samples..... 73

Figure 4.36 - Data fit to Power-law of the rheological property of FP3630 S under different polymer concentrations. The polymer solutions were prepared in 0.1% NaCl brine, adjusted to pH of 8.2 and tested at 25 °C. . 75

Figure 4.37 - Data fit to Power-law of the rheological property of C3525 under different polymer concentrations. The polymer solutions were prepared in 0.1% NaCl brine, adjusted to pH of 8.2 and tested at 25 °C. . 75

Figure 4.38 - Fitted curve showing relationship between consistency coefficient and polymer concentration for FP3630 S and C3525. The figure shows that both polymers have identical properties..... 77

Figure 4.39 - Fitted curve showing relationship between flow behaviour index and polymer concentration for FP3630 S and C3525. The figure shows similarity in flow behaviour for both polymers. 77

Figure 5.1 - Pore throat geometry model used for the simulation. The throat diameter is 3 mm, the inlet is 5 mm, and the outlet is 7 mm. 85

Figure 5.2 - Model simulation geometries and mesh arrangements: (a) 3 mm pore throat (b) 1.5 mm pore throat. 86

Figure 5.3 - Model domain velocity field: (a) 3 mm constriction, (b) 1.5 mm constriction..... 90

Figure 5.4 - Pressure distribution contour: (a) 3 mm constriction, (b) 1.5 mm constriction..... 90

Figure 5.5 - Model domain viscosity profile: (a) 3 mm constriction, (b) 1.5 mm constriction. 91

Figure 5.6 - Effects of varying shear rates on viscosity: (a) 3 mm constriction, (b) 1.5 mm constriction..... 92

Figure 5.7 - Pressure gradient effects on viscosity: (a) 3 mm constriction, (b) 1.5 mm constriction. 92

Figure 5.8 - Effects on viscosity of different shear rates for all inlet pressures: (a) 3 mm constriction, (b) 1.5 mm constriction. For Figure (a), onset of shear-thinning is at about 10 s^{-1} . Figure (b) suggests premature shear-thinning xanthan fluid behaviour induced by shear pre-deformation resulting from reduced constriction. 92

Figure 6.1 - Pore-throat size and permeability distributions (PSD) for the clashach core samples: (a) 2A, (b) 6A and (c) 7A. Continuous blue lines represent the pore throat size distributions (PSD); while the dashed red lines show the permeability distribution functions (Perm.).....103

Figure 6.2 - X-ray diffraction analysis: whole rock (for identification of mineral composition of the samples).105

Figure 6.3 - X-ray diffraction analysis $<2\mu\text{m}$ clay size fraction105

Figure 6.4 - Initial SEM/EDXA grain distribution and imaging of samples. The SEM shows clean rock samples that have been treated from its native state. The EDXA shows that silica or quartz (SiO_2) is the dominant component in the three cores representing 96.39% for core 6A, 92.63% for 2A and 80% for 7A; with potassium feldspar and Kaolinite in trace amounts. This is clearly shown by the various peaks. This result is similar to that obtained from XRD analysis.106

Figure 6.5 - Leica DFC420 Digital Microsystems used to capture high-resolution images of the silica sands.....108

Figure 6.6 - Microscopic image of the US silica sand sizes used for the polymer adsorption flood: (a) sample 20/40 sieve mesh, and (b) sample 40/60 sieve mesh (5x Objective magnification).108

Figure 6.7 - Mechanical shaker and mesh arrangement used for the sieve analysis.109

Figure 6.8 - Grain size distributions by weight percent of fractions retained for the 40/60 and 20/40 US silica sands: (a) Histogram (b) Scatter chart.112

Figure 6.9 - Cumulative grain size distributions by sieved weight for the 40/60 and 20/40 US silica sands.....	113
Figure 6.10 - Experimental rig design schematic and setup for the implementation of the polymer dynamic coreflood.....	116
Figure 6.11 - Pictorial view of the core flood rig.	117
Figure 6.12 - Layout of the National Instruments (NI) data logging interface design.	119
Figure 6.13 – Picture showing (a) Druck DPI 615 IS, (b) performing rig leakage test	121
Figure 6.14 – Picture showing transducer calibration using the Druck DPI 615 IS pressure calibrator.....	121
Figure 6.15 - Shear rate simulation in sandpacks: (a) 20/40 Silica sand (b) 40/60 Silica sand.....	123
Figure 6.16 - Shear rate simulation in Clashach cores: (a) Core 2A, (b) Core 7A, (c) Core 6A and (d) Core 1A.....	125
Figure 7.1 - Standard calibration curve for polymer solution concentration measurement for sample FP3330 S used for this study (according to the law of Beer-Lambert).	132
Figure 7.2 - Standard calibration curve for polymer solution concentration measurement for sample FP3630 S used for this study (according to the law of Beer-Lambert).	132
Figure 7.3 - Effects of mixing time on the calibration curve for FP3630 S.....	133
Figure 7.4 - IECCentra-4X centrifuge machine.	133
Figure 7.5 - UV-Visible Chemstation software (Agilent 8453 model) used for sample and effluent concentration determination.	134

Figure 7.6 - Some of the stock bottles used for static adsorption test measurements.....	136
Figure 7.7 - Pictorial view of some experimental polymer effluent prepared for analysis.....	137
Figure 7.8 - Static adsorption test plot of polymer concentration loss vs. time for sample FP3630 S	138
Figure 7.9 - Adsorption kinetics using silica sand 40/60: (a) Static polymer adsorption, microgram per gram of solid vs. time for sample FP3630 S; (b) Combined plot of static adsorption and concentration loss vs. time for sample FP3630 S. (NB): Adsorption reached a maximum within approximately 1 day and then levelled off; suggesting an imperfect monolayer-type of instantaneous adsorption.	139
Figure 7.10 - Comparison of (a) adsorbed and (b) concentration loss for static (batch) adsorption experiments for FP3630 S and FP3330 S on silica sand. Molecular weight: curve: (A) 8 million, (B) 20 million Dalton.	140
Figure 7.11 - Polymer adsorption kinetics on silica sand for FP3630 S: (a) 50 ppm, (b) all concentration.	141
Figure 7.12 - (a) Desorption kinetics for FP3630 S HPAM after rinsing in 3.0% TDS1 brine, (b) Langmuir condition comparison for the initial and residual adsorption cases after rinsing in 3.0% TDS1 brine in desorption test. After rinsing in brine (-), residual adsorption did not match up with the initial (+). Because the extended chain from high Mw polymers have the tendency to attach to different polar points on the rock surface, it is therefore statistically improbable for a polymer molecule to let go of all points of attachments simultaneously and proceeds towards total reversibility as proposed by Langmuir.....	144
Figure 7.13 - Readsorption test on used and fresh sands.	145
Figure 7.14 - Static adsorption isotherm of FP3630 S HPAM in silica sand.	145

Figure 7.15 - Laboratory area method for polymer adsorption and IAPV measurements as suggested by Dawson and Lantz. NB: For this illustration, adsorption is the sum of areas A and B.	147
Figure 7.16 - Laboratory mid-point method for measurements of polymer adsorption as suggested by Dominguez and Willhite.	147
Figure 7.17 - Picture showing measurement of effluent concentration by the Viscosity method using Capillary Viscometer. NB: temperature stability was taken as the most important precaution in the use of this method.	153
Figure 7.18 - Optical Emission Spectrometer used for the detection of tracer concentration in effluent samples (ICP).	157
Figure 7.19 - Normalised pore throat size distribution functions from mercury injection on clashach core samples 7A and 2A: (a) Semi-log plot, (b) Cartesian plot.	161
Figure 7.20 - Normalised permeability distribution functions for clashach core samples 7A and 2A: (a) Semi-log plot, (b) Cartesian plot.	162
Figure 7.21 - Capillary pressure (P_c) curves from mercury injection on clashach core plugs. The more uniform the pore sizes, the flatter the transition zone of the P_c curve. Hence, core 2A has more uniform pore sizes.	163
Figure 7.22 - Leverret J-Function for clashach cores 2A and 7A. The J-function is used to classify as to rock type. The two curves show that the samples 7A and 2A belong to the same rock type (i.e., quartz) and therefore, have geometric similarity. However, core 2A reflects much larger pore sizes as it has larger J-values.	163
Figure 7.23 - Dynamic adsorption isotherm of FP3630 S HPAM in silica sand.	167

Figure 7.24 - Rate-dependent retention behaviour of FP3630 S HPAM on silica sand: (a) during low rate injection cycle (0.8 ml/min), (b) during the first high rate injection cycle (3 ml/min), (c) during the next high rate injection cycle (6 ml/min).	169
Figure 7.25 - Concentration profiles of 500 ppm FP3630 S at 0.8 ml/min, 3 ml/min and 6.0 ml/min.	170
Figure 7.26 - Plot of concentration profiles of the dynamic method for the study of the effect of flow rate on polymer retention for all flow rates investigated.	172
Figure 7.27 - Effect of flow rate variation and polymer type on polymer adsorption.....	172
Figure 7.28 - Retention of FP3630 S HPAM in 20/40 sandpack at: (a) first injection, (b) second injection.....	173
Figure 7.29 - Dynamic tracer test with HPAM FP3630 S for the determination of inaccessible pore volume and retention in sandpack.	176
Figure 7.30 - Effect of salinity/hardness and polymer type on polymer adsorption on silica sand (0.043% Ca ²⁺ in TDS1 and 0.69% Ca ²⁺ in TDS1).....	178
Figure 7.31 - Shows that presence of divalent calcium ions in brine enhances adsorption of negatively charged polymer molecules onto quartzite by two probable mechanisms: (1) Bridging:- Ca ²⁺ ions create a link between the negatively charged polymer molecules and the negatively charged quartz surface, (2) Charge coordination:- Ca ²⁺ ions neutralizes part of the negative sites and reduces the electrostatic repulsion.....	179
Figure 7.32 -Pore size distribution effect on flow of 500 ppm of polymer FP3330 S through clashach in TDS1.	180
Figure 7.33 - Pore size distribution effect on reduction of clashach permeability after flowing 500 ppm of polymer FP3330 S in TDS1.	180

Figure 7.34 - Effect of pore size distributions on adsorbed layer regime after flowing 500 ppm of polymer FP3330 S through clashach in TDS1. ..	181
Figure 7.35 - Effect of permeability on retention of 500 ppm 3330 S HPAM on clashach cores in brine TDS1.	182
Figure 7.36 - Impact of adsorption on polymer bank injection.....	184
Figure 7.37 - Impact of adsorption on polymer bank injection for two different polymer products.	184
Figure 7.38 - Characteristic flowrate-pressure drop behaviour for brine before and after flow of polymer FP3330 S through Core sample 1A.....	185
Figure 7.39 - SEM image: (a) before (b) after polymer flow on core 1A. NB: Fig. 7.39b shows SEM image after polymer flow with polymer draping grains and restricting pores as indicated by red circles.....	185
Figure 7.40 - Measured and calibrated permeability damage variation as function of adsorbed polymer, showing the effect of salinity (300 ppm of FP3630 S with 0.043% Ca ²⁺ in TDS1 brine).....	189
Figure 7.41 - Measured and calibrated permeability damage variation as function of adsorbed polymer, showing the effect of salinity (300 ppm of FP3630 S with 0.69% Ca ²⁺ in TDS1 brine).	190
Figure 7.42 - Measured and predicted permeability damage variation as function of adsorbed polymer, showing the effect of salinity (500 ppm of FP3630 S with 0.043% Ca ²⁺ in TDS1 brine).....	192
Figure 7.43 - Measured and predicted permeability damage variation as function of adsorbed polymer, showing the effect of salinity (500 ppm of FP3630 S with 0.69% Ca ²⁺ in TDS1 brine).	192
Figure 7.44 - Polymer flow and brine flushed resistance factors for 500 ppm of FP3330 S and FP3630 S in TDS1 during flow in core 2A.	195

Table of Tables

Table 1.1 - Primary Functions of Oilfield Polymers.	6
Table 2.1 - Impact of Formation Damage on oil and gas Production. The 'skin' is an indication of increase or decrease in production. Positive skin value means production loss due to formation damage, and negative skin value implies production enhancement by stimulation..	21
Table 4.1 - Details and properties of the polymers used for the Research.	45
Table 4.2 - Percentage activity of polymer samples calculated from Eqn. 4.8.....	48
Table 4.3 - Power-law curve fitting parameters for FP3630 S and FloComb C3525.	76
Table 4.4 - Fitting constants for polymer rheological models.....	78
Table 5.1 - Simulation input values	89
Table 6.1 - Ionic composition of the brines used for the core flood tests: (a) Low salinity Brine composition (TDS1), (b) Hard, high-salinity Brine composition (TDS2).....	96
Table 6.2 - Clashach sample core dimensions	102
Table 6.3 - Clashach sandstones petrophysical properties.....	102
Table 6.4 - Whole rock X-ray diffraction analysis (for identification of mineral composition of the clashach cores). The table shows that the core samples are quartzitic in nature with low contents of Potassium Feldspar and Illite+Mica.	104
Table 6.5 - X-ray diffraction analysis <2 µm clay size fraction	105
Table 6.6 - Characteristics of the 20/40 US silica sand used in this study..	110
Table 6.7 - Characteristics of the 40/60 US silica sand used in this study..	111

Table 6.8 - Properties of the silica sands.	115
Table 7.1 - Residual adsorption for FP3630 S HPAM after rinsing in 3.0% TDS1 brine in desorption test.	143
Table 7.2 - Dynamic polymer retention in sandpacks. For this particular sand, a pre-calculated injection rate of 1.0 ml/min that will induce shear rates of about 10-100 s ⁻¹ that are comparable to field applications was used.....	149
Table 7.3 - IAPV literature values.....	156
Table 7.4 - Comparison of Static and Dynamic Retention in Silica sand for FP 3630 S.	167
Table 7.5 - Polymer and porous media properties used in calculating models parameters.	188
Table 7.6 - Input values and model results used in the models construction for 0.043% Ca ²⁺ concentrations in brine TDS1.....	188
Table 7.7 - Input values and model results used in the models construction for 0.69% Ca ²⁺ concentrations in brine TDS1.	189
Table 7.8 - Showing model fitting parameters and errors from Eqn. (7.12).	190
Table 7.9 - Screening Index for polymers (Eqn. 7.21).....	195

Abstract

Polymers are among the most important of various oilfield chemicals and are used for a variety of applications in the oil and gas industry (OGI) including water and gas shutoff, drilling mud viscosity modification, filtration loss control (FLC), swellable packers, loss circulation material (LCM) pills, enhanced oil recovery (EOR), fracture treatment and cleanup, chemical placement, etc. The deposition and retention of polymer molecules in porous media and their interactions with rock and fluids present complex phenomena that can induce formation damage. Formation damage due to polymer retention can occur via mobility reduction in three possible mechanisms of polymer-induced formation damage: 1) pore-throat blocking, 2) wettability alteration (which can alter permeability), and 3) increase in reservoir fluid viscosity. Physical adsorption can also cause permanent permeability impairment (formation damage). This polymer-induced formation damage (causing a reduction in net oil recovery) continues to be a fundamental problem in the industry owing to the rather shallow understanding of the mechanics of polymer-brine-rock interactions and the polymer-aided formation damage mechanisms.

Most models available for polymer risk assessments appear to be utilised for all scenarios with unsatisfying results. For example, only very little, if any, is known on how polymer type, particularly in the presence of brine type impact on formation damage. In other words, one of current industry challenges is finding effective polymers for high salinity environments. Also, the effect of polymer charge, as well as charges at the brine-rock interface are issues that require a deeper understanding in order to address the role polymer play in formation damage. Furthermore, no much recognition has been given to polymer rheological behaviour in complex porous media, etc. The OGI therefore still faces the challenge of the inability to correctly predict hydrolysed polyacrylamide (HPAM) viscosity under shear degradation; and consequently have not been able to meet the need of production predictions. The effect of the

above mentioned factors, etc have not been fully integrated into the polymer formation damage modelling.

In this PhD research work, theoretical, numerical, laboratory experiments and analytical methods were used to further investigate the mechanics of polymer-brine-rock interactions and establish the mechanisms for formation damage related to polymer application. Three different hydrolysed polyacrylamide (HPAM) products (SNF FP3630 S, 3330 S and FloComb C3525) were used in the experiments; while Xanthan gum was used in the simulation work. The following variables were considered: 1) polymer type, 2) effect of concentration, 3) effect of salinity/hardness, 4) effect of permeability and pore size distributions, 5) effect of inaccessible pore volume (IAPV) on retention, 6) effect of flow rate (where a special method was established to quantify the effect of flow rate on polymer retention). Laboratory rheological and adsorption experiments were designed and conducted. Experimental results indicate that higher concentration of calcium divalent ions in brine help promote polymer retention on rock surface. On the basis of the experimental results, empirical models were developed and validated to: 1) predict HPAM rheological behaviour over a wide range of shear rates, 2) predict salinity-dependent polymer-induced formation damage, 3) in addition, a modified screening model that can aid polymer selection for field application design is proposed. Overall, these models can therefore serve as useful tools, and be used for quick look-ahead prediction and evaluation of polymer related formation damage in oil and gas-bearing formations.

1

Chapter 1 – Introduction

1.1 General

Polymer flooding has been widely used as an attractive alternative to conventional water flooding in enhanced oil recovery (EOR) and in oilfield water and gas shut-off. The main objectives being to increase the oil recovery factor by decreasing the mobility ($\lambda=k/\mu$) between the displacement (water) and displaced (oil) fluid (Figure 1.1). According to Da Silva et al. (2010) and Needham and Doe (1987), polymer solutions can lead to increase in oil recovery by: 1) increasing the water phase viscosity (i.e. decreasing the water/oil mobility ratio) (Green and Willhite, 1998), 2) diverting the injected water from zones that have been swept, 3) the effects of polymers on fractional flow. Although polymer flooding cannot reduce residual oil saturation, it has been argued (Du and Guan, 2004; Da Silva et al., 2010) that it allows the residual oil saturation to be attained more economically and/or more quickly. Although polymer flooding has been used in matured reservoirs with positive results (Agnew, 1972), the appropriate time to apply polymer flooding most

effectively is in the early stages of water flooding while mobile oil saturation is still high (Chang, 1978).

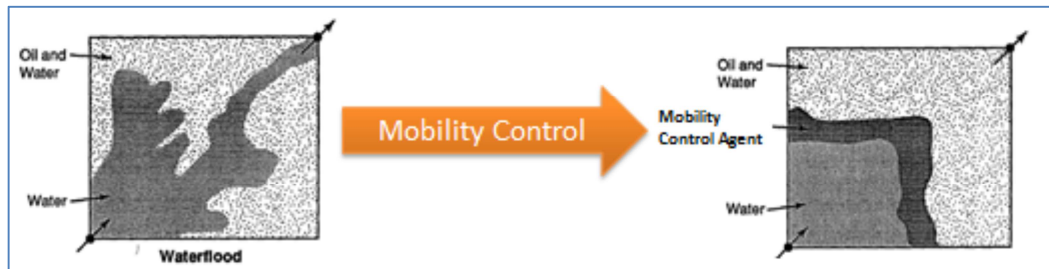


Figure 1.1: Mobility control for chemical flood (Green and Willhite, 1998)

However, it is widely recognised that when polymer solutions interact with a solid surface, the polymer molecules may be retained on the solid surface by both the physical forces of van der Waal's and hydrogen bonding forces (Figure 1.2). Retention refers to all mechanisms that remove polymer from the transported aqueous phase. These include: adsorption, mechanical entrapment and hydrodynamic (or rate) retentions. Polymer retention on petroleum reservoir rock surfaces is considered as a disadvantage in that polymer alter the rock absolute permeability, and of course, phase effective permeability via adsorption driven surface change. Furthermore, Polymer retention on rock surfaces represents additional resistance to flow, causes mobility control effect to be lost, causes a loss of the active chemical agent specie from solution to the reservoir, and a consequential net reduction in the polymer slug; thus a reduction in net oil recovery. All these make polymer injection project an expensive recovery method due to the high cost of polymer chemicals.

The deposition and retention of polymer molecules in porous media and their interactions with rock and fluids present complex phenomena that can induce formation damage. Formation damage due to polymer retention can occur via mobility reduction in three possible mechanisms of polymer-induced formation damage: 1) pore-throat blocking, 2) wettability alteration (which can alter permeability), and 3) increase in

reservoir fluid viscosity. Physical adsorption can also cause permanent permeability impairment (formation damage).

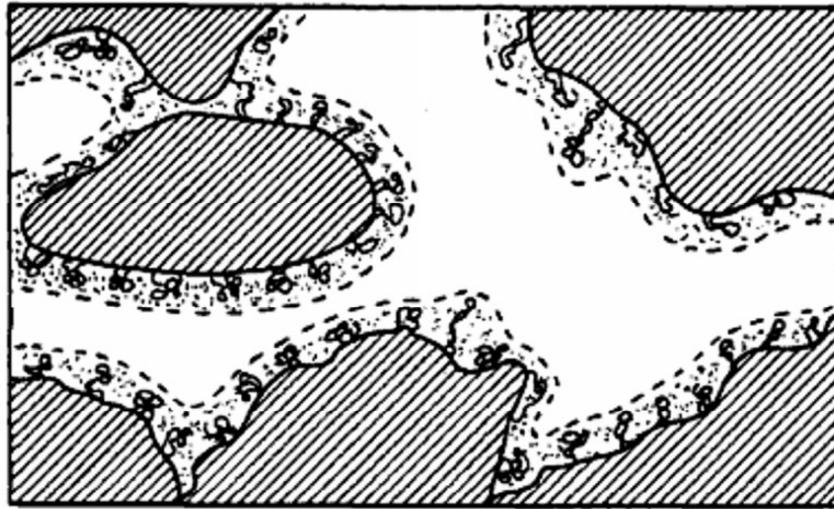


Figure 1.2 - Polymer adsorption on rock surface (Dang et al., 2014). The picture shows the adherence of polymer molecules (forming network) on pore surface by physical adsorption (provoked by the forces of van der Waal's and hydrogen bonding). In the case of chemisorption, full chemical bonds are formed between the polymer molecules and the solid surface.

According to Dang et al. (2011), loss of additive and loss of viscosity and elasticity arising from polymer retention leads to decrease in final oil recovery. Adsorption and retention are therefore factors that influence the success of chemical EOR flooding and other projects because the less the polymer adsorbed, the less the quantity of chemical agent required for the injection, and the less will be the project cost. It is believed (Da Silva et al., 2010) that pre-field laboratory evaluation methodology is a better option for selecting polymer for a specific target field conditions. Furthermore, polymer pre-selection should also be based on the market choice, availability, cost as well as its physicochemical characteristics criteria.

A lot of surveys have been conducted to show that polymer application is increasing (Roger et al., 2012; Dickson et al., 2010; Al-Bahar et al., 2004; Carcoana, 1982; Standnes and Skjevraak, 2014; Saleh et al., 2014; Hui and Xu, 2009) and the success of various projects have also been documented (Wang and Wu, 2002; Wang et al., 2011; Yang et al., 2004; Delamaide et al., 2014). Furthermore, evidences of improved efficiency in

the application (both in field and laboratory) have been shown to increase the number of potential reservoirs targeting polymer flooding as an EOR technology (Liu et al., 2007; Wang et al., 2011; Seright, 2010; Seright et al., 2011; Alvarado and Manrique, 2010). On the basis of literature data and probably personal experience, Saleh et al. (2014) published reports on some world polymer-flooding projects in some selected countries (Figure 1.3) and ranked these projects on their merits in terms of success or failure (Figure 1.4). Saleh et al. (2014) also showed that most of these applications were carried out in sandstone reservoirs (Figure 1.5); and HPAM being used in most of the projects (Standnes and Skjevrak, 2014).

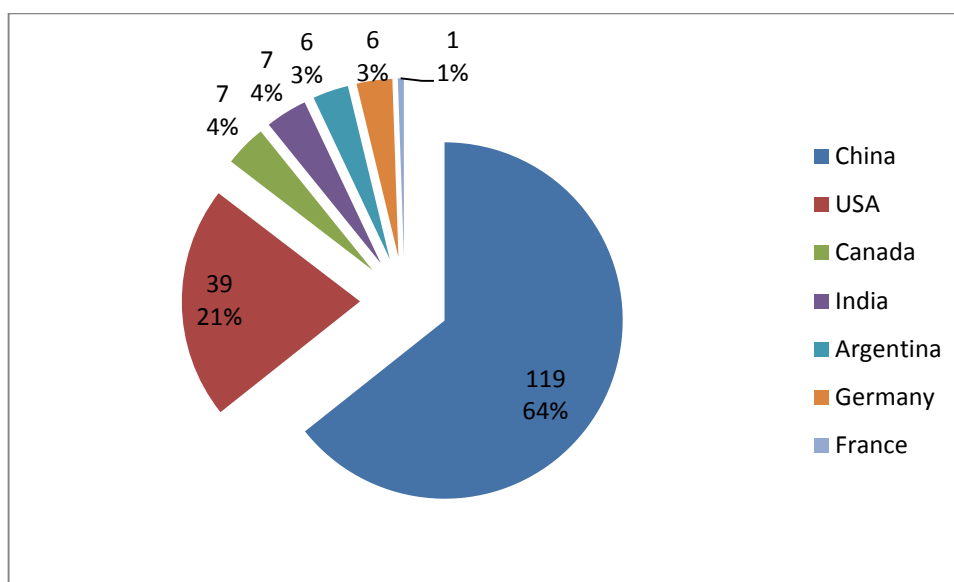


Figure 1.3 – Report of number of world polymer projects in selected countries (Saleh et al., 2014)

In some very recent surveys (Standnes and Skjevrak, 2014; Saleh et al., 2014) the failures recorded for some of the polymer-flooding projects were attributed to either technical (e.g., location, salinity and hardness, injectivity problems, formation temperature, etc), or economics (e.g., chemical and operating costs, world crude oil prices, investment and rate of return, etc) or to political problems (e.g., government policies, etc).

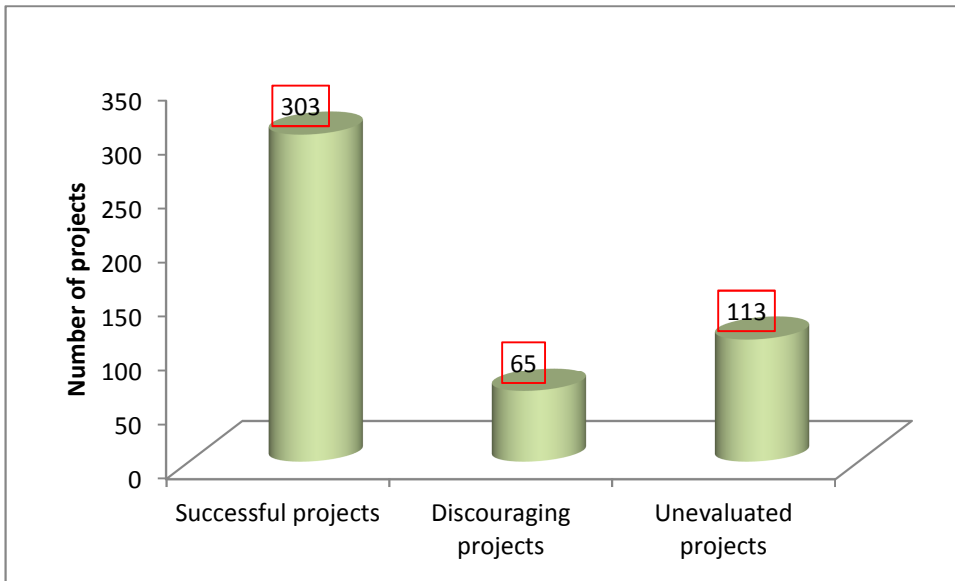


Figure 1.4 - Polymer-flooding project evaluation (Saleh et al., 2014)

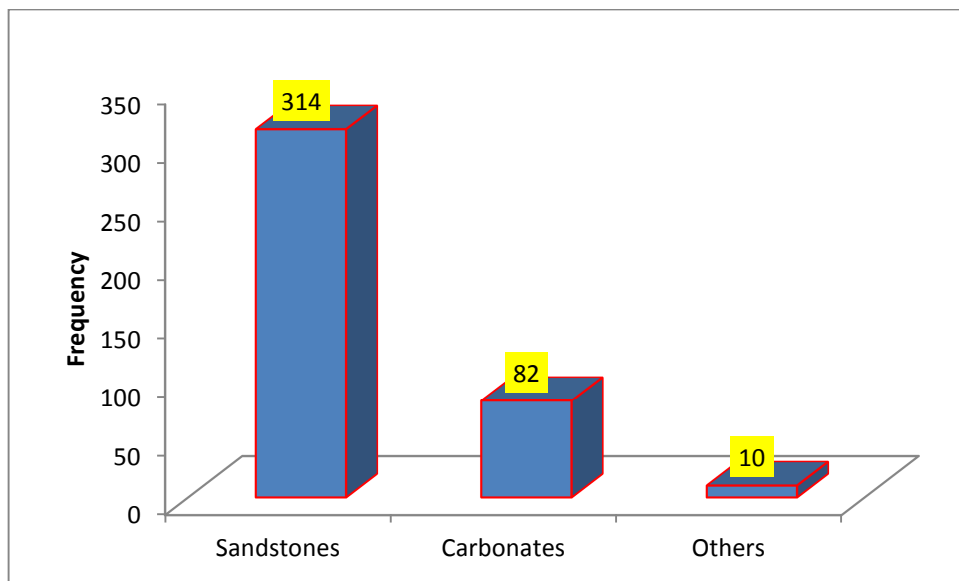


Figure 1.5 - Frequency of lithology for polymer-flooding application (Data source: Saleh et al. 2014)

1.2 Polymer Applications in Petroleum Engineering.

A polymer is an organic chemical substance composed of giant molecules formed by the union of many smaller molecules (Ezell et al., 2010). Polymers vary in function and basic properties and are classified as natural (e.g. starch, biopolymers, and guar gum), modified-natural (e.g. cellulosics (CMC, HEC), carboxymethyl starch) and synthetic (e.g.

polyacrylate, polyacryamide cationic polymers). Polymers are non-toxic, high viscosifying, degradable materials which do not cause environmental problems. These unique characteristics make them the best materials for use, both for drilling and EOR processes. In petroleum production, polymers lubricate and reduce friction in drill-hole in concentrations of about 0.1-0.4 %w/w; while in EOR, they reduce water mobility by increasing viscosity and decreasing absolute permeability in concentrations of about 0.05-0.2 %w/w (García-Ochoa et al., 2000).

Table 1.1 summarises the primary functions of polymers in oilfield operations; while Figure 1.6 (Moritis, 2000; Stosur, 2003; Stosur et al., 2003) shows the role of polymer in enhanced oil recovery (EOR). Figure 1.7 shows pictorial of a typical polymer flood facility.

Table 1.1 - Primary Functions of Oilfield Polymers (Krueger, 1988).

Viscosifiers	Filtrate Control	Flocculation	Shale Stability
✓ Xanthan Biopolymers	✓ Cellulosics	✓ Acrylates	✓ Acrylates
✓ Cellulosics	✓ Acrylamides	✓ Maleic Anhydride derivatives	✓ Acrylamides
✓ Guar gum	✓ Starch		
✓ Acrylamides			

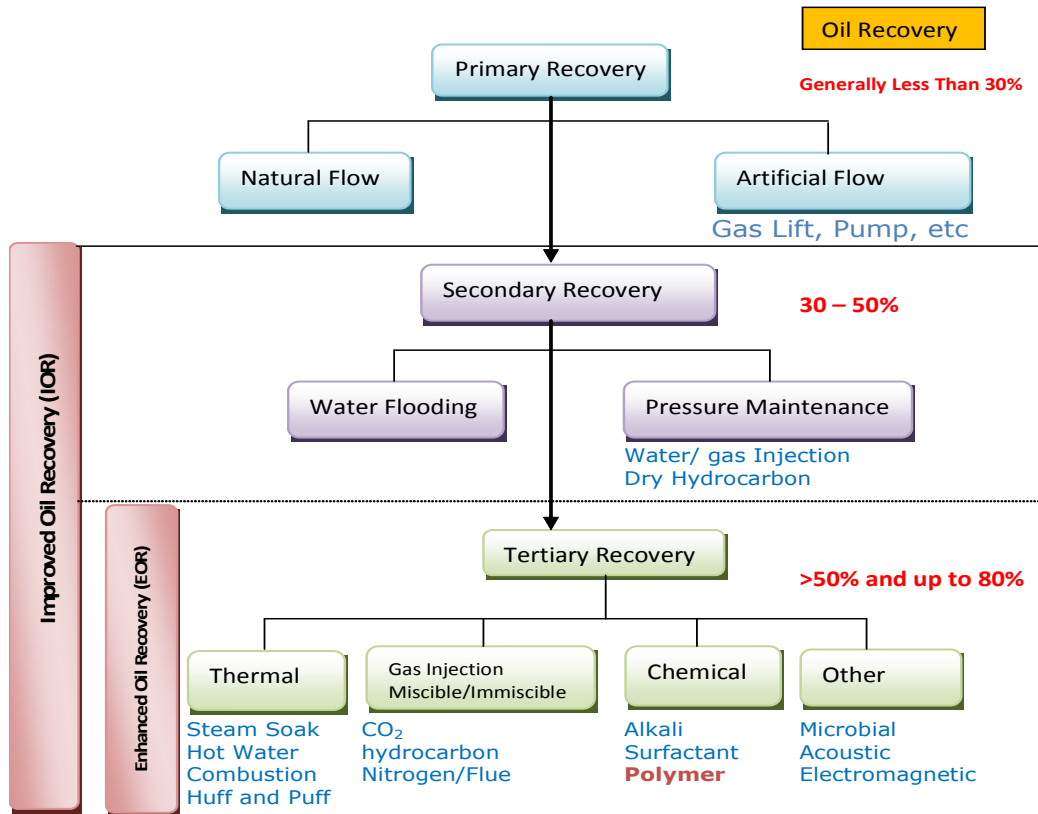


Figure 1.6 - Role of Polymer in Enhanced Oil Recovery (modified after Oil and Gas Journal: 20 March, 2000).

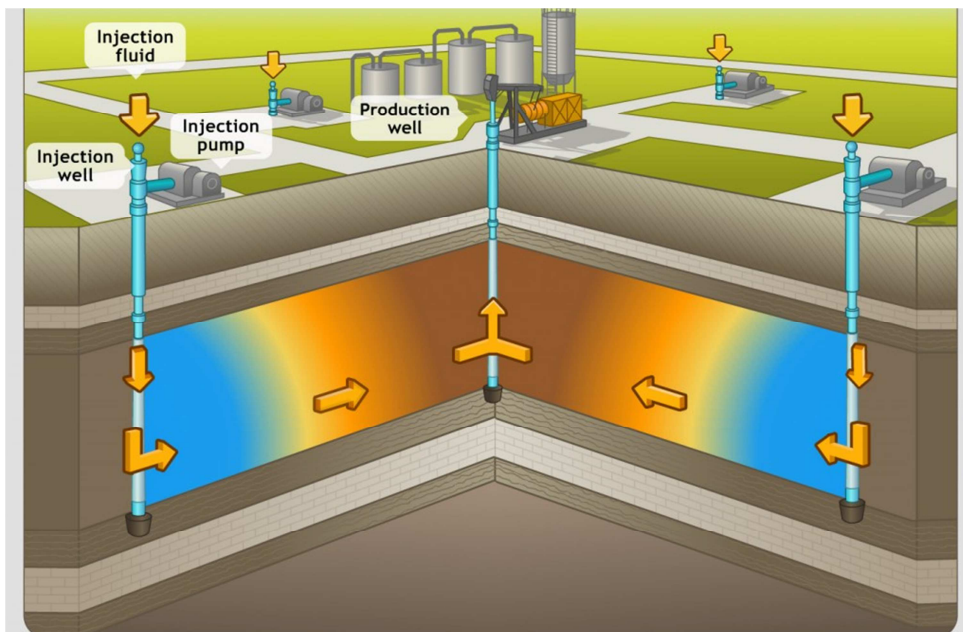


Figure 1.7 - Pictorial view of a typical polymer flood.

The loss of additive and loss of viscosity and elasticity arising from polymer adsorption/retention and the consequent increase in project costs are major issues to the OGI. Although several polymer-retention values for various conditions have been reported, majority of the experimental approaches, especially those involving multiphase flow systems, had difficulties in isolating the explicit polymer adsorption contribution to fluid permeability damage. Basically, most models available for polymer risk assessments appear to be utilised for all scenarios with unsatisfying results. For example, only very little, if any, is known on how polymer type, particularly in the presence of brine type and composition impact on formation damage. In other words, one of current industry challenges is effective polymers for high salinity environments. Also, the effect of polymer charge, as well as charges at the brine-rock interface are issues that require a deeper understanding in order to address the role polymer play in formation damage. Furthermore, no much recognition has been given to polymer rheological behaviour in complex porous media, etc. Polymer solutions are non-Newtonian fluids that conform to the power-law. Greater loss of polymer viscosity has been attributed to the effect of shear rate. However, most available models focussed on RRF in modelling rheological behaviour of polymers in porous media. Quite unfortunately, the oil and gas industry (OGI) still faces the challenge of the inability to correctly predict HPAM viscosity under shear degradation; and consequently have not been able to meet the need of production predictions. The effect of the above mentioned factors, etc have not been fully integrated into the polymer formation damage modelling. Generally, there still exists a lack of consensus among researchers on the basic mechanisms and the set of conditions under which the results of their various studies are applicable.

1.3 Research Aims and Objectives

1.3.1 Aims

The major aim of this research is to gain a deeper understanding of the explicit polymer adsorption contribution to formation damage during polymer project operations (e.g., EOR) that have not been well

investigated; and provide a benchmark for understanding the significance and scale of formation damage caused by polymer applications in oil and gas-bearing formations.

1.3.2 Objectives

The research specific objectives include the following:

- 1) To make critical review of formation damage conditions, the factors and mechanisms responsible for its occurrence and of the impact of polymer-induced formation damage on oil and gas productivity.
- 2) To conduct experimental rheological characterization and measurements of field parameters affecting polymers and develop viscosity models as tools for the prediction of HPAM viscosity in field applications.
- 3) To experimentally investigate the effect of electrostatic interactions between the solid surface and polymer molecules with respect to polymer type and brine composition as a means of understanding polymer-induced formation damage.
- 4) To develop rheology and formation damage models for polymers that can be used for either selection or quick look-ahead prediction or evaluation of polymer rheology and related formation damage.
- 5) To validate the models using experimental data obtained in objectives 1, 2 and 3.

1.4 Methodology

Mathematical modelling based studies provide a reliable means of evaluating potential benefits of polymer pre-injection. However, such studies require input data that permit the model to simulate the physical processes that may occur in the reservoir. The basic information that reflects the mechanism of the polymer adsorption process (such as rock type, polymer type, molecular weight, salinity/hardness, concentration,

pH, porous media structure, chemistry of the aqueous phase, porous media surface area, porosity and permeability of the porous media, pore-size distribution, grain-size distribution, flow rate, amongst others) is still to be obtained by laboratory experimental means. This means that adsorption studies are a vital part of laboratory evaluation of any recovery scheme that involves the use of adsorbable materials. Therefore, theoretical, numerical, laboratory and analytical methods were adopted for the realisation of the project objectives.

In this research, detail initial experimental rheological behaviour of the polymer samples was conducted as parametric study to investigate field factors that affect polymer application. Thereafter, a preliminary numerical simulation study using computational fluid dynamics (CFD) to predict single-phase flow behaviour of shear-thinning fluids (xanthan gum) in complex porous media was done. Monophasic laboratory core flood studies were designed and conducted to allow measurements and quantification of the extent or degree of the polymer-aided-damage and further visualization of the specific mechanisms. Two different HPAM products were used in the experiments as the products used in each field polymer applications are not the same. The effect of polymer adsorption during polymer application was studied in relation to adsorption and desorption kinetics. The mechanism of polymer-induced formation damage was quantitatively described using two different clashach cores having different permeabilities and pore size distributions. The following specific variables were considered in the research experimental work: 1) polymer type, 2) effect of concentration, 3) effect of salinity/hardness, 4) effect of permeability and pore size distributions, 5) effect of inaccessible pore volume (IAPV) on retention, 6) effect of flow rate (where a method was established to quantify the effect of flow rate on polymer adsorption); and analytical models suitable for the prediction of polymer-related formation damage in oil and gas-bearing formations were developed and validated.

On the basis of the generated experimental data, simple to use models for predicting HPAM rheological behaviour and polymer-induced formation damage as well as analytical correlations and/or models were developed to aid polymer screening and selection for field applications.

1.5 Contributions to knowledge

This research was conducted with the intention of making contributions to the body of knowledge with regard to a better understanding of the role of polymers in formation damage during polymer injection projects in the area of petroleum engineering. The following were achieved:

1.5.1 Polymer-induced formation damage prediction models

Simple to use empirical models were developed to predict salinity-dependent polymer-induced formation damage; and the validated models matched experimental data. With knowledge of adsorption profiles for different parameters, the model can also be used to predict polymer-induced formation damage based on concentration, permeability, polymer type, formation lithology, etc for similar high salinity conditions. In addition, a simple modified screening model that can aid polymer selection for field application design is proposed.

1.5.2 HPAM rheological behaviour prediction models

Simple empirical models to predict HPAM viscosity at a wide range of shear rate is developed. The models were found to effectively characterise the rheological behaviour of the HPAM polymer solutions investigated. These models can therefore serve as useful tools for HPAM viscosity prediction in field applications.

1.5.3 Limitation of the Langmuir isotherm

a) Langmuir isotherm was customarily used for the description of reversible adsorption of small gas and surfactant molecules. Dawson and Lantz (1972) first suggested its use for polymer adsorption without any experimental justification where they apparently presumed polymers would follow similar adsorption behaviour as surfactants (i.e., an

assumption that polymer adsorption proceeds towards zero and is reversible). However, experimental findings from this research indicate that most polymer retention was observed to be irreversible for EOR polymers that have high molecular weight and extended chains. This study proposes that Langmuir-law should be reformulated for polymer retention in conventional simulators as Langmuir-law was probably always not correct logically since the law was based on the assumption that polymer retention proceeds towards zero and is reversible. Notwithstanding, existing simulators would retain their credibility only if the Langmuir level is positioned to be reached at very low concentration, with high injection polymer concentration. Otherwise, it would be beneficial to integrate the results of this research in polymer flooding simulators.

b) In the re-adsorption test, it was found in this study that polymer adsorption was low when it was first treated with low-concentration polymer. When higher concentration was used to contact same rock, there was no significant change in retention because there were no vacant sites readily available for further attachments of polymer molecules. From the point of view of field operations, this work proposes therefore that it could be reasonable to first inject a low-concentration polymer solution bank before the main flood bank in order to reduce polymer retention and thereby maximise use of chemicals.

1.5.4 Unique experimental approach

a) The variation of polymer retention with flow rate was investigated and the magnitude of this retention as function of flow rate was determined. This research established a better method to quantify polymer incremental retention (both reversible and irreversible) in relation to flow rate increase.

b) An IAPV to polymer flow exists in both sandstones and unconsolidated sands. Field polymer flood is designed on the assumption that IAPV is zero. This, of course, is a conservative approach. An

inconsistent and unexplained behaviour on IAPV is revealed by the literature survey (Szabo, 1975). The results of this research show that rate variation increases retention and decreases IAPV. Specifically, the decrease in IAPV was observed to increase polymer retention.

1.5.5 Polymer Selection Model

On the basis of combination of experimental results, a simple modified screening model that would aid polymer selection prior to field operations was developed.

1.6 Description of Chapters

The content of this thesis has been arranged in the following format:

Chapter 1: This chapter discusses the background introduction of the research in relation to the application of polymers in the oil and gas industry (OGI), the research question, technical issues, as well as the gaps that inform the need for new work.

Chapter 2: This chapter discusses the general theory and mechanisms of formation damage.

Chapter 3: This chapter deals with critical and systematic review of the literature on polymer flooding technology and application in the OGI with particular emphasis on polymer-induced formation damage.

Chapter 4: In this chapter, a detailed experimental rheological behaviour of the polymers used in the research is presented. In addition, models developed for characterising polymer rheological behaviour are also presented.

Chapter 5: In the literature, no proper recognition has been given to the polymer fluid rheological behaviour, particularly in complex porous media. Therefore, a preliminary simulation study using computational fluid dynamics (CFD) method in COMSOL Multiphysics software to predict rheological behaviour of Single-Phase non-Newtonian shear-thinning

fluids (xanthan gum) polymer solutions in complex pore geometry was performed and is presented in this chapter.

Chapter 6: Detailed experimental material screening and characterisation before they were used for the implementation of core flood experiments are described and presented in this chapter.

Chapter 7: Experimental procedures, method overview (i.e., the justification for adopting a particular method) and experimental results are discussed and presented in detail in this chapter. The basic information that reflects the mechanism of the polymer adsorption process (such as rock type, polymer type, molecular weight, salinity/hardness, concentration, pH, porous media structure, chemistry of the aqueous phase, porous media surface area, porosity and permeability of the porous media, pore-size distribution, grain-size distribution, flow rate, amongst others) were all studied by laboratory experimental means and are also presented in this chapter.

Chapter 8: This chapter summarizes the entire research in a conclusion, contribution to the body of knowledge and possible recommendation for future work.

The appendix section describes the experimental details involved in the characterisation of experimental materials used in the research.

A discussion on the theory and mechanism of formation damage is presented in chapter two that follows.

2

Chapter 2 – Theory and Mechanisms of Formation Damage

2.1 General

Irrespective of the range of ideas, formation damage, for a long time, has persisted as collective or combined action of operations carried out in a well from the initial drilling, through the production and workover phases to final abandonment (Annie et al., 1999). Almost all field operations such as drilling, completion/intervention, oil and gas production, chemical injection for enhanced/improved oil recovery (EOR/IOR), perforation, etc. are potential sources of damage (or flow restriction) to oil and gas well productivity. For example, on application, polymer can adsorb on solid rock surfaces resulting in formation damage that represents additional resistance to flow, hence a loss of the active chemical agent specie from solution to the reservoir, and a consequential net reduction in the polymer slug; thus a reduction in net oil recovery.

Formation damage is said to occur when there is loss or impairment of permeability and porosity of a hydrocarbon or petroleum bearing formation by diverse processes (Civan 2007, 2011). Alternatively, it can be described as a situation that leads to lower than expected oil and gas

production rate from a hydrocarbon bearing rock due to barriers that develop within the vicinity of the near wellbore. (Amaefule et al., 1988). A more general definition for formation damage is anything that causes hindrance to well productivity/injectivity by deposition/adsorption and flow modification at and around the wellbore of a given reservoir formation arising from the combined effects of reduction in the formation absolute permeability, alteration in the relative permeability of the formation to a specific fluid; and alteration in the viscosity of the mobile fluid. Formation damage results from a combination of reservoir mechanics from drilling to abandonment. The mechanisms causing formation damage have been attributed mainly to migration and deposition of fines; including chemical molecular adsorption (Civan, 2007). Bennion (2002) sub-divided the types and common formation damage mechanisms according to their importance and significance:

- Formation damage resulting in reduction of absolute permeability due to:
 - Particle plugging due to solids in drilling and completion fluids invading the reservoir rock pore spaces.
 - Sensitive Swelling Clays: Insitu clays in reservoir rocks are very sensitive to fluids invasion and may swell thus blocking the pores.
 - Migration of Fines: Fines, debris, bacteria, and sand can become mobilised as a result of high production rate and/or due to wetting phase saturation increase. Such fines and material transport can cause particle plugging.
- Damage resulting from reduction in relative permeability - Invasion by wellbore fluids cause hydrocarbon saturation to decrease around the wellbore. This lowers the relative permeability to oil and, especially during early stages of production when a significant pressure drop is created around the wellbore.
- Temperatures, pressures, well flow rates and wellbore operating conditions can cause precipitation of solids forming scales.
- Damage due to emulsion blocking: Is a result of formation of emulsion between oil and water.

Formation damage leads to abnormal productivity and/or anomalous decline in injectivity or productivity of a petroleum/hydrocarbon bearing formation and has been one of the major problems facing the oil and gas industry. Formation damage can occur at any stage of development of a hydrocarbon bearing rock such as during drilling, completion, production, work-over and stimulation. The primary mechanisms that can induce formation damage include: mechanical, biological, chemical, physio-chemical, thermal and hydrodynamic interactions of porous formation particles and fluids.

Prior to human activities, a petroleum reservoir exists in both chemical and physical equilibrium that is maintained as long as there are no external influences or disturbances. The mechanisms mentioned above create a non-equilibrium disorder which causes particles, fluids and reservoir rocks to interact. This complex interactions result in fines migration into pore spaces, dissociation of solid from solid, which leads to absolute permeability blockage in more severe cases; and/or fluid-solid and fluid-fluid interactions that lead to the precipitation of produced and injected formation fluid (Civian, 2007).

Formation damage Treatment and remediation can be a difficult task as well as very expensive. Porter (1989) argued that formation damage is not necessarily and easily reversible; and preventing formation damage is a better approach in dealing with the situation rather than treating and remediating it. The need to strike a balance between financial cost and the health, safety and environment (HSE) of a project has compelled most operators to evaluate and continually seek to improve their management of projects. From the above, laboratory testing of formation damage is considered one of the best and most popular approaches to understanding formation damage. This is because laboratory testing provides additional information about the reservoir conditions and factors which lead to formation damage; as well as ways to deal with the situation when it occurs; thus aiding in better decision making. Laboratory testing is a risk reducing and cost effective method used in

modelling a reservoir formation and processes which cause changes to the formation. By laboratory method, damage causing factors can be determined and suggestions and/or recommendations for preventing damage can be stipulated.

Return permeability measurement is considered as one of the most successful approach of formation damage testing and quantification. This type of test involves the use of rock core samples from the reservoir being investigated; or synthesised sand pack materials can also be used. The process involves measurement of initial permeability of the rock material before subjecting it to operational fluids such as those used during enhanced oil recovery (EOR), completion, workover, drilling; and then again measuring its permeability afterwards. This is to show the extent of damage done by these fluids to the permeability of the reservoir. On the basis of this return permeability test, analysis and evaluation are done on results and appropriate fluids can then be recommended to avoid future damage re-occurrence.

Reduction in oil and gas productivity and non-economic operation from a reservoir is one of the negative impacts of formation damage in any oilfield. This in turn has often prompted a premature abandonment of some marginal reservoirs or fields as well as a delay in returns on investment and in severe cases a total loss of investment. From the industry viewpoint, it is difficult to quantify the total cost of deferred production and remedial treatment due to formation damage. However, it costs the UK oil and gas about over \$1.5 billion annually to the industry in delayed production and corrective treatment (Michael Byrne, 2009).

2.2 Formation Damage Mechanism

Petroleum reservoir rock formations act as filters and therefore vulnerable to plugging (damage) by solid materials suspended in and/or precipitated from injection fluids. Although the manner in which well productivity may be reduced (i.e. reduction in permeability) differs from operation to operation, investigation and diagnosis of specific problem

indicates that the reasons are usually associated with either the transport of fine solids, chemical reactions/molecular adsorption or a combination (Bennion, 2002; Krueger, 1988) as shown in Figure 2.1.

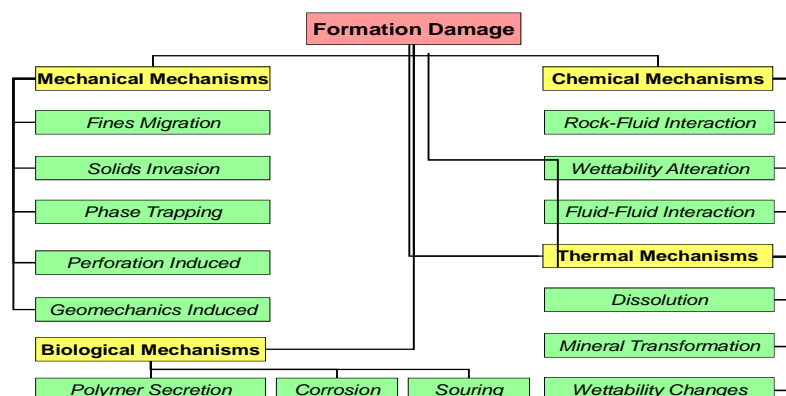
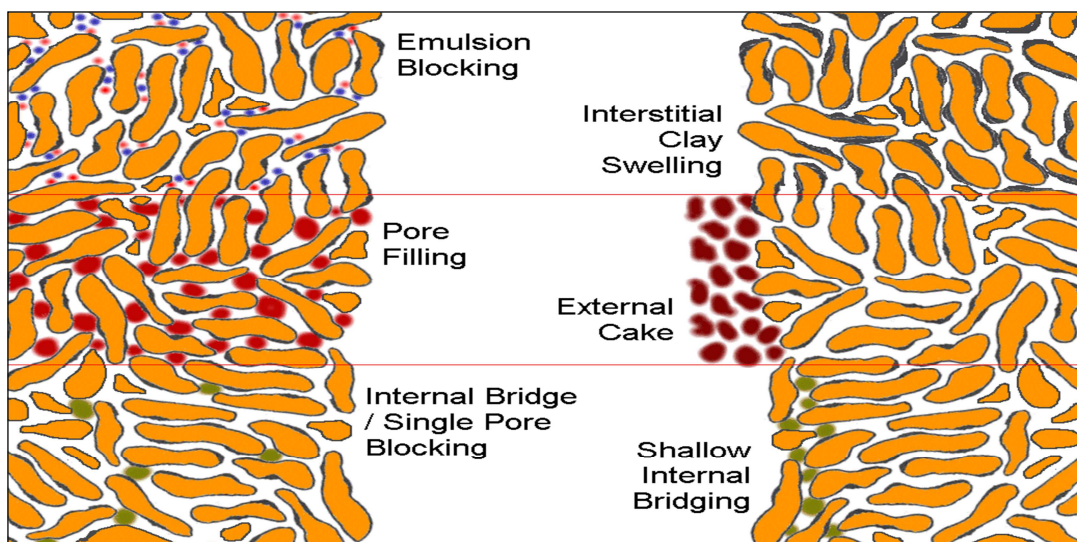


Figure 2.1 - Flow Chart of Common Formation Damage Mechanism (Bennion, 2002)

Absolute permeability reduction can result from particle plugging (due to solids in drilling and completion fluids invading the reservoir rock pore spaces) and chemical retention (such as polymer adsorption) amongst others. Polymer retention in porous media has been attributed to adsorption and mechanical entrapment mechanisms that are yet to be fully understood. Apart from the inadequacy of the polymer retention values available in the literature for different conditions, there have been difficulties in correlation as a result of discrepancies in measurement methodologies (Balestrini et al., 2009). Several workers (Clark, 2010; Da Silva et al., 2010; Dang et al., 2011; Stavland et al., 2010) have investigated the effects of various factors (such as molecular weight, concentration, salinity, salts, pH, surfactants, temperature, etc) affecting polymer rheological behaviours in porous media. Even then, the effects of these factors and how they affect polymer potential formation damage have not been totally quantified. For example, there are high, medium and low molecular weights polymers; but which one is best for a specific application including their operational efficiencies are still issues.


From well spudding, through to putting it on stream, the zone is exposed to a series of fluids and operations that will strongly affect the productive

capacity of the well. In reality, physical entrapment can cause pore plugging/bridging; while chemical adsorption (e.g. polymers) can cause permeability reduction, hence, productivity decline due to flow restrictions. For illustration purposes, a visualisation of the process of damage is depicted by [Figure 2.2](#); while [Table 2.1](#) illustrates the impact of damage on production. From this table, a zero skin value indicate a no formation damage condition, a higher positive skin value implies a damage condition that restricts further oil production resulting in a huge loss in revenue. To remedy this damage, additional cost is invested to stimulate the vicinity of the wellbore and restore the flow capacity of the well, thus, a negative skin value. Formation damage is undesirable as it represents a loss in revenue.



[Figure 2.2 - Common Formation Damage Mechanisms \(Bennion 2002\).](#)

Table 2.1 - Impact of Formation Damage on oil and gas Production. The 'skin' is an indication of increase or decrease in production. Positive skin value means production loss due to formation damage, and negative skin value implies production enhancement by stimulation. (Source: RGU 2007).

SKIN	RATE (BPD)	
-6	80,000	increasing stimulation
-3	32,000	
-1	22,857	
0	20,000	'(ideal)' no damage
+2	16,000	 increasing damage
+4	13,333	
+8	10,000	
+24	5,000	
+100	1,481	

3

Chapter 3 – Literature Review

3.1 Introduction

The use of conventional waterflood (as a means of secondary recovery) has been used to recover about half of world oil production (Detling, 1944; Albaugh, 1950; Binder et al., 1956; Meadors, 1960; Bernard, 1960; Jones, 1966). As conventional oil reserves are produced, the remaining resource becomes less favourable to waterflood due to high viscous fingering. In arctic environments, and offshore, in particular, improved methods of cold production for viscous oil become imperative because of the unlikely activity of introducing heat to thin viscous oil. One of the major and growing concerns of the oil industry during oil production is the increased amount of water produced through early breakthrough of injected or formation water; which in turn results in rapid oil production decline and increase in operational costs (pumping, treatment and disposal of produced water facilities, etc). Consequently, the use of polymer-augmented waterflood (polymer flood) as a means to curtail excess water and enhance oil production became the option for the oil and gas industry.

The technology of polymer flooding, which has found successful application in Enhanced Oil Recovery (EOR) operations first began in the early 1960s following the pioneering work of Sandiford (1964) and Pye et al. (1964); who first suggested that more oil can be recovered from polymer flood in comparison with that attributable to conventional waterflood. This noble beginning was followed up with further research works in order to understand the complex and non-Newtonian behaviour of polymer solutions (Savins, 1969; Marshall and Metzner, 1967; Jennings et al., 1970; Hill et al., 1974; Chauveteau, 1982; Rho et al., 1996; Szabo 1975a, 1975b, 1979; Dominguez and Willhite, 1977; Gleasure, 1990; Xue et al., 2005; García-Ochoa et al., 2000; Ye et al., 2013; Zhang et al., 2013). The argument in favour of polymer flood compared with conventional waterflood is that (Ali and Barrufet, 2001): 1.) the adsorbed polymer layer increases water wettability and correspondingly increases the irreducible water saturation (S_{iw}) thereby inducing a decrease in the relative water permeability (k_{rw}), 2.) in the case of oil-wet rocks, the adsorbed layer may change the rock surface to water-wet and thus induce a dramatic drop in residual oil saturation, 3.) it improves reservoir volume sweep and reduce the amount of fluid injection needed to recover a certain amount of oil (Needham and Doe, 1987; Du and Guan, 2004). Increased sweep efficiency, is nonetheless, dependent on lowering the mobility of the injected fluid for quite a distance into the reservoir. However, Low-mobility penetration into the reservoir is partially hindered by polymer adsorption onto the rock surfaces caused by passage of the polymer solution.

Polymers exhibit extremely complex rheological behaviour during flow in porous media (Cheng and Cao, 2013). This behaviour depends on the nature of the pore structure of the porous media and multisystem itself, as well as the interaction between the components in the polymer and the porous media (García-Ochoa et al., 2000; Yuan et al., 2000; Shiyi et al., 2000). In the field, partially hydrolyzed polyacrylamides (HPAM) and xanthan gums are commercially used in EOR processes. It is, however, believed that both polymers give unsatisfying performances (Zhang et

al., 2012). Xanthan gum exhibits shear-thinning or viscous behaviour while HPAM exhibits both viscous and elastic characteristics (Al-Sofi et al., 2009; Alsofi and Blunt, 2010). One common characteristic of polymer flooding is its flow through porous media. Therefore, a large amount of research efforts has been devoted to gaining a better understanding of polymer flow behaviour in porous media in the past recent years (García-Ochoa et al., 2000; Dang et al., 2011; Ezell et al., 2010; Clark, 2010; Da Silva et al., 2010; Stavland et al., 2010). In spite of these efforts, several issues have been only partially resolved (Zitha, 2001). For instance, finding effective polymers for high salinity environments is an issue. Furthermore, the lack of adequate and reliable relationships between adsorbed amount of polymer and average polymer layer thickness in non-gelification situations is also an issue.

Several authors have concentrated their research focus on investigating (single-phase) viscoelastic fluids experimentally and numerically in both porous media and constrictions representative of pores (Zhang et al., 2012; Cheng and Cao, 2010; Urbissinova et al., 2010; Aguayo et al., 2008; Binding et al., 2006; Fan et al., 1999; Bird, 1960). It has also been argued that apparent viscosity of polymers at low rates decreases with pore size (Chauveteau et al., 1982).

3.2 Overview of EOR polymers

Different types of polymers, including hydrolysed polyacrylamide (HPAM), xanthan gum, Carboxymethylcellulose (CMC), Hydroxyethylcellulose (HEC), polyacrylamide (PAM), dextran polyethylene oxide (PEO) have been applied in reservoirs worldwide. However, partially hydrolysed polyacrylamides (HPAM) and xanthan gums are commercially attractive polymers used in EOR processes (Lake, 1989). Xanthan gum (a biopolymer) has been used for field polymer flooding applications (Sandvik and Maerker, 1977). Field applications in this regard have been evaluated (Agnew, 1972; Sloat 1969, 1972; Chang, 1978; Zaitoun and Kohler, 1987). The results of these evaluations, for example, show that the amount of polymer required is a function of water salinity and rock

type. Higher total salinities and/or higher divalent cation concentrations need more polymers to achieve equivalent results.

3.2.1 Xanthan gum

Xanthan gum falls into the family of natural polysaccharides. It is highly soluble in cold and hot water because of the polyelectrolyte nature of the xanthan molecule (García-Ochoa et al., 2000). Solutions of xanthan are highly viscous even in very low concentrations. Xanthan solutions are shear-thinning, or pseudoplastic (i.e. viscosity decreases as shear rate increases). Xanthan gum is less sensitive to changes in salinity and mechanical degradation in comparison with polyacrylamide (Kohler and Chauveteau, 1981; García-Ochoa et al., 2000). Xanthan gum has molecular weight ranging from 2 to 50 x 10⁶ g/mol; and its viscosifying ability lies in both the molecular weight and in the rigidity of the polymer chains (García-Ochoa et al., 2000). [Figure 3.1](#) shows a typical structure of xanthan gum. It has been shown (Zaitoun and Kohler, 1987) that molecules of xanthan gum adsorb flat on rock surfaces without significant increase in adsorbed layer thickness. Zaitoun and Kohler (1987) observed a higher retention level with flexible polyacrylamide on same rock surfaces; and attributed these adsorption discrepancies between the two polymers to the differences in their functional groups. Specifically, flexible polyacrylamide has greater formation damage potential than xanthan gum.

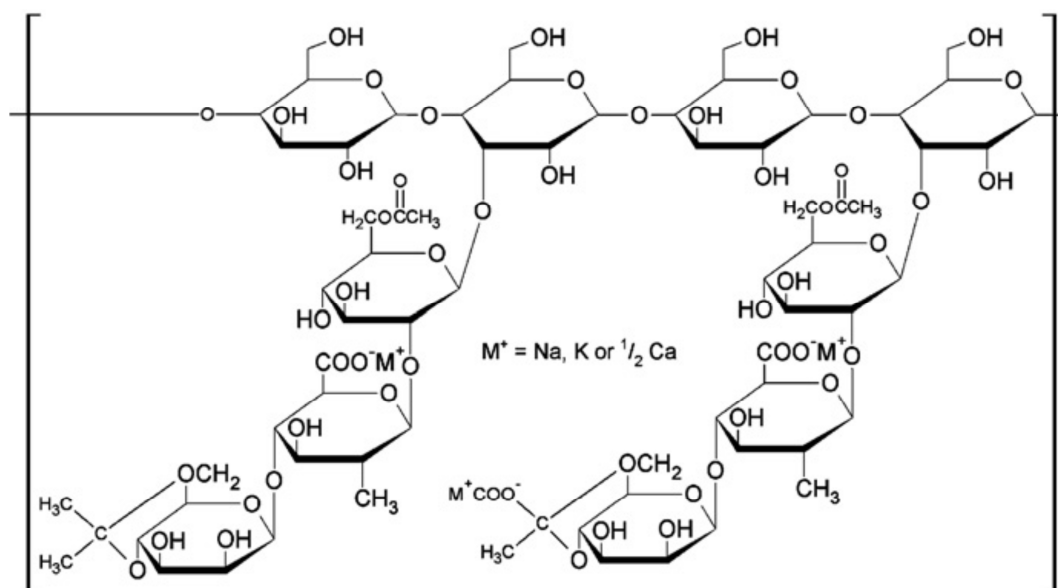


Figure 3.1 - Chemical structure of xanthan gum (Wever et al., 2011).

3.2.2 Hydrolysed polyacrylamide (HPAM)

HPAM is a synthetic, high-molecular weight, water-soluble, low-cost polymer which has undergone partial hydrolysis; hence the name 'partially hydrolysed polyacrylamide' (HPAM). It is a more widely used EOR polymer than xanthan gum since it can tolerate the high mechanical forces present during the flooding of a reservoir (Lake, 1989). About 95% of its use in field EOR applications has been reported (Lake, 1981). HPAM has a degree of hydrolysis between 25 to 35% (Lake, 1989; Borthakur et al., 1995). The ability of HPAM to viscosify is due to its high molecular weight as well as the electrostatic repulsion between polymer coils and between polymeric segments in the same coil (Lake, 1989). It has been reported to exhibit both pseudoplastic (Lake, 1989; Borthakur et al., 1995; Ait-Kadi, et al., 1987; Lewandowska, 2007; Hu, et al., 1995) and dilatant (Seright et al., 2009; Chauveteau, 1981) behaviours. HPAM degradation is by physical breakdown; and microbial attack has been reported (Seybold, 1994) to be difficult with HPAM. This is due to, perhaps, its very high molecular weight. HPAM exhibits permanent or irreversible permeability reduction in porous media (Lake, 1989). Figure 3.2 shows the chemical structure of HPAM (Wever et al., 2011).

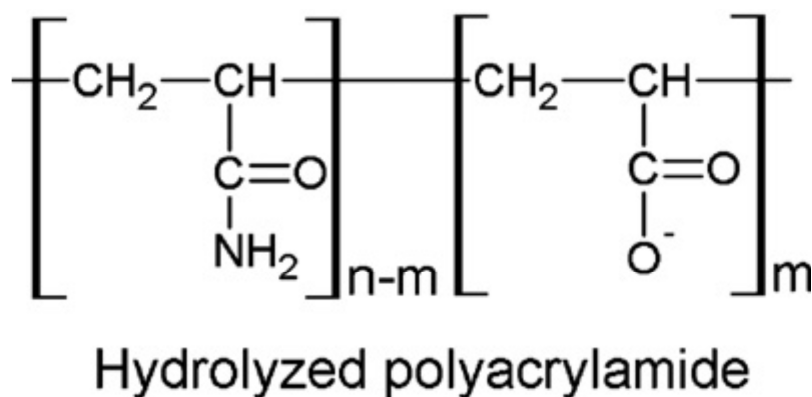


Figure 3.2 - Chemical structure of partially hydrolysed polyacrylamide (Wever et al., 2011)

3.3 Previous Work on Polymer-Induced Formation Damage.

Polymers are used for a variety of applications in the oil and gas industry including water and gas shutoff (Hughes et al., 1990), drilling mud viscosity modification (Navarrete et al., 2000), filtration loss control (Clark, 2010; Navarrete et al., 2000), swellable packers, loss circulation material (LCM) pills (Navarrete et al., 2000), enhanced oil recovery (Wang and Dong, 2009; Romero-Zerón et al., 2009), fracture treatment and cleanup (Pope et al., 1996; Samuelson and Constien, 1996), chemical placement (Taylor and Nasr-El-Din, 2002), sand control (Zhang and Huang, 2002), etc. The success and efficiency of polymer flooding has been attributed to a range of important variables such as rock type, polymer type, molecular weight, salinity/hardness, concentration, pH, porous media structure, chemistry of the aqueous phase, porous media surface area, porosity and permeability of the porous media, pore-size distribution, grain-size distribution, oil saturation, flow rate, amongst others (Mungan, 1969; Kazempour et al., 2011; Manichand and Seright, 2014). In the literature, studies have established that HPAM can cause permeability reduction by mechanical entrapment and adsorption onto rock surfaces (Szabo, 1975; Gogarty, 1966; Sorbie, 1991; Lee, 2010).

The dynamics of polymer adsorption has been known to be a complex process (Carpita et al., 2006) perhaps, due to the extremely complex rheological behaviour during polymer solution flow in porous media (Cheng et al., 2013). This behaviour depends on the nature of the pore

structure of the porous media and polymer system itself (Zitha, 2001), as well as the interaction between the components in the polymer and the porous media (Cheng et al., 2013).

Hirasaki and Pope (1974) conducted studies to model polymer adsorption based on the capillary tube model using low permeability sandstones. Their model did not match their experimental data. They attributed the mismatch to the inaccuracies in experimental measurements as well as other factors (such as pore size distribution, rock composition, clay content) not considered in their model. However, the capillary tube model can better be used to describe high permeability unconsolidated sandstones. Therefore, for low permeability sandstones utilised in Pope and Hirasaki's experiment, the capillary bundle model under-estimates permeability reduction (R_k). Nonetheless, Hirasaki and pope concluded that there was a direct relationship between the amount of polymer adsorbed and the surface area of the rock pore space. They also assumed that the polymer molecules were adsorbed on the rock surface in monolayer form.

In the literature, only a limited study (Chiappa et al. 1999; Martin et al., 1983; Mungan, 1969) has shown polymer adsorption to depend on salinity. Therefore, not much is known on how the polymer type, particularly in the presence of brine impact on formation damage. For example, using salinity between 0 and 13% KCl for cationic polyacrylamide (PAM) and with (8%) and without (0%) CaCl_2 in brine for anionic HPAM, weakly anionic PAM on quartzite porous media in static adsorption experiments, Chiappa et al. (1999) found that adsorption on quartzite increased from about 60 $\mu\text{g/g}$ without CaCl_2 to about 750 $\mu\text{g/g}$ with 8% CaCl_2 in brine; while the cationic PAM was almost independent of both salinity and CaCl_2 content. They explained the behaviour by proposing calcium bridging from the anionic rock to the anionic polymer.

Martin et al. (1983) observed retention values of 25.1 $\mu\text{g/g}$ in 2% NaCl and 15.5 $\mu\text{g/g}$ in 0.1% NaCl in their study of several HPAM retention in

Berea sandstones. Furthermore, Mungan (1969) did not observe any significant difference of HPAM retention in fresh water when compared with results obtained using 2% TDS NaCl. Remarkably, Martin et al. (1983) and Mungan (1969) studies were conducted independently with Dow Pusher 500 and 700 HPAMs in 2% NaCl solution. However, rather surprisingly, Martin et al. (1983) retention values were about 10 times lesser than those of Mungan's (1969) values; this probably indicates differences in experimental procedures and techniques. However, these works have not explored the correlation between the magnitude of polymer retention and flow rate.

Zaitoun and Kohler (1988) conducted two-phase flow through porous media to study the effect of an adsorbed polymer layer. They observed that the dilatant character of HPAM molecule in converging flow caused a high permeability reduction with shear rate; and that the flow regime which became dominated by elongational flow could no longer be accounted for by Poiseuille tube model. This is because the Blake-Kozeny model from which the Poiseuille tube model originates does not represent pore size distribution. Similar observation was made by Zitha et al. (1995).

In a different study, Zitha (1995) demonstrated the wide use of polymers for near-wellbore conformance control treatments for the purpose of permeability contrast correction between layers. Zitha (1995) concluded that polymers have the ability to invade deep into high-permeability layers compared with low-permeability layers which in turn enhances resistance to flow in the high-permeability watered-out zones.

It has also been reported (Chauveteau et al., 2002) that the thickness of an adsorbed polymer layer depends more on shear rates increase rather than on initial low injection rates. If, however, shear rates become higher, adsorbed layer thickness slowly increases to some maximum values, increasing with injection rates.

Zitha et al. (2003) conducted studies on the modelling of polymer adsorption under near-wellbore flow conditions. Their aim was to use experiment to validate theory of canonical filtration using flat cores and several flow rate conditions. Their results indicated that adsorption considerably increased with rate of injection.

Iscan et al. (2007) found out that studying different drill-in fluid types and their filtration conditions can help to understand formation damage caused by the fluids. Consequently, they used three different water based drilling fluids including Bentonite, carboxyl methyl cellulose (CMC) and polymer (XT) at different filtration pressures to study the sand face permeability. They used damage ratio concept to interpret formation damage and showed that there was filter cake increase with increasing differential wellbore pressures. However, their study did not specifically address the contribution of the polymers to formation damage.

Using a packing of negligible adsorption, Dominguez and Willhite (1977) conducted an experiment to show the effect of mechanical entrapment of HPAM solution in porous medium. Their results showed that the resistance factor (RRF) was lower than that for natural media by about two to three folds.

Reid et al. (2004) investigated the applications of polymers for invasion control in matrix permeability, tight micro-fractured rocks, and loss circulation control into fragile formations during drilling, completion, workover and cementing. Results showed that hydrophobically modified polymers greatly reduced fluid invasion.

Kazempour and Alvarado (2012) studied the effect of NaOH and Na₂CO₃ on the rheological behaviour of HPAM and on HPAM adsorption on Berea sandstones in both static and dynamic modes. Their results which were correlated with oil recovery and injectivity conditions showed that alkali can react with the rock and polymer to reduce polymer adsorption and decrease polymer-solution viscosity to allow higher injectivity.

It has equally been established (Pye, 1964; Gogarty, 1966; Marshall and Metzner, 1967; Marshall et al., 1997; Savins, 1969; Jennings et al., 1970; Wissler, 1971) that at higher flow rates, HPAM solutions exhibit viscoelastic behaviour which can be observed as increasing resistance factor. Unfortunately, the effect of adsorption arising from viscoelastic behaviour on permeability reduction is often unnoticed (Cohen and Christ, 1986).

Quite recently, Al-Hashmi and Luckham (2010) proposed a mechanism that attributed the multilayer formation of polymer/solid system to the formation of shear-induced-microgel structures in the bulk of the solution, and sufficiently high adsorption energy of the polymer.

Of note is the work of Cohen and Christ (1986) who conducted an experiment using silica sand bed to demonstrate that about 36.2% of total polymer retained on the silica sand was attributed to adsorption. They estimated the effective hydrodynamic thickness (EHT) of the adsorbed polymer layer of about 0.57 μm . In a later study, Cohen (1988) reported an EHT twice less than the previous and ascribed the difference to the intercommunications between adsorbed and flowing polymers.

Using pore systems in bundles of capillary tubes, Zaitoun et al. (1998) performed a two-phase flow experiment to study the effect of an adsorbed polymer layer on SiC pack. They estimated permeability reduction and used same to calculate the adsorbed polymer layer thickness. It is worth mentioning that the capillary bundle porous media model upon which their model was based does not account for the complex converging-diverging pore structure of natural rock systems; and the flow field in a smooth-bore capillary tube does not equally have a characteristic deformation time. In addition, they did not consider entrapment and retention in their model. Therefore, results obtained from their estimations using the tube model may have been in error (Stavland and Nilsson, 2001).

A study of polymer injection on two-phase flow in porous media conducted by Zaitoun et al. (1998) revealed that wall effect dominates during polymer flow, and that polymer adsorption plays an important role in relative permeability modification resulting in permeability reduction of porous media.

Some attempts, however, have been made to study the contributions of adsorptive retention relative to other mechanisms of retention in porous media (Szabo, 1975; Dominguez and Willhite, 1977). In 1977, Dominguez and Willhite presented studies on the three mechanisms by which polymer can get trapped in or adsorb on solid rock surfaces. These include adsorption, mechanical entrapment and hydrodynamic retention. They concluded that mechanical entrapment occurs when larger polymer molecules lodge in narrow flow channels of low permeability formations. Their studies appear to suggest that mechanical entrapment depend on pore size distributions.

According to Thomas (1976), Dominguez and Willhite (1977), Ranjbar et al. (1991) and Grattoni et al. (2004), mechanical entanglement between flowing and immobile polymer molecules is often the cause of retention during polymer solution flow in porous media. This multi-layer entanglement process (causing mechanical entrapment) has often obscured the role adsorption plays in polymer retention and mobility reduction (Dominguez and Willhite, 1977).

In the oil and gas industry, polymer evaluation and qualification screening prior to use in the field is a common practice. Kaminsky et al. (2007) and Mennella et al. (1998) have previously presented guidelines for polymer flooding evaluation and development. These studies concluded that correlation is difficult because of differing conditions of measurements. Although any two wells or even fields may have similar petrophysical character, field experience has shown that polymer chemical applications should be executed on a case by case basis for different field conditions.

The effective use of polymers for drilling and additional (enhanced) oil recovery is not an issue based on principles but rather a question of costs and economics. Chemicals are expensive on a unit basis compared with crude oil. Therefore, the quantity of polymer economically sacrificed for incremental reservoir crude oil recovery is the main concern for a practical EOR and other projects involving use of polymers.

A review of the literature reveals a little about qualitative and quantitative information on polymer adsorption. Most studies/models regarding polymer adsorption are focused on polymer gelification (Kozicki et al., 1987, 1988, 1993; Liang et al., 1993; Liang and Seright, 1997; Zaitoun and Bertin, 1998; Barreau et al., 1999; Liang and Seright, 2001; Stavland and Nilsson, 2001; Al-Sharji et al., 2001; Grattoni et al., 2002; Liu et al., 2013). Hence, adequate and reliable correlations between adsorbed amount of polymer and average polymer layer thickness in non-gelification situations are lacking. Also, there had been much focus on the use of polymers for water shut-off during enhanced oil recovery without much attention to the potential of polymers to damage the formation or cause restriction to flow of hydrocarbon in the reservoir.

Furthermore, majority of the experimental approaches, especially those involving multiphase flow systems, had difficulties in isolating the explicit polymer adsorption contribution to fluid permeability reduction (Carpita et al., 2006; Singleton et al., 2002). Generally, there still exists a lack of consensus among researchers on the basic mechanisms and the set of conditions under which the results of their various studies are applicable.

Most studies of polymer adsorption focused on the modification in relative permeabilities; and resistance factor has been used frequently with regard to the effect of polymer adsorption on permeability reduction. However, only few studies have been reported to investigate the combined effects of polymer adsorption and high salinity brine on

absolute permeability during the single-phase flow of polymer solutions in porous media.

The major aim of this research is to gain a deeper understanding of the explicit polymer adsorption contribution to formation damage during EOR operations that has not been adequately addressed. The basic information that reflects the mechanism of the polymer adsorption process (such as rock type, polymer type, molecular weight, salinity/hardness, concentration, pH, porous media structure, chemistry of the aqueous phase, porous media surface area, porosity and permeability of the porous media, pore-size distribution, grain-size distribution, flow rate, amongst others) is obtained experimentally.

Furthermore, mathematical model studies provide a reliable means of evaluating potential benefits of polymer pre-injection. However, such studies require input data that permit the model to simulate the physical processes that may occur in the reservoir. In this research, numerical simulation and laboratory studies were conducted to provide such data. However, in practice, the products used in each one of these applications are not the same. Also, correlation from one reservoir formation would not probably hold for another because of the likelihood of different factors mentioned earlier.

Therefore, in this work, polymer adsorption laboratory experiments and numerical study were designed and implemented to investigate the polymer adsorption related formation damage; the effect of polymer retention on oil recovery was studied in relation to adsorption and desorption kinetics. The mechanism of polymer retention was also quantitatively described. The following variables were considered in the research: 1) polymer type, 2) effect of concentration, 3) effect of salinity/hardness, 4) effect of permeability and pore size distribution, 5) effect of inaccessible pore volume (IAPV) on retention, 6) a method was established to quantify the effect of flow rate on adsorption; and

analytical models suitable for the prediction of polymer-related formation damage in oil and gas-bearing formations were developed.

The chapter that follows discusses the rheological characterization of polymer solutions.

4

Chapter Four – Rheological Characterization of Polymer Solutions

4.1 Introduction

Rheological systems can either be Newtonian or non-Newtonian. Viscosity is the most important property of polymers in EOR operations as well as other applications. However, a lot of factors can affect polymer viscosity. In this section, a laboratory study of the effects of shear rate, salinity, active polymer concentration, pH, hardness and temperature on polymer viscosity performance was conducted. The data from this study is used to compare and select polymer products for additional specific tests and ultimately for subsequent core testing.

4.2 Polymer Viscosification Mechanism

While in solution, the underlying principle of how polymers viscosify is still not quite understood. However, energy dissipation arising from the interaction of molecules is one physical interpretation of viscosity. It has been proposed (Flory, 1953; Flory and Flory, 1956) that it is the interaction between long polymer chains and the solvent molecules that govern the viscosifying effects of polymers and that the mechanisms is

related to the frictional effects observed in sedimentation and diffusion. The long polymer chains exhibit many motional patterns while interacting along its entire length with molecules of the solvent (Mezzomo et al., 2002; Sorbie, 1991). This leads to more energy dissipation and higher viscosity tendencies compared with liquids made of smaller molecules. It was noted (Sorbie, 1991; Sorbie et al., 2007) that polymers can increase water viscosity by factors of 10-100 even at low concentrations of a few hundred parts per million (ppm). The energy dissipation rate (\dot{Q}) within simple shear flow is given by Eqn. (4.1) (Sorbie, 1991):

$$\dot{Q} = \mu \dot{\gamma}^2 \quad (4.1)$$

Where; \dot{Q} directly depends on viscosity of the fluid (μ) and on the square of the shear rate ($\dot{\gamma}$).

4.3 Polymer Bulk Viscosity Theory

In the literature of polymer rheology, viscosity has been established to be the most important parameter for characterizing polymers (Stavland et al., 2010). Viscosity of a polymer solution is measured in a viscometer; this is known as the bulk viscosity. The theory of polymer bulk viscosity is well known (Flory, 1953; Flory and Flory, 1956; Sorbie, 1991; Zitha, 2001; Stavland et al., 2010). The polymer viscosity, μ increases non-linearly (Figure 4.1) as both the intrinsic viscosity, $[\mu]_0$, and polymer concentration, C_p increase up to the second order (Zitha, 2001); as given by Eqn. (4.2):

$$\mu = \mu_{sol} \left(1 + [\mu]_0 C_p + k' [\mu]_0^2 C_p^2 \right) + O^3 \quad (4.2)$$

where, μ_{sol} = solvent viscosity, O^3 = third order polymer concentration
 k' = Huggins parameter which describes solvent quality.

- $k' < 0.4$: good^a solvent conditions
- $k' > 0.4$: poor solvent conditions

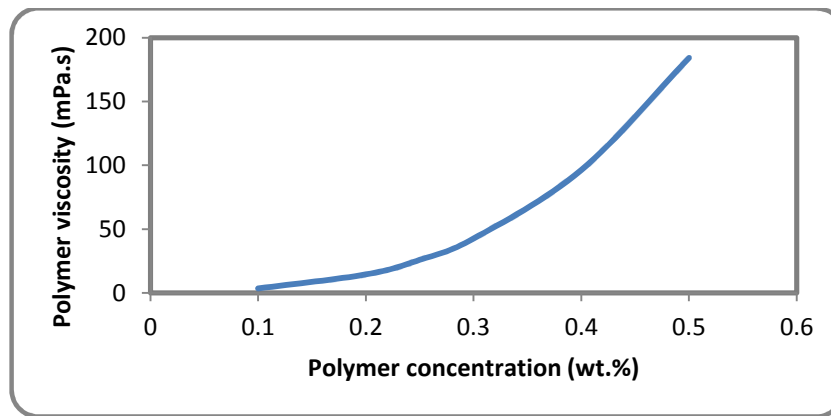


Figure 4.1 - Effect of concentration on polymer viscosity

The intrinsic viscosity is a measure of the size of a polymer molecule in solution, and consequently, a measure of its thickening ability (Lake, 1989). The intrinsic viscosity is a function of the polymer molecular weight; this is expressed in Mark-Houwink equation (Bird et al., 1977) given as Eqn. (4.3):

$$[\mu]_0 = K M_w^a \quad (4.3)$$

Where, M_w = polymer molecular weight

K , a = empirical constants for a given polymer at a given temperature in a particular solvent. Note: $3.0 \times 10^{-5} \leq K \leq 700 \times 10^{-5}$ = and $0.5 \leq a \leq 1.0$ (Sorbie, 1991).

For a given molecular weight, chemical structure, shear rate, chain branching, temperature, type of solvent, and charge are the factors that affect polymer intrinsic viscosity.

^a "Good" means repulsion at every short distance.

4.4 Polymer Molecular Radius

When in solution, the hydrodynamic radius of polymer is known as its radius of gyration (R_g). This parameter is difficult to measure experimentally in the laboratory. However, theoretical models have been developed to estimate this hydrodynamic parameter (Flory-Fox, 1953) depending on the macromolecular condition of the polymer in dilute solution. For instance, HPAM are flexible, long linear chains structures; and so as to neutralize electrostatic repulsion between carboxylate groups, the conformation of HPAM in high saline water are coils. For example, for 20 g/L NaCl salinity, HPAM macromolecular conformation is slightly an expanded coil (Chauveateau, 1981). The Flory-Fox hydrodynamic radius of gyration equation, R_g , for this case is given by Eqn. (4.4):

$$R_g = \left(\frac{M_w [\mu]_0}{\Phi} \right)^{1/3} \quad (4.4)$$

Where, R_g = radius of gyration which characterises polymer coil in dilute solution, Φ = universal constant = 2.1×10^{21} dl/g.mol.cm³, $[\mu]_0$ = polymer intrinsic viscosity, cm³/gm

For rigid, rod-like or hard sphere conformation of Xanthan gum, the radius of the molecular coil in a dilute solution can be determined from (Einstein 1953, 1955) equation for the viscosity of an infinite dilute suspension of hard spheres:

$$r_M = \left(\frac{30 M_w [\mu]_0}{\pi A} \right)^{1/3} \quad (4.5)$$

Where, r_M = radius of molecular coil in dilute solution

A = constant = Avogadro's number, 7.023×10^{23} molecules/mol

M_w = polymer molecular weight, g/mol.

4.5 Non-Newtonian Viscosity-Shear Rate Relationships

All polymers are shear-thinning, i.e. their viscosities decrease with increasing shear rates (Lake, 1989). Shear-thinning behaviour of polymers has been established and proved (Bird et al., 1987) as an intramolecular effect that occurs due to the polymer extensional and orientational character while in solution. A set of well-established expressions from the literature can be used to express their Viscosity-Shear rate relationships. Some of the proposed analytical expressions for viscosity vs. shear rate in simple shear flow include but not limited to the power-law and the Carreau models.

4.5.1 The Power-law (Ostwald-de Waele) Model

The Power-law model is the most widely used analytical form of viscosity-shear rate relationship which describes the pseudoplastic region of the polymer viscosity curve. This model is given by Eqn. (4.6) (Bird, 1960):

$$\tau(\dot{\gamma}) = K \dot{\gamma}^n \quad (4.6a)$$

and in terms of apparent viscosity:

$$\mu(\dot{\gamma}) = K \dot{\gamma}^{n-1} \quad (4.6b)$$

Where, τ = shear stress

$\dot{\gamma}$ = rate of deformation (or shear rate)

μ = fluid viscosity

K = constant known as fluid consistency coefficient ($\text{cp} \cdot \text{sec}^{n-1}$)

n = dimensionless constant known as flow behaviour index ($0.4 \leq n \leq 1$ for shear-thinning fluids).

4.5.2 The Four Parameter Carreau Model

The 5-parameter Carreau equation (Carreau, 1972; Bird et al., 1987a) covers and combines the power-law region and the two Newtonian

regions of the viscosity curve. Therefore, it has a better application compared with the power-law model (Eqn. 4.7). It is written as (Cannella et al., 1988):

$$\mu_{sh} = \mu_{\infty} + (\mu_p^0 - \mu_{\infty}) [1 + (\lambda \dot{\gamma}_{eff})^{\alpha}]^{(n-1)/\alpha} \quad (4.7)$$

where, μ_{sh} = apparent shear viscosity in porous media.

μ_p^0 = polymer viscosity at zero shear rate.

$\mu_{\infty} = \mu_w$ = viscosity at infinite shear rate.

λ = time constant (i.e. relaxation time for realignment of polymer rods in a shear flow field) is found from the measurements of bulk viscosity

$\dot{\gamma}_{eff}$ = rate of deformation; called effective shear rate in shear flow.

n = dimensionless constant known as the shear-thinning index that depends on the polymer concentration. $0.4 \leq n \leq 1$ for viscous, pseudoplastic or shear-thinning fluids.

Figure 4.2 shows shear-thinning behaviours of Xanthan gum and HPAM; while Figure 4.3 is a comparison of Power-law and Carreau models for polymer solutions (Chhabra et al., 2001)).

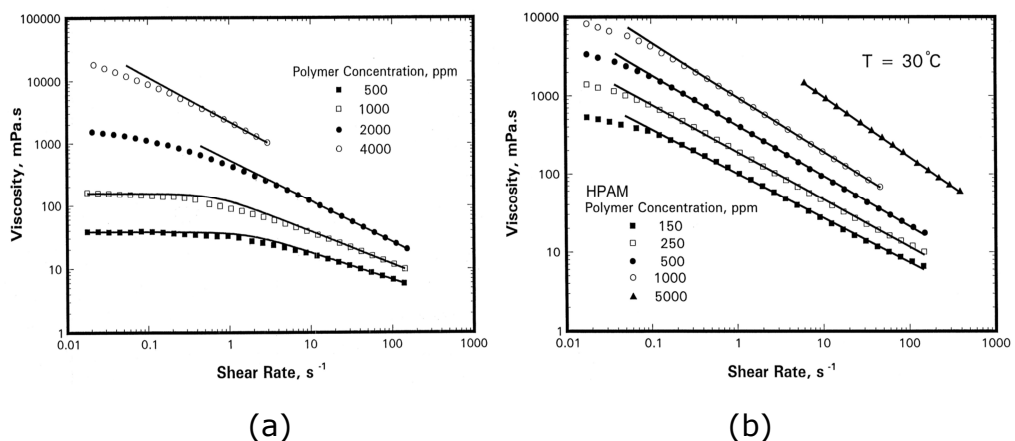


Figure 4.2 - Shear-thinning behaviour of polymers: (a) Xanthan gum, (b) HPAM (Taylor, 2003)

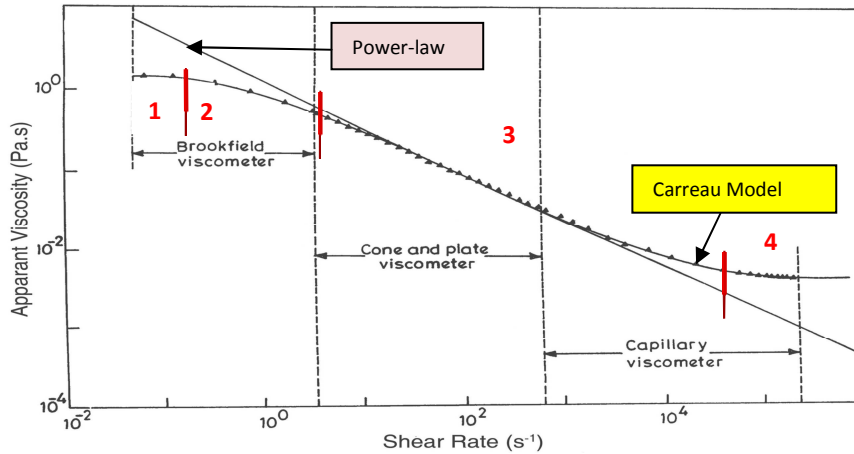


Figure 4.3 - Comparison of Power-law and Carreau Model for polymer solution (Chhabra, 2010).

Figure 4.2 shows that viscosity increases with concentration and decreases with shear rate. The ability of the Carreau model to account for both low and high regions of the viscosity curve is demonstrated by Figure 4.3. There are four distinguishable regions in this figure:

1. Constant-viscosity region in which the behaviour of the solution is Newtonian. This region is associated with low shear rates and/or low concentration.
2. Transition region, which correspond to the polymer molecules undergoing deformation due to the effect of the increasing shear rate.
3. Region in which the viscosity decreases as the shear rate increases. The greater the shear, the more the molecular chains orient in the direction of flow. The behaviour of the solution is pseudoplastic.
4. Transition region, which correspond to high degrees of shear. For HPAM, this is a region of shear-thickening (viscosity increase with shear rate) which has been attributed to the changes in the molecular conformation involving the formation of additional links between two chains.

4.6 Rheological Characterization and Measurements of Field Parameters Affecting Polymer Solutions

4.6.1 Overview of Laboratory Tests

Preliminary laboratory tests are used to compare polymer products under standardized conditions. This is because polymers exist with different molecular weights, structure, or ionic charge. In this section, a laboratory study of the effects of shear rate, salinity, active polymer concentration, pH, hardness and temperature on polymer viscosity performance was conducted. The data from this study is used to compare and select polymer products for additional specific tests and ultimately for subsequent core testing. The standard procedures (API RP 63, 1990) apparatus and method for each test are presented below.

4.6.2 Experimental – Materials and Methods

4.6.2.1 Materials and Procedures for Preparation of Synthetic Formation Brines

All brine solutions were synthetically formulated brines (SFB) and made to mimic reservoir formation water. The brine solutions were prepared in varying concentrations by adding calculated amount of NaCl alone and NaCl plus CaCl₂ in deionized water to enable the particular evaluation of the impact of salinity and hardness on polymer viscosity. Deionized water was used to prepare the brine in the required concentrations. The supplied tap water was deionized to a resistivity value of about 18 MΩ-cm (which is a threshold value indicating adequate removals of ions initially present) with the aid of a Millipore™ filter pumping unit ([Figure 4.4](#)).



Figure 4.4 - Millipore™ filter pumping/deionizing unit

Materials

The apparatus used include: 5 litre flask, Magnetic stirrer, analytical balance, 6 kg balance, 0.22 μm Millipore filter. Sodium chloride (NaCl) and calcium chloride anhydrous (CaCl_2) were the analytical reagents used.

Procedure

- A 5-litre flask with magnetic stirring bar was tared to zero on a 6 kg balance.
- Approximately 3 litres of deionised water was added to the flask and allowed to stir.
- Calculated amount of different salts necessary to prepare 4 litres of oil field synthetic brine was added to just below the upper curve or shoulder of the vortex created by the stirring bar.
- After addition of salts, the flask was allowed to stir till complete dissolution.

- When complete dissolution was assured, the flask was returned to the 6 kg balance and deionized water was added to a final weight of 4 kg (4000g).
- The solution was further stirred by magnetic stirrer for additional 20 minutes.
- The resulting synthetic brine was filtered through 0.22 μm Millipore filter.
- 2.0 g/L commercial formaldehyde was added to de-ionized water during stirring to act as oxygen scavenger, biocide or bactericide and stabilizer against free radical depolymerisation.
- Due to the hazardous nature of formaldehyde, the brine solution was prepared in a fume hood.

4.6.2.2 Polymers used for the research

Three grades (see [Table 4.1](#)) of commercial partially Hydrolysed Polyacrylamide (HPAM) were used for the rheological characterization. The HPAM were manufactured and supplied in powder form by SNF Floerger, ZAC de Milieux, 42163 Andrezieux, France.

Table 4.1 – Details and properties^b of the polymers used for the Research.

<i>Polymer product</i>	<i>Type of polymer</i>	<i>Monomer</i>	<i>Product form</i>	<i>Anionicity</i>	<i>Molecular weight</i>	<i>Manufacturer(s)</i>
Flopaam 3630 S	Copolymer	Acrylamide-Sodium acrylate	Powder	Medium to High	High (20m Dalton)	SNF Floerger
Flopaam 3330 S	Copolymer	Acrylamide-Sodium acrylate		Medium to High	Low (8m Dalton)	SNF Floerger
FloComb C3525	Calcium Tolerant	Acrylamide-Sodium		Medium	High	SNF Floerger

4.6.2.3 Laboratory Procedure for Preparation of Polymer Solutions from Dry Polyacrylamide Products.

Solutions of polyacrylamide powders were prepared as a stock solution (approximately 5000 ppm) and diluted to test concentrations as required (API RP 63, 1990). Vigorous agitation was necessary for the initial dispersion of the dry powder. A magnetically driven laboratory stirrer was

^b These are the only basic properties information given by the suppliers.

adjusted so that the bottom of the water vortex extends 75% into the solution (API RP 63, 1990). The dry polymer powder was sprinkled uniformly just below the upper curve or shoulder of the vortex within 30 seconds. If dispersion of the polymer was attempted over a longer time span, the higher viscosity resulting from the dissolved polymer may prevent proper wetting. Furthermore, adding the dry polymer in a big slug could lead to the formation of "fish eyes." Immediately upon adding all the polymer, the stirrer was again adjusted to a low speed (60-80 rpm) that just kept the solid particles from settling to the bottom. The lowest possible speed was used to avoid mechanical degradation of the polymer solution. The solution was allowed to stir at low speed for about 2 to 3 hours and left to stand overnight for proper hydration. Solutions were then ready for desired dilution by gently mixing the required amount of concentrate and brine solution by material balance. All diluted solutions were freshly prepared the day they were used. The step by step mixing procedures for preparing a 5000 ppm Stock Solution are detailed below:

1. A calculated amount of dry polymer product was weighed in a weighing boat and the weight recorded.
2. Calculated amount of the desired brine solution was weighed into a 2000 ml capacity beaker up to the lower meniscus of the 1000 ml mark. The weight was recorded; and a 1.5-inch coated magnetic stirring bar was added to the beaker.
3. The magnetic stirrer was used to adjust the vortex to extend 75% into the brine solution.
4. The polymer powder was sprinkled on the shoulder of the vortex over a period of 30 seconds. The solution was observed to ensure no particles or 'fish-eyes' were present.
5. The solution was stirred using the magnetic stirrer at low speed (60-80 rpm) for about 2-3 hours. This time was considered long enough for proper dissolution.
6. The solution was then left to sit overnight for proper hydration before diluting to the desired concentrations.

7. Stocks containing any undissolved particles were discarded.
8. Other diluted concentrations were prepared from the above stock solution using Eqns. (4.11) and (4.12) respectively.

4.6.2.4 Materials and Methods for Polymer Solution Preparations

The following apparatus were used for the preparation of solutions from dry polyacrylamide powders:

- *Top loading laboratory weighing balances:* Sensitivities $\pm 0.01g$; $\pm 0.001g$; $\pm 0.0001g$.
- Oven,
- ceramic dish,
- desiccator with silica gel desiccant,
- Magnetic stirrer,
- coated magnetic stirring bars,
- stopwatch or timer,
- pH meter
- weighing boats,
- spatula.
- *Containers:* 10, 20, 50, 100, 400, 600 and 2000-ml beakers,

4.6.2.5 Determination of Activity of Polymer Product (A_{pr}) by the oven method

Procedure

- i. An empty ceramic dish was weighed to the nearest 0.01g and recorded as W_d .
- ii. 10 g of polymer sample was added in this dish and re-weighed. The new weight was recorded as W_{d+HS} .
- iii. The sample was allowed to dry for 2 hours in an oven which was regulated and stabilized to 120 °C.
- iv. The sample was taken out of the oven after 2 hours and then cooled to room temperature in a desiccator containing silica gel.
- v. The ceramic dish containing the sample was re-weighed and recorded as W_{d+DS} .

Calculations

The percentage activity (A_{pr}) of the polymer sample was calculated using Eqn. (4.8) (API RP 63, 1990):

$$A_{pr} = \frac{W_{d+DS} - W_d}{W_{d+HS} - W_d} \times 100 \quad (4.8)$$

The percentages of active content of three test samples were thereafter calculated based on the above procedures as shown in [Table 4.2](#).

Table 4.2 - Percentage activity of polymer samples calculated from Eqn. 4.8

S/No.	Polymer Sample	Percentage Activity (A_{pr})
1	FP3630 S	90%
2	FP3330 S	91%
3	C3525	91%

4.6.2.6 Calculations for Preparing a Stock Solution Using Dry Polyacrylamide Products.

1. Product information from the manufacturers was used to calculate the amount of dry polymer product required to make up the appropriate amount of stock solution using Eqn. (4.9) (API RP 63, 1990):

$$W_{pr} = \frac{W_s \times C_s \times 10^{-4}}{A_{pr}} \quad (4.9)$$

Where:

W_{pr} = weight of polymer product, g.

W_s = weight of stock solution to be made, g.

C_s = concentration of polymer in stock solution, ppm.

A_{pr} = activity of polymer product, weight percent (usually 100%).

It is worth mentioning that the activity (A_{pr}) may have to be adjusted because dry polyacrylamide products gain weight due to exposure to the

atmosphere. The activity of the test samples were therefore calculated as described in section 4.6.1.5 above.

2. The amount of makeup water required to make the desired amount of stock solution was determined according to Eqn. (4.10) (API RP 63, 1990):

$$W_{bs} = W_s \times W_{pr} \quad (4.10)$$

4.6.2.7 Calculations for Dilution of Stock Solution.

The weight of stock solution required to make up the desired amount of diluted solution was calculated using Eqn. (4.11) (API RP 63, 1990):

$$W_s = \frac{W_d \times C_d}{C_s} \quad (4.11)$$

Where:

W_s = weight of stock solution, *g*.

W_d = weight of diluted solution to be made, *g*.

C_d = concentration of polymer in diluted solution, ppm.

C_s = concentration of polymer in stock solution, ppm.

Equation (4.12) was used to calculate the amount of makeup water required to make the desired amount of diluted solution (API RP 63, 1990):

$$W_{bd} = W_d - W_s \quad (4.12)$$

Where: W_{bd} = weight of makeup water used in the diluted solution, *g*.

4.7 Rheological measurements and characterization of polymer Solutions

TA Instruments Advanced Rheometer (model AR1000) was used to measure bulk viscosities of the polymer solutions over a wide range of shear rates (or flow velocities). This controlled stress device has a dynamic operating range of $\sim 1,000,000:1$ [highest torque:lowest torque] and can perform dynamic [oscillatory] tests as well as creep tests [step stress] and conventional and equilibrium flow. Figure 4.5 shows the pictorial views of the model device. Figure 4.7 shows a Jenway 3505 model digital pH/ion meter with combination electrodes used to measure samples pH before testing.

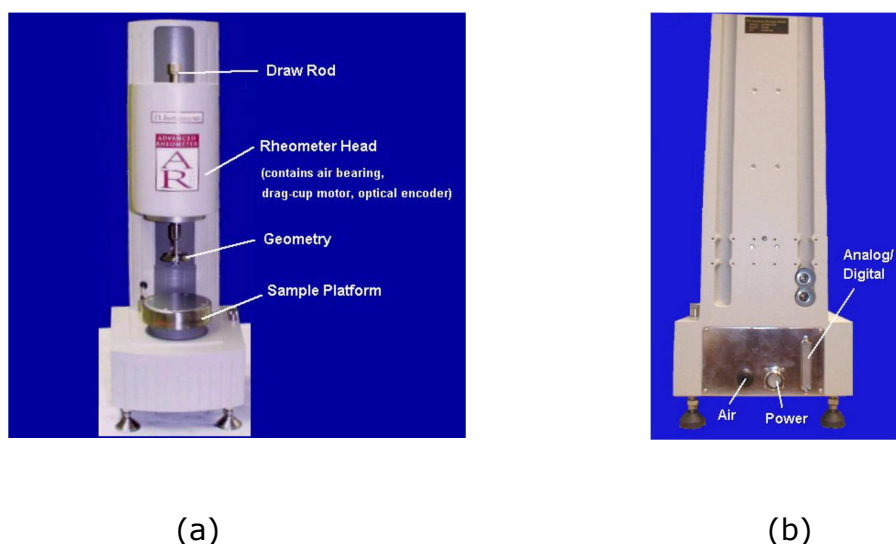


Figure 4.5 - Pictorial views of the AR1000 Rheometer: (a) front view, (b) rear view

Figure 4.6 depicts a pictorial view of the complete unit to which a conical geometry is attached making up a cone and plate system when the Peltier temperature control plate is used. The cone and plate geometry has advantages as it needs only small sample volume, is easy to clean, has low inertia, and high shear rate that is uniform throughout the sample. Figure 4.8 shows the cone and plate geometry and the geometric factors used in converting torque and displacement into stress and strain. In Figure 4.8(b) the stress factor $[\sigma]$ and the shear rate factor $[\dot{\gamma}]$ are defined based on the torque $[M]$, the radius $[R]$, the angular velocity $[\omega]$ and the cone angle $[\alpha]$.

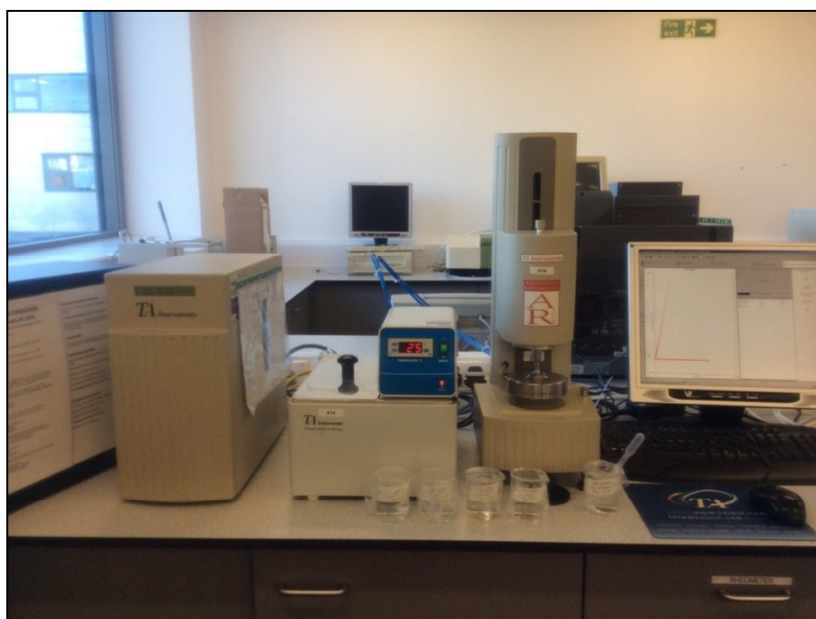


Figure 4.6 – Picture of TA Instruments advanced rheometer (model AR1000) used for the polymer characterisation



Figure 4.7 – Picture of a Jenway 3505 digital pH/ion-meter used for measuring pH of samples

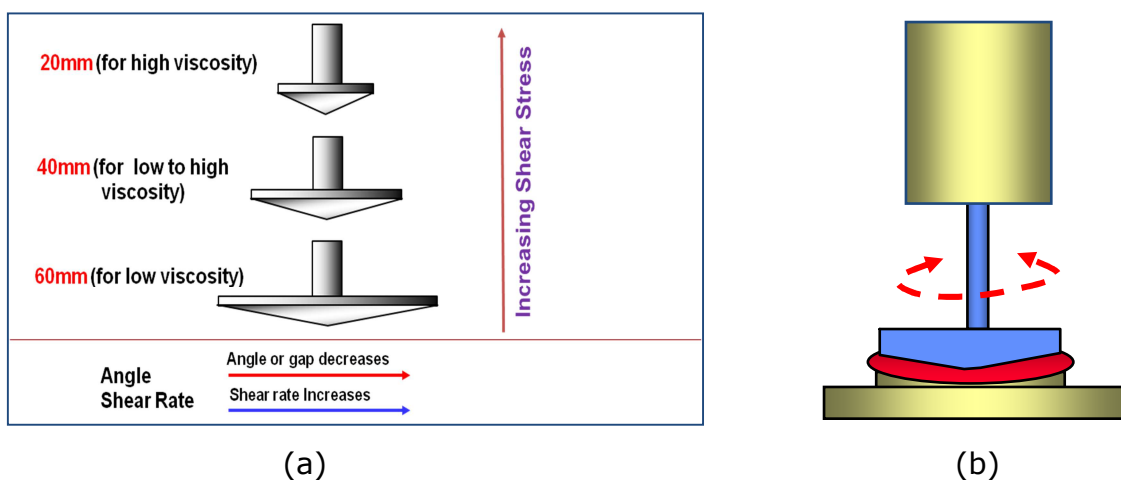


Figure 4.8 - The Cone and Plate geometry schemes: (a) shows variety of geometry for different viscosity conditions, (b) shows truncation gap or height (Source: TA Instruments)

4.7.1 Temperature Control - The Peltier Plate

Temperature control in the AR1000 standard configuration is via a Peltier plate, which uses the Peltier effect to rapidly and accurately control heating and cooling. The Peltier system uses a thermo-electric effect. This functions as a heat pump system with no moving parts, and is ideally suited to rheological measurements. By controlling the magnitude and direction of electric current, the Peltier system can provide any desired level of active heating or cooling directly in the plate. The Standard Peltier System temperature range is from -10°C to 99°C .

4.7.2 Samples preparation for rheological measurements

Prior to measurements, the samples were prepared according to standard procedures described in section 4.7.1.3 above (API RP 63, 1990). Synthetically formulated model brines (SFB) were applied to all solutions as previously stated. As a conditioning step, HCl or NaOH was added to adjust the pH of the sample solutions prior to testing. A Jenway 3505 model digital pH/ion meter with combination electrodes was used to measure samples pH before testing.

4.7.3 Methodologies

All the samples were tested using a steel 4mm 2° cone and plate geometry of the AR1000 rheometer (Figures 4.8 and 4.6) with acrylic solvent trap cover. All Flow tests were performed at 25°C except otherwise stated. The flow tests performed were all equilibrium flow measurements. That is, each data point was derived from a steady state test [step stress test] and the viscosity at that stress calculated from the steady state slope of the stress or shear rate response.

The following methods were used in the flow experiments conducted:

- Steady state flow/ Stepped flow
- Temperature ramp
- Continuous stress/rate ramp
- Peak Hold
 - Constant shear rate/stress

4.7.3.1 Steady state flow/ stepped flow

In this method, shear rate range of 0.1-100 s⁻¹ typical of field project was applied to 750 ppm of each sample solution of pH=8.2. Viscosity measurement was taken when material had reached steady state flow. The stress was increased (logarithmically) and the process was repeated yielding a viscosity flow curve (viscosity vs. shear rate and time) with a specified flow algorithm.

- a) During the test, the dependent variable (speed in controlled stress mode or torque in controlled shear rate mode) was monitored with time to determine when stability has been reached.
- b) An average value for the dependent variable was recorded over the sample period (10 seconds in this work).
- c) When consecutive average values (Consecutive within tolerance=5 in this work) were within the tolerance specified, the data was accepted.
- d) The software will also accept the point at the end of the Maximum point time, should the data still not be at a steady state value.

4.7.3.2 Temperature ramp

Temperature ramps tests were performed on 1000 ppm solution of each of sample FP3630 S, FP 3330 S and FloComb C3525 at pH of 8.2 applying a constant shear rate of 1 s^{-1} and sampling delay time of 10 seconds over a range of $10 \text{ }^{\circ}\text{C}$ to $70 \text{ }^{\circ}\text{C}$ to determine critical temperature response of sample materials. A time of 5 minutes was considered sufficient to ensure thermal equilibration of the sample prior to testing, i.e. Conditioning Step. To minimize thermal lag, a ramp rate of $3^{\circ}\text{C}/\text{min}$ was used. Viscosity data were recorded as function of temperature and time.

4.7.3.3 Continuous ramp

In order to measure the yield stress of samples, shear rate from 0 - 100 s^{-1} was applied to 750 ppm of each sample solution of $\text{pH}=8.2$ for a period of 3 minutes in linear mode. Resultant shear stress and shear rate data were monitored with time and recorded.

4.7.3.4 Peak Hold

This single point test was performed for the purpose of observing the time-based stability of the samples. A shear rate of 10 s^{-1} was applied to 750 ppm of each sample solution of $\text{pH}=8.2$ for duration of 1 minute with a sampling period of 1 second. The shear stress and viscosity data as function of time were recorded.

4.8 Results and Discussion

4.8.1 Dependence of Viscosity on Shear Rate

In order to attempt a discussion on the effect of shear on viscosity, an explanation of the reason for general flow curve is required. How liquid behaves or responds to stress is referred to as 'Viscous' response. At low shear rate, Brownian diffusion randomizes. At this low shear region, viscosity is almost independent of shear (Newtonian region). As the shear is gradually increased, shear field aligns particles or molecules along streamlines resulting in shear thinning (Figure 4.9). As the shear is

further increased, turbulent flow push particles out of alignment causing particles to bang into one another destroying order and causing increase in viscosity (shear thickening) (Figure 4.9). Figure 4.10 to Figure 4.13 show the effect of shear rate on viscosity of samples FP3630 S and FloComb C3525 in 0.1% NaCl. The application of shear causes structure breakdown, hence reduction in chain sizes under high shear leading to a consequent reduction in viscosity. The figures show a decreasing viscosity with increasing shear rate. The non-linear trend in the sample viscosity profiles is expected of typical non-Newtonian fluids. The combined curve of Figure 4.11 shows proportionate increase in viscosity with concentration. As the shear rate increases, the polymer solution viscosity reduces. As the shear rate increases further, the effect of concentration of polymer also vanishes.

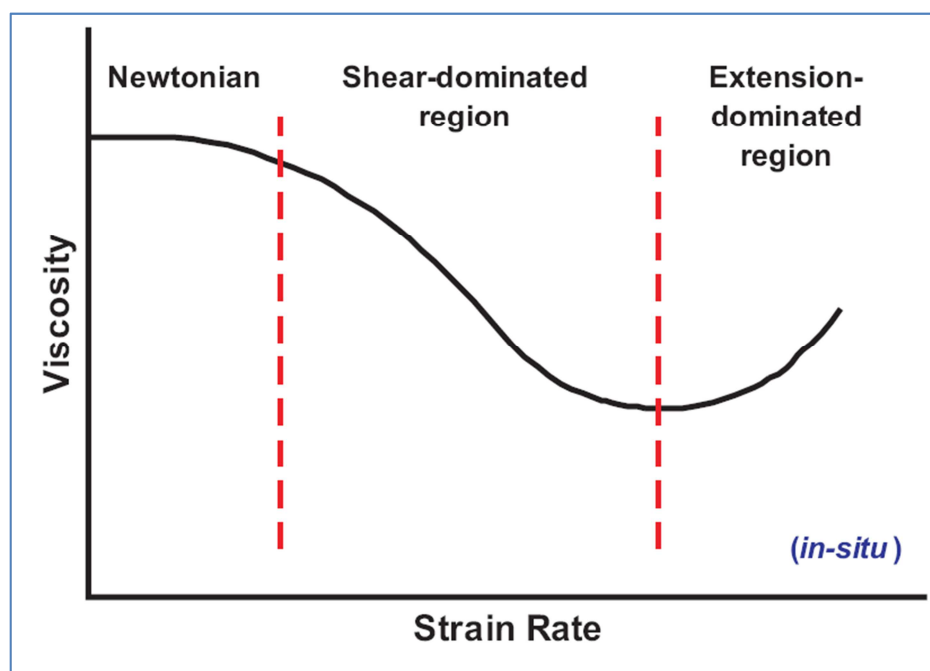
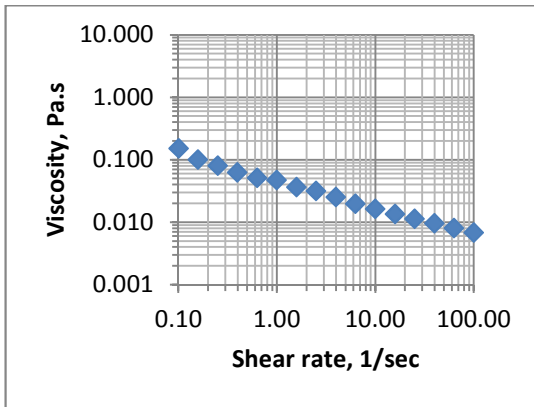
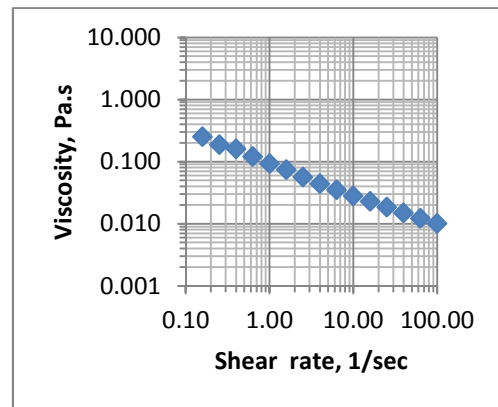


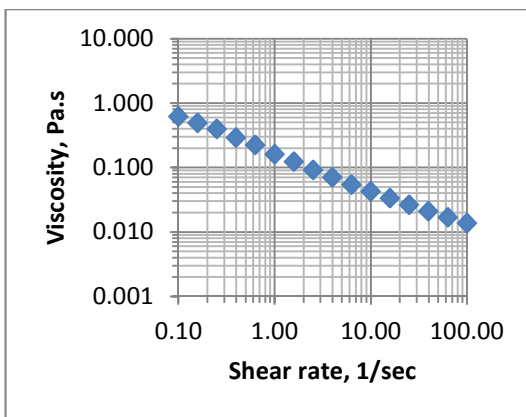
Figure 4.9 - Explanation for the effect of shear on the shape of general flow curve.



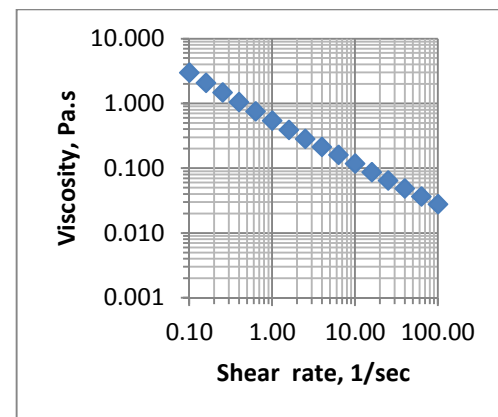
(a)



(b)



(c)



(d)

Figure 4.10 - Dependence of viscosity on shear rate for FP3630 S: (a) 500ppm, (b) 750ppm, (c) 1000ppm, (d) 2000ppm in 0.1% NaCl, pH=8.2 and 25 °C

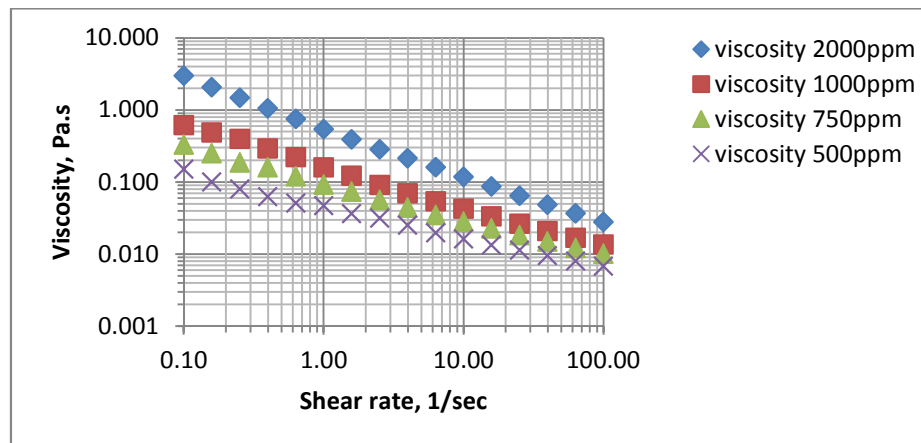
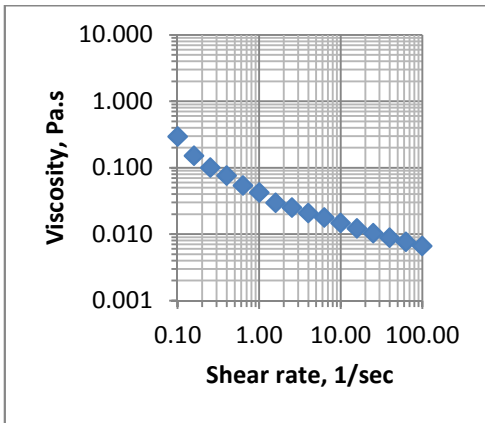
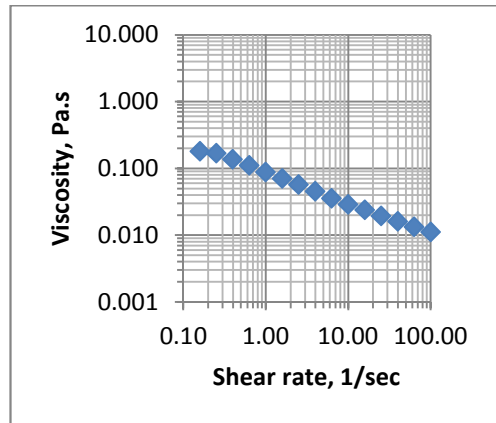


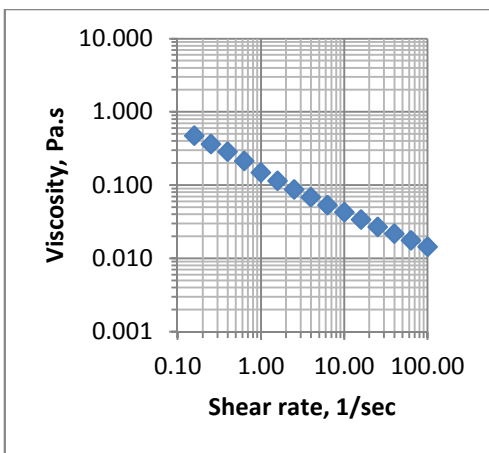
Figure 4.11 - Effect of shear rate on viscosity of FP3630 S solution at different concentrations in 0.1% NaCl, pH=8.2 and 25 °C



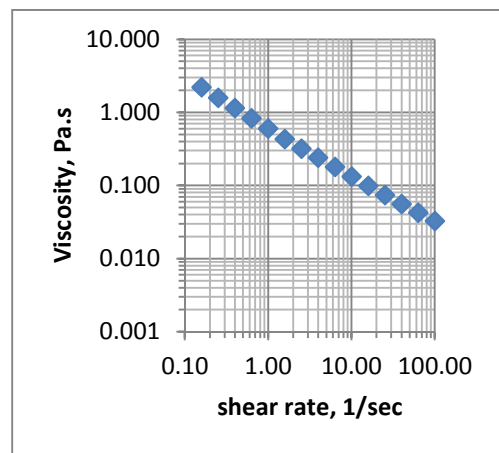
(a)



(b)



(c)



(d)

Figure 4.12 - Dependence of viscosity on shear rate for FloComb C3525: (a) 500ppm, (b) 750ppm, (c) 1000ppm, (d) 2000ppm in 0.1% NaCl, pH=8.2 and 25 °C

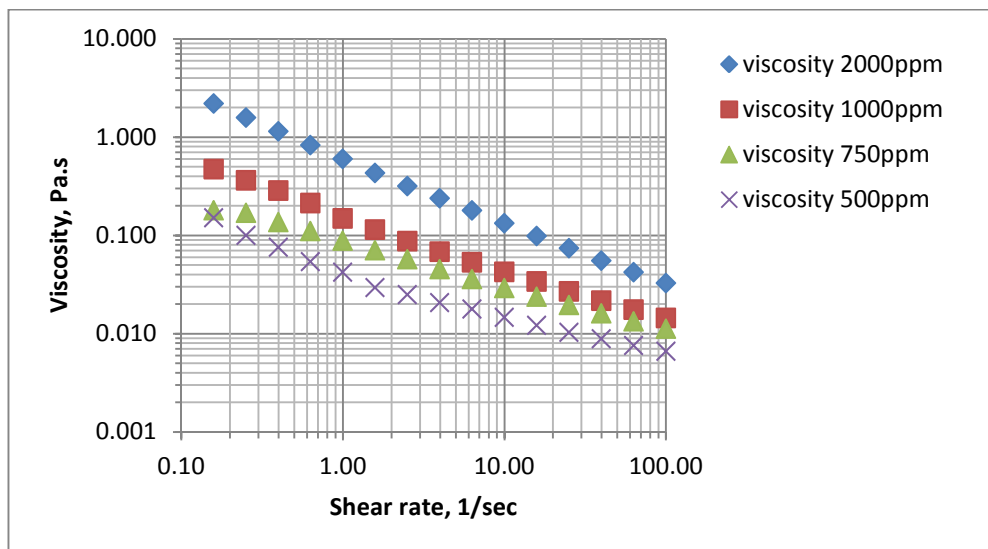


Figure 4.13 - Effects of shear rate on viscosity of C3525 solution at different concentrations in 0.1% NaCl, pH=8.2 and 25 °C

4.9 Flow data modelling

A basic form of data processing in rheology is the use of flow models which are used to predict flow behaviour over a wide range of shear stresses or shear rates. In general, the type of model used is determined by the experiment type. For instance, Newtonian to Herschel-Buckley should be used for simple linear flow curve; while the Carreau, Cross, or Sisko/Williamson models are preferable for logarithmic data set. [Figure 4.14](#) and [Figure 4.15](#) show the FP3630 S and FloComb C3525 results fitted to the Carreau model (Eqn. 4.7) using the TA Instruments *Advantage Data Analysis Software*. As the results of the fit shows, the standard error of less than 10% is an indication of good mathematical fit.

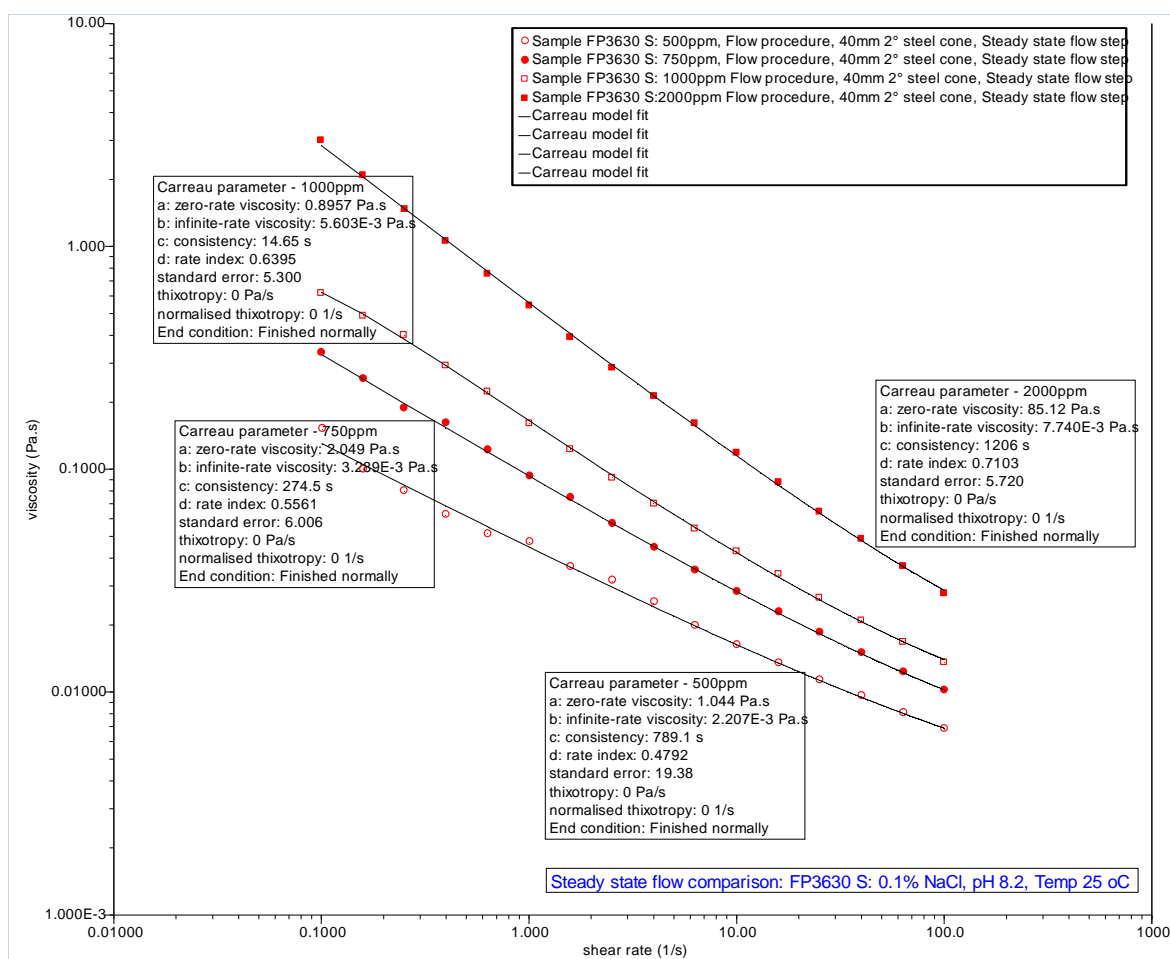


Figure 4.14 - Data fit to Carreau model for concentrations of FP3630 S in 0.1% NaCl, pH=8.2 and 25 °C

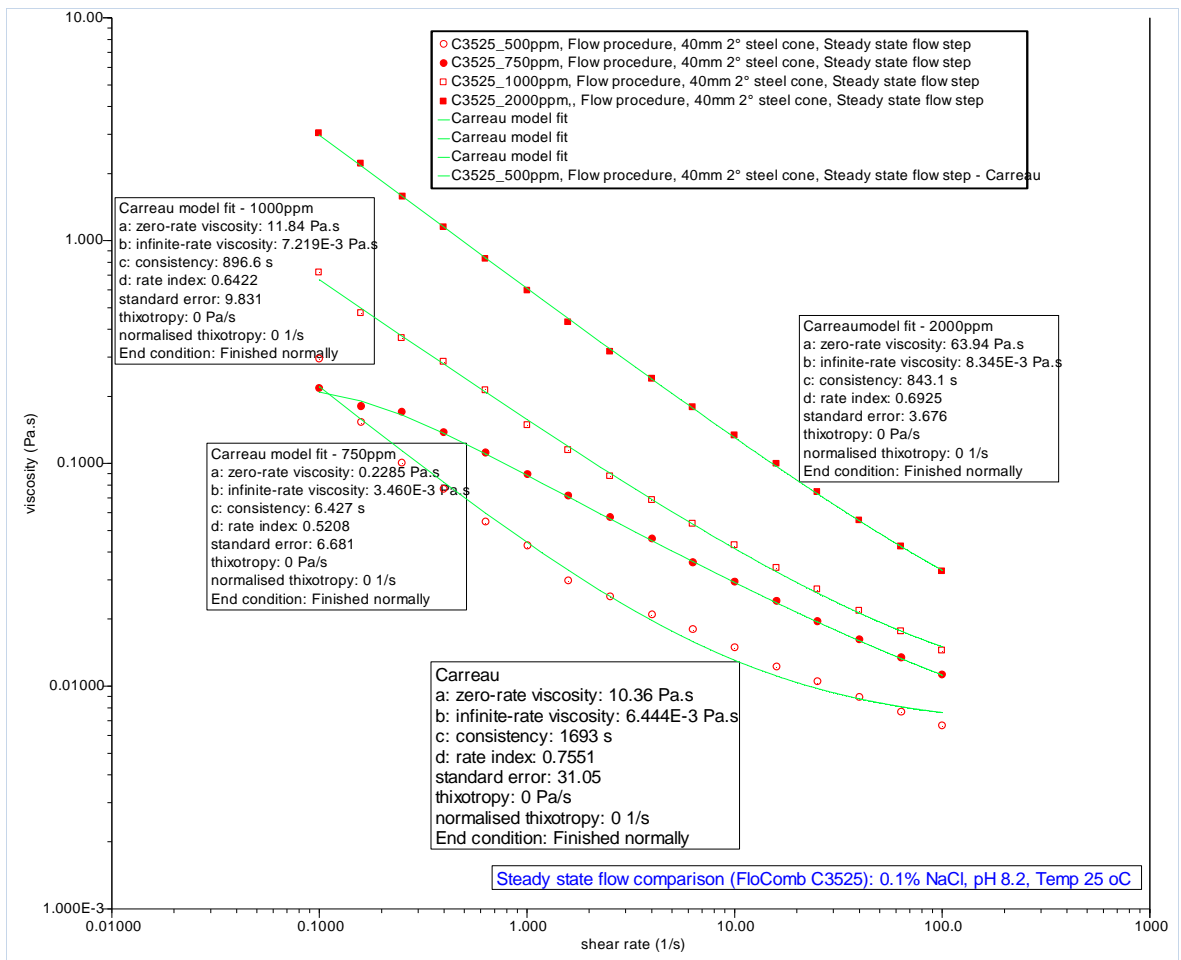


Figure 4.15 - Data fit to Carreau model for concentrations of FloComb C3525 in 0.1% NaCl, pH=8.2 and 25 °C

Figure 4.16 and Figure 4.17 show shear stress vs. shear rate and viscosity vs. time plots respectively for 500 ppm solution (pH=8.2) in 0.1% NaCl of sample FP3330 S. Figure 4.16 exhibits pseudoplastic behaviour. As stated before, shear disrupts the hydrophobic micro-domains (both intra- and interchain) resulting in a reduction in viscosity as shown in Figure 4.18.

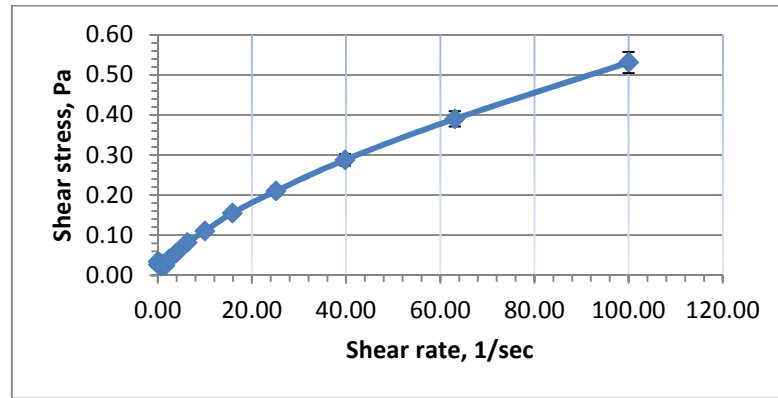


Figure 4.16 - Shear stress vs. Shear rate of 500 ppm solution of sample FP3330 S in 0.1% NaCl, pH=8.2 and at 25 °C

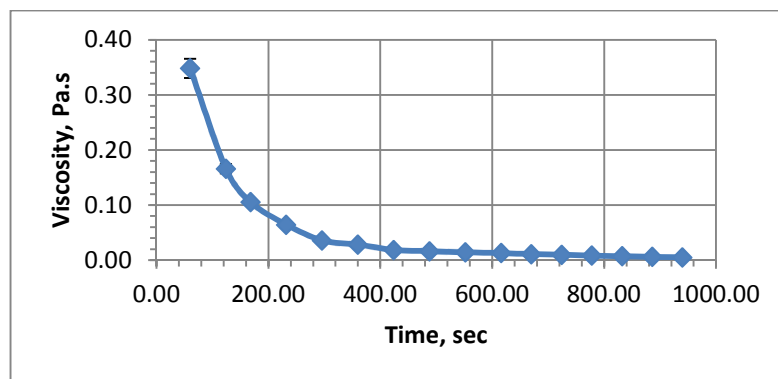


Figure 4.17 - Viscosity vs. time of 500 ppm solution of sample FP3330 S in 0.1% NaCl, pH=8.2 and 25 °C

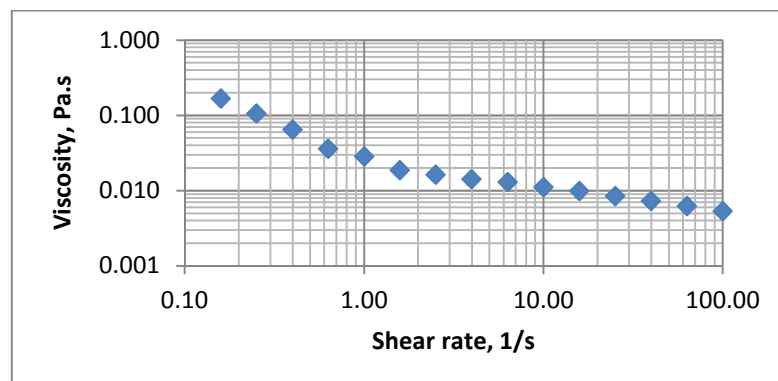
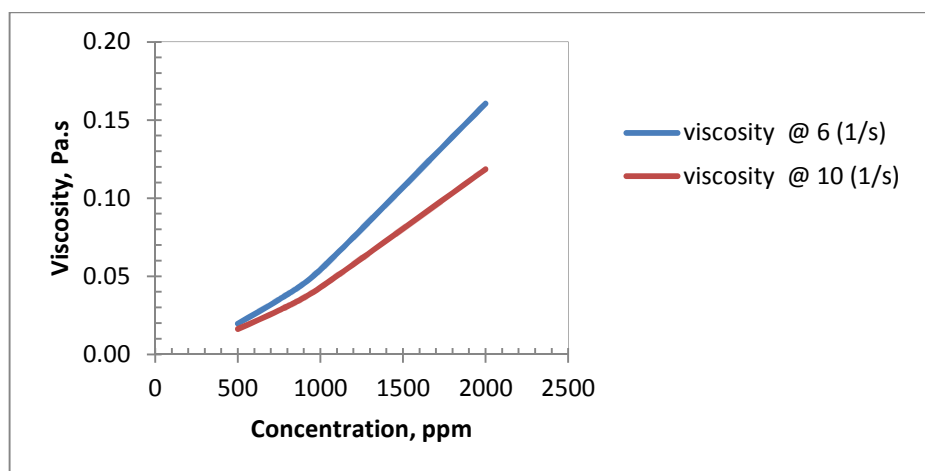


Figure 4.18 - Dependence of viscosity on shear rate of 500 ppm solution of sample FP3330 S in 0.1% NaCl, pH=8.2 and 25 °C

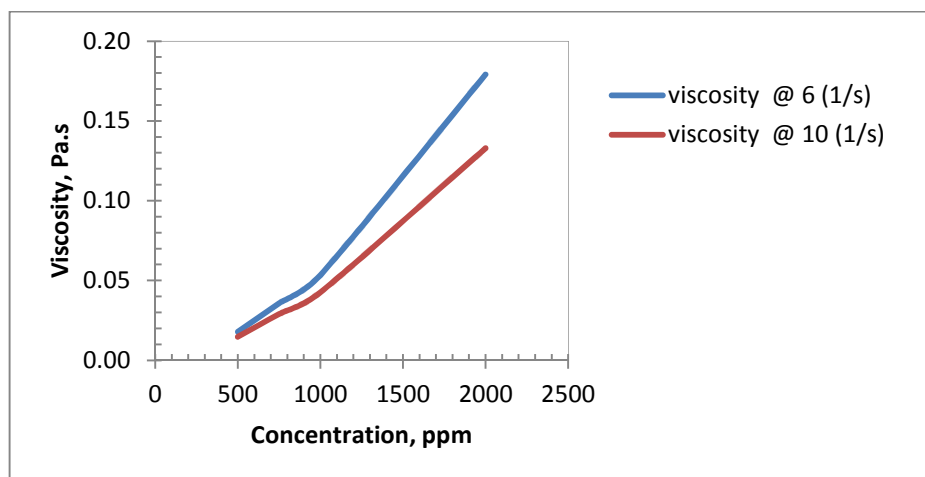
4.10 Relationship of Polymer Concentration and Viscosity

Figure 4.19 shows that the viscosity of dilute solutions increases non-linearly with concentration for samples FP3630 S and FloComb C3526. At low polymer concentrations (the so-called dilute region), intramolecular

associations dominate leading to a reduction in the hydrodynamic volume, and hence the reduction in viscosity. On the other hand, the solution transits to the semi-dilute region (at higher concentration) where intermolecular associations dominate. The resulting transient network causes a significant increase in viscosity (Wever et al., 2011).



(a)



(b)

Figure 4.19 - Plot of polymer concentration vs. viscosity @ shear rates of 6 s^{-1} and 10 s^{-1} : (a) FP3630 S (b) FloComb C3525 in 0.1% NaCl, pH=8.2 and 25°C

4.11 Effect of pH on Viscosity

Steady state flow procedure was performed on sample FP3330 S in 0.1% NaCl, concentration of 750ppm, and at pH of 4.0, 7.0, 8.2 and 10.0 respectively. The test was conducted at shear rates of 6.3 s^{-1} and 10 s^{-1} . The data recorded in Figure 4.20 shows that solution viscosity increases

gradually to a maximum as pH increases from 4 to 10. The observed behavior is due to the neutralization effects of the carboxylic groups which causes both intramolecular electrostatic repulsion, thus chain extension (dominant at low pH); and disruption of intermolecular associations resulting from intermolecular electrostatic repulsion (dominant at high pH) (Zhang et al., 2008). Furthermore, polyanions are known to have low viscosity at low pH and high viscosity at high pH (Wever et al., 2011).

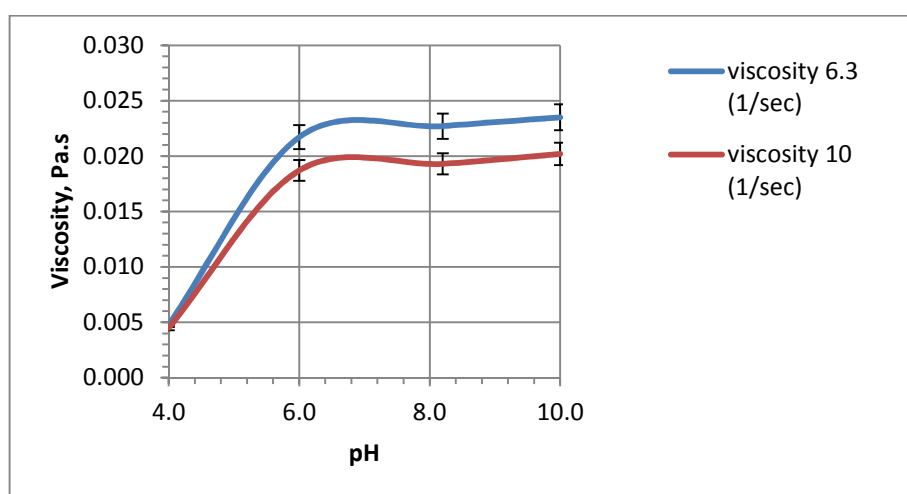


Figure 4.20 - Effects of pH on viscosity of 750 ppm of sample FP3330 S in 0.1% NaCl measured at 25 °C and pH=8.2

4.12 Effect of Temperature on Viscosity

Temperature is an important variable in translating laboratory measurement of oil and gas related operations (e.g., EOR, etc) to reservoir conditions. The viscosity of polymer solution is quite sensitive to temperature. At a low shear rate, the polymer solution apparent viscosity (μ_p) decreases with temperature according to the Arrhenius equation:

$$\mu_p = A_p \exp\left(\frac{E_a}{RT}\right) \quad (4.13)$$

where, A_p =frequency (or pre-exponential) factor, E_a = activation energy of the polymer solution, R =universal gas constant, T =absolute temperature. Equation (4.13) shows that the viscosity decreases rapidly

as the temperature increases. The plausible explanation for the mechanism is that as the temperature increases, the activity of the polymer chains and molecules is enhanced, and the friction between the molecules is reduced; thus, the resistance to flow is reduced, and consequently the viscosity decreases. Different polymers have different E_a . Polymers with higher E_a are more sensitive to temperature. For example, HPAM has two E_a s: 1.) at temperature less than 35 °C, E_a is low, and the viscosity does not change appreciably as the temperature increases; 2.) at temperature greater than 35 °C, E_a is high, and the viscosity is more sensitive to temperature variations. Furthermore, it is presumably believed that random scission of the polymer chain is the principle mechanism of polymer decomposition in-situ (i.e., primarily as a result of polymer decomposition by random scission cleavage of the backbone) (Lange and Huh, 1994). According to the random scission model, the polymer molecular weight distribution (MWD) changes due to thermal degradation. Specifically, higher molecular weight (M_w) polymer components degrade to lower M_w components, causing loss of polymer viscosity. In reservoir condition, since particle/molecular adhesion force is sensitive to temperature, shear resistance is also temperature dependent (Civan, 2007). Therefore, knowledge of temperature dependence of viscosity is a prerequisite for modelling formation damage in reservoirs. From the above, the effect of temperature on viscosity can then be explained.

Figure 4.21 through Figure 4.24 show that solution viscosity decreases as temperature increases for all three samples because an increase in temperature causes a decrease in the association strength of the hydrophobes. Furthermore, Figure 4.23 shows that viscosity dependence on temperature is a linear function of time. The figure also shows a pronounced viscosity oscillation as temperature increases further. Sample FP3630 S is more temperature stable compared with the other two samples. The order of temperature stability (FP3630 S > C3525 > FP3330 S) is shown in a combined curve of Figure 4.24 for the three samples. The plausible explanation for this observation is that FP3630 S has a

reticular structure with tendency to reduce the effect of temperature on its chain to a certain possible extent (Wever et al., 2011). The same explanation is likely applicable to C3525 over FP3330 S.

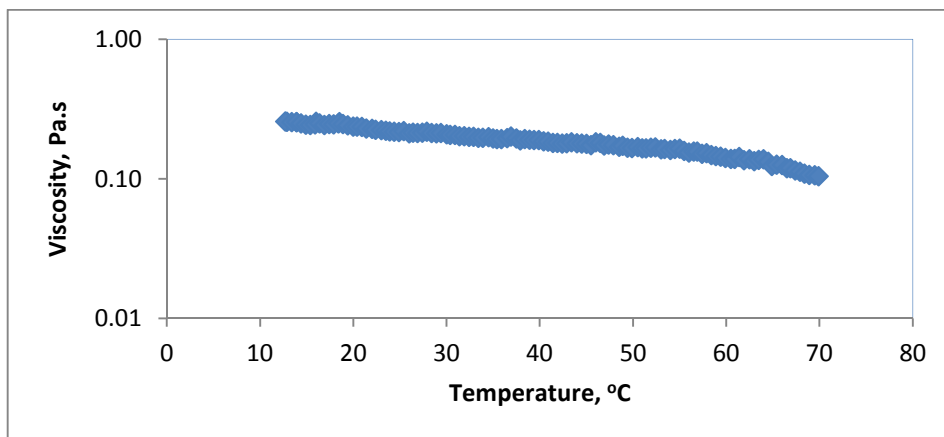


Figure 4.21 - Viscosity as function of temperature for 1000 ppm of FP3630 S at pH=8.2 and at constant shear rate of 1 s^{-1} from $10 \text{ }^\circ\text{C}$ to $70 \text{ }^\circ\text{C}$

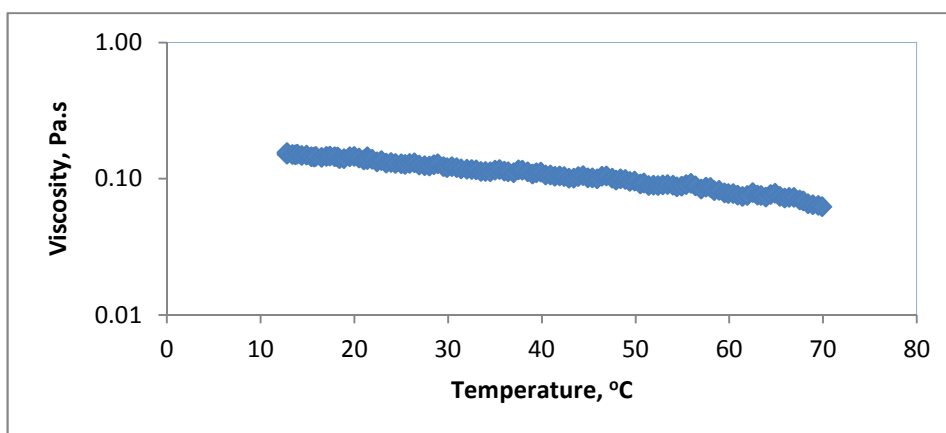


Figure 4.22 - Viscosity as function of temperature for 1000 ppm of FloComb C3525 at pH=8.2 and at constant shear rate of 1 s^{-1} from $10 \text{ }^\circ\text{C}$ to $70 \text{ }^\circ\text{C}$

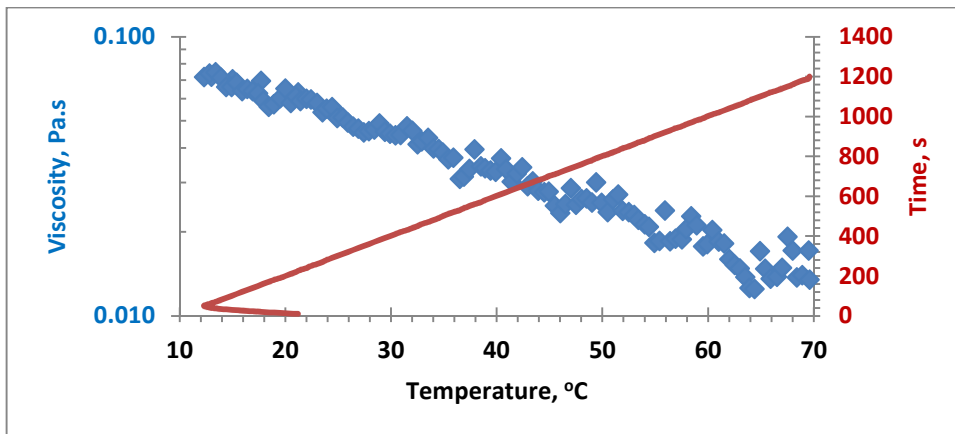


Figure 4.23 - Viscosity as function of temperature for 1000 ppm of FP3330 S at pH=8.2 and at constant shear rate of 1 s^{-1} from $10 \text{ }^\circ\text{C}$ to $70 \text{ }^\circ\text{C}$

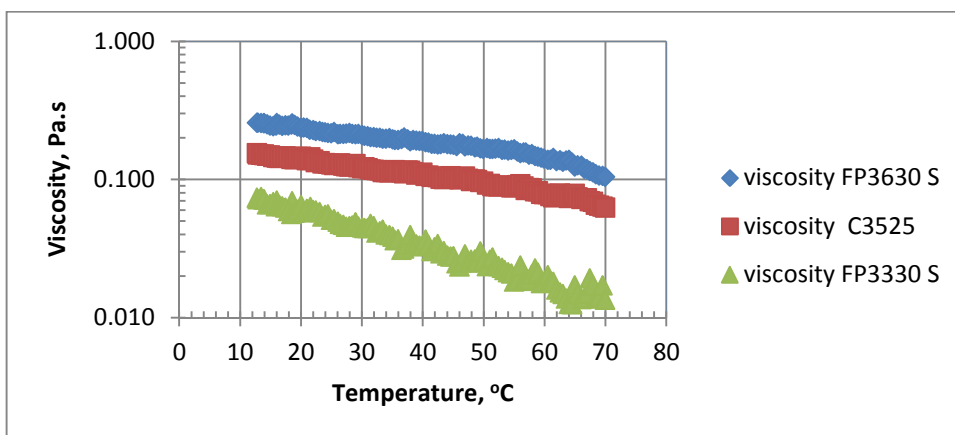


Figure 4.24 - Effect of temperature on viscosity for 1000 ppm of three samples at pH=8.2. The temperature ramp test was performed over a range of $10 \text{ }^\circ\text{C}$ to $70 \text{ }^\circ\text{C}$ at constant shear rate of 1 s^{-1}

4.13 Effect of molecular weight

A material viscosity in the low shear plateau is related to the polymer molecular weight (M_w). Therefore, the higher the M_w , the higher the viscosity plateau (zero-shear viscosity). The data of Figure 4.25 shows that samples C3525 and FP3630 S (with almost similar M_w) have higher molecular weight and higher viscosity than FP3330 S.

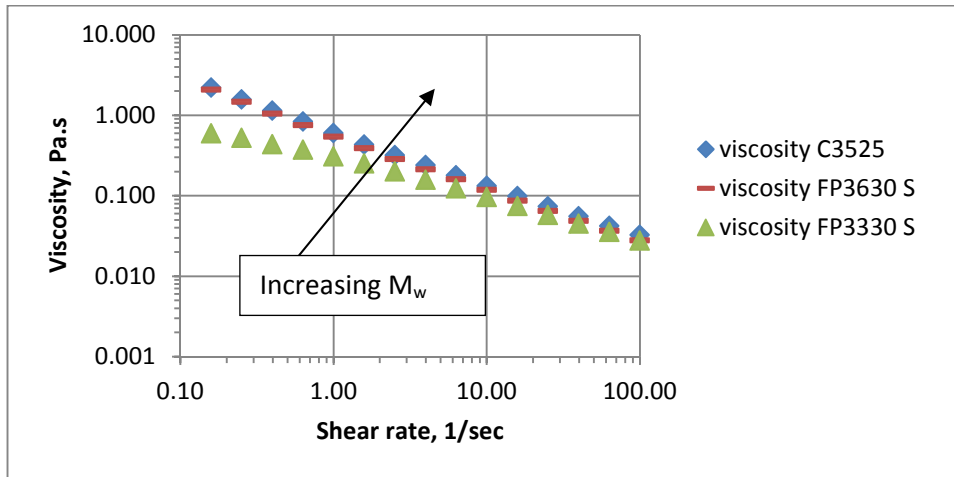


Figure 4.25 - Effect of molecular weight on viscosity for three samples (750 ppm each) in 0.1% NaCl brine, pH of 8.2 and test temperature of 25 °C. Shear rate range of 0.1-100 s⁻¹ typical of field project was applied to the samples.

4.14 Effects of Salinity and Hardness on Viscosity

Salinity: Refers to the presence of the major dissolved inorganic solutes, essentially Na⁺, K⁺, Mg²⁺, Ca²⁺, Cl⁻, SO₄⁻, HCO₃⁻, and CO₃²⁻, in aqueous samples. Salinity is quantified in terms of total concentration or content of such soluble salts (TDS).

Hardness: Is the poly-valent-cation concentration of water (generally Ca²⁺ and Mg²⁺). OR A measure of the quantity of divalent ions (e.g. Ca²⁺, Mg²⁺, etc) in water, usually reported in mg/L or ppm. Hardness can be a mixture of divalent salts (referred to as total hardness); however, Ca²⁺ and Mg²⁺ are the most common sources of hard water. Hardness is measured by chemical titration.

Dependence of viscosity on Salinity and Hardness were tested on samples FP3630 S and C3525. Each sample was diluted to 750 ppm at pH of 8.2 in brines containing both NaCl and CaCl₂ in ratios of 10 to 1 as follows:

Brine A: 0.04% NaCl + 0.004% CaCl₂

Brine B: 0.4% NaCl + 0.04% CaCl₂

Brine C: 1.0% NaCl + 0.1% CaCl₂

Brine D: 10% NaCl + 1% CaCl₂

Figure 4.26 to Figure 4.29 show the steady state flow procedure results at 7.3 s^{-1} for the three samples. Figure 4.26 shows that as the brine salinity increases, the viscosity reduces for C3525. The trend is similar for sample FP3630 S shown in Figure 4.27. Similar results have been reported by Ali and Barrufet (2001) for HPAM solutions. However, sample FP3330 S shows a higher level of viscosity loss with increasing brine salinity concentration (Figure 4.28). The shielding effect of the charges on the polymer causes a reduction in electrostatic repulsion and thus to less significant expansion of polymer coils in solution. This, in turn, leads to lower hydrodynamic volume which translates to reduction in viscosity. Furthermore, the polyion-metal complexes formed by the Ca^{2+} have greater effect on solution viscosity reduction (Wever et al., 2011). Figure 4.29 shows combined plots of the effect of salt concentrations on the viscosity of the three samples. The figure shows that FloComb C3525 exhibits lower viscosity loss with increasing calcium ion concentration. This result confirms the manufacturer's claim that FloComb C3525 is calcium tolerant.

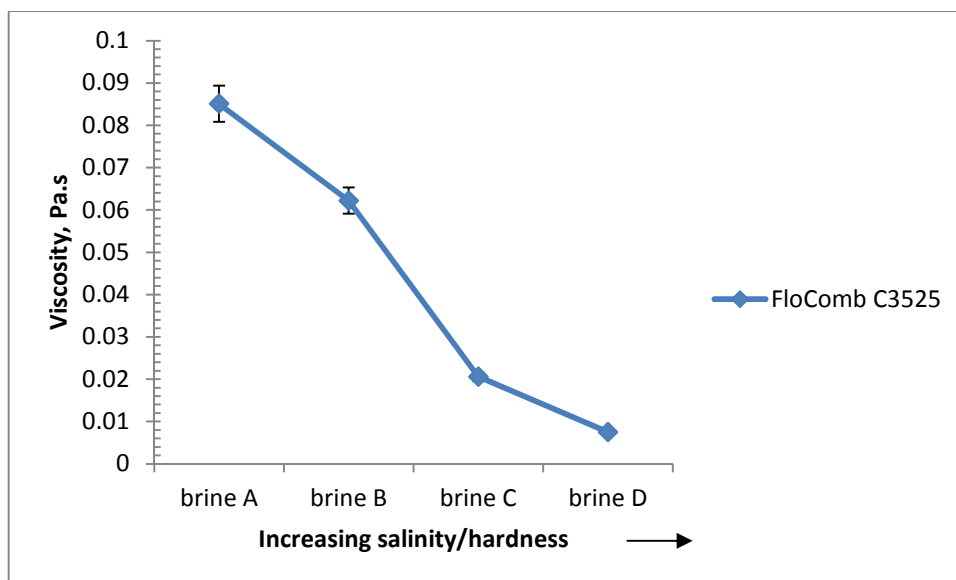


Figure 4.26 - Effect of salinity and hardness on viscosity of 750 ppm of FloComb C3525 solution of pH=8.2 measured at constant shear rate (7.3 s^{-1}) and $25 \text{ }^{\circ}\text{C}$

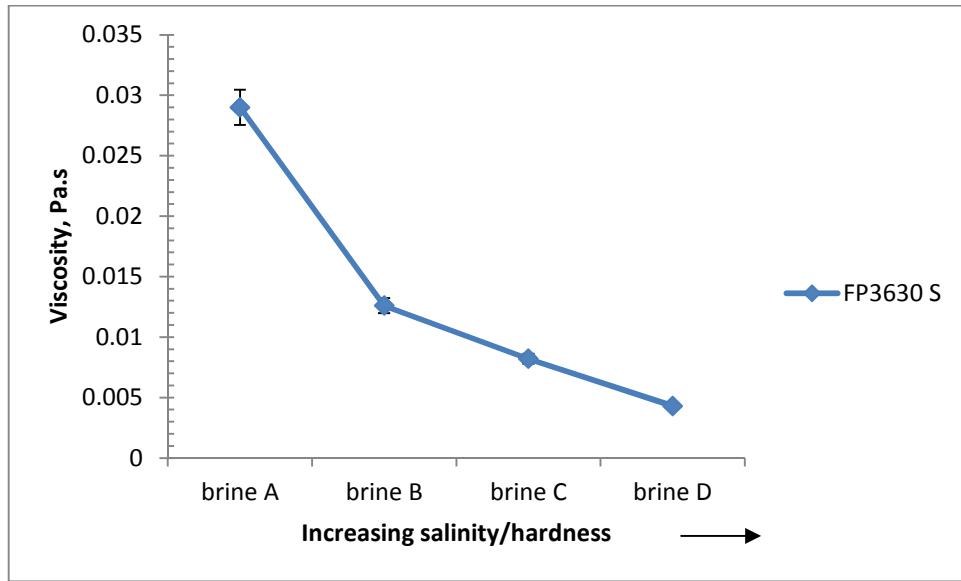


Figure 4.27 - Effect of salinity and hardness on viscosity of 750 ppm of FP3630 S solution of pH=8.2 measured at constant shear rate (7.3 s^{-1}) and $25 \text{ }^{\circ}\text{C}$

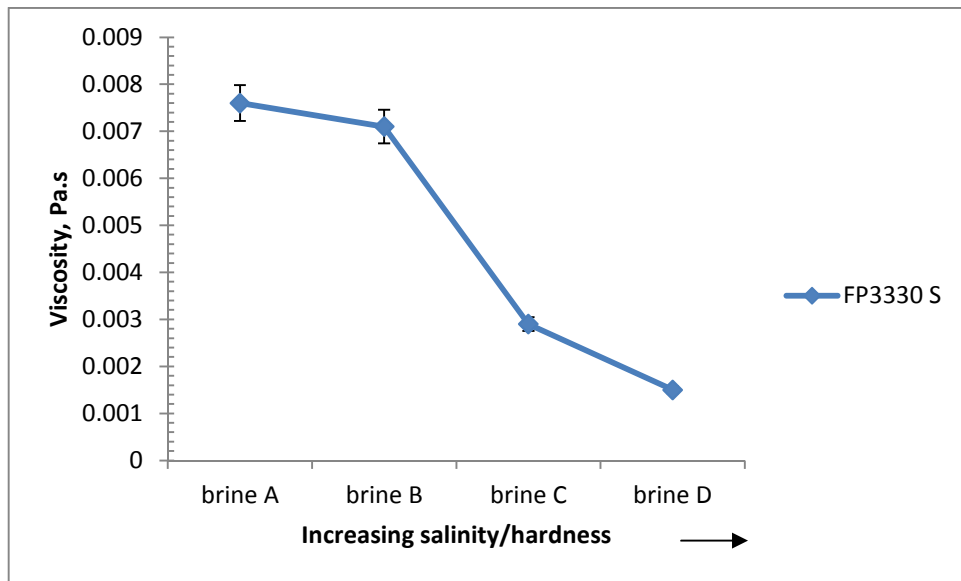


Figure 4.28 - Effect of salinity and hardness on viscosity of 750 ppm of FP3330 S solution of pH=8.2 measured at constant shear rate (7.3 s^{-1}) and $25 \text{ }^{\circ}\text{C}$

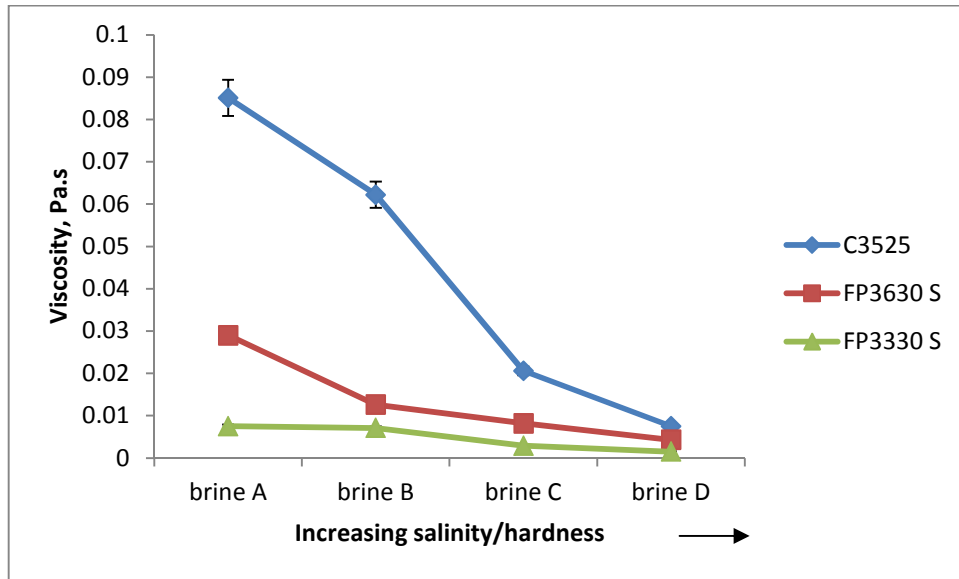


Figure 4.29 - Effect of salinity and hardness on viscosity of 750 ppm for the three samples solutions of pH=8.2 measured at constant shear rate (7.3 s^{-1}) and $25 \text{ }^\circ\text{C}$. This result confirms the manufacturer's claim that FloComb C3525 is calcium tolerant as it has lower viscosity loss as calcium ion concentration increases

4.15 Peak Hold Procedure

Figure 4.30 to Figure 4.32 show the results of the peak hold procedures conducted on two samples at 10 s^{-1} . Figure 4.30 shows stress overshoot and gradual relaxation to steady state viscosity, a trend typical of viscoelastic fluids. The steady state viscosity at 10 s^{-1} is about 0.0148 Pa.s for FP3630 S (Figure 4.30) and 0.013 Pa.s for C3525 (Figure 4.31). Figure 4.32 shows that sample FP3630 S has higher steady state viscosity than C3525.

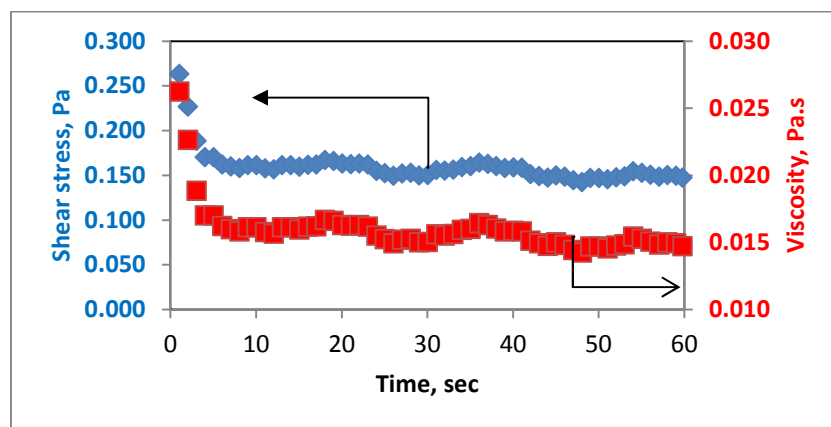


Figure 4.30 - Peak hold procedure showing time-based viscosity stability for 750 ppm solution (pH=8.2) of FP3630 S in 0.4% NaCl measured at 10 s^{-1} and $25 \text{ }^\circ\text{C}$

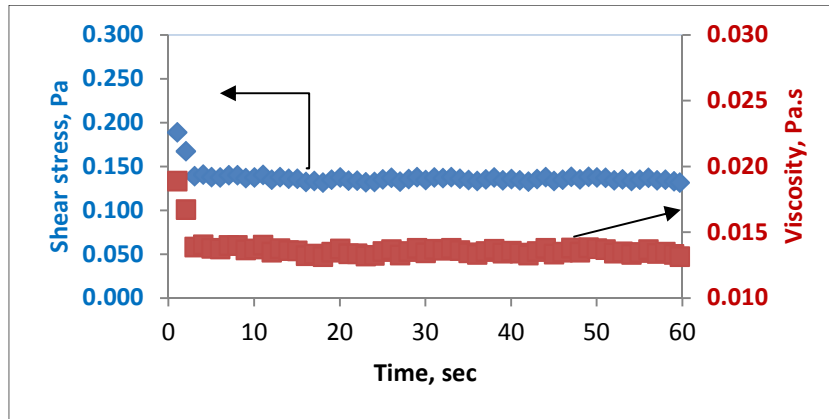


Figure 4.31 - Peak hold procedure showing time-based viscosity stability for 750 ppm solution (pH=8.2) of FloComb C3525 solution in 0.4% NaCl measured at @ 10 s^{-1} and $25 \text{ }^{\circ}\text{C}$

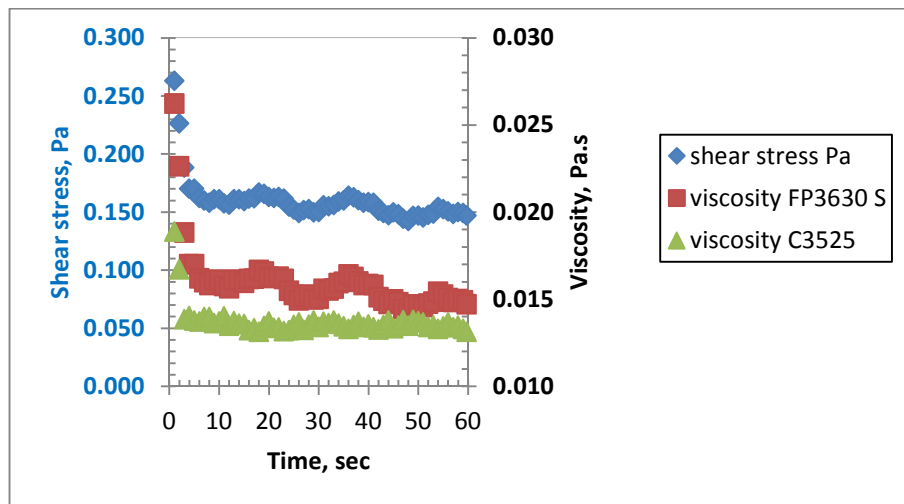


Figure 4.32 - Peak hold comparison showing time-based viscosity stability for 750 ppm solutions (pH=8.2) of FP3630 S and FloComb C3525 @ 10 s^{-1} in 0.4% NaCl

4.16 Continuous Ramp Test

Figure 4.33 and Figure 4.34 show the continuous ramp step results for 750 ppm solutions (pH=8.2) of FP3630 S and FloComb C3525 in 0.1% NaCl measured at $25 \text{ }^{\circ}\text{C}$ from $0.1\text{-}100 \text{ s}^{-1}$. The ramp step was conducted to compare the yield property of the two samples. Data fit to Herschel-Bulkley model using TA Instruments advantage data analysis software shows that both samples (FP3630 S and FloComb C3525) have almost similar yield stresses (Figure 4.35).

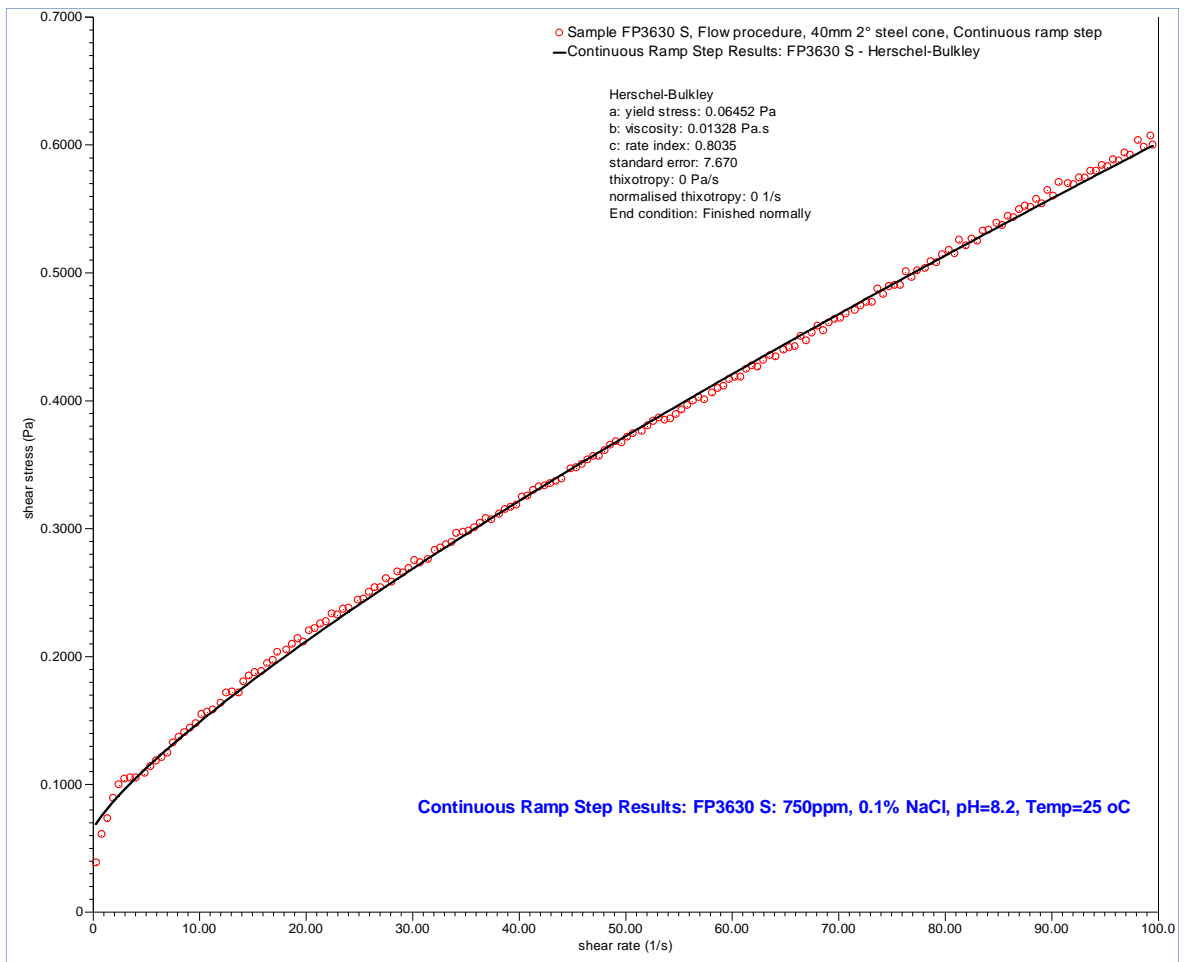


Figure 4.33 - Continuous ramp results for sample FP3630 S in 0.1% NaCl: open cycles (o) is experimental data and dash (—) is Herschel-Bulkley model fit to experimental data. The sample has a yield stress of about 0.06452 Pa

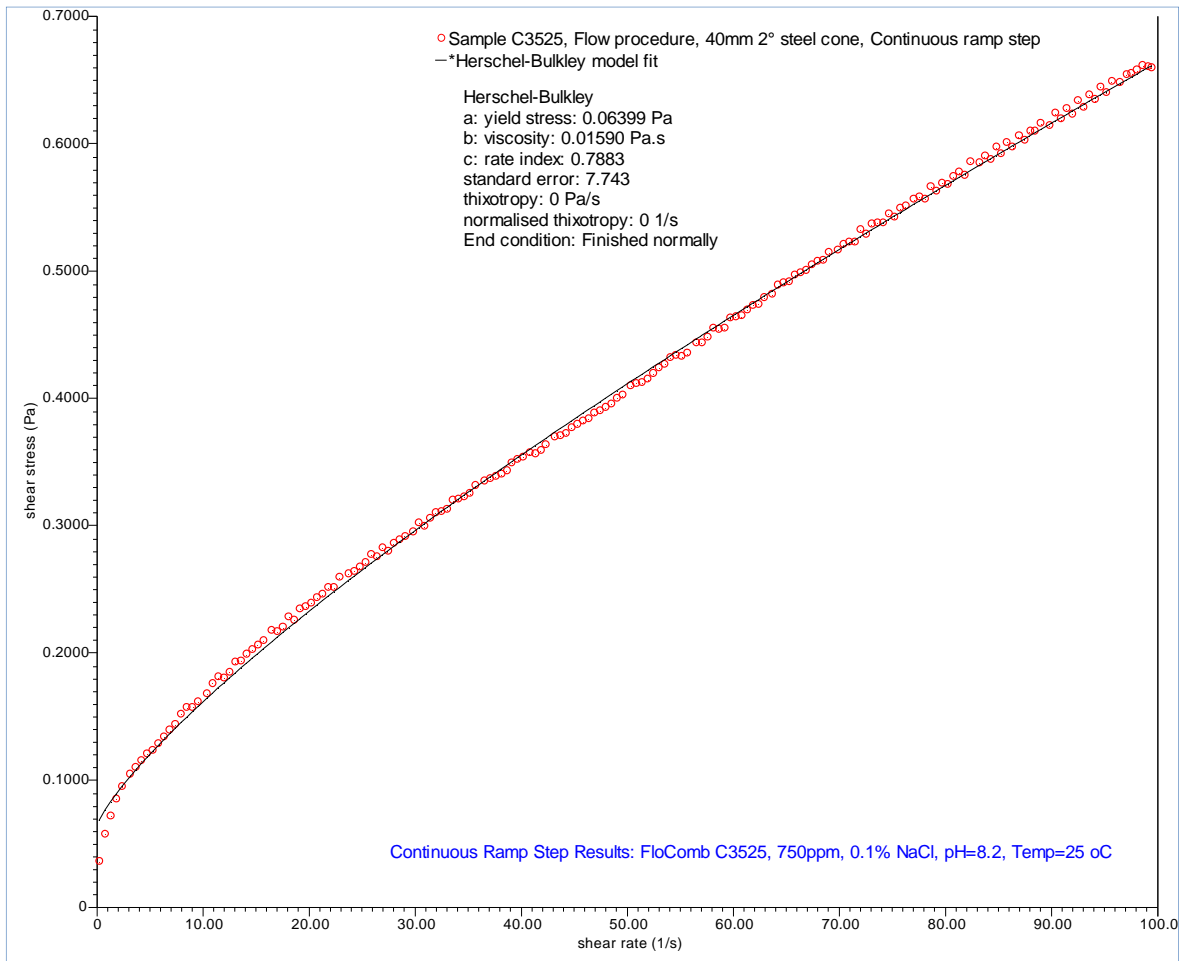


Figure 4.34 - Continuous ramp step results for sample FloComb C3525 in 0.1% NaCl: open cycles (o) is experimental data and dash (—) is Herschel-Bulkley model fit to experimental data. The sample has a yield stress of about 0.06399 Pa

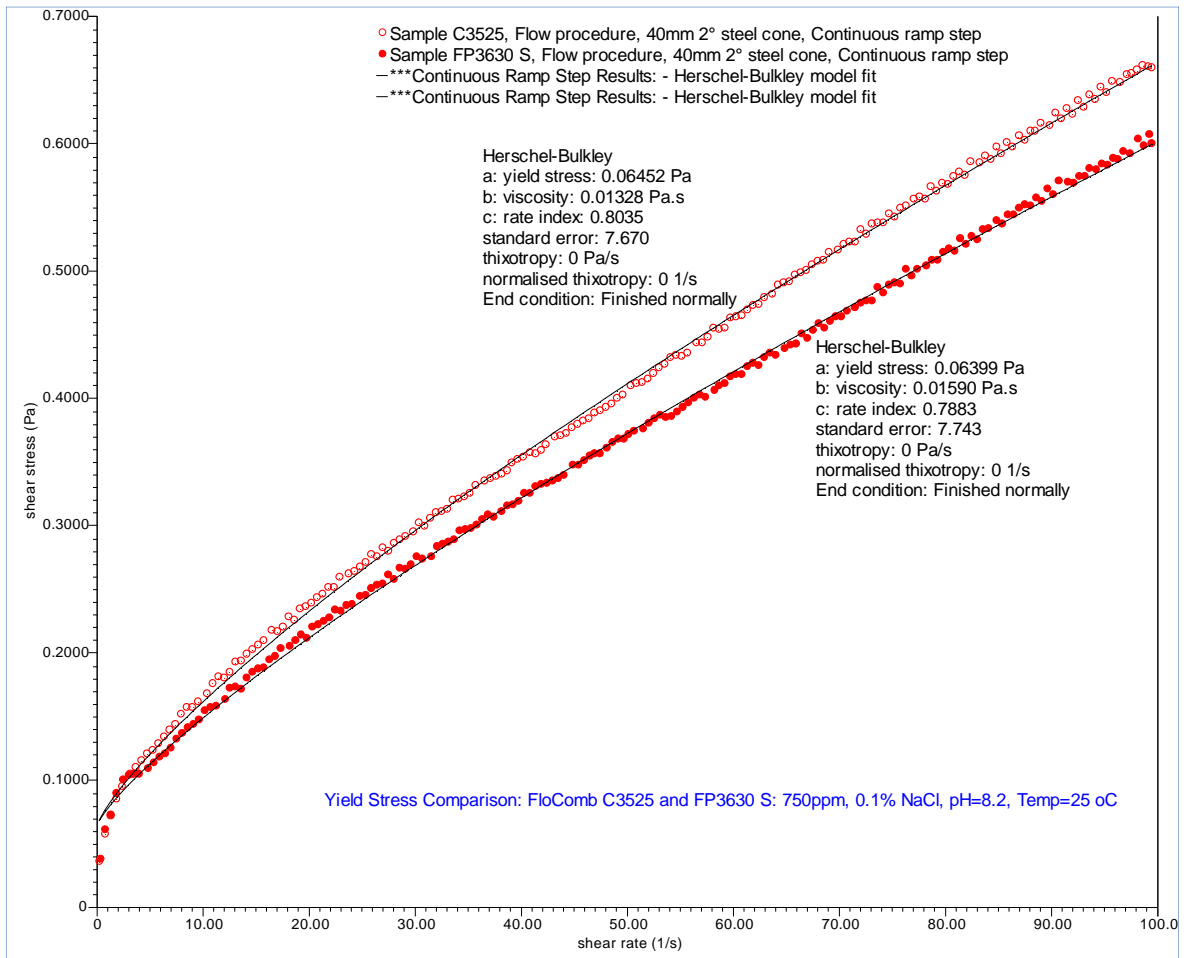


Figure 4.35 - Data fit to Herschel-Bulkley model for samples FP3630 S and FloComb C3525: open cycles (○) is experimental data for FloComb C3525, closed cycles (●) is experimental data for sample FP3630 S; and dash (—) is Herschel-Bulkley model fit to experimental data for both samples. The figure shows similarity in yield stress for both samples

4.17 Modelling rheological behaviour of polymer solutions under shear and concentration

Polymer solutions are non-Newtonian fluids that conform to the power-law given by Eqn. (4.6) in chapter four. Greater loss of polymer viscosity has been attributed to the effect of shear rate.

Factors such as salinity/hardness, shear rate, molecular weight, concentration, temperature, pore structure, etc are known to affect polymer viscosity performance. For example, previous studies have shown that HPAM degradation is by physical breakdown resulting from shear (Jennings et al., 1970; Thomas et al., 2012, 2013). Interestingly though, the results published by Seright et al. (2011) appears to suggest that shear has little effect on HPAM flow in actual reservoirs. Similarly, Ward and Martin (1981) showed that salinity/hardness adversely affects viscosity of HPAM solution. However, it appears models available for polymer risk assessments are being utilised for all scenarios with questionable results; with most of the models focussing on residual resistance factors (RRF) in modelling rheological behaviour of polymers in porous media. The oil and gas industry therefore still faces the challenge of the inability to correctly predict HPAM viscosity under shear degradation; and consequently have not been able to meet the needs of OGI production predictions.

In this section, viscosity measurements of two HPAM polymer products (SNF FP3630 S and FloComb C3525), each of different concentrations were conducted in the laboratory as discussed in the previous sections of this chapter. The rheological data obtained by the method and procedure described earlier were characterised using the power-law (Ostwald-de Waele) function given by Eqn. (1) (Bird et al., 1987, 1960). Viscosity and shear rate relationship for the two polymers are shown in [Figure 4.36](#) and [Figure 4.37](#) respectively. To ensure data validation, each measurement was conducted three times. Any data distortion arising from the effect of instrument start up was rejected.

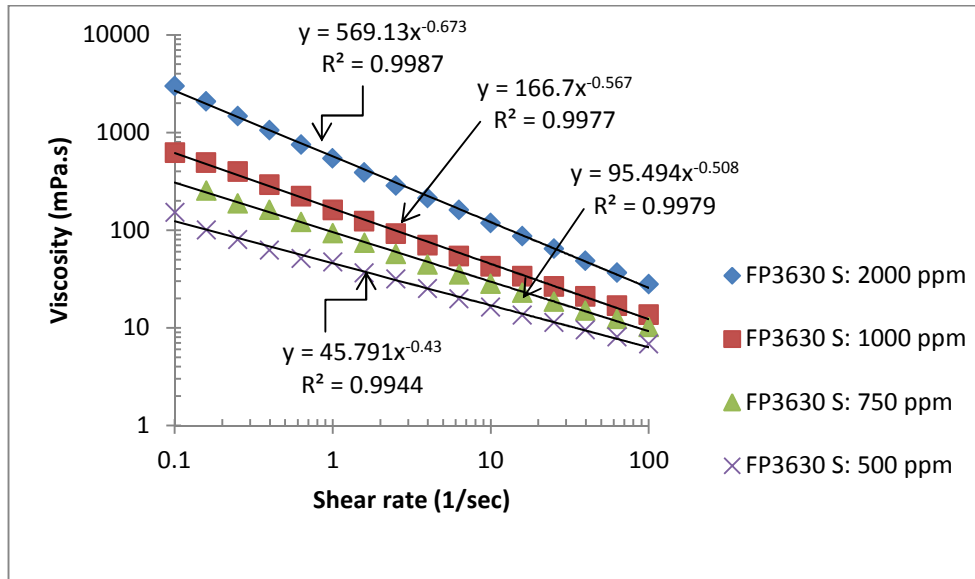


Figure 4.36 - Data fit to Power-law of the rheological property of FP3630 S under different polymer concentrations. The polymer solutions were prepared in 0.1% NaCl brine, adjusted to pH of 8.2 and tested at 25 °C.

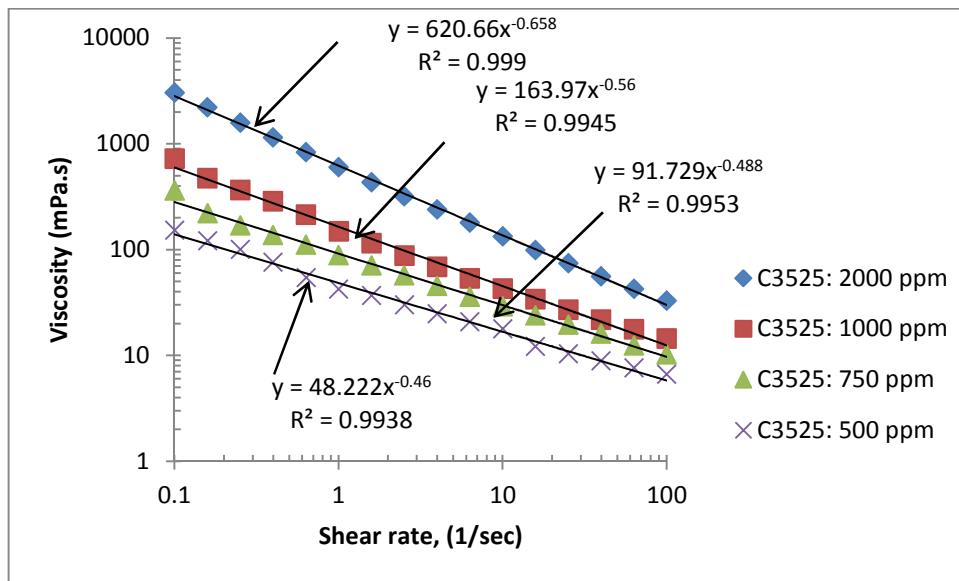


Figure 4.37 - Data fit to Power-law of the rheological property of C3525 under different polymer concentrations. The polymer solutions were prepared in 0.1% NaCl brine, adjusted to pH of 8.2 and tested at 25 °C.

The experimental data and their power-law matching parameters for two polymer types are shown in Table 4.3. From the table, it is shown that polymer concentration affect the consistency index (K), i.e., as polymer concentration increases, K increases. In contrast, the flow behaviour index (n) reduces as polymer concentration (C_p) increases.

Table 4.3 - Power-law curve fitting parameters for FP3630 S and FloComb C3525.

Polymer type	Concentration (mg/L)	Power-law parameters		
		K (mPa.s ⁿ⁻¹)	n	Variance
FP3630 S	500	45.79	-0.430	0.999
	750	95.50	-0.508	0.998
	1000	166.70	-0.567	0.998
	2000	569.13	-0.673	0.994
FloComb C3525	500	48.222	-0.460	0.999
	750	91.729	-0.488	0.995
	1000	163.97	-0.560	0.995
	2000	620.66	-0.658	0.994

A generalised relationship between consistency coefficient (K) and polymer concentration (C_p) can be expressed as Eqn. (4.14 or 4.15); while the relationship between flow behaviour index (n) and polymer concentration (C_p) is written as Eqn. (4.16):

$$\ln(K) = a + b \ln(C_p) \quad (4.14)$$

$$\text{Or } K = C_p^b e^a \quad (4.15)$$

$$n = c + d \ln(C_p) \quad (4.16)$$

where, a , b , c , and d are parameters measured in the laboratory. By use of Eqns. 4.14 to 4.16, HPAM viscosity at 25 °C can be predicted under shear if the concentration of the polymer is known. Figure 4.38 plots and shows the relationship between and; while Figure 4.39 shows the relationship between and. Figure 4.38 and Figure 4.39 clearly show that the two HPAM products have the similar properties. Equations 4.14 to 4.16 can serve as useful tools for the prediction of HPAM rheological

behaviour in field applications. The fitting parameters in Eqns 4.14 to 4.16 are tabulated in Table 4.4.

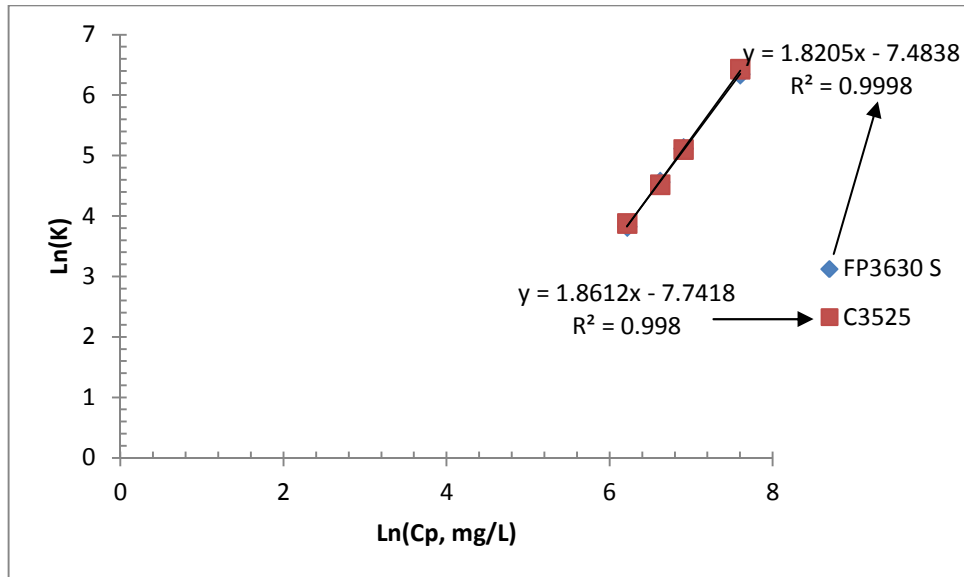


Figure 4.38 - Fitted curve showing relationship between consistency coefficient and polymer concentration for FP3630 S and C3525. The figure shows that both polymers have identical properties.

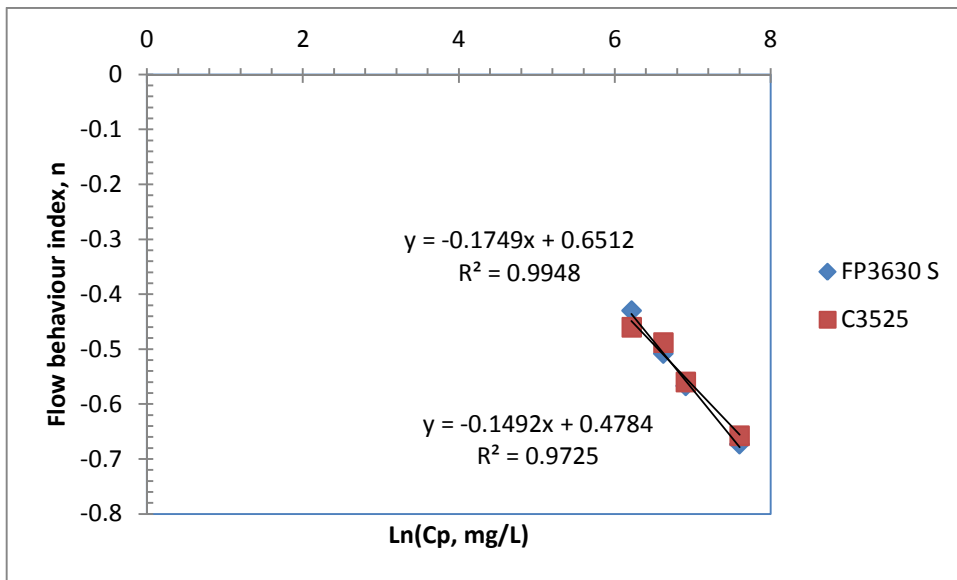


Figure 4.39 - Fitted curve showing relationship between flow behaviour index and polymer concentration for FP3630 S and C3525. The figure shows similarity in flow behaviour for both polymers.

Table 4.4 - Fitting constants for polymer rheological models.

Polymer type	Parameters and values					
	a	b	r ²	c	d	r ²
FP3630 S	-7.4838	1.8205	0.999	0.6512	-0.1749	0.995
FloComb C3525	-7.7418	1.8612	0.998	0.4784	-0.1492	0.973

4.18 Conclusion

In this chapter, rheological behaviour of polymer solutions is discussed and materials and methods for measuring the factors that affect polymer solutions in the field are presented. Method for synthetic brine formulation is described. Standard methods for determination of activity (A_{pr}) of polymer product as well as laboratory procedures for preparation of polymer solutions from dry polyacrylamide products are presented. The following conclusions can be drawn from the above polymer laboratory experimental rheological studies:

- The viscosity of the tested polymer samples depend on the shear rate, pH, salinity/hardness, molecular weight, temperature and concentration.
- The samples undergo thermal degradation between 12 and 72 °C with sample FP3630 S showing more resistance to temperature degradation.
- Sample C3525 was observed to exhibit less viscosity loss in the presence of Ca²⁺ in brine. This result confirms the manufacturer's claim that FloComb C3525 is more calcium tolerant.
- Peak hold results show that FP3630 S has higher steady state viscosity (or greater time-based viscosity stability) compared to FloComb C3525 and FP3330 S.
- Results from the continuous ramp test show that both FloComb C3525 and FP3630 S have similar yield stresses.
- Simple models to predict HPAM viscosity at a wide shear rate range is developed. The models were found to effectively characterise the rheological behaviour of the HPAM polymer solutions. These models can therefore serve as useful tools for HPAM viscosity prediction in field applications.

- One major limitation of viscometric rheological characterization of fluids is the inability of the viscometer to detect viscoelasticity (which is of particular interest in the case of HPAM polymers). This is because in the viscometer the normal stress differences cannot be measured, but only the tangential stress dependence on shear rate can be measured.

The chapter that follows focuses on the simulation of shear-thinning fluid rheology in porous media.

5

Chapter 5 – Simulation of Shear-Thinning Fluid Rheology in Porous Media.

5.1 Introduction

Polymers are used for a variety of applications in the oil and gas industry including drilling mud viscosity modification (Navarrete et al., 2000), Filtration Loss Control (Clark, 2010; Navarrete et al., 2000), Enhanced oil Recovery (EOR) (Wang and Dong, 2009), chemical placement (Taylor and Nasr-El-Din, 2002), sand control (Zhang and Huang, 2002), etc. One of the most important criteria for evaluating chemical enhanced oil recovery (EOR) processes that use polymers is the rheological behaviour of the polymers used which in turn account for other physical effects of adsorption and resistance factors during polymer-formation rock interactions. Polymer viscosity loss is an indication of polymer adsorption on rock surfaces. The viscosity loss is a function of shear rate, and shear in turn depends on the reservoir pore structure. However, complete knowledge of behaviour of polymer solution in porous media has not yet been fully gained. The selection of appropriate polymers for drilling or EOR is based on operational efficiency, costs and economics. Chemicals are expensive on a unit basis; therefore, the quantity of polymer

economically sacrificed for incremental reservoir crude oil recovery is of priority concern for a practical EOR project.

Rheology is one most important attribute of polymers. Therefore, accurate computation of polymer rheological behaviour in porous media is considered as an important aspect for accurate well pressure representation, pressure distribution (Aguayo et al., 2008) far away from the wellbore and accurate predictions of injection rates since the economics are quite sensitive to rates of injection. As the viscosity of non-Newtonian polymer solution depends on shear rate, shear rate calculations must be accurate.

Polymers exhibit extremely complex rheological behaviour during flow in porous media (Cheng and Cao, 2013). This behaviour depends on the nature of the pore structure of the porous media and polymer system itself (Zitha, 2001), as well as the interaction between the components in the polymer and the porous media (Cheng and Cao 2013; Yuan et al., 2000); because viscous dispersion is assumed to be localised only in the pore throats while grain size determines the spacing between pore throats (Chauveteau 1982, 2002; Alves et al., 2003). In the field, partially hydrolysed polyacrylamides (HPAM) and xanthan gums are commercially used in EOR processes (Zhang et al., 2012; Wang and Dong, 2009; Afsharpoor et al., 2012). It is, however, believed that both polymers give unsatisfying performances (Zhang et al., 2012). For instance, effective polymers for high salinity environments are an issue. In furtherance to performance issues, it is desirable for a polymer solution to have a low pressure drop at injection wells to achieve higher injectivity and greater viscosity at low rates in the reservoirs to enhance sweep efficiency. However, the displacement efficiency of polymer solution is affected by shear-thinning behaviour, particularly on a pore scale. Xanthan gum exhibits shear-thinning or viscous behaviour while HPAM exhibits both viscous and elastic characteristics (Al-Sofi et al., 2009; Alsofi and Blunt, 2010). Therefore, a large amount of research efforts has been devoted to gaining a better understanding of polymer

flow behaviour in porous media in the past recent years. In spite of these efforts, several issues have been only partially resolved (Zitha, 2001). For instance, effective polymers for high salinity environments are an issue. Furthermore, the lack of adequate and reliable relationships between adsorbed amount of polymer and average polymer layer thickness in non-gelification situations is also an issue.

Several authors have focused their research on investigating (single-phase) viscoelastic fluids experimentally and numerically in both porous media and constrictions representative of pores (Zhang et al., 2012; Aguayo et al., 2008; Binding et al., 2006; Fan et al., 1999; Bird, 1960; Cheng and Cao, 2010). It has also been argued that apparent viscosity of polymers decreases with pore size. In this study, a computational fluid dynamics (CFD) simulations implemented in COMSOL multiphysics interface is used to simulate a 1-D single-phase, non-elastic xanthan gum flow in geometries approximating pore throats. To ensure dependable results, the COMSOL software was calibrated by repeating simulations of known results and comparing the output results with the known results. Furthermore, COMSOL was deemed fit because it has been successfully used for similar simulation works (Craven et al., 2006). The goal of this work is not only predictive in nature, but also to obtain a better fundamental understanding of the physics of viscous fluid dynamics at the pore-constriction level.

5.1.1 Objective

A simulation study to predict single-phase flow of shear-thinning fluids (xanthan gum) in complex porous media was carried out. This was to enable us fully visualize and understand the fundamental interaction mechanisms of polymer-formation rock and to account for other physical effects of adsorption and resistance factors (i.e. permeability reduction), etc. The objective is to study and physically visualize the effect on viscosity of different inlet pressures in complex converging-diverging pore geometries which is different from straight capillary tubes. Furthermore, polymer mechanical entrapment is related to the ability of the polymer to

pass through a constriction in porous media and is subject to the size of the polymer relative to the constriction (Zitha et al., 1995). The findings from the simulation can be beneficial for the better understanding of the microscopic/macroscopic displacements during polymer core flooding.

5.2 Mathematical and Numerical Framework

5.2.1 Model Definition

Xanthan molecules can be approximated as "rigid rod"; therefore, its dilatant effect during flow in porous medium is negligible (Al-Sofi et al., 2009). For this reason, it is more suitable for simulation studies since it can be assumed that xanthan solution exhibits only viscous or shear-dependent viscosity. In the model, a COMSOL iterative approach was used to solve the pressure field because the pressure depends on the aqueous phase viscosity which for non-Newtonian fluids is a function of shear rates and the pressure itself. The momentum and continuity equations are those that govern the velocity and pressure of an incompressible fluid (Craven et al., 2006). For complex pore throat geometries (such as the type considered in this section), these equations are impossible to solve analytically, and hence numerical method such as the finite element method (FEM) must be implemented. For non-Newtonian flow therefore, the equations to solve are the momentum and continuity equations:

$$\rho \frac{\partial \mathbf{u}}{\partial t} - \nabla \cdot \mu (\nabla \mathbf{u} + (\nabla \mathbf{u})^T) + \rho \mathbf{u} \cdot \nabla \mathbf{u} + \nabla p = 0 \quad (5.1)$$

$$\nabla \cdot \mathbf{u} = 0 \quad (5.2)$$

where, μ = viscosity (kg/(m.s)), ρ = fluid density (kg/m³), $(\nabla \mathbf{u})^T$ = shear effects which describe viscous forces and the extra stress contribution from the polymer, p = pressure (Pa), u = velocity (m/s), ∇ = del operator.

To account for polymers' viscous or thinning behaviour, we chose to use the Carreau model (Eqn. 5.3) (Carreau, 1972) for the problem because it covers and combines the power-law region and the two Newtonian regions of the viscosity curve.

$$\mu_{sh} = \mu_{\infty} + (\mu_p^0 - \mu_{\infty}) [1 + (\lambda \dot{\gamma}_{eff})^2]^{(n-1)/2} \quad (5.3)$$

where, μ_{sh} = apparent shear viscosity in porous media, μ_p^0 = polymer viscosity at zero shear rate (i.e., the plateau viscosity), $\mu_{\infty} = \mu_w$ = viscosity at infinite shear rate, λ = time constant (i.e. relaxation time for realignment of polymer rods in a shear flow field) is found from bulk viscosity measurements, $\dot{\gamma}_{eff}$ = rate of deformation (also called effective shear rate in a shear flow), n = dimensionless constant known as the shear-thinning index that depends on the polymer concentration. $0.4 \leq n \leq 1$ for pseudoplastic or shear-thinning fluids.

For an axisymmetry model (discussed in the following section), the shear rate in Carreau equation is written in cylindrical coordinates as (Eqn. 5.4):

$$\dot{\gamma} = \sqrt{\frac{1}{2} \left((2u_r)^2 + 2(u_z + v_r)^2 + (2v_z)^2 + 4\left(\frac{u}{r}\right)^2 \right)} \quad (5.4)$$

Where u, v are velocity vectors, and in particular,

$$\check{p}(r, 0, z) = p(r, z) \quad (5.5)$$

$$\check{u}(r, 0, z) = u(r, z) \quad (5.6)$$

$$\text{and } u = (u_r, u_z) \quad (5.7)$$

5.2.2 Model Geometrical Domain

The model geometry is shown in [Figure 5.1](#). The figure shows the modelling interest in the region of contraction (throat) and expansion with different cross-sectional areas. However, the effects at the inlet and outlet regions with different cross-sectional areas are also evaluated. To reduce the computational efforts without affecting the model dimension, the domain, the initial and the boundary conditions and other body forces were approximated as symmetric with respect to a straight line ([Figure 5.1](#)).

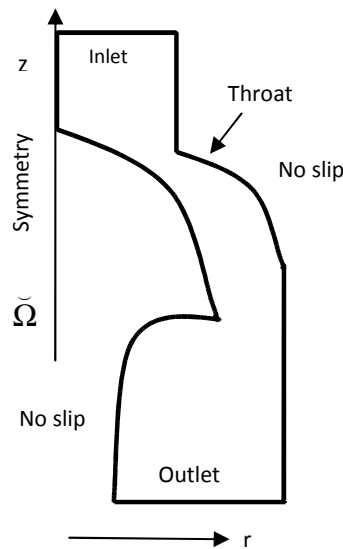


[Figure 5.1](#) - Pore throat geometry model used for the simulation. The throat diameter is 3 mm, the inlet is 5 mm, and the outlet is 7 mm.

In this case, the flow can be modelled by the 3-D axisymmetric Stokes or Navier-Stokes equations which take advantage of the hypothesis of symmetry (Bernardi et al., 1999). The axisymmetric model, in particular, is also easily coupled with an axisymmetric 1-D model (Lagana et al., 2002). Therefore, we use the axisymmetric 2-D model to reproduce a 3-D effect in the region of interest where there is pore contraction-and-expansion as shown in the geometry ([Figure 5.1](#)). This reduces the size of the problem without losing the 3-D features and without any assumption on the velocity profile.

5.2.3 Constriction (Pore Throat) Geometry used for the Simulation

Figure 5.2 shows the dimensions of the pore constriction used in the simulation. Though the geometry is hypothetical, it however provides the insight needed for understanding the fundamental physics underlying fluid behaviour at the diverging-converging flows mimicking natural reservoir porous systems. The geometry has varying cross-section perpendicular to flow direction. The number of elements and mesh configurations differ for the different cases as discussed under results and discussions section.

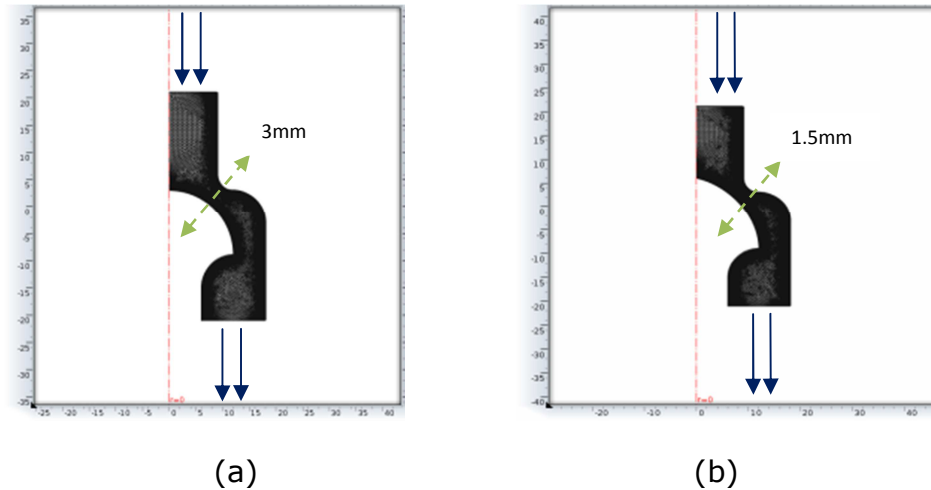


Figure 5.2 - Model simulation geometries and mesh arrangements: (a) 3 mm pore throat (b) 1.5 mm pore throat.

5.3 Boundary Condition Settings

5.3.1 Pressure outlet

Equations 5.5 through to 5.7 imply that for an axisymmetric flow, the pressure (P) and the cylindrical velocity components, u_r , u_θ , u_z are independent of the angular variable θ with unknown (\mathbf{u}, p) , $\mathbf{u} = (u_r, u_z)$; where z and r are symmetry directions. We use the Dirichlet boundary condition (BC) form for the momentum and extra stress application modes; while the Neumann BC form was used for the pressure outlet condition (Craven et al., 2006) since application of the Neumann form to the momentum application mode enforces the pressure out boundary

condition equal zero (Eqn. 5.8). Therefore, inlet and outlet boundary conditions are given and set to fixed pressures (Eqn. 5.8) and vanishing viscous stresses as in fully developed flow (Eqn. 5.9). To study the effect on viscosity at different inlet pressures, the model makes use of the parametric solver to vary P_{in} from 10kPa to 210 kPa.

$$\left. \begin{array}{l} p = p_{in} \\ p = 0 \end{array} \right\} \quad (5.8)$$

and

$$\mathbf{n} \cdot [\eta(\nabla \mathbf{u} + (\nabla \mathbf{u})^T)] = 0 \quad (5.9)$$

Where, \mathbf{n} is the boundary unit normal vector.

5.3.2 Slip or Axial Symmetry Boundary Condition

Due to the axisymmetric nature of the geometry, a symmetry BC at $r=0$ is used since one half of the domain is modelled (Figure 5.1). The rotational axial symmetry condition (as expressed by Eqn. 5.10) is described as zero flow normal to the boundary.

$$\mathbf{u} \cdot \mathbf{n} = 0 \quad (5.10)$$

5.3.3 Wall Boundary Condition

The wall effect (i.e. fluid velocity is zero at a wall) imposes the no-slip boundary condition at the wall which justifies setting the normal component of the boundary stress contribution from the polymer equal to zero (Eqn. 5.11):

$$\mathbf{u} = 0 \quad (5.11)$$

5.4 Numerical Solution of Axisymmetric flow

Let Ω be the 2-D half section of the axisymmetric 3-D domain $\check{\Omega}$ under consideration as shown in [Figure 5.1](#), and V (fluid space) and Q (fluid flux) are weighted Sobolev spaces (recall that: a Sobolev space is a space of functions with sufficiently many derivatives for some application domain, such as partial differential equation and equipped with a norm that measures both the size and regularity of a function) (Bernardi et al., 1999). Assuming the data are axisymmetric with zero angular components, then the axisymmetric Stokes problem is (Bernardi et al., 1999):

(\mathbf{u}, p) , $\mathbf{u} = (u_r, u_z)$, in $V \times Q$ such that

$$\begin{cases} v \int_{\Omega} (\nabla u : \nabla v) r dx + v \int_{\Omega} u_r v_r \frac{1}{r} dx \\ - \int_{\Omega} (\text{div} v) p r dx - \int_{\Omega} v_r p dx = \int_{\Omega} f \cdot v r dx \\ - \int_{\Omega} (\text{div} u) q r dx = \int_{\Omega} u_r q dx = 0 \end{cases} \quad (5.12)$$

for all (v, q) in $V \times Q$.

To recover the 3-D solution (\check{u}, \check{p}) from (u, p) , the 3-D domain $\check{\Omega}$ is described in cylindrical coordinates (r, θ, z) as in Eqn. (5.13):

$$\check{u}(r, \theta, z) = \begin{pmatrix} \check{u}_x \\ \check{u}_y \\ \check{u}_z \end{pmatrix} = \begin{pmatrix} u_r(r, z) \cos \theta \\ u_r(r, z) \sin \theta \\ u_z(r, z) \end{pmatrix} \quad (5.13)$$

And

$$\check{p}(r, \theta, z) = p(r, z). \quad (5.14)$$

The model simulation input parameter for 2000 ppm Xanthan gum is shown in [Table 5.1](#) (Escudier et al., 2001).

Table 5.1 - Simulation input values (Escudier et al. 2001)

Parameter	μ_{∞} (Pa.s)	μ_p^0 (Pa.s)	n	λ (s)	P (kg/m ³)	P_{in} (kPa)
Value	0.0015	15.6	0.38	0.01	500	range (10, 40, 210)

5.5 Results and Discussion

5.5.1 Comparative Analysis of the Effects of Different Constrictions and Inlet Pressures on Viscosity.

Figure 5.2 shows the mesh arrangements of the pore constrictions on which the simulations were performed. Due to the challenging nature of fluid behaviour in such constrictions, the required mesh is extra fine. Mesh sensitivity analysis was carried out to establish mesh arrangements and/or refinements. This was done to ensure that the solution was not affected by further mesh refinements. Figure 5.2a (3 mm pore throat) has 20827 elements and mesh area of 395.4 mm² with an average quality of 90.41%. While Fig. 5.2b (1.5 mm throat) has 20923 elements and mesh area of 377.4 mm² with an average quality of 90.45%. It was therefore believed that no further refinement was required for a better solution to the problem.

Figure 5.3 compares the velocity field of the non-Newtonian xanthan fluid for the different pore throats (3 mm and 1.5 mm). Due to the outlet greater cross-section, there is a higher velocity distribution at the inlet compared to the outlet. Interestingly, the figure also shows that the greatest velocity gradient and shear rates occur at the centre of the constriction compared to the near wall due to the no-slip boundary conditions imposed. This higher velocity distribution at the centre is however more pronounced in 1.5 mm constriction geometry (Fig. 5.3b) compared to the 3mm constriction geometry (Fig. 5.3a) due to its reduced constriction.

Notably, Figure 5.4 shows that the contours of the model domain are smooth in the vicinity of the constriction. The figure shows the magnitude or rate of change of the pressure parameters. Therefore, the smoother

the contours in the 1.5 mm constriction geometry (Fig. 5.4b), the faster the change in the pressure difference parameter across the constriction compared to the 3 mm constriction geometry (Fig. 5.4a). Hence, in Figure 5.5 the higher pressure drop at the constriction induces a greater velocity at that point which in turn causes severe solution viscosity degradation in the 1.5 mm constriction geometry (Fig. 5.5b) compared to the 3 mm constriction geometry (Fig. 5.5a). The plausible explanation for this is that, at a wall, fluid velocity is zero; hence polymers are unable to exert a force on the wall as no polymer can span the wall boundary. Figure 5.5b therefore suggests premature shear-thinning behaviour induced by shear pre-deformation resulting from the reduced (1.5 mm) constriction.

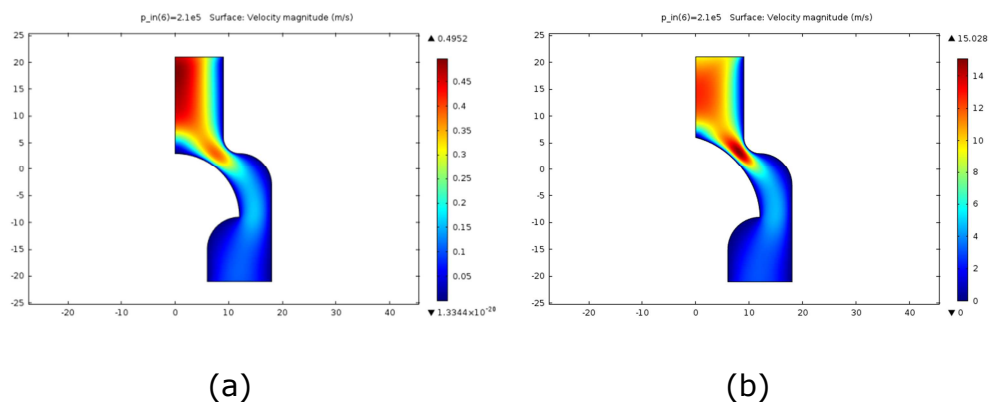


Figure 5.3 - Model domain velocity field: (a) 3 mm constriction, (b) 1.5 mm constriction.

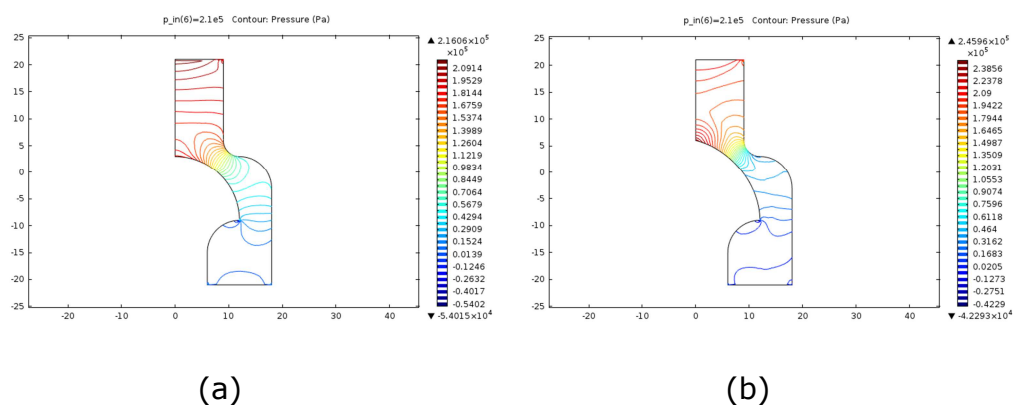


Figure 5.4 - Pressure distribution contour: (a) 3 mm constriction, (b) 1.5 mm constriction.

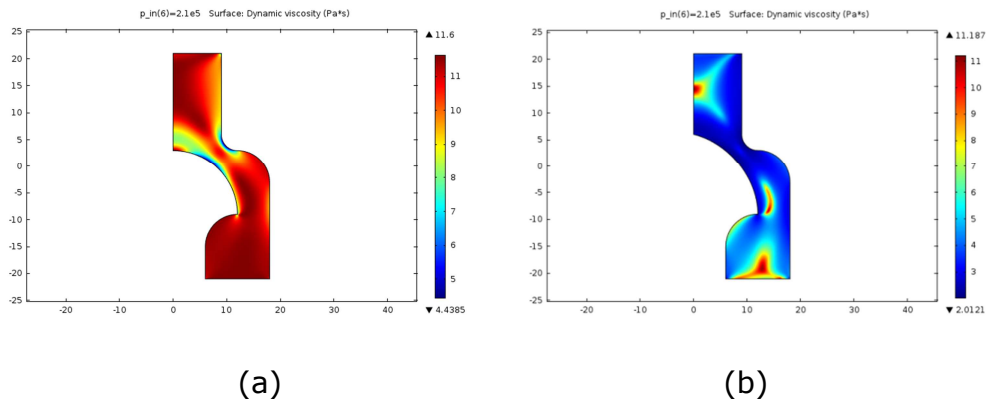


Figure 5.5 - Model domain viscosity profile: (a) 3 mm constriction, (b) 1.5 mm constriction.

As the xanthan fluid is shear-thinning, its viscosity is a function of shear rates (Figure 5.6). Compared to the 3 mm constriction geometry (Fig. 5.6a) for the same inlet pressure of 10 KPa, the reduced throat depicting the 1.5 mm constriction geometry (Fig. 5.6b) causes a resultant increase in shear rates which consequently decreases the xanthan fluid viscosity from about 11.5 Pa.s to about 6.33 Pa.s.

Figure 5.7 shows the effects of increasing inlet pressures (and pressure gradients) on viscosity across the throat. The figure shows that the greater the inlet pressure, the more the velocity gradient and shear rates; and the more the viscosity is degraded across the constriction. The viscosity degradation is more evident in the 1.5 mm constriction geometry (Fig. 5.7b) compared to the 3 mm constriction geometry (Fig. 5.7a).

Figure 5.8 further emphasizes the effects of shear rates on viscosity for all pressures. The 3mm constriction geometry (Figure 5.8a) shows that the onset of shear-thinning is at about 10 s^{-1} ; while the 1.5 mm constriction geometry (Fig. 5.8b) suggests premature and excessive shear-thinning behaviour induced by shear pre-deformation resulting from the reduced (1.5 mm) pore constriction.

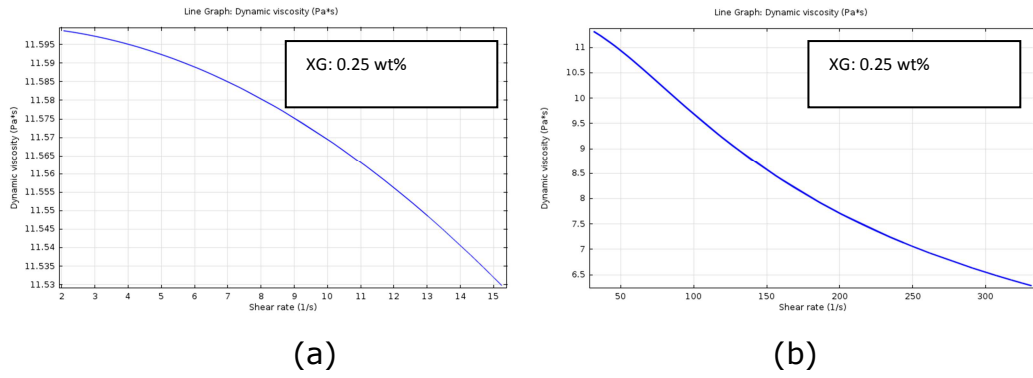


Figure 5.6 - Effects of varying shear rates on viscosity: (a) 3 mm constriction, (b) 1.5 mm constriction.

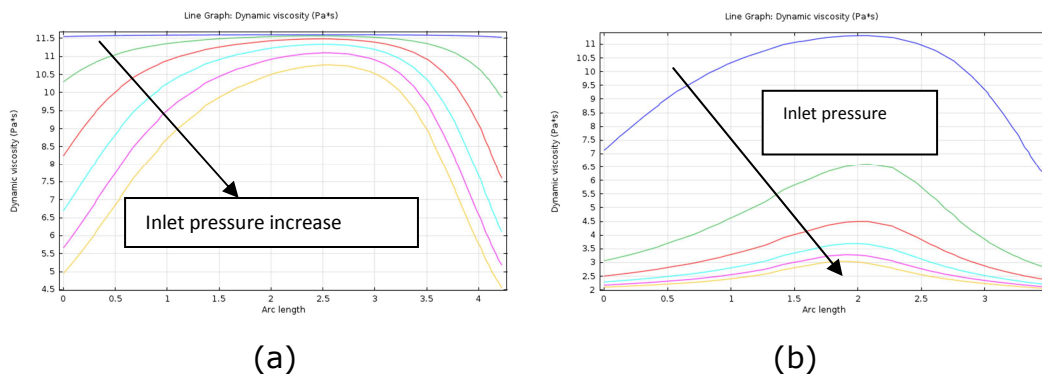


Figure 5.7 - Pressure gradient effects on viscosity: (a) 3 mm constriction, (b) 1.5 mm constriction.

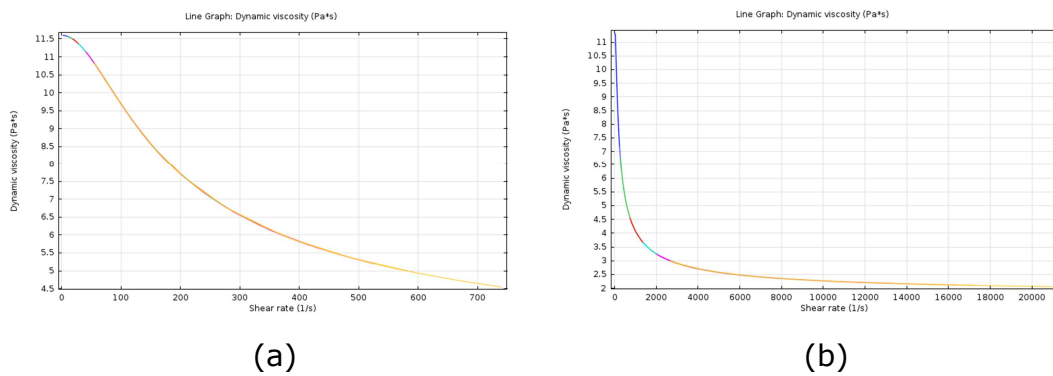


Figure 5.8 - Effects on viscosity of different shear rates for all inlet pressures: (a) 3 mm constriction, (b) 1.5 mm constriction. For Figure (a), onset of shear-thinning is at about 10 s^{-1} . Figure (b) suggests premature shear-thinning xanthan fluid behaviour induced by shear pre-deformation resulting from reduced constriction.

5.6 Conclusion

Numerical simulations were performed using COMSOL Multiphysics 4.3a software to solve a coupled momentum and continuity equations for the purpose of studying the dynamic rheological behaviour of non-elastic xanthan gum polymer solution in porous media contraction-and-expansion geometries approximating pore throats. Results showed that

the Carreau equation sufficiently described the viscosity behaviour of the solution at the pore constriction. As the pore throat decreases, the solution viscosity drastically reduces. Also, the greater the inlet pressure, the more the velocity gradient and shear rates; and the more the viscosity is degraded across the constriction. Furthermore, CFD simulations showed that shear-thinning behaviour can affect the solution displacement efficiency. Finally, this study offers the possibility for reliable prediction of the rheological behaviour of non-elastic, non-Newtonian fluid such as xanthan gum (by extension other polymers) in porous media, and the design and interpretation of laboratory tests including the predictions of the performances of polymer solution applications in actual field operations. The results also illustrate the successful application of COMSOL for predicting the role of shear rate dependent viscosity in relation to reservoir geometry in efficiency of polymer flooding. Therefore, effective control of this parameter can reduce the effect of formation damage induced by polymer adsorption and help minimize mass of chemical loss and thus, improve economic efficiency of the chemical flooding process.

Discussion on the equipment, materials, preparation and methods used in the polymer core flooding is presented in the chapter that follows.

6

Chapter 6 – Polymer Core Flooding: Equipment, Material Preparation, and Methods

6.1 Introduction

Quantitative evaluation of the formation damage likely to be caused by polymer solution injection over the life time of a polymer project is desirable. In this regard, evaluating the performance of a polymer flood in a given field requires an understanding not only of the rheological behaviour of solution under reservoir conditions (i.e. the mobility and permeability reductions of the aqueous phase), but also of their interactions with the reservoir rock (i.e. mainly retention and including other changes in the solution during contact with the porous media). Yet the rheological behaviour depends to a great extent on the phenomenon of overall retention, whether due to adsorption or to flow dynamics. Retention refers to all mechanisms that remove polymer from the transported aqueous phase. These are: adsorption, mechanical entrapment and hydrodynamic (or rate) retentions. Adsorption, in particular, is related to the surface properties of the porous media. Therefore, an accurate reproduction of field conditions will be required in the laboratory to obtain meaningful information on polymer behaviour in

porous media. In order to both qualify and quantify the explicit polymer adsorption contribution to polymer retention and formation damage, the basic information that reflects the mechanism of the polymer adsorption process (such as rock type, polymer type, molecular weight, salinity, concentration, pH, porous medium structure, chemistry of the aqueous phase, porous medium surface area, porosity and permeability of the porous medium, pore-size distribution, grain-size distribution, amongst others) needs to be obtained experimentally. To achieve this objective, a carefully and professionally designed constitutive experimental setup using representative reservoir formation fluids and core samples in a laboratory is required to obtain equally representative data for model (process) validation. In this PhD study, three approaches were adopted in quantifying formation damage: 1) initial rheological characterization and selection of samples for core flooding (already presented in chapter four), 2) clashach core flooding and 3) sandpack flooding. In the sandpack and clashach core flood tests, a known signal (flow and rate) was applied to an unknown system (the rock) and the response of that system (change in permeability) was measured and analysed during the test.

6.2 Equipment, Materials and Methods

The equipment, materials, methods and procedures used for the polymer core flooding experiments are presented in the following sections.

6.2.1 Synthetic Brine Formulation

Synthetically formulated brines (SFB) were made to mimic reservoir waters. Sodium chloride (NaCl), anhydrous calcium chloride (CaCl₂), potassium chloride (KCl), sodium hydrogen carbonate (NaHCO₃) and magnesium chloride hexahydrate (MgCl₂.6H₂O) were the analytical reagents used. Prior to their use in all flow experiments, the brine solutions were filtered with 0.22 µm filter paper. This was done to ensure that no particles interfered with the reliable operation of the pump piston seals and check valves; as well as cause undue pore blockage during core tests. 2.0 g/L commercial formaldehyde was added to the brine as

oxygen scavenger, biocide or bactericide and stabilizer against free radical depolymerisation. The ionic composition of the brines used for the polymer core flood tests is shown in [Table 6.1](#).

Table 6.1 - Ionic composition of the brines used for the core flood tests: (a) Low salinity Brine composition (TDS1), (b) Hard, high-salinity Brine composition (TDS2).

(a)		(b)	
Ion	Parts per million, ppm (mg/litre)	Ion	Parts per million, ppm (mg/litre)
Na ⁺	10392	Na ⁺	43300
Ca ⁺⁺	426	Ca ⁺⁺	6860
K ⁺	208	K ⁺	875
Mg ⁺⁺	630	Mg ⁺⁺	1110
Cl ⁻	18831	Cl ⁻	83054
TDS	30,487	TDS	135,199

6.2.2 Polymers used for core flooding

Two grades (see [Table 4.1](#) in chapter four) of commercial partially Hydrolysed Polyacrylamide (HPAM) were used for the core flood experiments. The HPAM were manufactured and supplied in powder form by SNF Floerger, ZAC de Milieux, 42163 Andrezieux, France.

6.2.3 Polymer Solutions Preparation for core flooding

Polymer solutions for the core flooding were prepared in concentration range 50 to 2000ppm respectively. In order to ensure optimum solution properties, the polymers were mixed in strict compliance with the recommended procedures provided by the manufacturers and in accordance with API RP 63 (1990) guidance. The detailed procedures were earlier presented in section 4 of chapter four of this thesis. For the core flooding tests, all polymer solutions were prepared as “*smart*” solutions as they were spiked with 0.004M (0.034%) sodium bicarbonate to counteract undesired pH changes in adsorption experiments. As previously stated, the bicarbonate buffered against an acidic reaction

when silica contacted water and against an alkaline reaction with calcium carbonate. The brine to which 2.0 g/L commercial formaldehyde (to act as oxygen scavenger, biocide or bactericide and stabilizer against free radical depolymerisation) was added in deionised water was the same as that used for preparing the polymer solutions. To ensure flow rate consistency, the brine and polymer solutions were doubly evacuated using both ultrasonic and helium degassing. Specifically, after sonicating, the solvents were then sparged with 99.99⁺ % standard laboratory grade helium. Helium presents the best practical technique for degassing because it is only sparingly soluble in HPLC solvents, so other gases dissolved in the solvent diffuse into the helium bubbles and are swept away from the system. The solutions were continually blanketed with the helium during use to keep atmospheric gases from dissolving back into the mobile phase.

6.3 Porous Media Description, Preparation and Characterization

6.3.1 Clashach Cores

Commercial clashach sandstones of diameter 4.0 cm and length 2.0 cm (small cylindrical cores) were used as the porous medium. Small cylindrical cores were chosen so as to simulate conditions of the near-wellbore by injecting a large number of pore volumes. Clashachs have been reported (Annie et al., 1999) to have wide and good permeability distributions (50<-2000 mD) that are representative of actual reservoir formation. The initial core condition was characterised by using Mercury Injection Capillary Pressure (MICP) for the core sample with similar grain-size/pore-throat size and permeability distributions (details of the high pressure MICP experiment is presented in appendix A). X-ray diffraction (XRD), scanning electron microscopy (SEM) and energy dispersive X-ray analysis (EDXA) were used for rock samples similar mineral composition/lithology imaging and distributions respectively (experimental detail of the XRD analysis is given in appendix B).

6.3.1.1 Petrophysical Properties Determination for Clashach Cores

The clashach pore volume, porosity and grain density were determined by the Helium porosimeter method. Bulk volumes were measured by mercury displacement using Archimedes principle. The samples were then placed in a mercury oven. Gas permeability was measured using a calibrated steady state permeameter with air as the flowing medium. The flow was allowed to stabilise before the readings were taken. Table 6.2 and Table 6.3 summarize the samples characteristics. A porosity and grain density procedure is presented in appendix C.

6.3.1.2 Calculation of Mercury Injection Data

(a) Sample weight, combined sample and penetrometer weight with and without mercury were used to calculate grain density and bulk density respectively. The following relations are used:

$$V_g = \frac{W_s}{W_\rho} \quad (6.1)$$

$$V_b = V_p + V_g \quad (6.2)$$

$$V_p = V_b - V_g \quad (6.3)$$

$$\phi = \frac{V_p}{V_b} \times 100 \quad (6.4)$$

Where, V_g = grain volume (cc), W_s = sample weight (g), W_ρ = grain density (g/cc), V_b = injected bulk volume (cc), V_p = injected pore volume (cc), ϕ = porosity (%). The injected pore volume is the cumulative of the injected mercury volume.

(b) Volumes of mercury injected at each injection pressure were recorded.

- (c) Initial apparent intrusion at low pressures may be the result of mercury conforming to the surface irregularities of the core sample. These irregularities are not representative of the pore structure. The threshold pressure, where mercury injection into the pore structure begins, is identified at the pressure where the rate of mercury injection increases rapidly. Cumulative apparent injection up to this threshold pressure is subtracted as surface porosity from measured data before subsequent calculations are made.
- (d) Cumulative volumes of mercury injected are expressed as a fraction of the total pore volume of the sample.
- (e) At any mercury displacement pressure the minimum radius of pore throat which can be penetrated by mercury is given by Eqn. (6.5) (Leverett, 1941):

$$r = \frac{2\sigma \cdot \cos\theta \cdot C}{P_c} \quad (6.5)$$

Where,

r = pore throat radius, μm

σ = interfacial tension between air and mercury, dynes/cm (485)

θ = contact angle between air and mercury, degrees (140)

P_c = capillary pressure, psia

C = conversion constant (0.145)

Using this relationship, a graph of fraction of pore volume injected (PV) versus pore throat radius can be constructed. The differential of this gives a pore throat size distribution (PSD) function expressed as Eqn. (6.6):

$$PSD = \frac{dv}{d(\log(r))} \quad (6.6)$$

PSD is smoothed using 1-2-1 smoothing in form of Eqn. (6.7):

$$PSD_i = \frac{(PSD_{i-1} + 2PSD_i + PSD_{i+1})}{4} \quad (6.7)$$

The PSD is then normalised to 1 using Eqn. (6.8):

$$PSD_{normalised\ i} = \frac{PSD_i}{PSD_{max.}} \quad (6.8)$$

Normalised PSD is presented in graphical form along with saturation against pore throat radius and permeability distribution function against pore throat radius. The normalised pore throat size distribution function displayed graphically can be used to identify pore throat size groupings and the relative proportions of pore volume controlled by Macro pore throats (>1.5µm), Meso pores throats (1.5 to 0.5 µm) and Micro pore throats (<0.5 µm) respectively.

(f) Oil-brine capillary pressure (reservoir) data is obtained from air-mercury data by the following conversion (Leverett, 1941):

$$P_{C_{o-b}} = P_{C_{a-Hg}} \cdot \frac{\sigma_2 \cdot \cos \theta_2}{\sigma_1 \cdot \cos \theta_1} \quad (6.9)$$

Where,

$P_{C_{o-b}}$ = oil-brine capillary pressure (reservoir), psia

$P_{C_{a-Hg}}$ = air-mercury capillary pressure, psia

σ_2 = interfacial tension between oil and brine (reservoir), dynes/cm (30)

σ_1 = interfacial tension between air and mercury, dynes/cm (485)

θ_2 = contact angle between oil and brine (reservoir), degrees (30)

θ_1 = contact angle between air and mercury, degrees (140)

- (g) The mean hydraulic radius (MHR) tabulated in [Table 6.3](#) below, is the average pore throat size of the sample and is given by Eqn. (6.10):

$$MHR = \frac{\sum_{i=0}^n (r_i^2 \cdot (S_i - S_{i-1}))}{2 \cdot \sum_{i=0}^n (r_i \cdot (S_i - S_{i-1}))} \quad (6.10)$$

where, S = mercury saturation, fraction of pore volume.

- (h) A method for averaging capillary pressure data from various systems is the use of the Leverett J-function (Leverett, 1941). The J-function is a dimensionless capillary pressure function expressed as Eqn. (6.11):

$$J = \frac{0.2166 P_c \cdot \sqrt{\left(\frac{k}{\phi}\right)}}{\sigma \cdot \cos \theta} \quad (6.11)$$

Where,

J = Leverett capillary pressure function, dimensionless

P_c = Capillary pressure, psia

σ = Air-mercury interfacial tension, dynes/cm (485)

θ = Air-mercury contact angle, degrees (140)

k = Permeability, mD

ϕ = Porosity, fraction.

- (i) The theoretical cumulative permeability (k_{ti}) of a sample with a given pore size distribution, (r_0 to r_i), can be expressed as Eqn. (6.12) (Purcell, 1949):

$$k_{ti} = \sum_{i=0}^n r_i^2 \cdot \Delta S_i \quad (6.12)$$

Where S_i = mercury saturation, fraction of pore volume (i.e., the volume of each capillary expressed as percentage).

(j) The k_{ti} in Eqn. 6.12 is then normalized such that the maximum is 1.0. Then a cumulative Permeability Distribution Function (PDF) is given by Eqn. (6.13) (Purcell, 1949):

$$PDF_{normalised\ i} = \frac{k_{ti}}{k_{t\max.}} \quad (6.13)$$

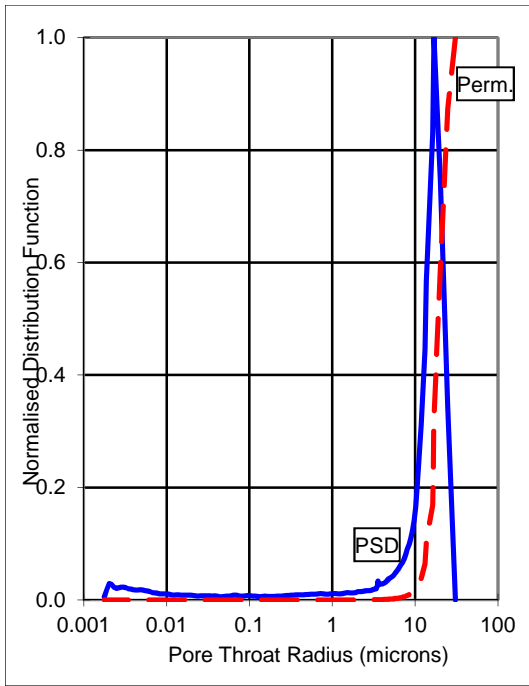
Table 6.2 - Clashach sample core dimensions

Sample	Diameter [cm]	Length [cm]	Cross-sectional area [cm ²]	Mass (g)
2A	3.80	1.80	11.34	44.30
6A	3.90	2.00	11.95	52.88
7A	3.80	2.00	11.34	52.44

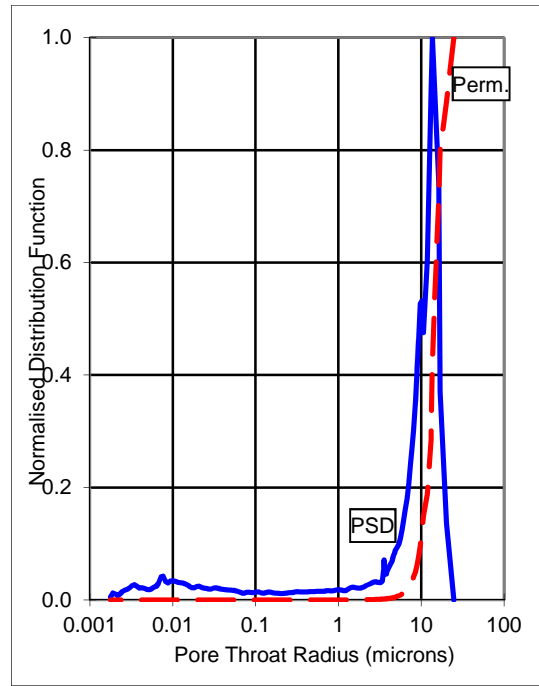
Table 6.3 – Clashach sandstones petrophysical properties

Sample	Porosity (%)	Pore volume (cm ³)	Gas permeability @ 400 Psig (mD)	Grain density (g/cc)	Mean hyd. radius (µm)
2A	17.7	0.748	1094	2.65	9.126
6A	14.6	0.331	287	2.65	7.741
7A	12.2	0.245	74.3	2.65	6.817

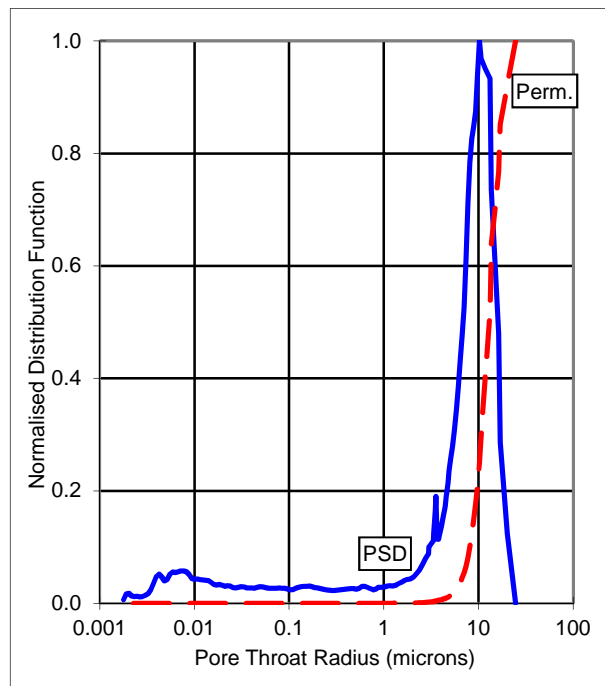
Figure 6.1 shows the normalised pore-throat size distribution (PSD) presented in graphical form along with saturation against pore throat radius and permeability distribution function against pore-throat radius obtained from MICP.



(a)



(b)



(c)

Figure 6.1 - Pore-throat size and permeability distributions (PSD) for the clashach core samples: (a) 2A, (b) 6A and (c) 7A. Continuous blue lines represent the pore throat size distributions (PSD); while the dashed red lines show the permeability distribution functions (Perm.).

Table 6.4 and Figure 6.2 show the X-ray diffraction analysis (XRD) of whole rock for identification of the mineral composition of the clashach cores. Table 6.5 and Figure 6.2 show that the clashach samples are quartzitic (i.e., quartz range between 94 to 96%). Table 6.5 and Figure 6.3 show the clay mineral assemblages present in the cores with respect to the whole rock by reference to the amount of <2 micron clay fractions respectively. Specifically, the samples have insignificant or zero clay content. Clays are known to increase specific area of reservoirs or cores and reduce their permeabilities if present in sufficient amount; and consequently increase the adsorptive capacity of polymers. Generally, because the clashachs used in this research do not contain clays, any observed adsorption or resistance factor may be caused by differences in their pore structures and permeabilities (Figure 6.1). The initial SEM/EDXA grain distributions and imaging of samples is shown in Figure 6.4.

Table 6.4 - Whole rock X-ray diffraction analysis (for identification of mineral composition of the clashach cores). The table shows that the core samples are quartzitic in nature with low contents of Potassium Feldspar and Illite+Mica.

Sample	Quartz	Potassium Feldspar	Illite +Mica	Kaolinite	Plagioclase Feldspar	Dolomite	Pyrite	Illite/ Smectite	Chlorite	Calcite	Siderite	Total
2A	95.6	2.5	1.1	0.0	0.0	0.8	0.0	0.0	0.0	TR	0.0	100.0
6A	94.2	3.6	1.5	0.0	0.0	0.7	0.0	0.0	0.0	TR	0.0	100.0
7A	95.5	2.8	1.1	0.0	0.0	0.6	0.0	0.0	0.0	TR	0.0	100.0

TR=Trace amount

WHOLE ROCK X-RAY DIFFRACTION ANALYSIS

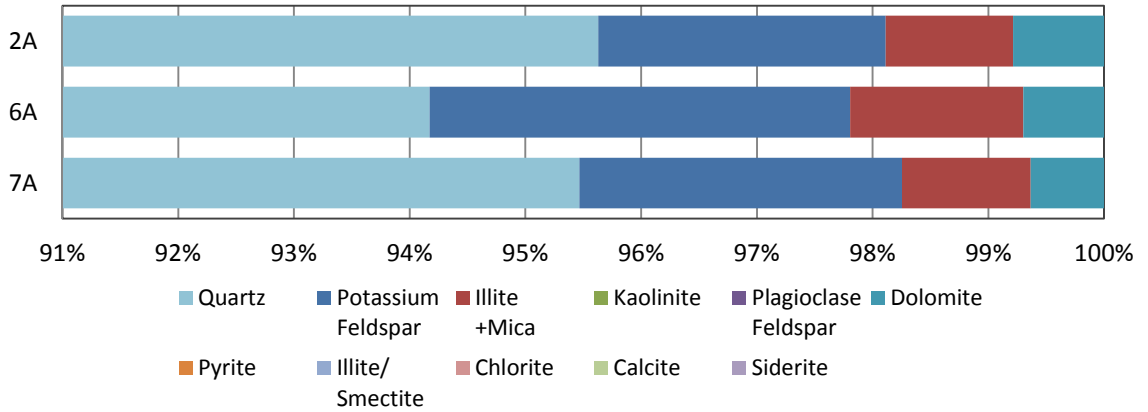


Figure 6.2 - X-ray diffraction analysis: whole rock (for identification of mineral composition of the samples).

Table 6.5 - X-ray diffraction analysis <2 μm clay size fraction

Sample Number	Wt.% < 2μm	ILLITE/SMECTITE			ILLITE			QUARTZ		KAOLINITE			CHLORITE			TOTAL %A	
		%A	%B	Order	%Illite	%A	%B	Crys	%A	%B	%A	%B	Crys	%A	%B		Crys
2A	1.2	0.0	0.0			90.1	1.1	P	9.9	0.1	5E-05	6E-07		0.0	0.0		100.0
6A	1.7	0.0	0.0			87.9	1.5	P	12.1	0.2	4E-05	7E-07		0.0	0.0		100.0
7A	1.2	0.0	0.0			88.1	1.1	P	11.9	0.1	4E-05	5E-07		0.0	0.0		100.0

A=Weight % relevant size fraction, B= Weight % bulk sample, P=poorly crystallised.

X-RAY DIFFRACTION ANALYSIS <2 μm CLAY SIZE FRACTION

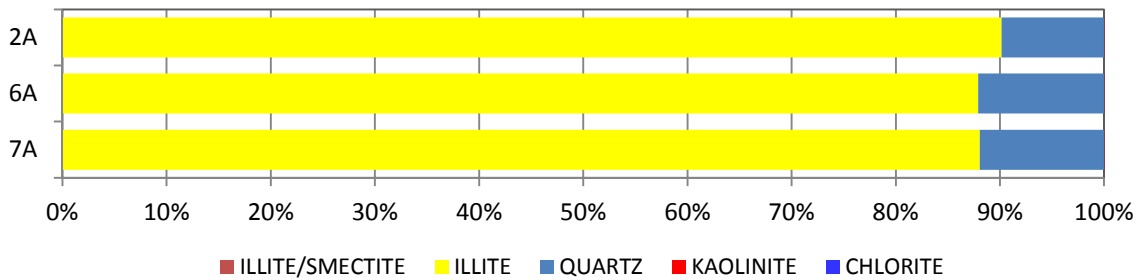


Figure 6.3 - X-ray diffraction analysis <2μm clay size fraction

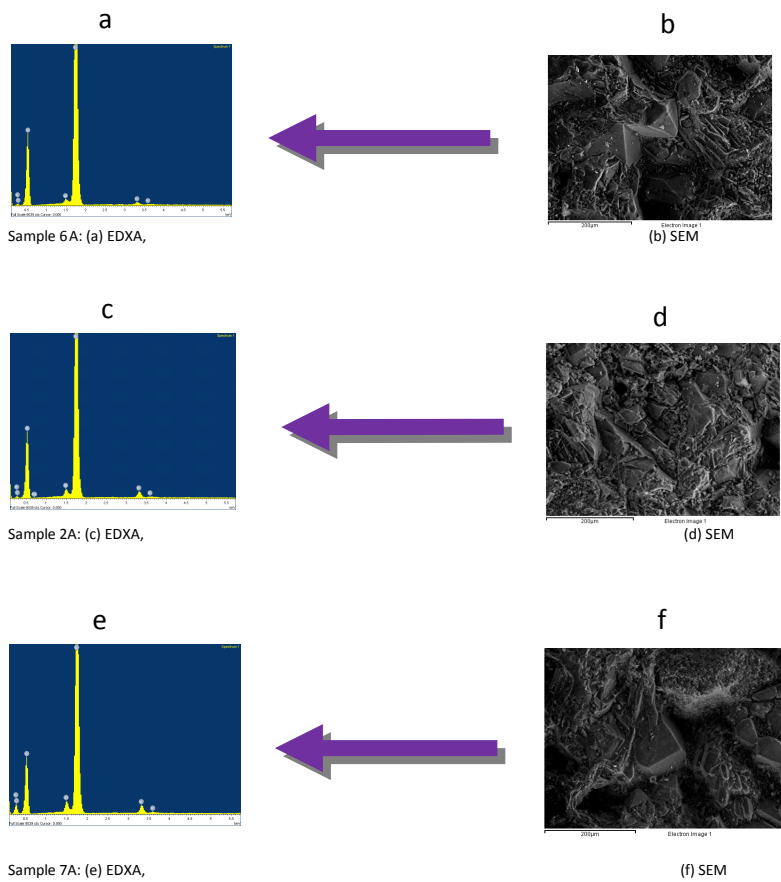


Figure 6.4 - Initial SEM/EDXA grain distribution and imaging of samples. The SEM shows clean rock samples that have been treated from its native state. The EDXA shows that silica or quartz (SiO_2) is the dominant component in the three cores representing 96.39% for core 6A, 92.63% for 2A and 80% for 7A; with potassium feldspar and Kaolinite in trace amounts. This is clearly shown by the various peaks. This result is similar to that obtained from XRD analysis.

6.3.2 Commercial Silica Sand

Two different grades of commercial silica sands (20/40, 40/60 mesh sizes) were used to make sand packs of either different or similar permeabilities for the sand pack experiments^c ^d. Their interactions with polymer molecules in solutions as well as with salts are quite comparable to those of natural sands (Zitha et al., 1995). The sands were characterized using the following methods:

- Pycnometer method (for porosity and grain density determination)
- Sieve analysis (for particle size distributions)
- Optical microscopy (for sand shape identification)
- SEM/EDXA (for imaging and mineralogy composition)

Optical microscopy (Leica DFC420 Digital Microsystems ([Figure 6.5](#))) was used to capture high-resolution images of the silica sands for shape identification. Both the 20/40 and 40/60 US silica sands were observed to be spherical in shape as shown in [Figure 6.6](#). The figure appears to depict uncemented and unconsolidated loose sand showing particular packing of loose spheres. The geometry of this type of shape enables its porosity to be calculated. The shape and packing of the sand determines its surface area. The specific surface of a porous material is the total area exposed within the pore space per unit volume; and the unit volume may either be the solid-mineral framework or the pore space with each having different representations. The sand with higher surface area causes higher polymer adsorption/potential for higher formation damage.

^c Dry-packing technique was used to introduce sand via a small funnel into the vertical steel-column pack-holder. When sand materials had evenly dispersed and reached the desired level in the holder the flow of sand was stopped. However, shaking and tapping of the holder was continued for reasonable time period to ensure complete settling of the sand materials.

^d The wet-packing technique (Szabo, 1972) could also have been used. In this method, the sands are packed into a flow cell under brine while keeping and maintaining the brine level slightly higher than the top of the sand in the column. In this way, a particle size separation is minimized. Also, having placed a new layer of sand, this layer is mixed with the top section of the previously packed sand resulting in a relatively homogeneous pack. This wet sand packing method proved to be very reliable that in no case would any fracturing or channelling occur in the packs.

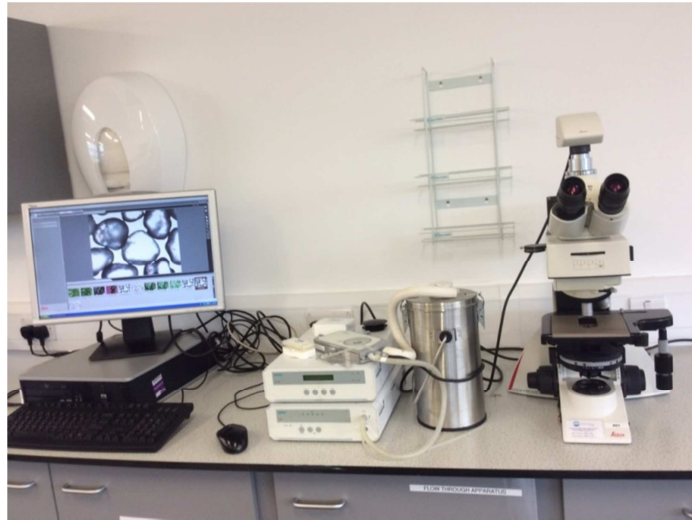
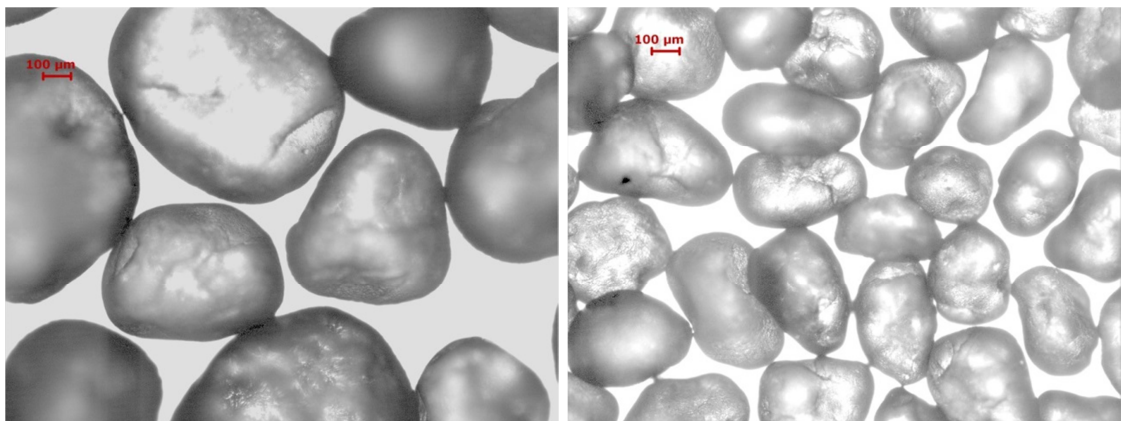


Figure 6.5 - Leica DFC420 Digital Microsystems used to capture high-resolution images of the silica sands.



(a)

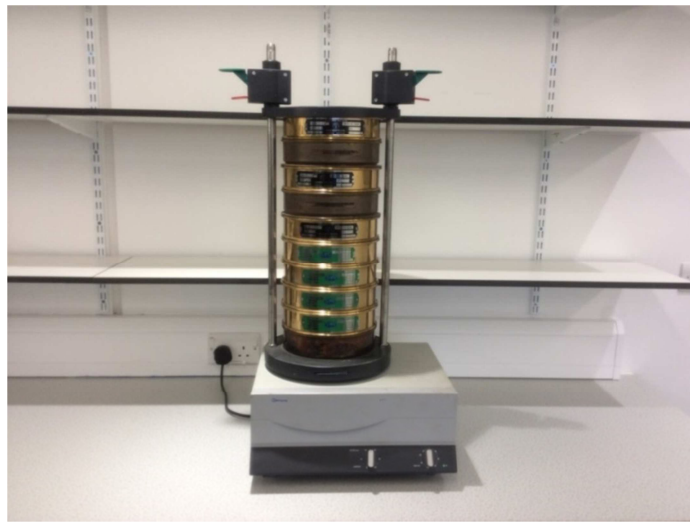
(b)

Figure 6.6 - Microscopic image of the US silica sand sizes used for the polymer adsorption flood: (a) sample 20/40 sieve mesh, and (b) sample 40/60 sieve mesh (5x Objective magnification).

6.3.2.1 Grain Size Distribution Analysis of the Silica Sands

Analysis of the grain size distributions of the sands was done by direct sieving of the samples. The mechanical shaker and mesh arrangement used for the sieve analysis is shown in Figure 6.7. The results of the sieve analysis are reported in both tabular and graphical form. The data generated during the experiment and the main characteristics of the US silica sand sizes used in this study are shown in Table 6.6 and Table 6.7 respectively. The weight fractions retained on each sieve used in the test

and in the pan were recorded and converted to percentages of the original test sample weight. [Figure 6.8](#) shows the weight percent retained on individual screens for both sands. In order to estimate the percentages of material larger or smaller than a certain mesh size, the cumulative percentage weight of these remains were calculated and plotted against the mesh size of the sieves, resulting in distribution curves ([Figure 6.9](#)). The experimental detail of the sieve analysis is given in appendix D).



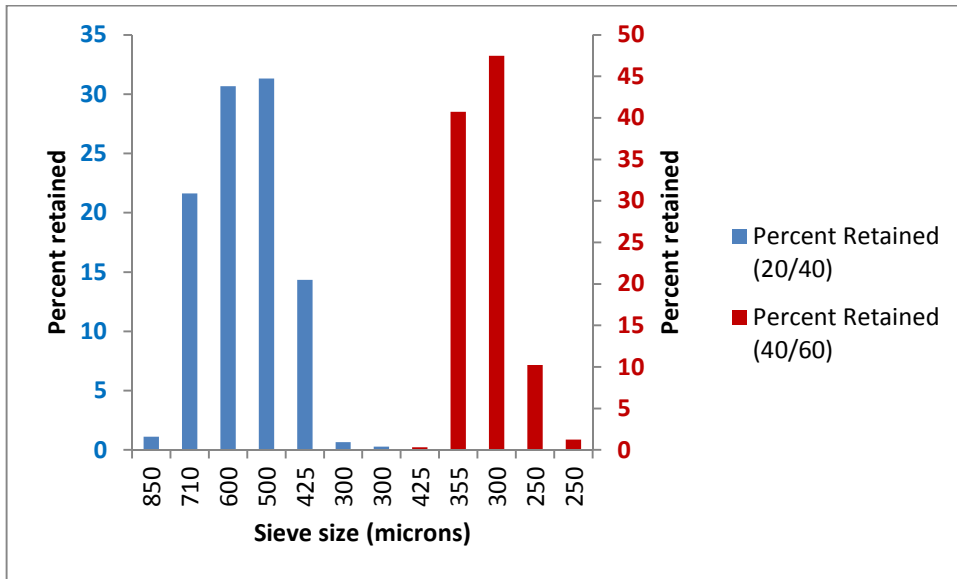
[Figure 6.7](#) - Mechanical shaker and mesh arrangement used for the sieve analysis.

Table 6.6 - Characteristics of the 20/40 US silica sand used in this study.

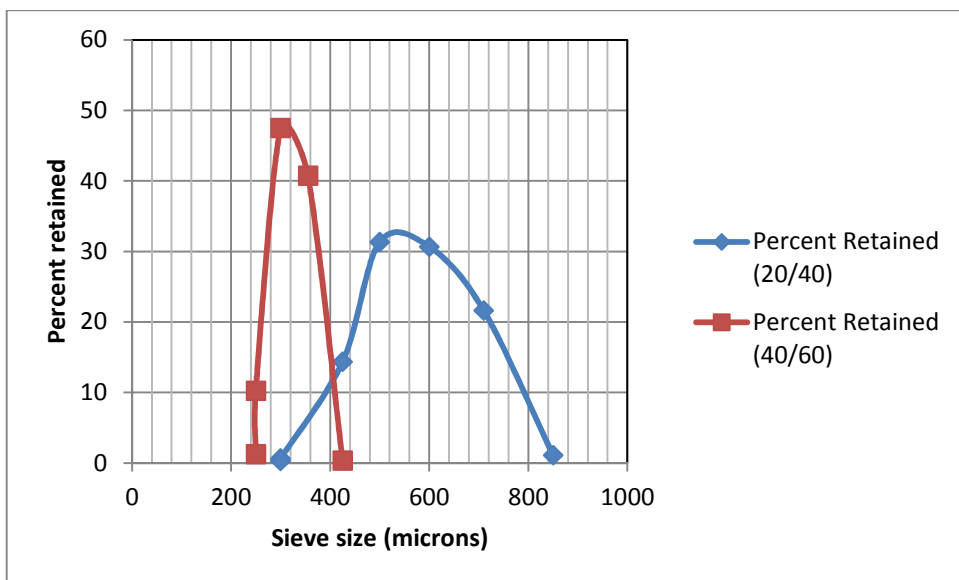
US Sieve Designation (or Sieve Mesh)	Sieve Opening (or Sieve Size)		% Retained		Cumulative % Passing
	mm	µm	Individual	Cumulative	
16	1.180	1,180	0.000	0.000	
20	0.850	850	1.112	1.112	98.888
25	0.710	710	21.626	22.738	77.262
30	0.600	600	30.658	53.398	47.604
35	0.500	500	31.324	84.720	16.280
40	0.425	425	14.350	99.070	0.939
50	0.300	300	0.656	99.726	0.274
Pan	<0.300	<300	0.274	100.00	0.000
Typical physical properties of the 20/40 sand size					
Colour	White		Mineral	Quartz	
Grain shape	Round		Bulk density	1.54 g/cc	
Hardness (Mohs)	7		Specific gravity	2.65 g/cc	
Melting point (°F)			pH	7	
Typical chemical analysis					
Silicon Dioxide (SiO₂)	99.5+		Magnesium Oxide (MgO)	<0.01	
Aluminium Oxide (Al₂O₃)	0.06		Sodium Oxide (Na₂O)	<0.01	
Iron Oxide (Fe₂O₃)	0.02		Potassium Oxide (K₂O)	<0.01	
Titanium Oxide (TiO₂)	0.012		Loss on Ignition (LOI)	0.1	
Calcium Oxide (CaO)	<0.01				

Table 6.7 - Characteristics of the 40/60 US silica sand used in this study.

US Standard Sieve Mesh (or Sieve No.)	Sieve Opening (or Sieve Size)		% Retained		Cumulative % Passing
	mm	µm	Individual	Cumulative	
35	0.500	500	0.000	0.000	100.000
40	0.425	425	0.312	0.312	99.688
45	0.355	355	40.730	41.042	58.958
50	0.300	300	47.488	88.530	11.470
60	0.25	250	10.234	98.764	1.236
Pan	<250	<250	1.236	100.000	0.000
Typical physical properties of the 40/60 sand size					
Colour	White		Mineral	Quartz	
Grain shape	Round		Bulk density	1.54 g/cc	
Hardness (Mohs)	7		Specific gravity	2.65 g/cc	
Melting point (°F)			pH	7	
Typical chemical analysis					
Silicon Dioxide (SiO₂)	99.5+		Magnesium Oxide (MgO)	<0.01	
Aluminium Oxide (Al₂O₃)	0.06		Sodium Oxide (Na₂O)	<0.01	
Iron Oxide (Fe₂O₃)	0.02		Potassium Oxide (K₂O)	<0.01	
Titanium Oxide (TiO₂)	0.012		Loss on Ignition (LOI)	0.1	
Calcium Oxide (CaO)	<0.01				



(a)



(b)

Figure 6.8 - Grain size distributions by weight percent of fractions retained for the 40/60 and 20/40 US silica sands: (a) Histogram (b) Scatter chart.

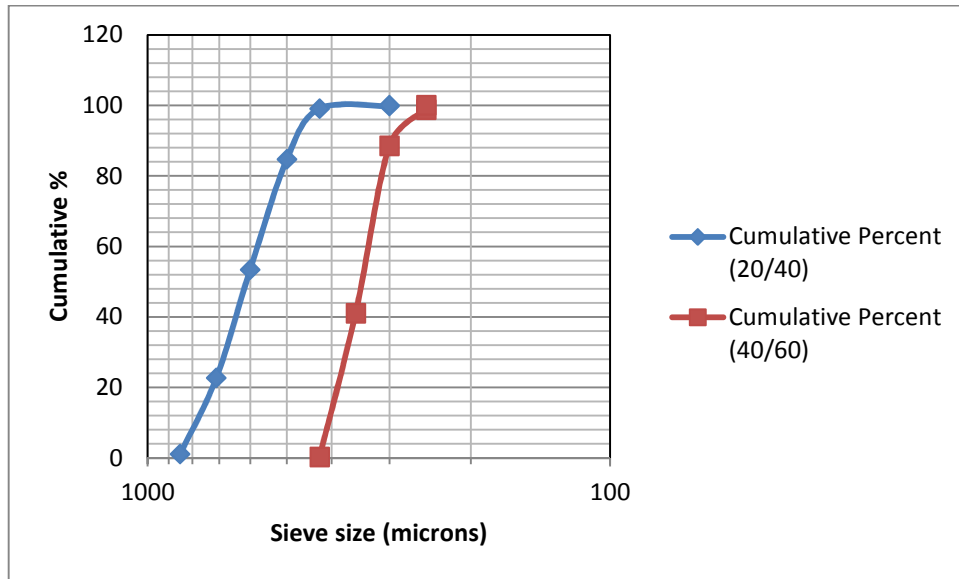


Figure 6.9 - Cumulative grain size distributions by sieved weight for the 40/60 and 20/40 US silica sands.

6.4 Sand pack porosity and pore volume measurements

Pore volume and porosity were determined for each sand pack using the direct method as follows:

- a) The internal volume of the core holder was determined from its dimensions. The cell holder has length of 2.28 cm, diameter of 4.40 cm, cross-sectional area of 15.21 cm², and internal volume of 34.67 cm³.
- b) The sand material loaded into the holder was weighed and recorded.
- c) The volume of the sand grain material was determined accurately from knowledge of the grain density.
- d) The pore volume of the porous medium was then calculated using the direct method (i.e. by subtracting the volume of the sand grain material in the holder from the bulk volume).
- e) The porosity was thereafter determined from the pore volume and bulk volume data using Eqns. 6.1 through to 6.4 as previously described.

6.5 Clashachs and Sand pack permeability measurements

After the samples' pore volume and porosity measurements, the brine absolute permeability was experimentally determined for each sample

using the cell holder. The sands were packed into the flow cell using the dry sand packing technique. For the purpose of this section, both the clashach plugs and the sandpacks will be referred to as "cores". Two 80 mesh count (i.e., 180 μm) screens were placed one each on both ends of the sandpack holder to act as fluid distributors and to contain the sand inside the holder during flow without disrupting the fluid passage. An O-ring which forms integral part of the cell holder design is to ensure pressure seal during fluid flow. The cell holder was connected to an Edwards's high vacuum pump (model ED50) to evacuate the core. The deaerated, filtered synthetically formulated brine (SFB) was used as the flowing medium in the permeability calibrations. The following procedure was adopted:

- After mounting it in the core holder, the core sample was placed under vacuum for a sufficient time period to remove all air from the sample using Edwards's high vacuum pump (model ED50). It's worth mentioning that for a reliable test, gas/air must not be present in the core as gas usually manifests as higher permeability at high flow rates.
- The SFB was flowed through the core at low rates. In the case of the clashach cores, the low rates were to avoid eventual fines migration and disruption of the core geological character; while for the sandpacks, the low flow rates used were to avoid particle separation/sand redistribution and/or re-stratification within the test holder. Furthermore, as Darcy's law does not apply at excessive rates, the flow rate must be reasonably low.
- The measurements at different flow conditions were obtained so that an average value for permeability can be calculated as well as detect presence of gas saturation.
- The pressure differentials (measured with the aid of pressure transducers) were noted and recorded for the different flow rates used after steady-state conditions were reached (i.e. a constant flow rate was attained at a constant pressure differential).
- Core absolute permeability to brine from the pressure and flow rate data was calculated using Darcy's law (Darcy, 1856) (Eqn. 6.14):

$$k_b = \frac{q \mu_{app} \cdot L}{A \cdot \Delta P} \quad (6.14)$$

where,

k_b = permeability to brine, Darcies

μ_{app} = apparent fluid viscosity, cp

ΔP = pressure drop across length L, atm

q = volumetric flow rate, cm³/s

A = cross-sectional area of core, cm²

L = length of core, cm

- A straight line through the origin was then fitted to the plot of q vs. ΔP by the no-intercept regression model (Abu-Khamsin, 2004). The slope (m) of this straight line is the core sample's permeability multiplied by $A/\mu L$, i.e.

$$k = \frac{m \mu L}{A} \quad (6.15)$$

Table 6.8 shows the properties of the 40/60 and 20/40 silica sands used in the study.

Table 6.8 - Properties of the silica sands.

Sieve mesh	Particle size range, μm	Average particle dia., μm	Porosity, fractions	Permeability, mD	Specific surface area, m^2/g
40/60	250-425	333	0.373	147.0	0.202
20/40	300-850	564	0.372	348.8	0.128

6.6 Core flooding Experimental Setup

Figure 6.10 shows a simplified schematic of the core flood experimental apparatus setup; while Figure 6.11 shows the pictorial view of the rig. The important and required key equipment are indicated on the schematic drawing of Figure 6.10. In the flow system, lines and valves are set up to minimise dead volumes in which fluids can be lost. There is a heating tape cabinet (with thermocouples) to house the test core and holder.

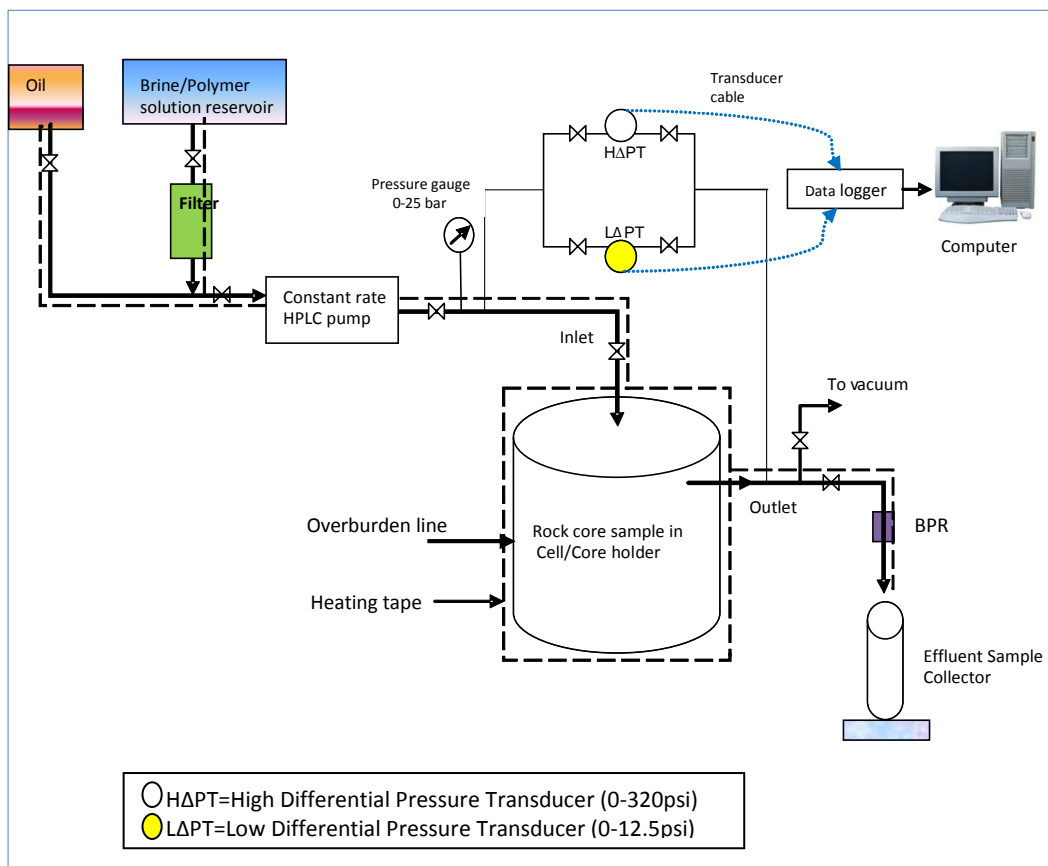


Figure 6.10 - Experimental rig design schematic and setup for the implementation of the polymer dynamic coreflood.



Figure 6.11 - Pictorial view of the core flood rig.

The coreflood setup for the polymer flooding experiments consisted of a stainless steel radial core holder designed in-house and set-up to simulate reservoir radial flow. However, the core holder was operated as a linear flow model during the core flooding. In Figure 6.10, a high performance, dual head syringe pump model HPLC 1500 (manufactured by Scientific Systems, Inc. (SSI), USA) was used to deliver a varying, pre-defined fluid volume at constant injection or flow rate across the core sample. The pump (which has a maximum pressure of 6000 psi and can deliver at rates up to 12.0 ml/min) was used to provide a non-pulsating flow during the experiment. The pump has pressure accuracy of $\pm 1\%$ of full-scale pressure. Electronic balance was used for flow rate measurements (rate verification). This is vital in order to obtain accurate flow rate information. All in-place pressure monitoring and measurements were electronic and digitised with the aid of a high-speed National Instruments data acquisition system (NIDAQ) through Validyne pressure transducers of varying capacities mounted across the core and a personal computer to which pressure readings were automated (Figure 6.11). The transducers have pressure accuracy of $\pm 0.25\%$ of full-scale pressure (including effects of non-linearity, hysteresis and non-repeatability). The interface design of the NIDAQ system is shown in Figure 6.12. The low (0-12.5 psi) and high (0-320 psi) capacity transducers were chosen

according to the pressure range and the requirements of the measurement resolution.

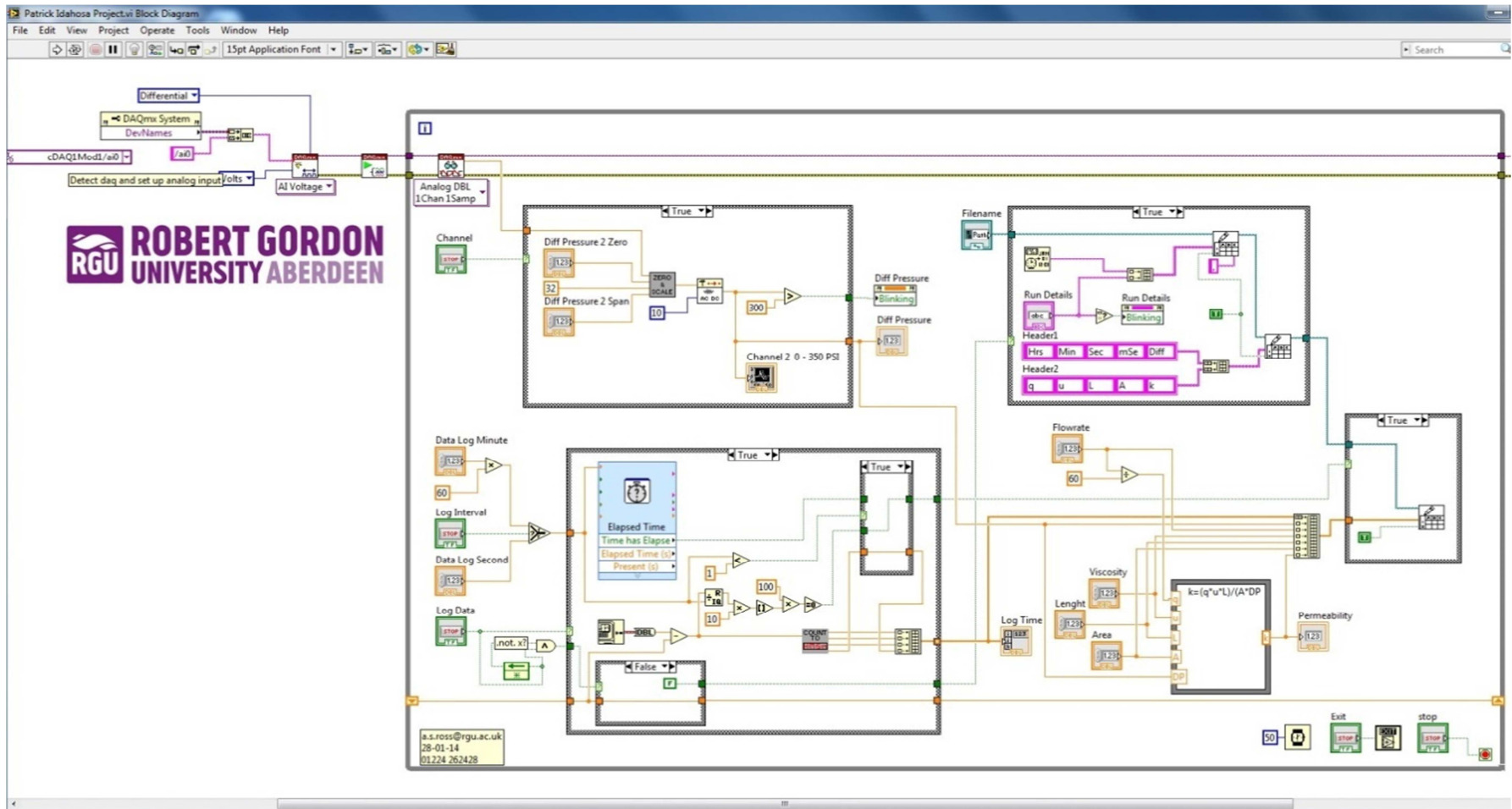
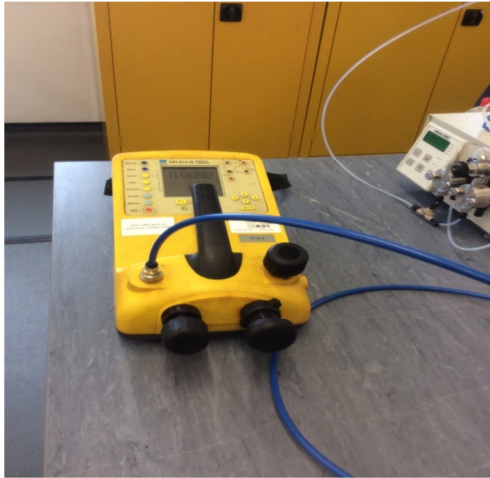


Figure 6.12 - Layout of the National Instruments (NI) data logging interface design.

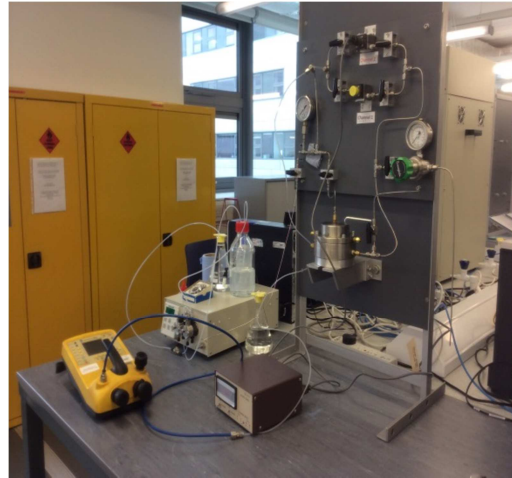
A Validyne carrier demodulator model CD223 (manufactured by Validyne Engineering, USA) was used to provide the correct sensor excitation and demodulate the returned Alternating Current (AC) signal from the sensors into a +/-10 Vdc signal appropriate for the data acquisition input. The CD223 accepts two transducer inputs but the display and signal follow a front panel switch so that the readings from only one sensor at a time are displayed. As the analog output follows the display, it was not possible to record both transducer readings simultaneously. Furthermore, an absolute pressure gauge (0-360 psi) range was mounted at the pump outlet. This was done in order to monitor inlet pressure and avoid over-pressuring the transducers along the core. Other accessories used in the experiment in addition to those of [Figure 6.10](#) included: weighing balance (used for measurements of all components required for preparing the brine and polymer solutions and including the mass of the clashach sandstone cores and the sand pack), electrically powered magnetic stir/hot plate and stirring bars (for mixing brine and polymer solutions), graduated cylinders for collecting effluent samples, filter unit (used to filter the polymer and formation brine solutions before injection into the core).

6.6.1 Flow rig leakage test and Transducer calibration

Prior to start of experiments, a flow rig leak test was conducted. Druck DPI model 615 IS (an intrinsically safe portable pressure calibrator/tester from General Electric) was used for the rig leakage test ([Figure 6.13](#)). Using this device, air pressure of 100psi was applied and held within the system apparatus for duration of 5 minutes. When there was drop in the applied pressure (an indication of system leakage), the leak point was detected by brushing on a solution of LEAK-TEC detergent and looking for bubbles. For any detected bubbles, fittings were then tightened and the process was repeated until no further drop in pressure (or leak) was detected. The Druck DPI model 615 IS device was also used to calibrate the pressure transducers ([Figure 6.14](#)).



(a)



(b)

Figure 6.13 – Picture showing (a) Druck DPI 615 IS, (b) performing rig leakage test



Figure 6.14 – Picture showing transducer calibration using the Druck DPI 615 IS pressure calibrator.

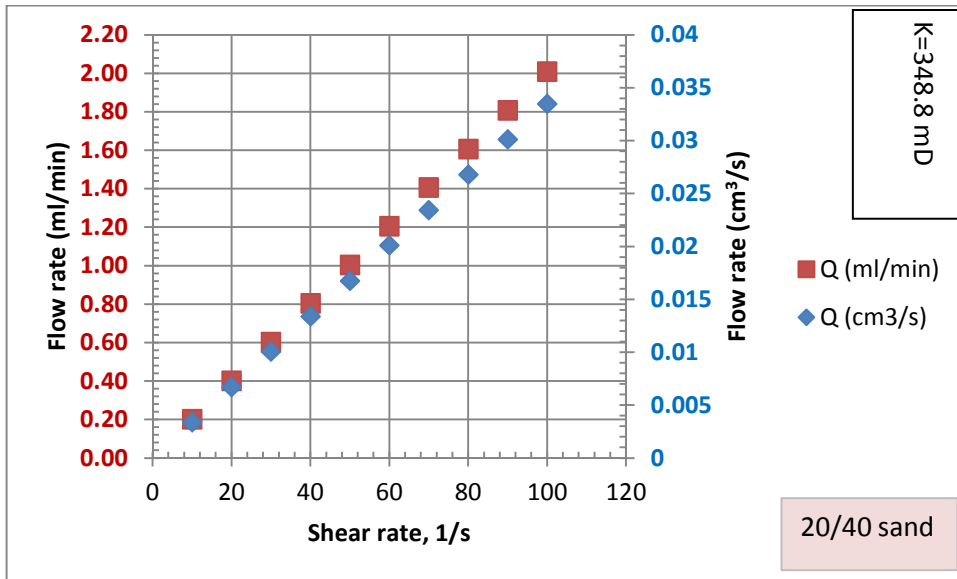
6.7 Flow rate determination and in-situ estimation of shear rates in cores/sandpacks.

The in-situ rheological behaviour of non-Newtonian polymer fluid system is a function of shear rate. Equation (6.16) relates the porous media physical characteristics and fluid velocity to the shear rates (API RP 63, 1990; Urbissinova et al., 2010; Christopher and Middleman, 1965; Gleasure, 1990; Jennings et al., 1970):

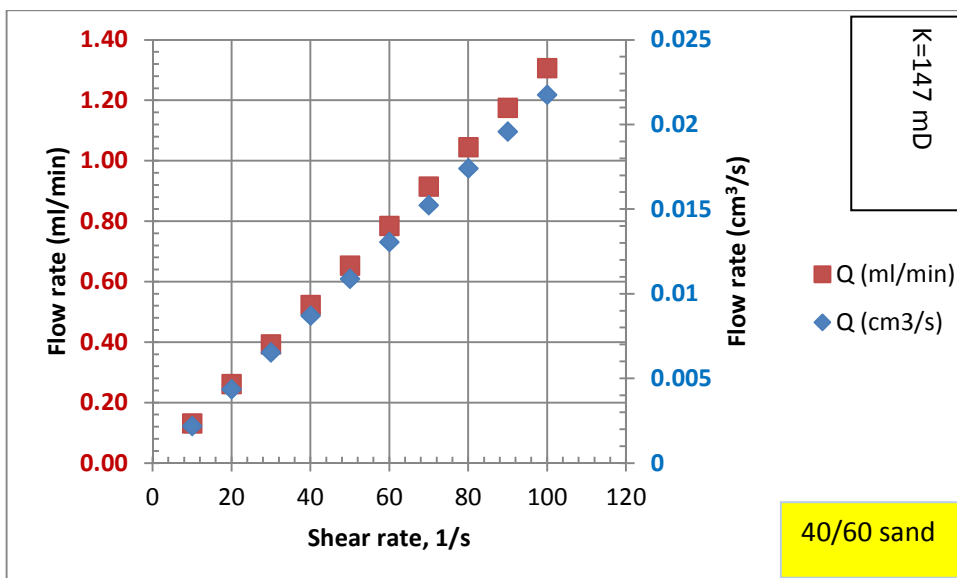
$$\dot{\gamma} = \frac{3n+1}{4n} * \frac{4\alpha Q}{A(8k\phi)^{0.5}} \quad (6.16)$$

Where, $\dot{\gamma}$ =porous media effective shear rate, 1/s; Q =flow rate, cm³/s; A =core cross-sectional area, cm²; α =geometrical factor to account for the porous media structure (assumed as 1.15 for natural sand packs and SiC packs (Chauveteau 1982, 2002; Chauveteau et al., 2002); k =formation permeability, cm²; ϕ =formation porosity, fraction; and $(3n+1)/4n$ =Rabinowitsch correction factor or the non-Newtonian correction for power-law fluids.

From Eqn. (6.16), the desired flow rate in core (or sandpack) that will induce shear rates about 10-100 1/s that are comparable to field applications can be estimated. For the sand pack, a flow rate of 2.0 ml/min (20/40 sand) and 1.3 ml/min (40/60 sand) was estimated to induce the shear rates in the pack that lie within the initially stated shear rate range (Figure 6.15); while for the Clashach cores, the range of shear or flow rates (between 0.4 to 1.80 ml/min) were estimated to induce the shear rates in the core that lie within the initially stated shear rate range (Figure 6.16).

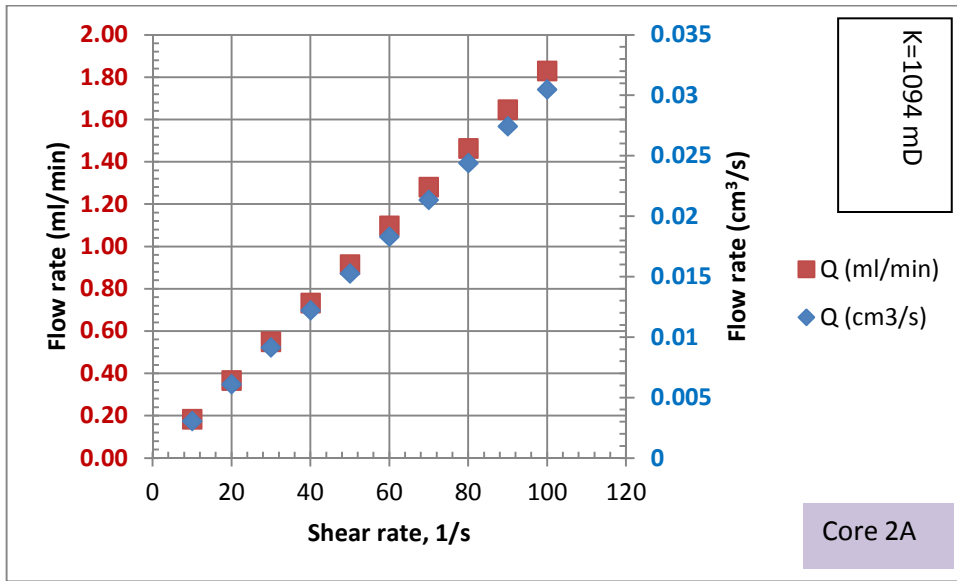


(a)

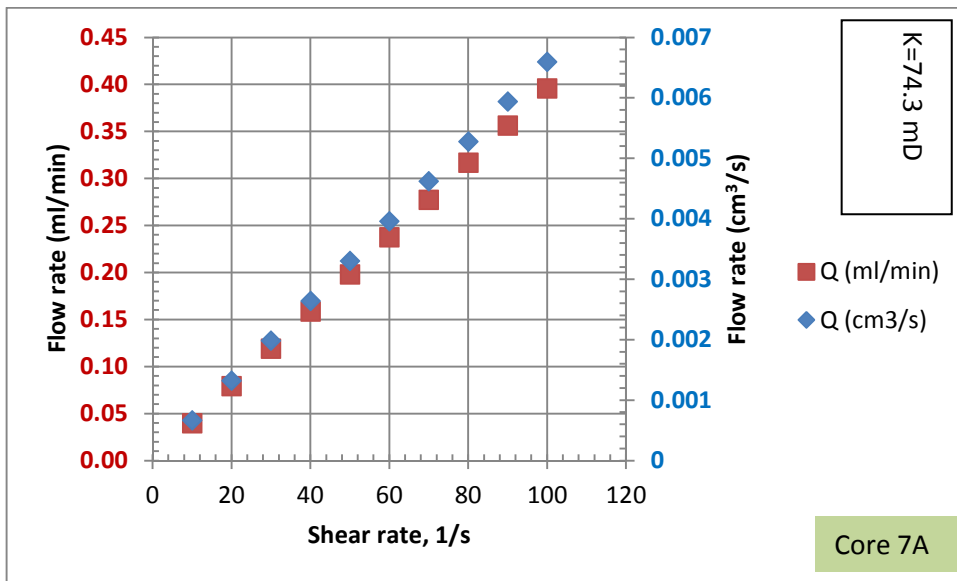


(b)

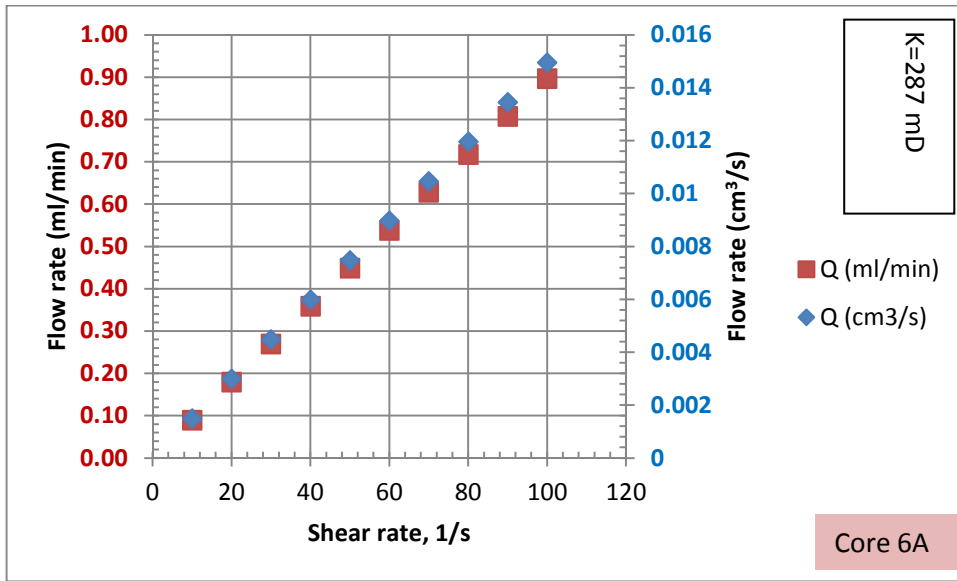
Figure 6.15 - Shear rate simulation in sandpaks: (a) 20/40 Silica sand (b) 40/60 Silica sand.



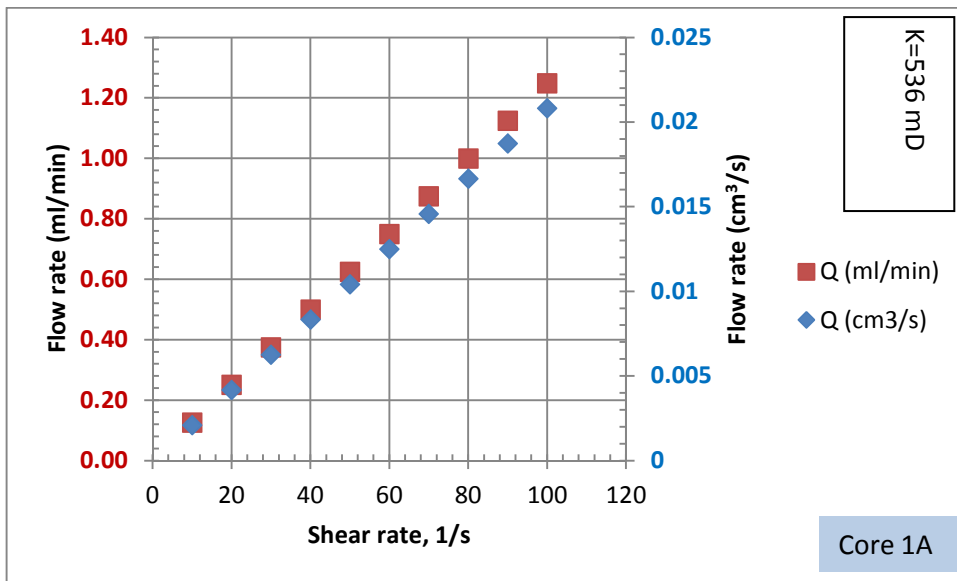
(a)



(b)



(c)



(d)

Figure 6.16 - Shear rate simulation in Clashach cores: (a) Core 2A, (b) Core 7A, (c) Core 6A and (d) Core 1A.

6.8 Conclusion

Since the affinity of reservoir rock for polymer depends on many factors such as mineralogy composition, particle size, pore size distribution, etc, then as a preliminary study, a suite of non-destructive petrophysical methods such as Mercury Injection Capillary Pressure (MICP) for porosity and pore size distribution, X-Ray Diffraction (XRD) for mineralogy quantification, Helium porosimetry, Scanning Electron Microscopy (SEM) imaging technique, Energy Dispersive X-ray Analysis (EDXA) were used to characterise the cores' petrophysical properties as these properties are considered important in any resource evaluation and devaluation. For example, pore and pore throat sizes controlling permeability are directly related to particle sizes. The results of the MICP, for example, shows the existence of two families of pore throat sizes around 0.01 and 10 μm for sample 7A; and around 0.003 and 20 μm for sample 2A respectively. Some other specific results show that core sample 2A has wider permeability distributions than 7A. As expected, it was observed that for mercury displacing air from these plugs, the capillary pressures was higher than for core 7A having smaller pore openings; and that at any given mercury saturation the corresponding pore sizes are smaller for the low-permeability sample than for the larger one. Sand 20/40 equally has larger particle sizes and broader distributions than sand 40/60. Material requirements for the polymer static and dynamic adsorption tests were selected, described, prepared and characterised in this chapter. This enables the selection of each core or sand type that was used in the subsequent polymer core flood. The core flood rig design, setup, and rig testing procedures as well as the data acquisition system are described. Finally, in-situ flow rate determination procedures in porous media are also described in this chapter.

The next chapter presents the experimental procedures, method overview (i.e., the justification for adopting a particular method) and experimental results and discussion.

7

Chapter 7 – Experimental Procedures, Results, and Discussion for Polymer Core Flooding

7.1 Introduction

Experimental procedures, method overview (i.e., the justification for adopting a particular method) and experimental results are discussed and presented in detail in this chapter.

7.1.1 Experimental

Polymer adsorption tests can either be static or dynamic. These two tests form the basis for the polymer pre-field application evaluation. The methods and procedures for evaluating polymer performances on the basis of these tests are presented in the sections that follow. The various experimental procedures and methods are presented and discussed in turn beginning with an overview.

7.2 Experiment A: Effect of concentration on polymer retention

Concentration has been said to be controversial among the factors that affect polymer retention (Manichand and Seright, 2014). While some researchers (Szabo 1975a, 1975b; Szabo, 1979; Kolodziej, 1988; Zheng

et al., 2000; Deng et al., 2006) believe polymer adsorption is a strong function of concentration, others (Vela et al., 1976; Shah et al., 1978; Friedmann, 1986; Green and Willhite, 1998) showed that polymer adsorption has weak concentration dependence. A recent study (Zhang and Seright, 2013) showed that polymer retention behaviour depends on the concentration regime: 1.) low retention at low concentration (but insensitive to concentration); 2.) Intermediate concentrations with gradual increase in retention; and 3.) High retention at high concentration (also concentration-insensitive). Kolodziej (1988) and Manichand and Seright (2014) proposed a conceptual model to explain this behaviour. A closer and careful look shows that the static method was used for most of these studies. Furthermore, most of the dynamic investigations repeatedly used one and the same core for the tests; i.e., after a given core was flooded with low concentration polymer and retention accessed, the same core was again flooded with high concentration polymer to determine the possibility of further retention on the same core. Only a very few studies (Szabo, 1975b; Huang and Sorbie, 1993; Sorbie, 1991; Manichand and Seright, 2014) have attempted to use new cores or sand packs for each concentration where only moderate concentration dependence for retention were reported. It is better to compare the results from any study only when conducted under same or similar test conditions, particularly when it relates to comparing the results from dynamic with those of static tests.

In this section, the influence of polymer concentration on retention was tested using both static and dynamic methods. The other objective of this section was to do a cost-benefit analysis of two polymer products and then recommend which one is best for EOR operation in terms of retention and/or formation damage particularly in the dynamic or flow condition. Each test was performed on a fresh soft clashach core and/or commercial silica sandpack (grade 40/60 and 20/40) for different HPAM concentration respectively. In one case (for the 20/40 sand), a single sandpack was flooded with polymer solutions of increasing concentrations in order to compare its adsorption with used and fresh sandpacks of

similar properties. The commercial silica sands were used for the static measurements; while both clashachs and commercial silica sands were used for the dynamic measurements. Both porous media have been prepared geologically and petrophysically conditioned as previously described in chapter six.

7.2.1 Experiment AI: Static (or batch) adsorption test

Static (or batch) adsorption tests have been used to measure polymer retention/adsorption and to provide a preliminary screening of field EOR polymers (API RP 63, 1990; Chiappa et al., 1999). The tests are fairly simple and inexpensive compared to procedures involving flow in cores. It is possible to hold the adsorbent constant for a series of tests thereby isolating the effects of changing properties of the polymer solution. Also, the properties of the adsorbent can be varied in a controlled way, for example, by adding various amounts of clays. However, results from these tests may not be representative of field values for several reasons. First, in disaggregating consolidated rock, surfaces are exposed which may not be the same as surfaces of the consolidated rock (Green and Willhite, 1998). This effect should be minimized if the reservoir rock is unconsolidated. Second, the mechanical entrapment component of polymer retention is not measured by the static test (Zaitoun and Kohler, 1987; Chiappa et al., 1999). However, it may be used in combination with a flow type retention test to attempt to separate the retention mechanism from adsorption. Third, the wettability of the disaggregated rock may be different from that of the reservoir rock (API RP 63, 1990). Nonetheless, static tests are significant as they are more diagnostic of adsorption on all grain surfaces of the sands. Therefore, results could serve a basis for comparison with flow tests where polymer solution is not accessible to small pore throats in which the polymer is mechanically obstructed from entry; i.e. the inaccessible pore volume (IAPV) effect.

Static adsorption measurement involved mixing polymer solution with crushed rock sample until no further change is observed in the supernatant concentration. The difference in concentration before and

after rock contact was calculated as the static adsorption polymer by dividing the loss of mass from the solution by the weight of the exposed sand. The polymer concentration in solution was determined by the bleach method (see section appendix F).

7.2.1.1 Procedures for Static (or batch) Adsorption Experiment AI

In this section, series of static (or batch) adsorption experiments were conducted. The first two sets of measurements were performed in order to first explain the kinetics of static polymer adsorption. The others were performed to investigate equally the kinetics of static desorption and re-adsorption respectively. The first test was carried out with two different polymer samples (FP3330 S and FP3630 S) using 40/60 US silica sand as porous medium in order to compare their adsorption differences. The second test was performed with very low concentration (50 ppm) of FP3630 S. The influence of concentration in static adsorption was also studied using a range of concentrations of FP3630 S HPAM. The following procedures were followed:

- a) 100 g of 40/60 US silica sand was weighed in 350ml stock bottles.
- b) In the first set of polymer adsorption kinetics investigation, 150 g of 200 ppm polymer solutions of FP3330 S and FP3630 S were mixed with the sand in the bottles, capped and stirred gently to expel trapped air.
- c) In a separate set of experiments, 150 g of 50, 200, 750, and 1000 ppm polymer solutions of only FP3630 S HPAM were also mixed with the sand in the bottles, capped and stirred gently to expel trapped air.
- d) The mixtures were kept in an oven stabilised at 50 °C and agitated periodically (30 minutes intervals) to maintain good contact between liquid and substrate.
- e) To ensure adsorption equilibrium and track the polymer adsorption on the Silica sand over time, samples from the bottle containing 50, 200, 750 and 1000 ppm of FP3630 S were collected every 2 hours while samples from both FP3330 S and FP3630 S were collected daily for final supernatant concentration determination using the Bleach

method and the generated standard calibration curve for each sample (Figure 7.1 and Figure 7.2).

- f) Figure 7.3 shows the effect of mixing time on the calibration curve for sample FP3630 S. It was noted that there is a constant shift in the curve for different mixing times. The experimental run for various mixing times show that the maximum concentration was observed after about 20 minutes following which concentration began to decrease owing, probably, due to particle settling and precipitation. However, the final results are not affected if either of the curves is used consistently.
- g) Before use, the wavelength, mixing time, pH and slit sizes, were all adequately and properly calibrated (Figure 7.1 to Figure 7.3).
- h) A Jenway 3505 model digital pH/ion meter with combination electrodes was used to measure samples pH (if required) before testing.
- i) Prior to absorbance measurements in the static test, the upper-phase polymer solutions were centrifuged using IEC Centra-4X centrifuge machine (Figure 7.4) to remove any sand particles. While polymer effluent solutions from the dynamic test were filtered through 6.0 micron Whatman paper.
- j) Measurements of polymer concentrations were carried out on a double-beam ratio recording Hewlett Packard Diode Array UV-visible Spectrophotometer (Agilent 8453 model) with micro-computer electronics (Figure 7.5) by use of turbidimetric method as previously presented by Foshee et al. (1976) and recommended by API RP 63 (1990).
- k) If a polymer solution was too viscous, dilutions were made before measurement; and the dilution factor was noted.
- l) A detailed description of the procedures of turbidimetric method for determining polymer concentration is presented in appendix section (F).

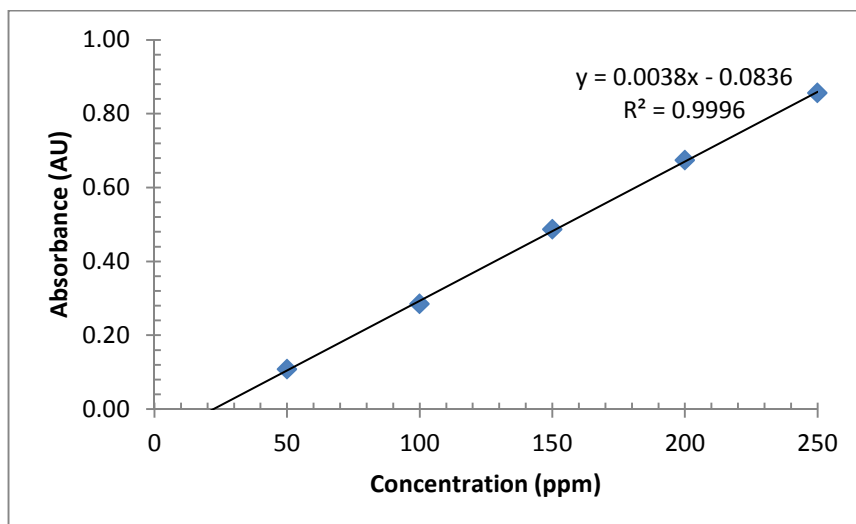


Figure 7.1 - Standard calibration curve for polymer solution concentration measurement for sample FP3330 S used for this study (according to the law of Beer-Lambert).

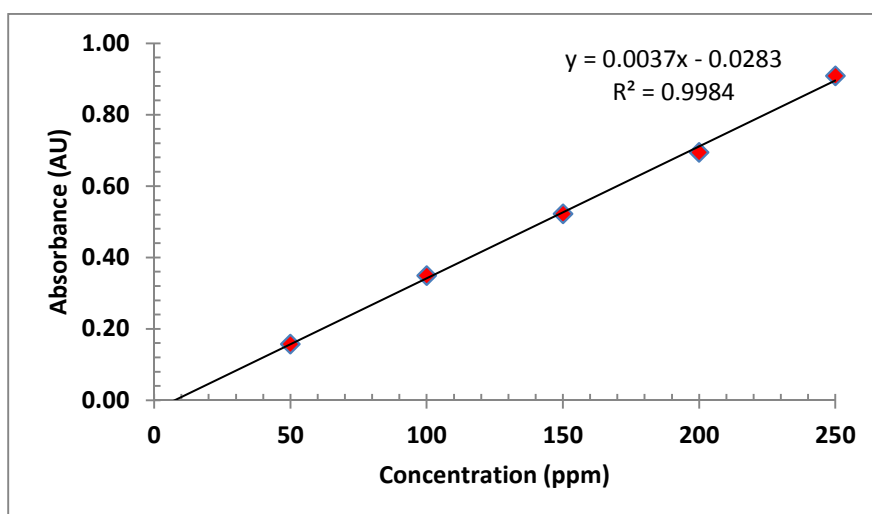


Figure 7.2 - Standard calibration curve for polymer solution concentration measurement for sample FP3630 S used for this study (according to the law of Beer-Lambert).

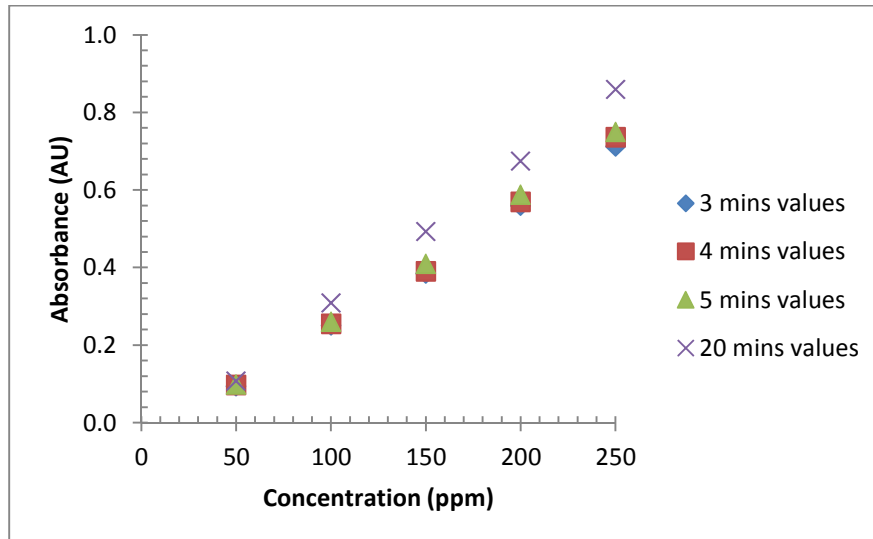


Figure 7.3 - Effects of mixing time on the calibration curve for FP3630 S.



Figure 7.4 - IEC Centra-4X centrifuge machine.

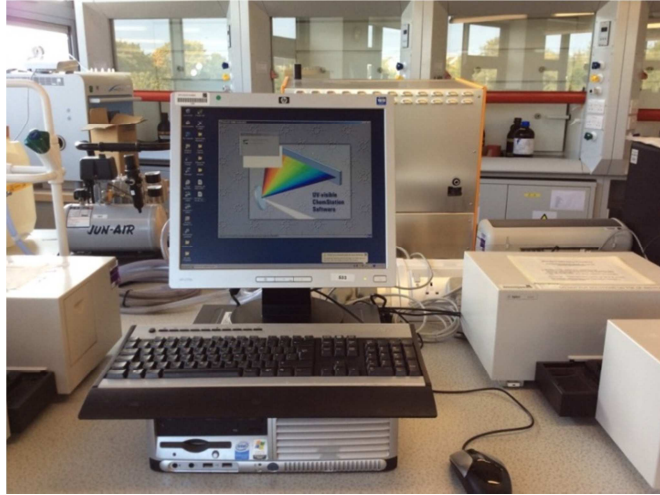


Figure 7.5 - UV-Visible Chemstation software (Agilent 8453 model) used for sample and effluent concentration determination.

7.2.1.2 Calculation of Static (or batch) Adsorption from Experimental Data.

Adsorption levels calculations required the measurement of HPAM concentrations before and after equilibration of the adsorbent with the solution. The turbidimetric method was used as previously stated. On the basis of a mass balance (i.e. retention=polymer injected - polymer produced), the amount of polymer statically adsorbed at different time was calculated using Eqn. (7.1):

$$\Gamma_p(t) = \frac{\Delta C(t) \cdot W_p}{W_s} = \frac{(C_i - C_f) \cdot W_p}{W_s} \quad (7.1)$$

Where;

$\Gamma_p(t)$ = polymer adsorption, microgram adsorption per gram of solid ($\mu\text{g/g}$) as function of time; W_p = weight of polymer solution, g; W_s = weight of solid, g; C_i = initial concentration of polymer solution, ppm; C_f = final equilibrium concentration of polymer solution, ppm. Both brine and polymer densities were assumed to be 1.0 g/cm^3 .

7.2.2 Static Desorption Experiment

Desorption tests were conducted immediately after the adsorption tests to determine how much polymer can be desorbed or removed after the static adsorption. Bottles containing 50, 200, 750 and 1000 ppm of only FP3630 S HPAM solutions were used for the desorption tests. To do this, excess polymer solution was decanted from the top of the sand in the bottles. However, it was not possible to decant all the liquid-phase in the bottles during the decantation process. 150 ml of fresh brine (same TDS1 as previously used for the static tests) was added to the sand during each soaking. To enhance desorption, the bottles were shaken 4 times each at 30 minutes intervals. This implies a soaking period of 2 hours each. Following sand settlement, the upper-phase solution was again decanted and samples from each bottle taken for concentration measurement and calculation of the residual polymer adsorption by use of mass balance. This soaking procedure was repeated 4 times. The pore volume of the 100 g sand was calculated to represent about 17.58 ml. Therefore, during the 4 soakings about 9-fold dilution of the polymer solution in the pore space took place. The brine/sand ratio (w/w) for each soaking was also calculated.

7.2.3 Static Re-adsorption Experiment

On completion of the desorption test cycles it was decided to check the possibility of polymer re-adsorbing on already used sands (i.e. sand in which certain concentrations of polymer solutions had previously contacted in static mode). To achieve this objective, the 50ppm and 200 ppm sands were again selected and additional 750 ppm polymer solution was added to each bottle containing the sands in which the 50 and 200 ppm polymer solutions had previously contacted. The samples were again left in an oven stabilized at 50 °C. Following periodic agitation and sand settling, upper-phase solutions of each of the two bottles were collected at intervals for polymer-concentration determination. The amount of polymer re-adsorbed was again calculated by mass balance. This procedure enables the determination of the polymer retention differences between used and fresh sands in static condition.

7.3 Static Adsorption Experiment II - Influence of Polymer Concentration

In a separate batch experiment to study the specific effect of concentration on adsorption, 100 g of same 40/60 US Silica sand was weighed into 350 ml stock bottles (Figure 7.6). Fresh sand was used in each bottle. This time around 150 g of different concentrations (50-2000 ppm) of FP3630 S HPAM solutions prepared in the same TDS1 as was used in the first batch test were poured into the bottles, mixed and left in an oven stabilized at 50 °C. After the sands had settled following periodic agitation, upper-phase solutions of each bottle of different concentrations were collected at intervals in separate test tubes. The tubes were marked and centrifuged at 2500 rpm using IEC Centra-4X centrifuge machine (see Figure 7.4) to settle any sand particles, and thereafter, prepared for equilibrium polymer-concentration determination using the bleach method as described previously. Using the mass balance concept (Eqn. 7.1) the adsorption ($\mu\text{g/g}$ solid) of the polymer was calculated for each concentration as function of time. Figure 7.7 shows Pictorial of some experimental polymer effluent prepared for analysis.



Figure 7.6 - Some of the stock bottles used for static adsorption test measurements.

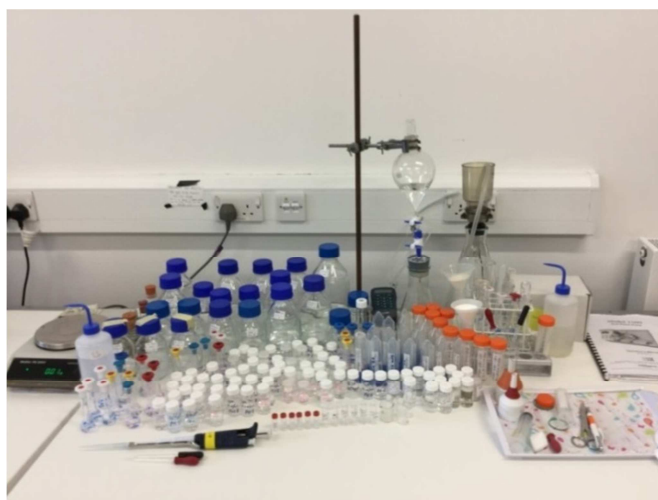


Figure 7.7 - Pictorial view of some experimental polymer effluent prepared for analysis.

7.4 Results and Discussion of Static Experiments

Using the calibration curve of absorbance versus known polymer concentration generated from the Bleach method, the effluent polymer concentrations for the samples were estimated. Plots of polymer concentration loss vs. time; and polymer adsorption, microgram per gram of solid vs. time for sample FP3630 S are shown in [Figure 7.8](#) and [Figure 7.9](#) respectively. As the adsorption kinetics of [Figure 7.9](#) shows, polymer adsorption reached a maximum (about 42 $\mu\text{g/g}$ for FP3630 S and about 31 $\mu\text{g/g}$ for FP3330 S) within approximately 1 day and then levelled off; suggesting an instantaneous polymer adsorption reaction on the surface of the silica sand and indicating an imperfect monolayer-type adsorption (Szabo, 1975).

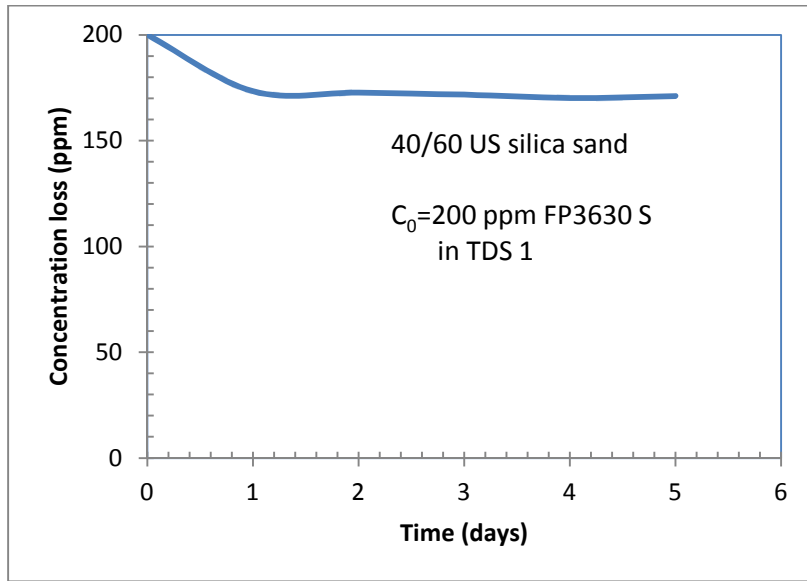
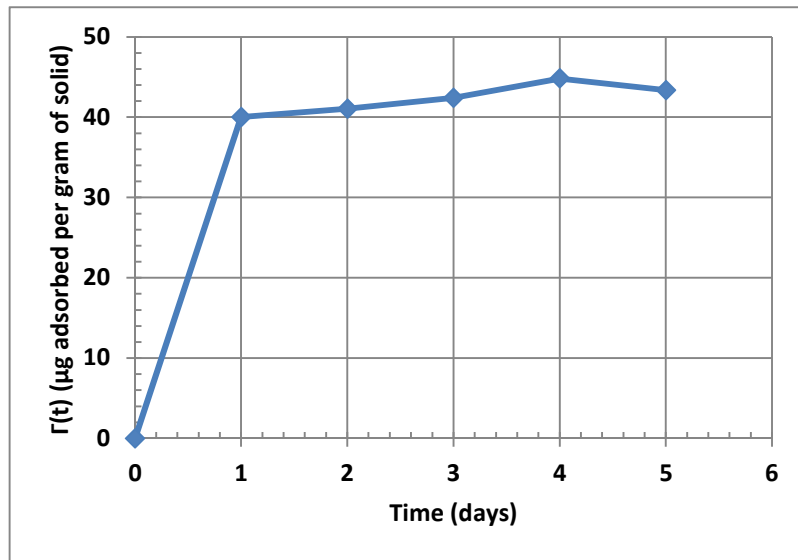
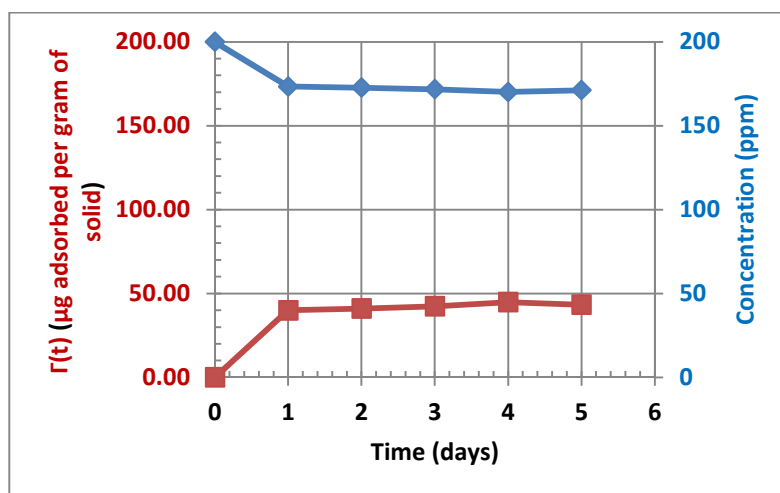


Figure 7.8 - Static adsorption test plot of polymer concentration loss vs. time for sample FP3630 S



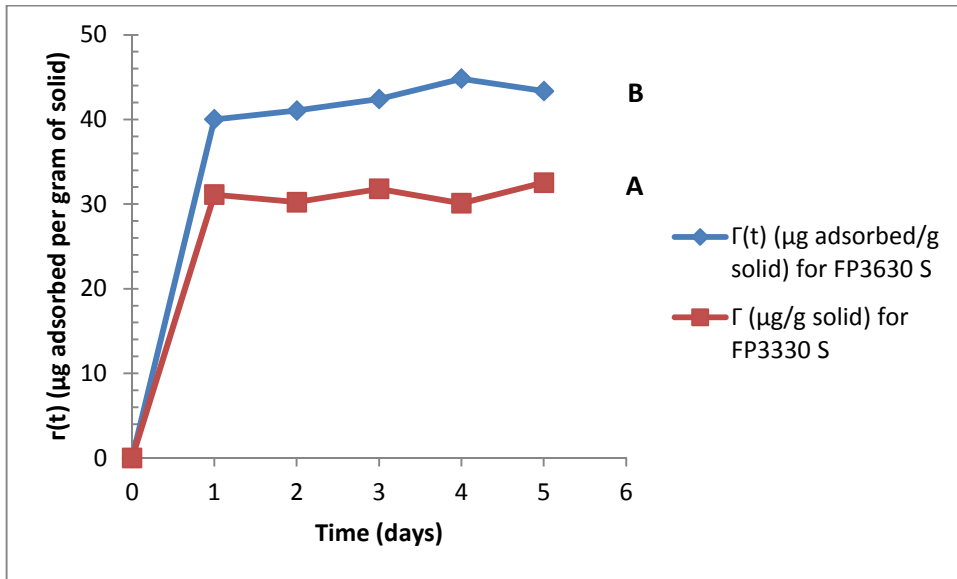
(a)



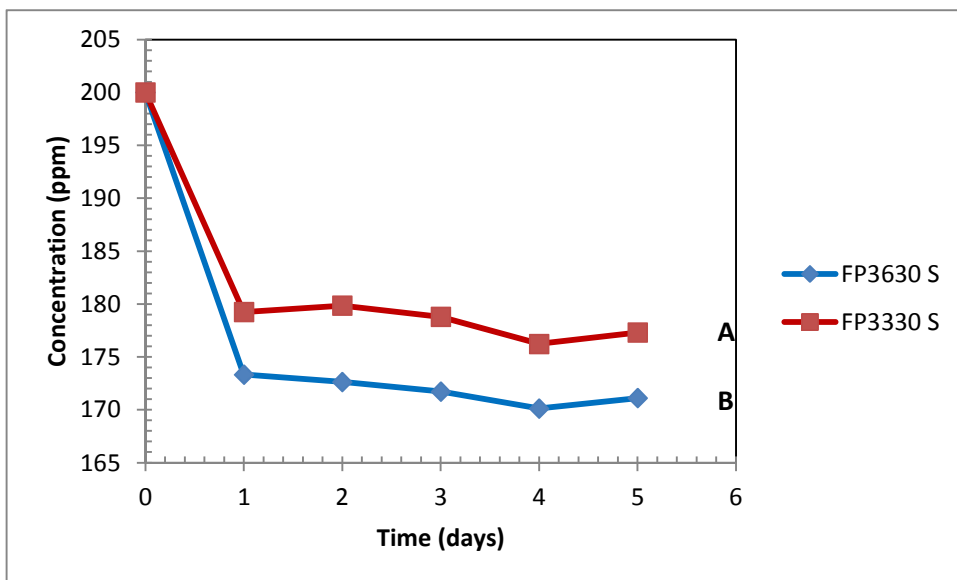
(b)

Figure 7.9 - Adsorption kinetics using silica sand 40/60: (a) Static polymer adsorption, microgram per gram of solid vs. time for sample FP3630 S; (b) Combined plot of static adsorption and concentration loss vs. time for sample FP3630 S. (NB): Adsorption reached a maximum within approximately 1 day and then levelled off; suggesting an imperfect monolayer-type of instantaneous adsorption.

Figure 7.10 compares static (or batch) adsorption result for both polymer samples FP3630 S and FP3330 S on 40/60 silica sand. As the Figure shows, the static adsorption capacity of the sand appears to be high for both samples, reducing the initial concentration value of 200ppm to about 180 ppm for FP3330 S and to about 172 ppm for FP3630 S. Also, the batch adsorption in the silica sand increases with increase in the molecular weight, although the effect is not large. Though, not always the case, similar results have been reported previously for dynamic adsorption on silica sand (Lakatos et al. 1981, 1999, 2000).



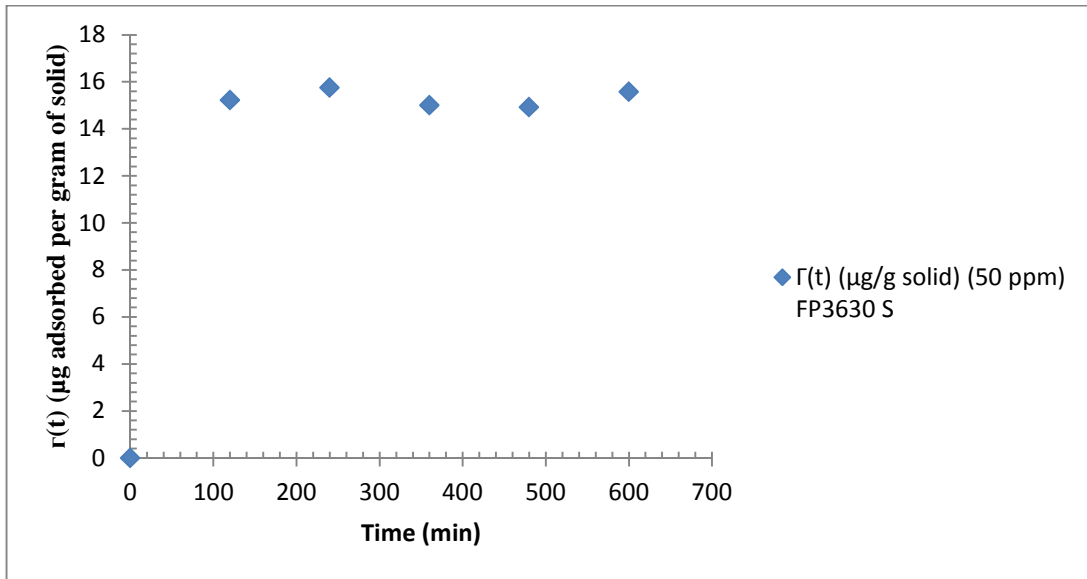
(a)



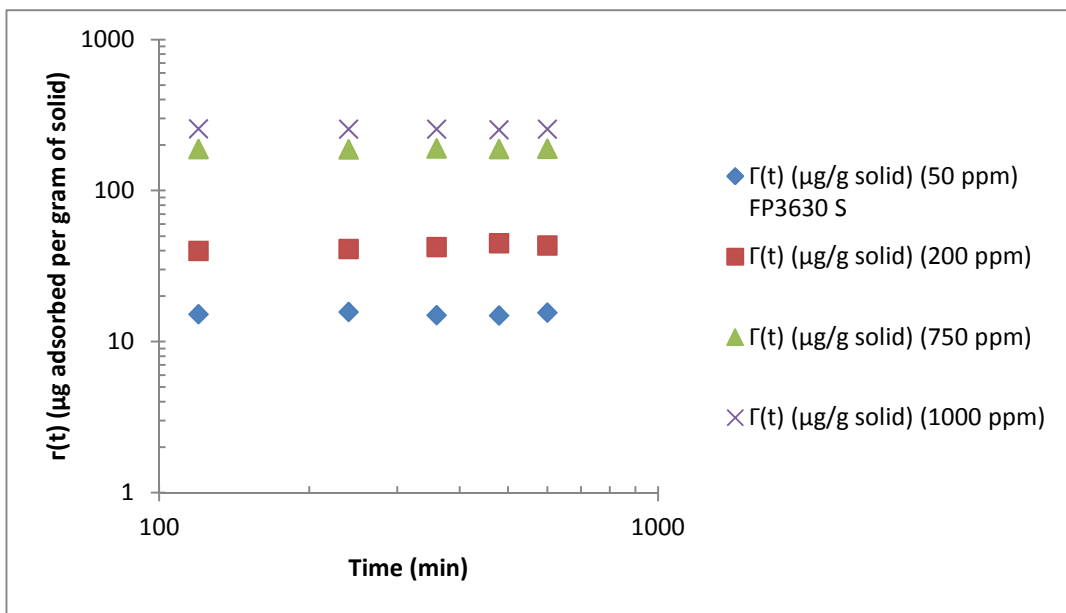
(b)

Figure 7.10 - Comparison of (a) adsorbed and (b) concentration loss for static (batch) adsorption experiments for FP3630 S and FP3330 S on silica sand. Molecular weight: curve: (A) 8 million, (B) 20 million Dalton.

For the 50 ppm FP3630 S HPAM, Figure 7.11 shows that adsorption also reached its maximum (approximately 15 µg/g) before 2 hours after which it levels off. This also indicates an instantaneous adsorption on the sand surface.



(a)



(b)

Figure 7.11 - Polymer adsorption kinetics on silica sand for FP3630 S: (a) 50 ppm, (b) all concentrations.

Table 7.1 and Figure 7.11 shows the calculated (using mass balance) residual polymer adsorption ($\mu\text{g/g}$) for the 50, 200, 750 and 1000 ppm FP3630 S HPAM during the desorption test. From these calculations, the percentage of reversible adsorption for the selected cases was 5.33, 3.6, 1.34 and 1.47% respectively. Similar results have been obtained by

(Szabo, 1975b; Deng et al., 2006; Manichand and Seright, 2014). From the results, the amounts of reversible adsorption for the 3 cases are quite small. These results seem to suggest that polymer adsorption on sand surfaces could be seen as an almost irreversible phenomenon (Figure 7.12). Specifically, since the extended chain from high molecular weight EOR polymers have the tendency to attach to different polar points on the rock surface, it is therefore statistically improbable for a polymer molecule to let go of all points of attachments simultaneously; hence the low desorption level observed in these cases (Figure 7.12). Figure 7.12b compares the Langmuir conditions for the initial and residual adsorption cases after rinsing in 3.0% TDS1 brine in desorption test.

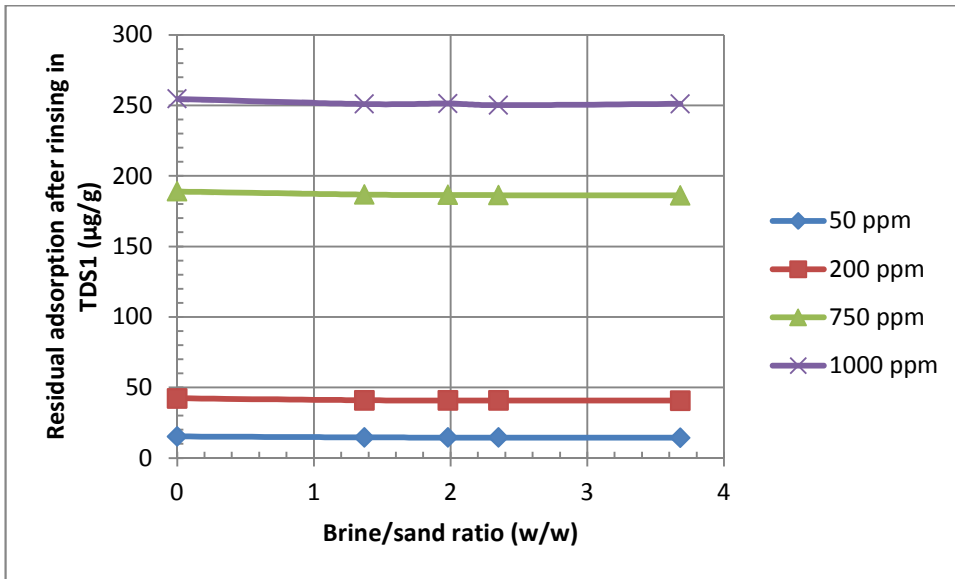
Figure 7.13 shows the results of the readsorption test. The data of Figure 7.13 indicate that just little amount of polymer was readsorbed unto the surface of the already used sands. Specifically, adsorption increased by about 23.13% for the 50 ppm concentration case (rising from 15.29 to 19.89 $\mu\text{g/g}$); and by about 14.02% for the 200 ppm case (i.e. from 46.0 to 53.5 $\mu\text{g/g}$). Furthermore, the Figure reveals that the difference between the adsorption at 750 ppm (188.93 $\mu\text{g/g}$) and the used sands is substantial. The plausible explanation for this difference is that the low-concentration polymer molecules had already fully covered the sand surface such that even when the 750ppm concentration was later added, there were no vacant sites readily available for further attachments of polymer molecules. From the point of view of field operations, it could therefore be reasonable to first inject a low-concentration polymer solution bank in order to reduce polymer retention and thereby maximise use of chemicals.

The data of Figure 7.14 illustrates FP3630 S HPAM polymer adsorption as a function of equilibrium polymer concentration for static measurements. The Figure shows a near constant adsorption at the low-concentration region (roughly between 50 and 100 ppm); then adsorption increases at the mid-concentration region (around 150 to a little above 750 ppm); and finally begin to stabilize at the higher-concentration region more than

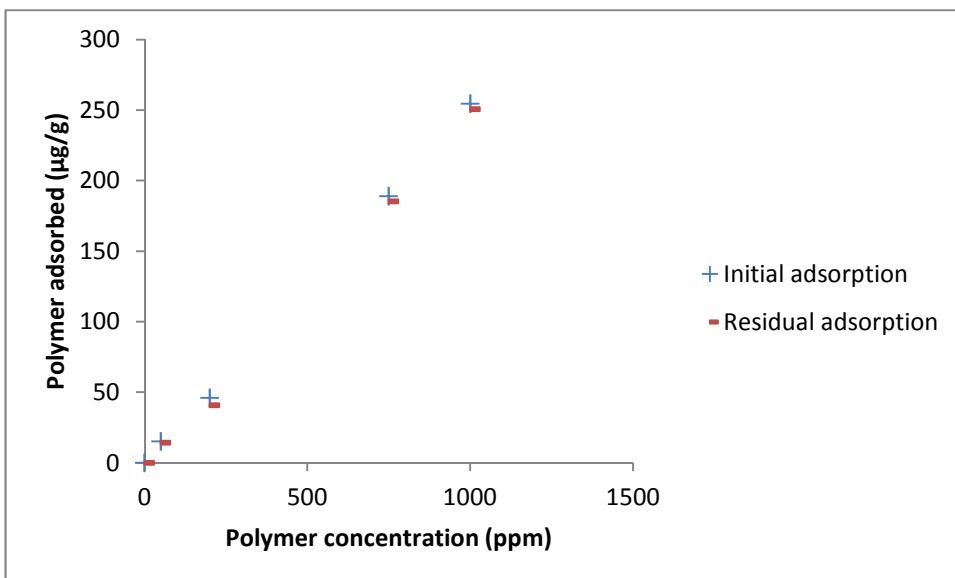
1000ppm. This concentration-related adsorption as observed in this study is in agreement with some previous studies (Seright et al., 2011; Stutzmann and Siffert, 1977; Green and Willhite, 1998; Mungan, 1969) and seems to support the fact that polymer adsorption does not obey the Langmuir law; it is worth noting that Langmuir isotherm finds common application in describing the reversible adsorption of small molecules of surfactants and gas, etc and assumes that polymer retention proceeds towards zero and is reversible). According to these authors, as the polymer molecules continue to adsorb at very low concentration, there is a limiting occupation value of the sites, beyond which a destabilization of the negatively charged colloids by the polyanions take place. When this maximum coverage is reached, only few adsorbed molecules are possibly released or detached from the surface; hence, the low concentration adsorption of polymer proceeds towards a constant nonzero value different from that described by Langmuir isotherm (Figure 7.12b).

Table 7.1 - Residual adsorption for FP3630 S HPAM after rinsing in 3.0% TDS1 brine in desorption test.

Concentration	50 ppm	200 ppm	750 ppm	1000 ppm
<i>Initial adsorption</i>	15.29	42.32	188.93	254.60
Repeat Run	Residual adsorption (µg/g)			
Run 1	14.62	40.94	187.70	250.90
Run 2	14.50	40.78	187.46	251.32
Run 3	14.46	40.74	187.31	250.12
Run 4	14.32	40.69	187.15	251.05
<i>Run average</i>	14.32	40.79	186.41	250.85
<i>% difference</i>	5.33	3.6	1.34	1.47



(a)



(b)

Figure 7.12 – (a) Desorption kinetics for FP3630 S HPAM after rinsing in 3.0% TDS1 brine, (b) Langmuir condition comparison for the initial and residual adsorption cases after rinsing in 3.0% TDS1 brine in desorption test. After rinsing in brine (-), residual adsorption did not match up with the initial (+). Because the extended chain from high Mw polymers have the tendency to attach to different polar points on the rock surface, it is therefore statistically improbable for a polymer molecule to let go of all points of attachments simultaneously and proceeds towards total reversibility as proposed by Langmuir.

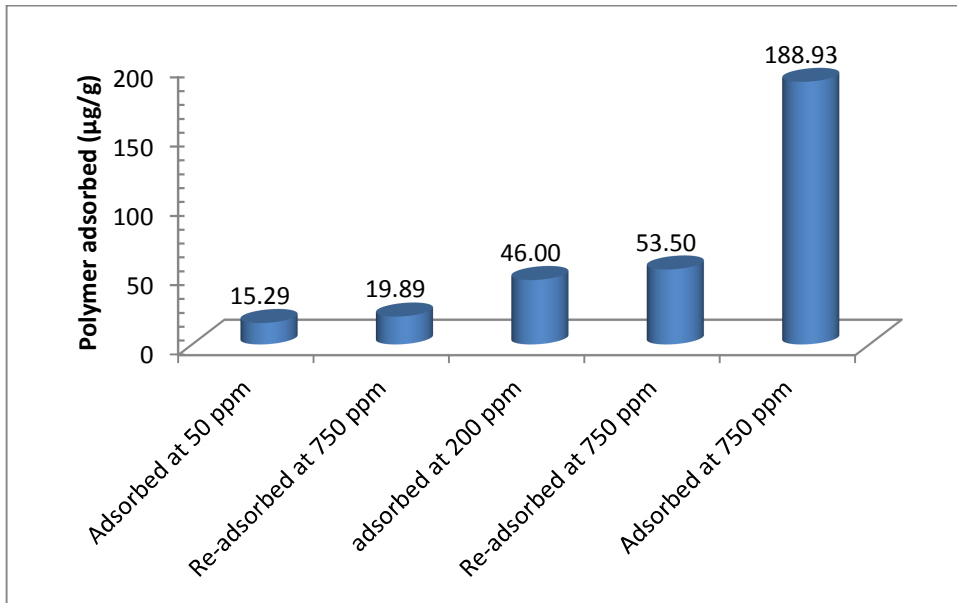


Figure 7.13 - Readsorption test on used and fresh sands.

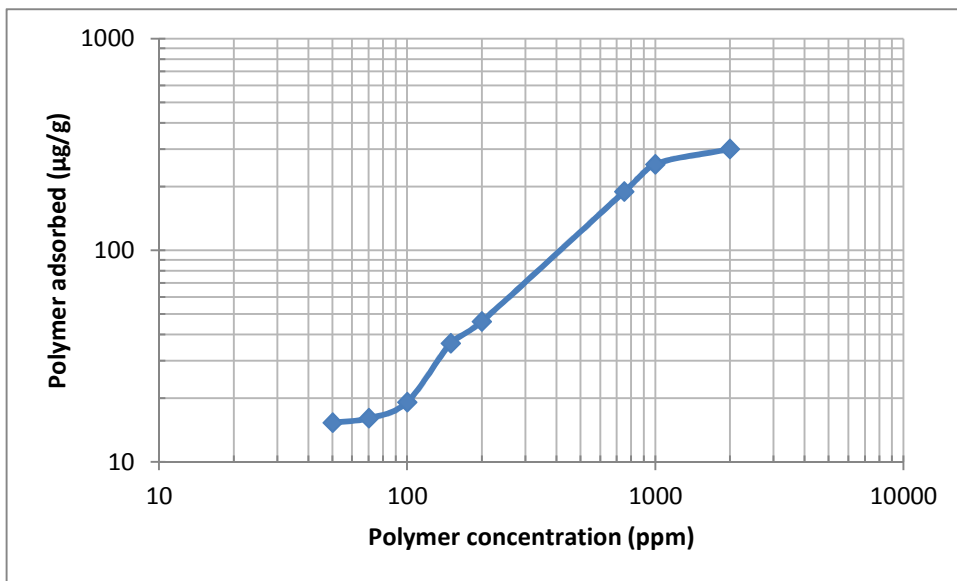


Figure 7.14 - Static adsorption isotherm of FP3630 S HPAM in silica sand.

7.5 Polymer Dynamic (or flow) retention experiments

Polymer retention and IAPV (inaccessible pore volume) are the two components that govern polymer propagation through porous media in the dynamic mode. While polymer retention retards polymer propagation in rocks, IAPV (the porosity into which the polymer does not penetrate)

accelerates it relative to the rate of solvent propagation; because large molecules of polymer cannot go through all pore space that is available to the small molecules such as solvents, salts/ions, or tracers (Dawson and Lantz, 1972). In the literature, several methods have been proposed to measure polymer retention/adsorption and IAPV in the dynamic or flow condition. Dynamic polymer retention measurements involve the injection of polymer solution into a porous medium at constant (preferably low) flow rates and measuring polymer-concentration in core effluent. This residual retention is best measured by injecting a polymer slug, followed by brine until no polymer is detected in the effluent, and then performing a mass balance on the polymer (Dawson and Lantz, 1972; Szabo 1975, 1979; Dominguez and Willhite, 1977; Castagno et al., 1987; API RP 63, 1990; Huh et al., 1990; Mezzomo et al., 2002; Manichand and Seright, 2014). It is however believed that this method has key shortcomings in that polymer recovery may require prolonged period of brine injection due to the unfavourable displacement; and the cumulative errors associated with measurements of low-concentrations in the produced fluid can introduce considerable uncertainty to the mass balance (Manichand and Seright, 2014).

In the double-polymer/tracer-bank method proposed by Dawson and Lantz (1972), Lotsch et al. (1985), Hughes et al. (1990), Osterloh and Law (1998) and used recently by Manichand and Seright (2014), two equal and identical banks of polymer solution are injected at the same flow rate into a sandpack or core with a tracer (chemical species which does not interact chemically or physically with the porous material) and separated by large volumes of brine flushing. The effluent concentration profiles (usually normalised to the input concentration) is the key measurement that is normally made in this type of experiment. The plot of the two effluent polymer-concentration profiles vs. pore volume (PV) injected are then used to determine the amount of polymer retained (in $\mu\text{g/g}$ of rock). In other words, polymer retention is calculated by subtracting the PV-concentration difference associated with the first polymer bank from that associated with the second polymer bank (i.e.,

the difference in breakout curves when polymer was displacing brine). As suggested by Dawson and Lantz (1972), this method also yields the IAPV for a particular set of conditions, whereas the others do not (Figure 7.15). Retention can also be measured in the laboratory from the shift of the 50% value at the front or leading edge (Figure 7.16) as suggested by Dominguez and Willhite (1977).

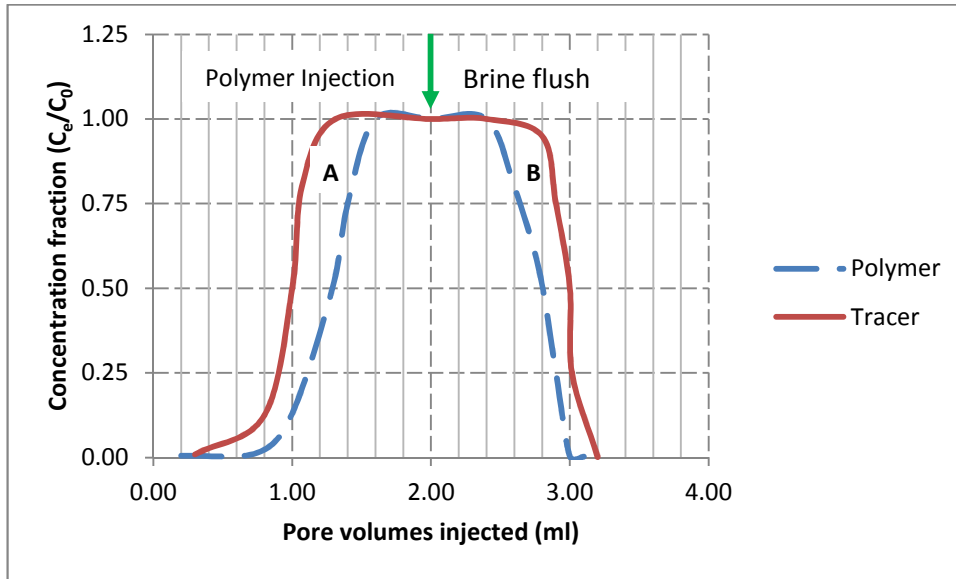


Figure 7.15 - Laboratory area method for polymer adsorption and IAPV measurements as suggested by Dawson and Lantz (1972). NB: For this illustration, adsorption is the sum of areas A and B.

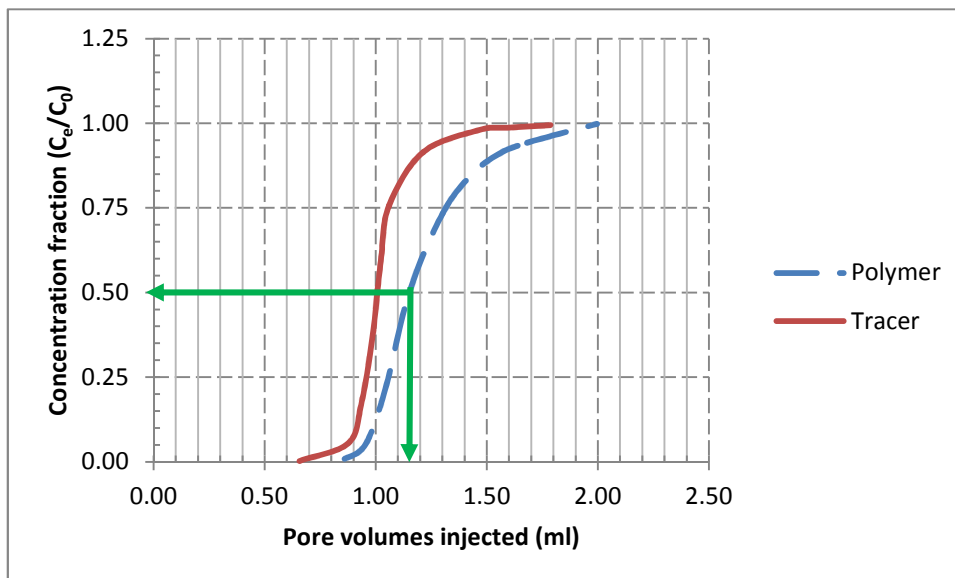


Figure 7.16 - Laboratory mid-point method for measurements of polymer adsorption as suggested by Dominguez and Willhite (1977).

The principle of this method is that the period of extended brine flush should rinse any reversibly retained polymer from the core or sandpack; and if this retention reoccurred during the following or second polymer flood, then the second effluent concentration profile will move closer to the first one (i.e., shift to the right). In this way, only irreversible retention is measured by means of this dynamic method while reversible retention is excluded. Although the method is presumably the most rigorous in determining the polymer loss, it is also the most time-consuming and probably requires the most analyses. However, compared with the mass balance, this double-polymer/tracer-bank method currently presents the most reliable method for polymer retention determination. In this research both methods were adopted.

However, in order to determine concentration in flow effluents (in the mass balance method), the turbidity developed at a certain time was measured in a spectrophotometer at a wavelength that provided the best correlation coefficient for the calibration curve (Foshee et al., 1976). For predictions of polymer flooding in numerical simulators, an adsorption curve (i.e. the amount of equilibrium polymer adsorbed as a function of aqueous phase concentration for a constant temperature - Langmuirian isotherm) is usually an input parameter among others (Shiyi et al., 2000; Dang et al., 2011, 2014). The Langmuirian isotherm is given by Eqn. (7.2). However, the above experimental results and data seem to suggest that the Langmuir law does not properly depict polymer retention.

$$C_{ads} = Ad_{max} \cdot \frac{k_1 \cdot C_p}{1 + k_1 \cdot C_p} \quad (7.2)$$

Where,

C_{ads} = equilibrium adsorbed for a particular concentration

Ad_{max} = theoretical maximum adsorption capacity for the system

k_1 = adjustable equilibrium or affinity constant for adsorption

C_p = bulk aqueous phase concentration at equilibrium.

7.5.1 Dynamic Retention Experiments in Sandpacks and Soft Clashach Cores

In this section, series of tests were designed and performed (each on fresh soft clashach cores or commercial sandpacks grade 40/60 and 20/40 for different HPAM concentration respectively) to study the effect of different variable factors (e.g. permeability/pore size distributions, surface area, concentration, pH, salinity, flowrate, IAPV, etc) on polymer retention. The various polymer dynamic experiments are sequentially discussed starting with an overview of the procedures.

Table 7.2 - Dynamic polymer retention in sandpacks. For this particular sand, a pre-calculated injection rate of 1.0 ml/min that will induce shear rates of about 10-100 s⁻¹ that are comparable to field applications was used.

Sandpack ID(mesh)	Length (cm)	Dia. (cm)	Area (cm ²)	Sand wt. (g)	Perm. (mD)	Porosity (fraction)	Pore vol. (cm ³)	Polymer Conc. (ppm)	Retained (µg/g solid)
40/60	2.28	4.40	15.21	57.55	147	0.372	12.96	50	5.47
								70	6.33
								100	6.88
								150	8.14
								200	11.72
								750	19.40
								1000	20.09
20/40	2.28	4.40	15.21	57.60	348.8	0.373	12.93	300	^e
								500	^f

7.5.2 Experiment A2: Polymer Dynamic Retention in Sandpacks: Effect of Concentration

In order to be able to quantify retention differences in flow and static conditions, dynamic measurements were conducted in sandpacks using

^e This part was used to study the the effect of high salinity on polymer retention. The results are discussed in sections 7.9 and 7.9.1

^f This part was used to study the the effect of flow rate and inaccessible pore volume (IAPV) on polymer retention. The results are discussed in sections 7.7.2 and 7.7.3

the same sand source (Table 7.2) that was used in the static measurements. Fresh sand was also used for each concentration case. The previously described brine (3.0% TDS1) and polymer (SNF Flopaam 3630 S HPAM) were used. Table 7.2 shows the range of solution concentrations investigated using an injection rate of 1.0 ml/min. The equipment of Figure 6.10 was used.

7.5.2.1 Polymer injection procedure

The following polymer injection procedure was adopted:

- a) Polymer solutions were prepared in concentrations of 50-2000 ppm using sample FP3630 S.
- b) The pump was set to scheduled rate as planned for the polymer injection.
- c) Brine was injected until pressure stabilized (determination of brine permeability, k_b).
- d) Polymer solution was injected at controlled constant flow rate through the core until a steady pressure drop was obtained. At this point, sufficient volume of the polymer solution was flowed so that steady-state is attained. Failure to attain a stabilized pressure drop is indicative of plugging and polymer mobility data will be of questionable value.
- e) When pressure exceeded the limits of the low-pressure calibrated transducer, it was then switched to the higher calibrated pressure transducer.
- f) Effluent cuts were collected in graduated tubes and marked to record events of the fluid and rate changes that occurred during flow.
- g) Pump rates were changed for other injection velocities (as and when required), and polymer injection was continued until pressure stabilized again; and data were collected and recorded for particular polymer concentration.
- h) Using the same pump rate as the final polymer injection rate, brine was again injected until pressures were stabilized and the presence of polymer was undetected. This was done to measure permeability to

brine after polymer injection (i.e. to determine the post-polymer flow permeability), also called the final or residual brine permeability.

- i) To obtain a retention isotherm, steps (b) to (h) were repeated for any increasing polymer concentrations.

7.5.3 Experiment B: Effect of flow-rate on polymer retention

The variation of polymer retention with flow rate has been investigated previously (Maerker, 1973; Dominguez and Willhite, 1977; Huh et al., 1990; Aubert and Tirrell, 1980). For example, using 100 to 300 mD Berea cores at residual oil saturation, Huh et al. (1990) showed that xanthan retention was only about 6% greater at 1 ft/d than at 0.333 ft/d. Using different xanthan solution in similar cores in a separate experiment, the same authors observed that the retained polymer was 40% more at 5 ft/d than at 1 ft/d. In a similar manner, Maerker (1973) showed evidences of xanthan retention in a 121 mD Berea core as the fluid velocity was increased and proposed that the higher pressure gradient resulting from the increased fluid velocity caused the deformation of the xanthan molecules and got trapped within the core in relatively smaller pores. Maerker further argued that as flow reduces, the molecules relax to a random coil and then diffuse to larger pore channels, causing temporary increase in polymer concentration until the excess polymer is flushed from the core. This reversible occurrence has been described as hydrodynamic retention. However, Maerker (1973) and others did not determine the magnitude of this retention as function of flow rate.

In this section of the study, we performed two sets of experiments using two grades of HPAM (SNF Flopaam 3630 S and 3330 S). The first was done in order to compare the retention of the two different polymers on 20/40 silica sand (see sand property in [Table 7.2](#)). The second was conducted to quantify flow rate dependency of polymer retention using only FP3630 S HPAM. To study the flowrate-dependent retention for this experiment, the double-polymer/tracer-bank dynamic method proposed by Lotsch et al. (1985), Hughes et al. (1990), Osterloh and Law (1998)

and used recently by Manichand and Seright (2014) was adopted. 500 ppm of SNF Floerger FP3630 S HPAM polymer solution prepared in brine TDS3 was flowed through 40/60 sand. Sieve analysis was used to characterise the sand (see [Table 7.2](#)). The setup of [Figure 6.10](#) was used for this dynamic flow experiment. Specifically, the following procedure was followed:

- 1) 3.2% TDS3 brine was injected at fixed low rate of 0.8 ml/min until stabilisation. This sand conditioning step enables the achievement of stabilised baselines of viscosity and spectral absorbance for the effluent from the sandpacks.
- 2) About 2.5 PV of 500 ppm KI traced FP3630 S HPAM solution (in 3.2% TDS3 brine) was injected also at fixed low rate of 0.8 ml/min. This is the first low rate polymer injection cycle.
- 3) Subsequently, 130 ml (about 10 PV) of brine was injected to flush all non-adsorbed polymers from the core.
- 4) Then, step (2) was repeated (this is the second low rate polymer injection cycle).
- 5) Then step (3) was repeated.
- 6) When effluents concentration reached injected concentration, samples were periodically collected in small pore volume (PV) increments for polymer-concentration determination using the viscosity method by reading and converting capillary viscometer efflux times ([Figure 7.17](#)). Note: 1 PV in this case is 12.96 cm³.
- 7) Steps 1-6 were repeated for different slug sizes and concentrations.
- 8) Pressure drops during steps 3 and 5 were recorded and (if required) used to calculate residual resistance factor (RRF); by dividing the pressure drop at these stages by that measured in step 1.
- 9) Polymer retention was calculated by comparing polymer effluent curves in steps 2 and 4 (i.e., by plotting two effluent polymer-concentration profiles vs. pore volumes (PV) injected).

7.5.3.1 Method to detect flowrate-dependent retention

To study and quantify the influence of flowrate on retention, two banks of polymer solutions were injected each at a fixed high rate of 3 ml/min and 6 ml/min through the sand pack of similar properties as was used for the low rate retention determination. The same procedure as the low rate retention determination was followed. This double-polymer/tracer-bank dynamic method also allowed for the determination of IAPV due to rate variation.



Figure 7.17 – Picture showing measurement of effluent concentration by the Viscosity method using Capillary Viscometer. NB: temperature stability was taken as the most important precaution in the use of this method.

7.5.4 Experiment C: Measurement of inaccessible pore volume (IAPV)

Polymer retention and IAPV are the two components that govern polymer propagation through porous media. While polymer retention retards polymer propagation in rocks, IAPV (the porosity into which the polymer does not penetrate) accelerates it relative to the rate of solvent propagation; because large molecules of polymer cannot go through all pore space that is available to the small molecules such as solvents, salts/ions, or tracers (Dawson and Lantz, 1972). The authors showed that a 35% IAPV was experienced in 681 mD Berea sandstone with

xanthan; 24% IAPV in 2090 mD Bartlesville sandstone with HPAM; and 22% IAPV was experienced with Pusher 700 HPAM in 470 mD Berea core. Working with HPAM-2 in 11000 mD sandpacks Osterloh and Law (1998) observed an IAPV value of about 48%. They however acknowledged that they had difficulties in ascertaining IAPV values accurately. Also, Dabbous (1977) observed 19% IAPV in 761 mD Berea core with residual oil saturation (ROS) using Pusher 500 HPAM, and 17-37% IAPV in 49-61 mD Berea without ROS using the same Pusher 500 HPAM. A 35% IAPV was observed by Pancharoen et al. (2010) in 12600 mD sandpack with FP3630 S HPAM.

7.5.4.1 Mechanism of inaccessible pore volume (IAPV)

Several possible mechanisms have been proposed for the IAPV. The two most generally accepted include: 1.) total pore exclusion (Dawson and Lantz, 1972; Lotsch et al. 1985; Shah et al. 1978) and 2.) pore wall exclusion (Patton et al. 1971; Shah et al. 1978; Hoagland et al. 1984; Chauveteau et al. 1984; Kolodziej, 1988). IAPV can be envisaged as a size exclusion effect in which the polymer cannot enter the fraction of the pore space with pore throat radii smaller than the effective pore size of the polymer molecule. This is known as the total pore exclusion effect (Dawson and Lantz, 1972). Although the solvent and polymer both flow through the same accessible pores, the polymer does not flow along the same streamlines as the solvent. The solvent transport through the pore space can be described as a continuum phenomenon because their molecules are several orders of magnitude smaller than the size of a pore. As a result, solvent velocities redistribution occurs with a maximum value at the centre of the pore, and a zero velocity at the pore wall. On the other hand, the large size of the polymer molecule prohibits its centre from getting any closer to the pore wall than a distance equal to its effective radius. The result is an exclusion of the polymer molecules from the regions where the velocity is lowest. As the total volumetric flow rate is fixed, the polymer must move at a velocity that exceeds the mean velocity of the solvent. This is the pore wall exclusion effects (Hoagland et al. 1984).

From the above, and from the literature reported values of IAPV shown in [Table 7.3](#), one need to raise questions on why there are very high IAPV values reported for high permeability rocks! As the [Table 7.3](#) shows, a limited number of IAPV values have been reported in the literature. These reported IAPV variations may be partly due to experimental limitations and errors. Field polymer flood is designed on the assumption that IAPV is zero. This, of course, is a conservative approach. An IAPV to polymer flow exists in both sandstones and unconsolidated sands (Szabo, 1975). An inconsistent and unexplained behaviour on IAPV is revealed by the literature survey; it is therefore clear that more work is required to understand the phenomenon of IAPV. Specifically, the high values reported for IAPV in high-permeability rocks need more validation to be credible.

Table 7.3 - IAPV literature values.

Porous medium type	Perm., mD	Polymer	Salinity, % TDS	IAPV, %	Reference
Sandpack	147-349	FP3630 S HPAM	3.2	15-32 [†]	This work
Berea	90-120	Pusher700HPAM	0.05	0-4	Knight et al. (1974)
Berea	277	Pusher700HPAM	2	18.7-24*	Shah et al. (1978)
Berea	470	Pusher700HPAM	1-2	22	Dawson and Lantz (1972 (Dawson and Lantz 1972))
Bartlesville	2090	Pusher700HPAM	1-2	24	Dawson and Lantz (1972 (Dawson and Lantz 1972))
Reservoir sand	30-453	Pusher700HPAM	13.3	32-37	Vela et al. (1976)
Teflon	86	Pusher700HPAM	2	19	Dominguez & Willhite (1977)
Berea	49-61	Pusher500HPAM	1.2	17-37	Dabbos (1977)
Berea	761	Pusher500HPAM	1.2	19	Dabbos (1977)
Sandpack	12600	FP3630 S HPAM	-	35	Pancharoen et al. (2010)
Sandpack	2500-11000	HPAM	1.3	18-48	Osterloh and Law (1998)
Berea	681	Xanthan	1-2	35	Dawson and Lantz (1972 (Dawson and Lantz 1972))
Sandstone (10-12% clay)	300-2400	Xanthan	3-4	25-31 [§]	Hughes et al. (1990)
Berea	450-680	Xanthan	3	18-41	Gupta & Trushenski (1978)
Brent	157-253	Xanthan/Sclerog.	7.4	14-22	Fletcher et al. (1991)
Bentheim	1600-2000	Xanthan	9	10 [†]	Lotsch et al. (1985)
Bentheim	1600-2000	Scleroglucan	9	11 [†]	Lotsch et al. (1985)
Ballotini glass	1270	Scleroglucan	2	Appr. 20	Huang and Sorbie (1993)
Berea	300	Dextran	-	11	Liauh et al. (1979)
<p>* IAPV decreased from 24 to 18.7% when HPAM increased from 51.5 to 1,070 ppm [†]IAPV was 25% with no ROS and 29% with ROS [‡]IAPV was the same with/without 30% ROS [§]29-31% ROS; 25% with no ROS ^{††}IAPV decreased from 32 to 15% as flow rate increased from 0.8 to 6.0 ml/min</p>					

In this section of the research, flow measurements to estimate polymer retention and determine IAPV in porous media was performed using the double-polymer/tracer-bank dynamic method proposed by Lotsch et al. (1985), Hughes et al. (1990), Osterloh and Law (1998) and used recently

by Manichand and Seright (2014) as earlier described. This time, the polymer solution was injected with a tracer. Specifically, a bank of 300 ppm SNF Floerger FP3630 S HPAM polymer solution (prepared in 3.2% TDS3 brine) spiked with 40 ppm Potassium Iodide (KI) as tracers was injected into 40/60 sandpack or core (first polymer flood cycle). Substantial volumes of brine were injected to flush all mobile (non-adsorbed) polymers from the core after the effluent concentrations for both polymer and tracer reach the injected concentrations. Then, a second bank of polymer solution was injected with the tracer (second polymer flood cycle); and again flushed with high volume brine. Again effluents samples were periodically collected in pore volume (PV) increments for tracer concentration determination via Inductively Coupled Plasma Spectroscopy (ICP) (Figure 7.18); and for polymer-concentration determination by reading and converting capillary viscometer efflux times. Note: 1 PV in this case is 12.96 cm³. By comparing the tracer and polymer effluent curves during the second polymer flood cycle, the inaccessible pore volume (IAPV) was calculated.



Figure 7.18 - Optical Emission Spectrometer used for the detection of tracer concentration in effluent samples (ICP).

7.5.4.2 IAPV and Polymer Retention Calculations from Experimental Data

The difference in area between the polymer-breakout curve and the tracer-breakout curve during the first flood cycle gives a value for the polymer retained in $\mu\text{g/g}$ of solid (Eqn. 7.3) (Manichand and Seright (2014):

$$\Gamma_p = \left\{ \left[\sum \left[\left(C_p / C_{p0} \times \Delta PV \right) - \left(C_{tr} / C_{tr0} \times \Delta PV \right) \right] \right] + IAPV \right\} \times C_{p0} \times PV / M_{rock} \quad (7.3)$$

While the difference in area between the polymer-breakout curve and the tracer-breakout curve during the second flood cycle is used to determine IAPV in fractions (Eqn. 7.4) (Manichand and Seright (2014):

$$IAPV = \sum \left[\left(C_p / C_{p0} \times \Delta PV \right) - \left(C_{tr} / C_{tr0} \times \Delta PV \right) \right] \quad (7.4)$$

Where, Γ_p = polymer retained, C_p = concentration of polymer effluent, C_{p0} = injected-polymer concentration, C_{tr} = effluent tracer concentration, C_{tr0} = injected-tracer concentration, PV = the volume in 1 pore volume (PV), ΔPV = PV increment (i.e., the volume of each produced fraction of relative concentration, C_e/C_0), and M_{rock} = the mass of rock in the core (g).

Note however that, the use of Eqn. (7.3) requires the IAPV to be known and corrected for adsorption *a priori*; this usually, is not the case.

7.5.5 Experiment D: Effect of salinity and polymer type on polymer retention.

In the literature, only a limited study (Chiappa et al. 1999; Martin et al., 1983; Mungan, 1969) has shown polymer retention to depend on salinity. Therefore, not much is known on how the polymer type, particularly in the presence of brine impact formation damage. For example, using salinity between 0 and 13% KCl for cationic polyacrylamide (PAM) and with (8%) and without (0%) CaCl_2 in brine for anionic HPAM, weakly

anionic PAM on quartzite porous media in static adsorption experiments, Chiappa et al. (1999) found that adsorption on quartzite increased from about 60 $\mu\text{g/g}$ without CaCl_2 to about 750 $\mu\text{g/g}$ with 8% CaCl_2 in brine; while the cationic PAM was almost independent of both salinity and CaCl_2 content. They explained the behaviour by proposing calcium bridging from the anionic rock to the anionic polymer. Martin et al. (1983) observed retention values of 25.1 $\mu\text{g/g}$ in 2% NaCl and 15.5 $\mu\text{g/g}$ in 0.1% NaCl in their study of several HPAM retention in Berea sandstones. These various authors, however, did not model these retention behaviours. Furthermore, Mungan (1969) did not observe any significant difference of HPAM retention in fresh water when compared with results obtained using 2% TDS NaCl. Remarkably, Martin et al. (1983) and Mungan (1969) studies were conducted independently with Dow Pusher 500 and 700 HPAMs in 2% NaCl solution. However, rather surprisingly, Martin et al. (1983) retention values were about 10 times lesser than those of Mungan's (1969) values; this probably indicates differences in experimental procedures and techniques. Therefore a deeper understanding of the polymer-rock-brine interactions is required in order to model the specific impact of polymers on formation damage in the presence of brines.

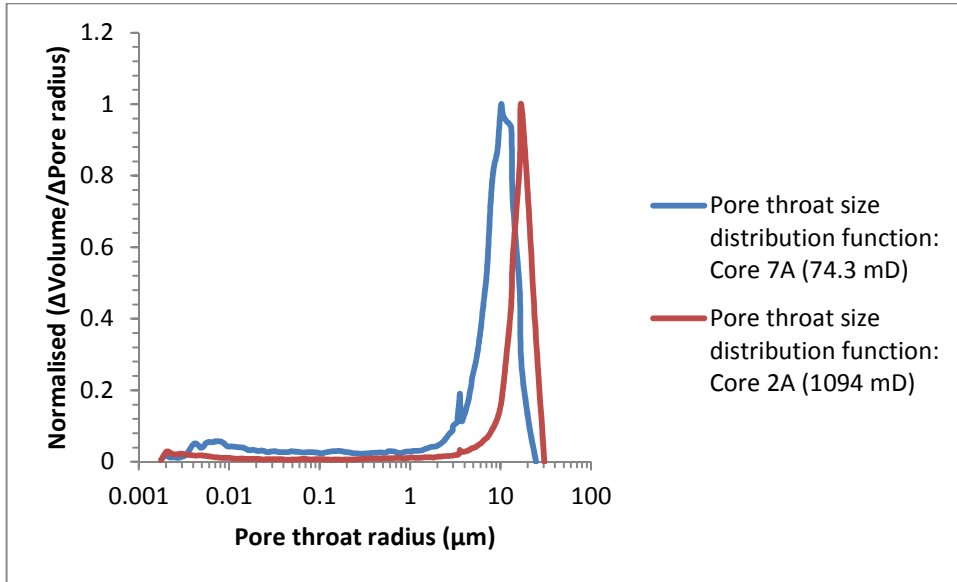
In this section, experiments to investigate the role of electrostatic interaction in the adsorption of molecules of polymers on rock surfaces were conducted. Specifically, two different polymer types were dissolved in brines of different composition and ionic strength and tested on pure silica quartzite following the procedures earlier described. The polymers were prepared in brines containing 0.043% Ca^{2+} TDS1 and 0.69% Ca^{2+} TDS1 respectively.

7.6 Polymer dynamic (flow) adsorption experiment with Clashach Cores

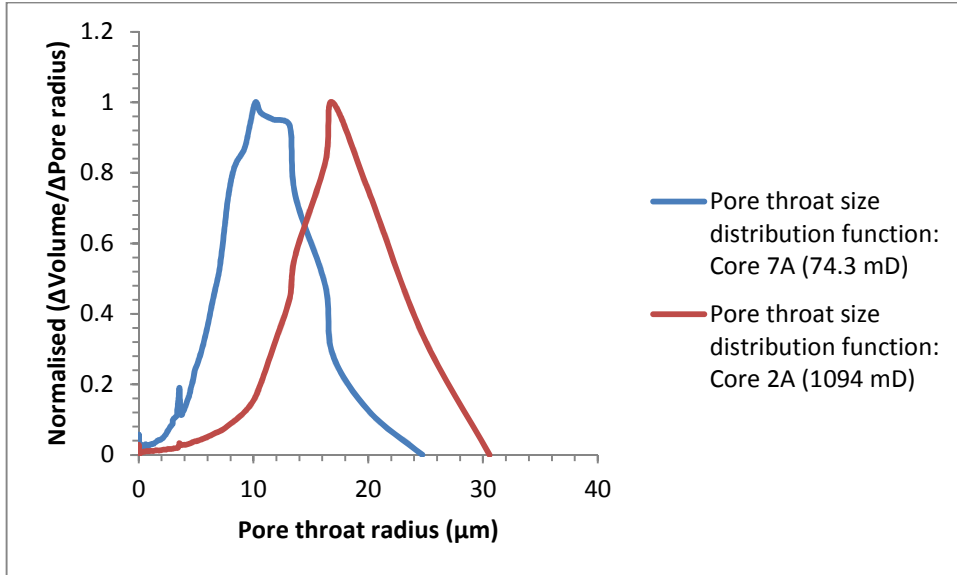
7.6.1 Experiment E: Effect of permeability and pore size distributions

Just as it is believed (Smith, 1970) that larger polymer units are more effective than those of smaller units, it also appears reasonable to conclude that polymer solutions will have some adverse effect in porous media with small pore openings compared with those having large pore openings. The capillary pressure required to force the entry of a non-wetting phase is inversely proportional to the size of the tubes of a bundle of equal-diameter capillary tubes (Smith, 1970). A similar inverse proportionality is expected to apply to porous media. Therefore, as a preliminary study, capillary pressure experiments (details presented in appendix A) were run on two clashach core plugs having differing permeabilities (1094 mD and 74 mD) and near similar porosities (0.177 and 0.150) in order to determine the effect of pore size on polymer retention/adsorption. [Figure 7.19](#) and [Figure 7.20](#) show the results of pore throat sizes and normalised permeability distribution functions for both core samples. [Figure 7.19](#) shows the existence of two families of pore throat sizes around 0.01 and 10 μm for sample 7A, and around 0.003 and 20 μm for sample 2A; the figure also indicates that about 88% of the pore volume (PV) is in pores with a pore throat radius of less than 24 μm for sample 7A; while 96% of the pore volume (PV) is in pores with a pore throat radius of less than 30 μm for sample 2A. [Figure 7.20](#) shows that core sample 2A has wider permeability distributions. As expected, it was observed that for mercury displacing air from these plugs, the capillary pressures was higher for the core having smaller pore openings ([Figure 7.21](#)). [Figure 7.21](#) also shows that at any given mercury saturation the corresponding pore sizes are smaller for the low-permeability sample than for the larger. Based on Eqn. 6.11 and on the basis of experimental data, the dimensionless Leverett J-function (Leverett, 1941) was equally used to compare the measured capillary pressure curves ([Figure 7.22](#)). In [Figure 7.22](#), the J-function value where most of the saturation change occurs is close to 0.08 for both samples.

However, the wetting phase saturation appears to asymptote at about 0.0065 for core 7A, and at about 0.03 for core 2A; indicating that drainage is slower in core 7A than in 2A.

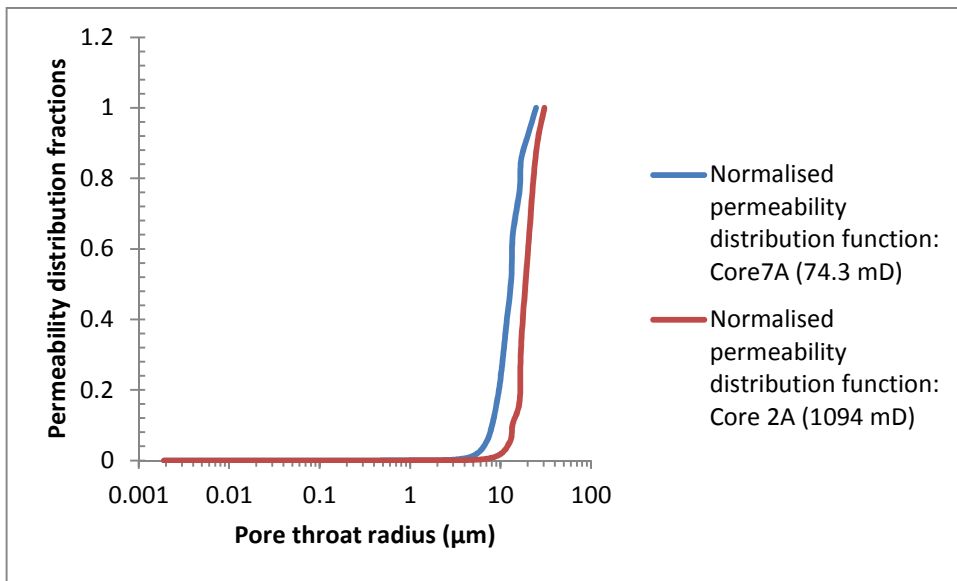


(a)

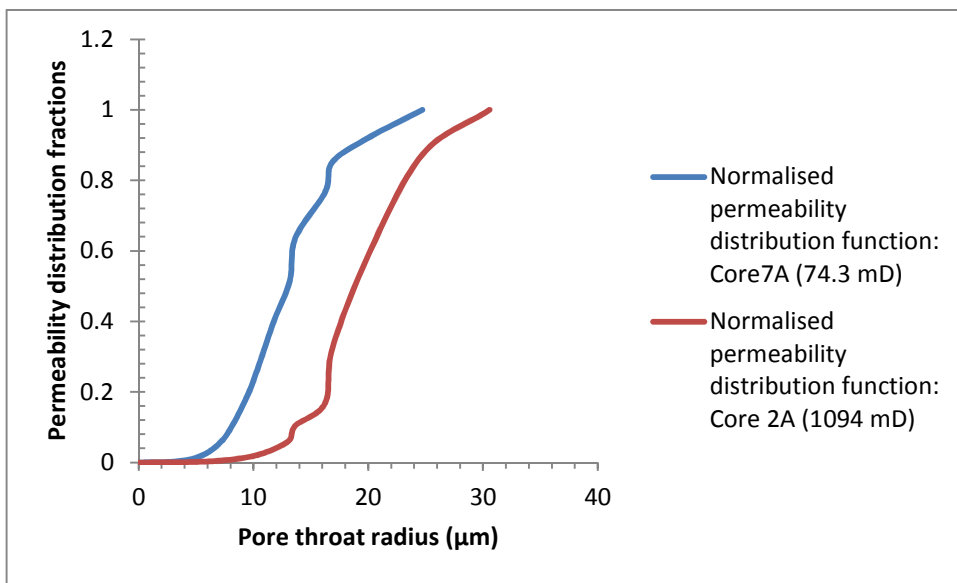


(b)

Figure 7.19 - Normalised pore throat size distribution functions from mercury injection on clashach core samples 7A and 2A: (a) Semi-log plot, (b) Cartesian plot.



(a)



(b)

Figure 7.20 - Normalised permeability distribution functions for clashach core samples 7A and 2A: (a) Semi-log plot, (b) Cartesian plot.

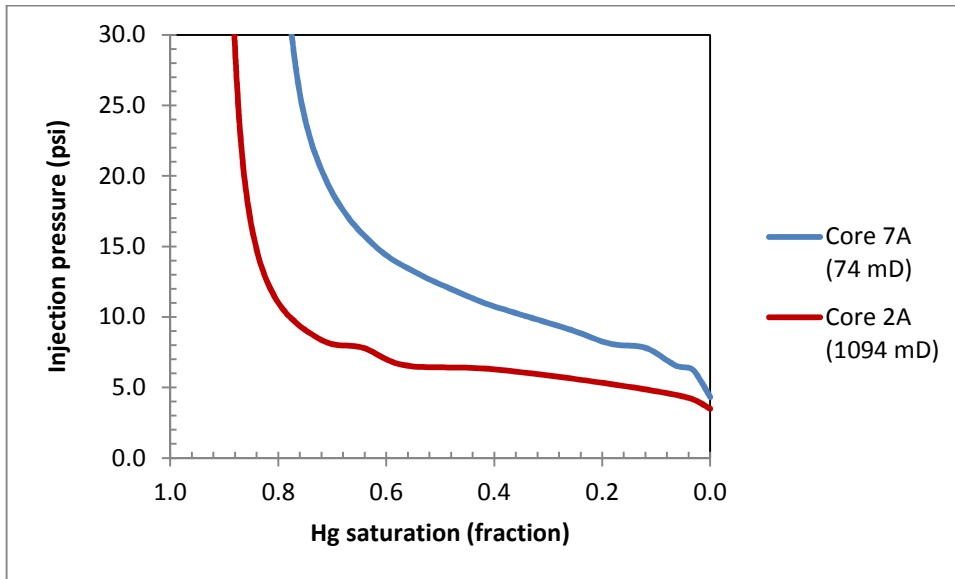


Figure 7.21 - Capillary pressure (P_c) curves from mercury injection on clashach core plugs. The more uniform the pore sizes, the flatter the transition zone of the P_c curve. Hence, core 2A has more uniform pore sizes.

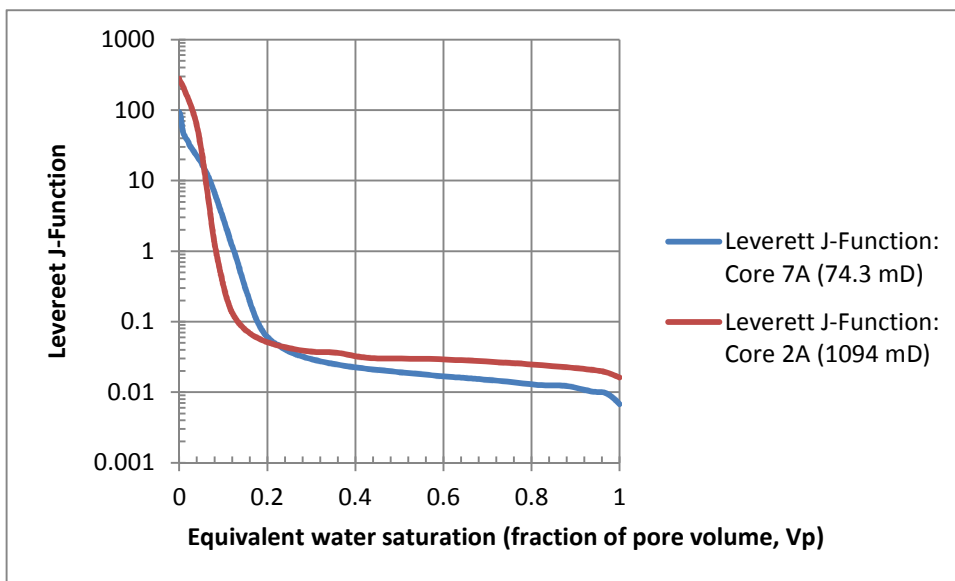


Figure 7.22 - Leverett J-Function for clashach cores 2A and 7A. The J-function is used to classify as to rock type. The two curves show that the samples 7A and 2A belong to the same rock type (i.e., quartz) and therefore, have geometric similarity. However, core 2A reflects much larger pore sizes as it has larger J-values.

7.6.2 Determination of mobility reductions and residual resistance factors

Pressure drops measured during flow experiments were then converted and used to define mobility reductions, R_m (or resistance factor), and permeability reductions, R_k (or residual resistance factor, RRF) versus

shear rate. The following expressions were used (Chauveteau et al., 2002; Ali and Barrufet, 2001; Zitha et al., 1995):

$$R_m = F_r = \frac{\Delta P_{pol}}{\Delta P_{w0}} \quad (7.5)$$

$$R_k = RRF = F_{rr} = \frac{(\Delta P/Q)_w}{(\Delta P/Q)_{w0}} \quad (7.6a)$$

If the injection rate is kept constant before and after the polymer treatment, then Eqn. 7.6a may be expressed as Eqn. 7.6b:

$$R_k = RRF = F_{rr} = \frac{\Delta P_w}{\Delta P_{w0}} \quad (7.6b)$$

Where,

ΔP_{pol} = pressure drop during polymer solution flow (at flow rate Q_s).

ΔP_{w0} = pressure drop during brine flow before polymer injection (at Q_s).

ΔP_w = pressure drop during brine flow after polymer (at flow rate, Q_s).

The frontal velocities (cm/s) associated with these mobilities was computed using Eqn. (7.7):

$$v = \frac{q}{A\phi} \quad (7.7)$$

Where, q = volumetric flow rate, cm^3/s ; A = core cross-sectional area, cm^2 ;

ϕ = original core porosity, fraction.

Permeability reduction (R_k) defines water mobility before and after polymer flow. It is used to describe reservoir permeability reduction after

polymer flooding. Mobility reduction (R_m) is a measure of the apparent dimensional viscosity during polymer solution flow through porous media.

The adsorbed layer thickness (ε_H) due to polymer flow was determined from the measurement of RRF (or R_k) using Eqn. 7.8; with the assumption that the hydrodynamic or effective pore radius (R_p) is reduced by an impenetrable polymer layer with thickness (ε_H) (Zitha et al., 1995):

$$\varepsilon_H (cm) = R_p (cm) (1 - R_k^{-0.25}) \quad (7.8)$$

The hydrodynamic or effective pore radius (R_p) is given by Eqn. 7.9:

$$R_p (cm) = \alpha_s \sqrt{\frac{8k_b (cm^2)}{\phi (fraction)}} \quad (7.9)$$

Where,

α_s = geometrical factor depending on the porous medium structure. This factor is close to 1.15 for packs of natural sands and SiC packs (Chauveteau et al; 2002); k_b = pack or core sample brine permeability; ϕ = pack or core sample porosity.

The in-situ rheological behaviour of non-Newtonian polymer fluid system is a function of shear rate. The following expression (Eqn. 7.10) relates the porous media physical characteristics and fluid velocity to the shear rates (API RP 63, 1990; Urbissinova et al., 2010; Christopher and Middleman, 1965; Gleasure, 1990; Jennings et al., 1971):

$$\dot{\gamma} = \frac{3n+1}{4n} * \frac{4\alpha Q}{A(8k\phi)^{0.5}} \quad (7.10)$$

Where, $\dot{\gamma}$ =porous media effective shear rate, 1/s; Q =flow rate, cm³/s; A =core cross-sectional area (cm²), α =shape parameter characteristic to account for the porous media structure (assumed as 2.5 for natural sand packs (Chauveteau, 1982; Chauveteau et al., 2002); k =formation permeability (cm²), ϕ =formation porosity (fraction), and $(3n+1)/4n$ =Rabinowitsch correction factor or the non-Newtonian correction for power-law fluids.

7.7 Results and Discussion of Dynamic Experiments

7.7.1 Experiments A2: Effect of concentration

The dynamic retention of FP3630 S HPAM in 40/60 commercial silica sand is shown in both [Table 7.4](#) and [Figure 7.23](#). The Figure shows that retention increases gradually with concentration. It was earlier stated that the same concentrations were used for both the static and dynamic measurements on same fresh sandpacks for each concentration case. [Table 7.4](#) shows that the amount retained for the static measurements are higher than for the dynamic case. This is understandable, because more desorption takes place during dynamic brine flushing. Another reason for the low dynamic retention values in [Table 7.4](#) as compared with the static measurement might, perhaps, be due to the fact that a fraction of the total pore volume was inaccessible to the flow of polymer solution in the very small pores of the 147-mD sand used in this case. Furthermore, the high surface-area rock resulting from disaggregated sand removes a substantial portion of the polymer from solution if this result were compared with retention in clashach cores. This result also shows concentration-related behaviour consistent with that of the static measurement as previously explained in the static result section; where adsorption shows a near constant at the low-concentration region; then increases at the mid-concentration region; and finally begins to stabilize at the higher-concentration region.

Table 7.4 - Comparison of Static and Dynamic Retention in Silica sand for FP 3630 S.

Conc. (ppm)	50	70	100	150	200	750	1000	2000	
Polymer retained ($\mu\text{g/g}$)	Static	15.29	16.05	19.11	36.30	46.0	188.93	254.6	300.40
	Dynamic	5.47	6.33	6.88	8.14	11.72	19.40	20.09	24.16

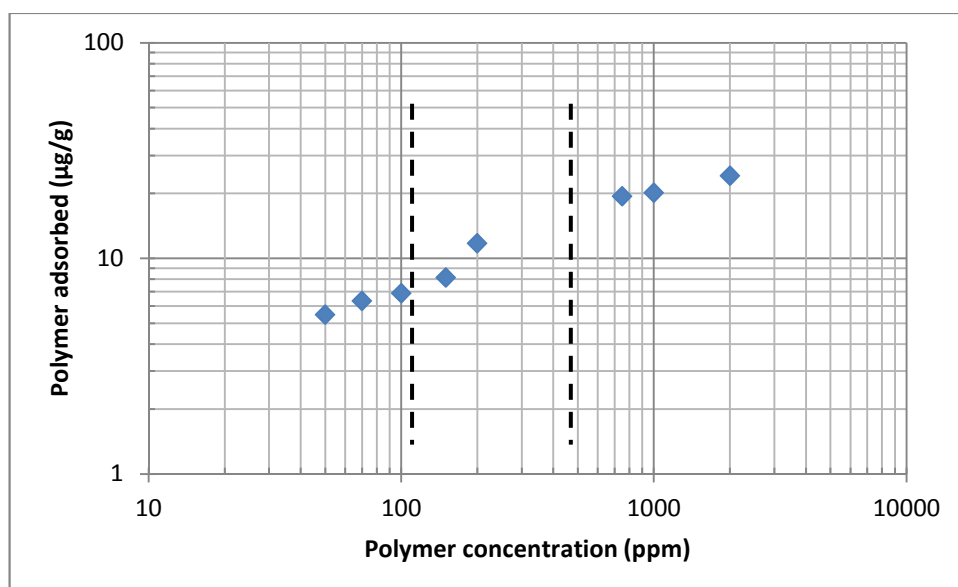


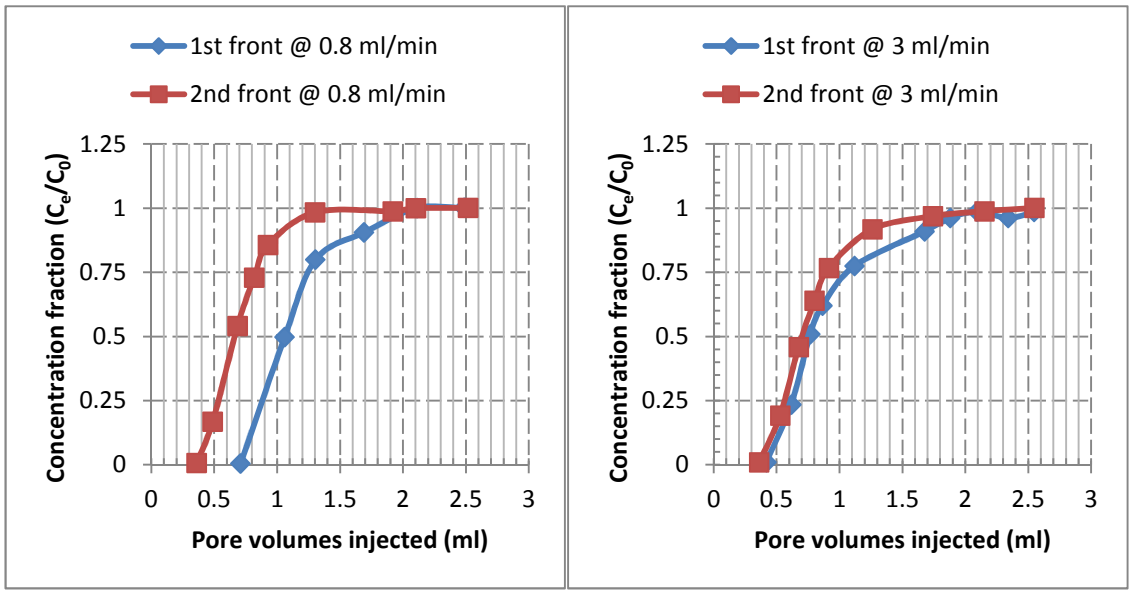
Figure 7.23 - Dynamic adsorption isotherm of FP3630 S HPAM in silica sand.

7.7.2 Experiment B: Effect of flow-rate on polymer retention

Figure 7.24 shows plot of the concentration profiles vs. pore volumes injected for a 500 ppm FP3630 S HPAM in 348 mD 20/40 sandpack using 3.2% TDS3 brine. The polymer injections were performed at 0.8 ml/min, 3.0 ml/min and 6.0 ml/min respectively. The breakout curves for both the low and higher rates injection cycles are plotted. Assuming the absence of all other sources of retention, the difference in area between

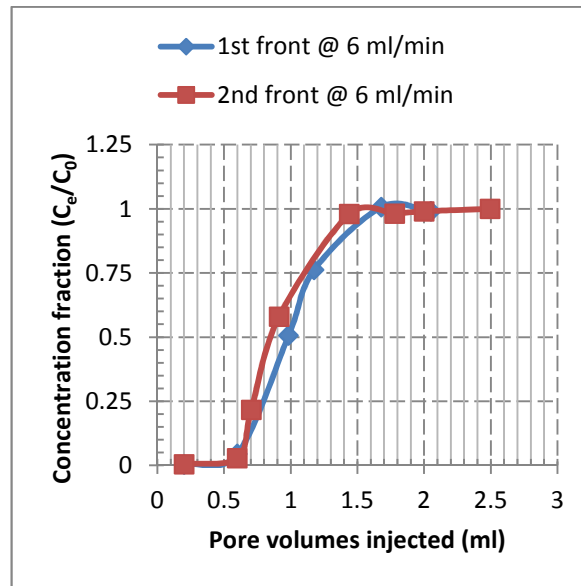
curves (or the difference in breakthrough between the two polymer fronts) during each of the low and high rate injections gives a measure of the amount of polymer retained. Any adsorption resulting from flow rate increase was then calculated from the difference between the 2nd breakout curve at the first low rate and the 1st breakout curve associated with the subsequent increased flow rates.

This method was used to quantify the effect of rate variation on retention in terms of reversible and irreversible total incremental retentions. To achieve this, retention was first measured at low rate of 0.8 ml/min by the method described above, where a value of 0.36 PV (27.32 µg/g) was observed. In order to determine flow-rate-induced retention, the same 500 ppm FP3630 S HPAM was again injected into the sand at higher rates of 3.0 ml/min and 6.0 ml/min respectively; and each slug was also separated by sufficient brine to rinse the “core” of all non-retained polymers after injection at the elevated rates. [Figure 7.25](#) shows the breakout curves for these cases.



(a)

(b)



(c)

Figure 7.24 - Rate-dependent retention behaviour of FP3630 S HPAM on silica sand: (a) during low rate injection cycle (0.8 ml/min), (b) during the first high rate injection cycle (3 ml/min), (c) during the next high rate injection cycle (6 ml/min).

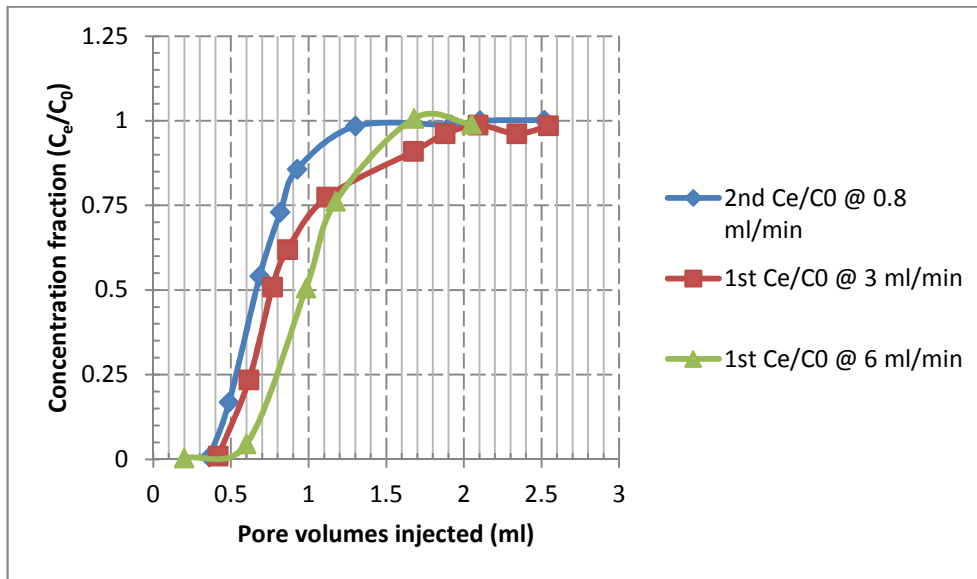


Figure 7.25 - Concentration profiles of 500 ppm FP3630 S at 0.8 ml/min, 3 ml/min and 6.0 ml/min.

Plot of the effluent profiles show that the area between the 2nd breakout curve at low rate and the 1st breakout curve at the subsequent higher rates was not zero (i.e., no overlap) (Figure 7.25). The total incremental retention induced by this rate variation was determined by the difference in polymer breakout between 2nd breakout curve at low rate (0.8 ml/min) and 1st breakout curves at subsequent higher injection rates (i.e., 3 and 6 ml/min). For these cases, the total incremental retention (reversible and irreversible) was observed to be 0.087 PV at 3 ml/min and 0.304 PV at 6 ml/min (Figure 7.25).

The incremental reversible retention was determined by the difference in breakouts between 2nd breakout curves at higher rates (3 and 6 ml/min) and 2nd breakout curve at low rate (0.8 ml/min); this gives 0.04 PV at 3 ml/min and 0.17 PV at 6 ml/min. The incremental irreversible retention was determined by the difference in breakouts between two polymer fronts at higher rates (3 and 6 ml/min); this gives 0.047 PV at 3 ml/min (Figure 7.24b) and 0.134 PV at 6 ml/min (Figure 7.24c). This result shows that during the first high rate injection stage at 3 ml/min the additional polymer retained was presumably desorbed; hence the incremental retention for this case was nearly all reversible. The next higher injection stage at 6 ml/min shows higher total incremental

retention. It is suspected that more brine flush could have driven this to lower value. [Figure 7.24a](#) shows that the viscous polymer reached the end of the core after about 1.059 PV during the first cycle of polymer injection and after about 0.68 PV during the second front at 0.8 ml/min. Assuming polymer adsorption and retention sites were supposed to be satisfied during the first injection front in this case; the front arrival of 0.68 PV during the 2nd stage indicates an IAPV of 0.32 (i.e., 1-0.68). By similar inferences, IAPV was calculated as 0.28 at 3 ml/min and 0.15 at 6 ml/min respectively ([Figure 7.24](#) through to [Figure 7.26](#)). These results probably indicate that IAPV decreases as flow rate increases; the consequence being the additional loss of polymer chemicals.

However, these results seem compatible with the permeability level and the quartzitic nature of the sand used for these cases. Overall, these experimental results show that retention of polymer was impacted by flow rate. For this set of experimental conditions, it was also observed that rate-dependency of polymer retention reveals that nearly half the total incremental retention was reversible. Although Maerker (1973) and Dominguez and Willhite (1977) obtained similar results, the method and results presented here gives better understanding of reversibility of retention. [Figure 7.27](#) shows effect of flow rate variation and polymer type on polymer adsorption.

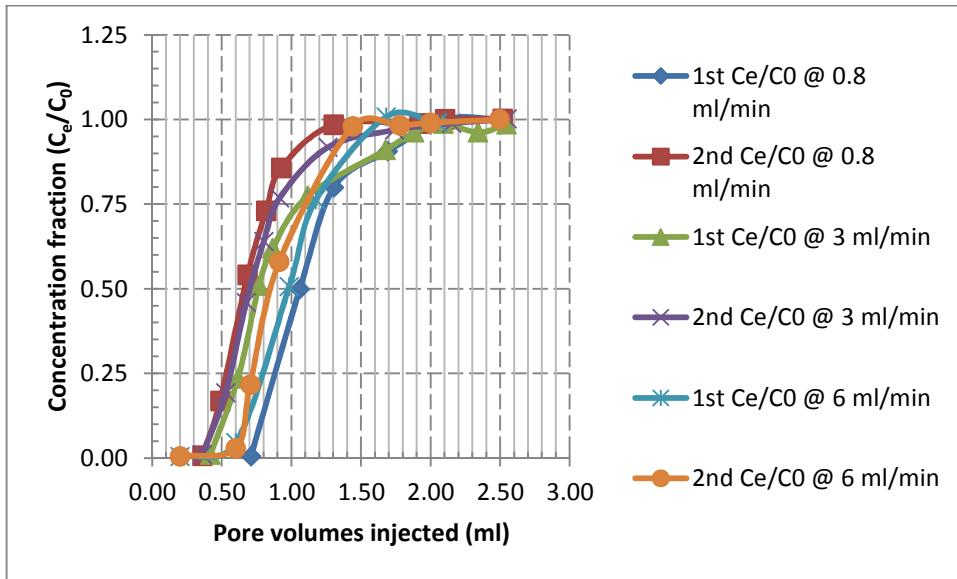


Figure 7.26 - Plot of concentration profiles of the dynamic method for the study of the effect of flow rate on polymer retention for all flow rates investigated.

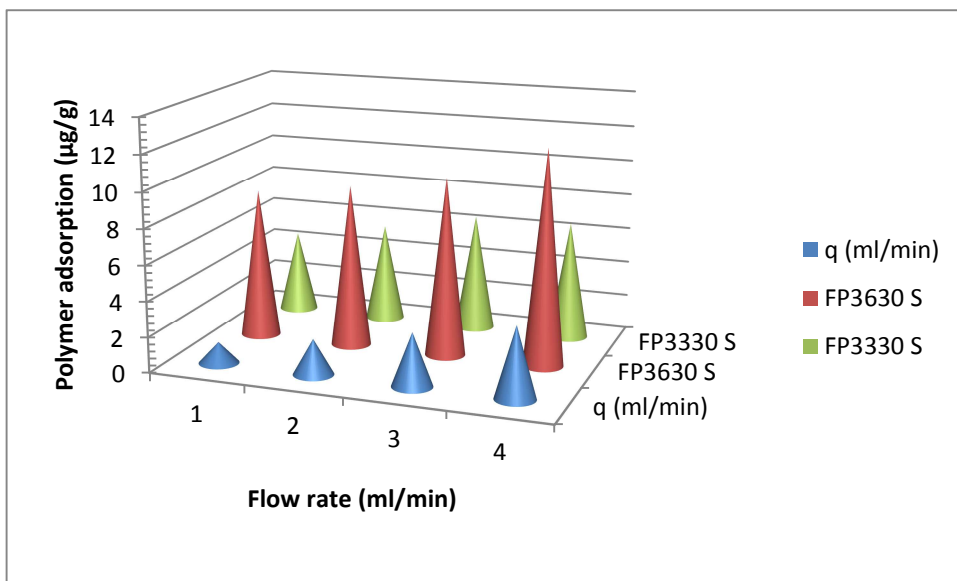


Figure 7.27 - Effect of flow rate variation and polymer type on polymer adsorption.

7.7.3 Experiment C: Effect of inaccessible pore volume (IAPV)

For this test, two banks or cycles of FP3630 S HPAM polymer solution traced with 40 ppm potassium iodide (KI) were injected into 20/40 sandpack. Figure 7.28 shows the plot of tracer and polymer effluents for the 1st and 2nd cycles respectively. The effluents concentrations were normalised to the injected values, and captured as function of injected pore volumes (time); thus, forming two concentration pulses. The

amount of polymer and tracer produced from the core is equal to the total area under each pulse. Therefore, because the tracer is non-adsorbing, the difference between the areas under separate pulses is a measure of the amount of polymer adsorbed. As previously stated, this method measures only the irreversible retention because desorption can occur during the post-polymer brine flush. However, two different performances are observed from the effluent analyses from the first and second polymer floods. Whereas the tracer leads the polymer in the first flood, the polymer leads the tracer in the second flood. The breakout curves shown in these figures reveal that the two fronts emerged at different times having passed through the core at different velocities.

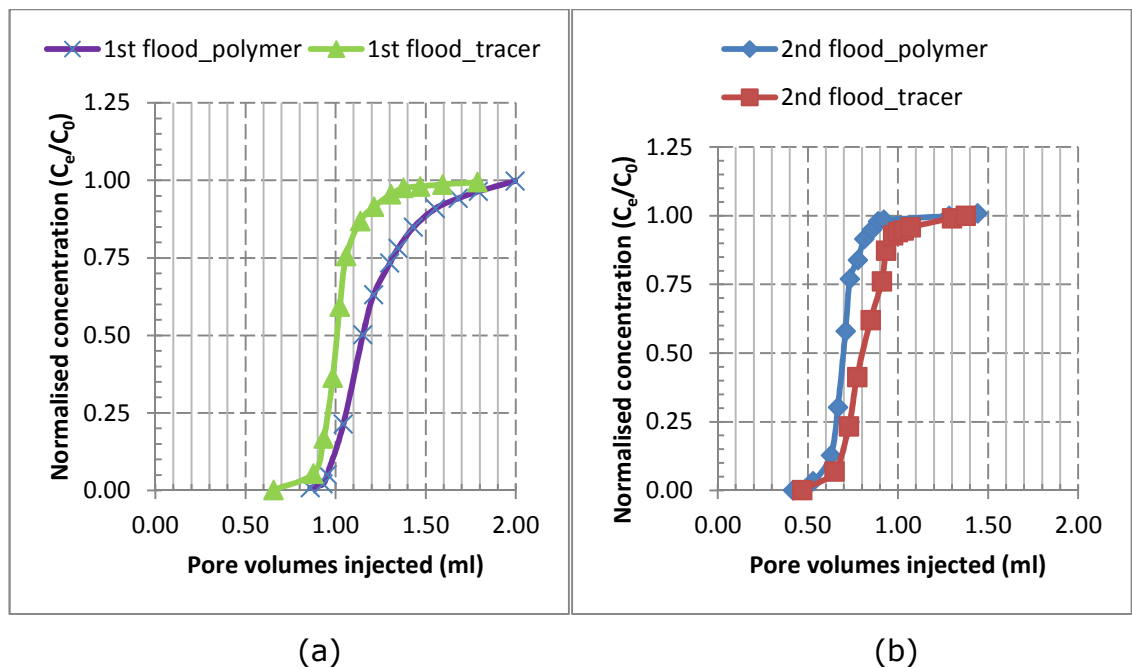


Figure 7.28 - Retention of FP3630 S HPAM in 20/40 sandpack at: (a) first injection, (b) second injection.

Because the rate of propagation of polymer is delayed by retention, Retention mechanism dominates during the 1st flood (Figure 7.28a). Hydrodynamic effect accelerates polymer propagation rate that may be demonstrated in terms of IAPV and this mechanism exercise control during the second flood (Figure 7.28b). The concentration profiles of the polymer effluents show steep characteristics from about 0.10 to 0.80, and thereafter developed moderately long tail that finally reached

$C_e/C_0=1.0$; except for the first polymer breakout curve which gently spread out of the first flood (after $C_e/C_0=0.5$) compared to the second one due to mass separations between polymer molecules and adsorption kinetics.

This tracer test method can be used to determine the ratio of polymer-to-solvent velocities during injections. In field predictions, IAPV has been said to have some beneficial effects in that the injected polymer response is quickly seen at the production wells (Dawson and Lantz, 1972); the argument being that the connate water bank and the polymer-depleted injection water preceding the water bank is reduced by the amount of IAPV. However, at higher rate of injection, the unswept region that is pre-dominated by brine can be penetrated by the polymer solution leading to a decrease in IAPV. This means that increase in flow rate may cause decrease in IAPV, which can also delay polymer propagation rate; resulting in an increase in polymer adsorption. This effect was discussed during the analysis under experiment B.

7.7.3.1 Retention and IAPV Calculation method

Adding tracer in the polymer solution allows adsorbed value to be corrected by the fraction of pore volume rendered inaccessible after polymer adsorption as earlier stated. Both retention and IAPV affected the polymer used for this study. As previously stated, the difference between the areas under separate pulses is a measure of the amount of polymer adsorbed; this method measures only the irreversible retention because desorption can occur during the post-polymer brine flush. For instance, [Figure 7.28a](#) shows that the polymer front reached the end of the core after a delay of about 1.15 PV injected during the first stage of polymer injection and after 0.69 PV during the second injection ([Figure 7.28b](#)). This delay is attributed to adsorption. The difference between these two fronts gives 0.46 PV. Similarly, the difference between the two tracer fronts is $1.0-0.79=0.21$ PV ([Figure 7.29](#)). Therefore, retention for this case is given by $0.46-0.21=0.25$ PV (or 17.88 $\mu\text{g/g}$) of sand. Furthermore, a little earlier polymer breakthrough with regard to the

tracer is observed during the 2nd flood cycle (Figure 7.29). The velocity ratio, R_{ps} (i.e., the ratio of polymer-to-solvent velocities) for this set of conditions was calculated from the experimental data as $R_{ps}=0.46/0.21=2.19$.

In Figure 7.28b, the polymer bank was observed to emerge early due to the presence of IAPV; shifting the breakout curve forward (i.e., to the right) by the amount of the missing pore volumes. On the basis of the tracer test, there are different possible means of computing the extent or magnitude of the IAPV (Shah et al., 1978; Dawson and Lantz, 1972; Gupta and Trushenski, 1978): (1) from the difference in area between the tracer and polymer curves during the second polymer injection cycle (Eqn. 7.4); i.e., measuring the pore volume difference between the trailing edges of the polymer and tracer effluent profiles at their 0.5 normalised concentration value. Again, due to viscous fingering or instabilities in the trailing edge profiles, this method is said to be highly uncertain (Kolodziej, 1988); (2) from the shift of the 50% value at the front or leading edge (i.e., from the difference between the pore volumes at which the 0.5 normalised polymer concentration and the 0.5 normalised tracer concentration would be detected in the effluent stream following a step change in concentration at the inlet). Knowledge of the pore volume fraction of adsorbed polymer is required to apply this method. (3) from the area between the two profiles at the front or leading edge; (4) from the area between the two profiles at the rear or trailing edge respectively. Using all the methods with a set of polymer effluent flooding data, (Shah et al., 1978) produced IAPV values where he reported notable differences between methods. Although he did not comment on which method would be preferred, he advised that a range of IAPV values could be specified at best for a set of conditions.

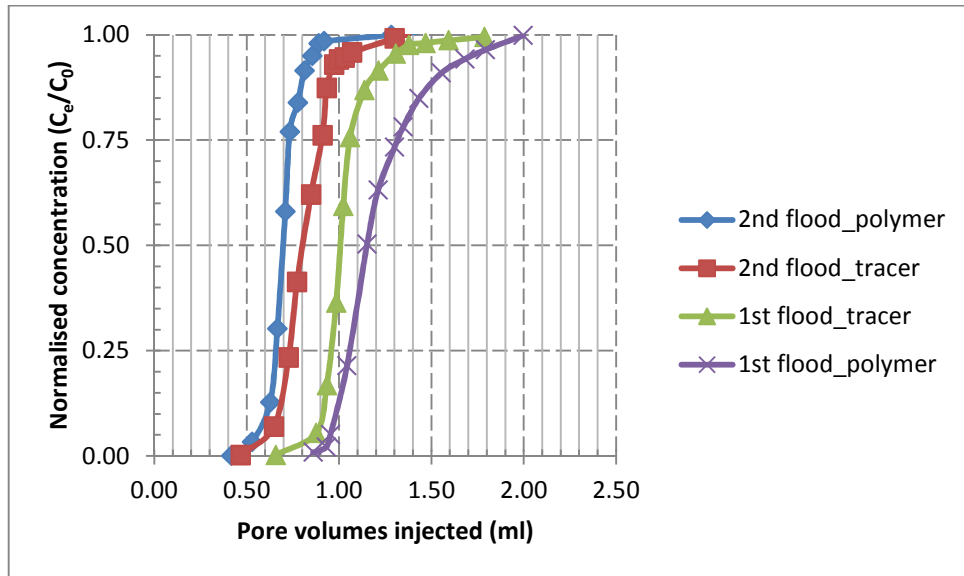


Figure 7.29 - Dynamic tracer test with HPAM FP3630 S for the determination of inaccessible pore volume and retention in sandpack.

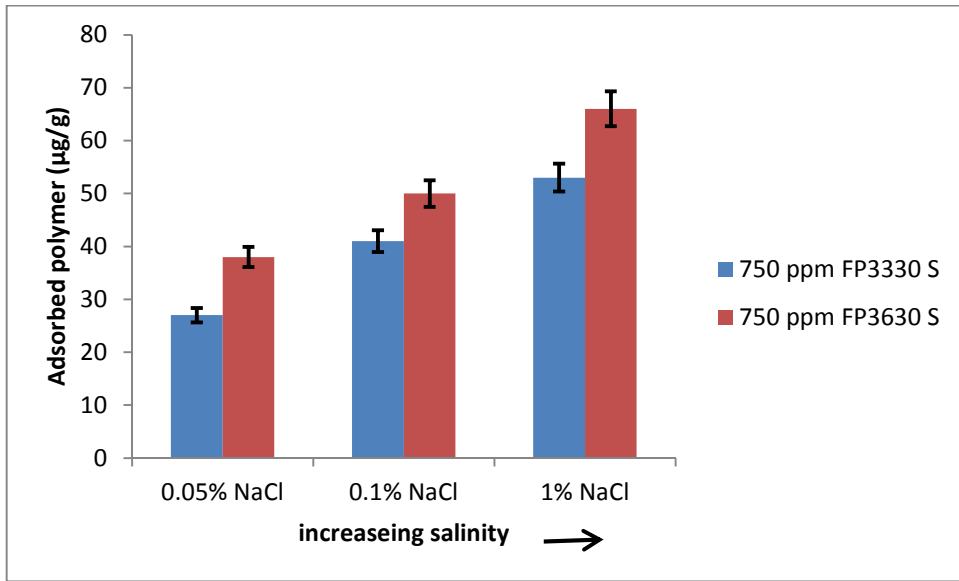
During the 1st flood, most of the retention and adsorption demand had been supposedly satisfied. The concentration data acquired during the 2nd stage of the polymer flood were used to calculate the IAPV using method 2 above (Dawson and Lantz, 1972). By this method, the 0.5 normalized concentration on the leading edge of the polymer-concentration plot (Figure 7.29) was seen at about 0.70 PV, which indicates an inaccessible pore volume of 0.30 (i.e., 1-0.70) for this sand. This value shows that IAPV was a little more than polymer retention for this particular flood, hence triggering early breakthrough of the polymer front ahead of the tracer front.

7.7.4 Experiment D: Effect of salinity and polymer type on adsorption.

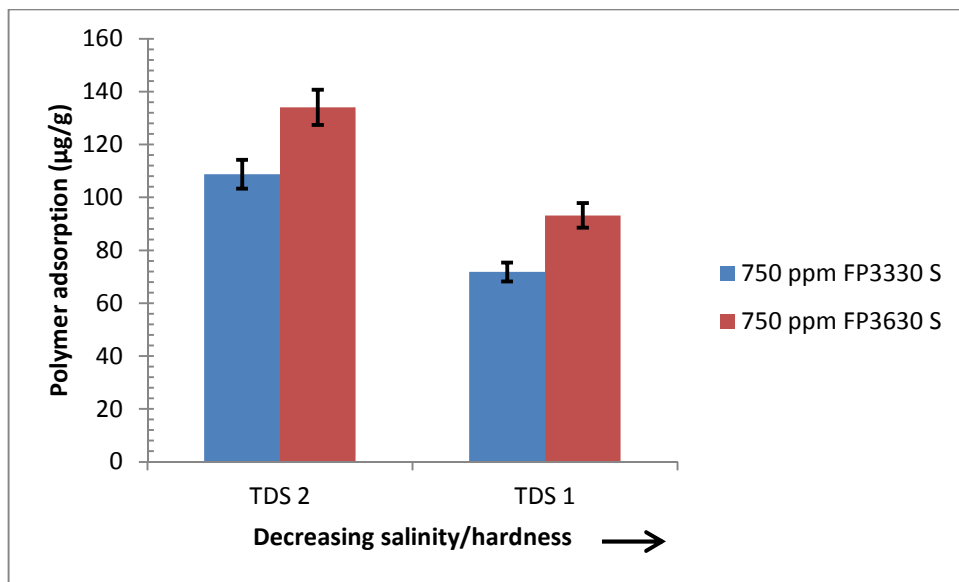
As previous stated, series of experiments were carried out to access how polymer adsorption is influenced by brine composition vs. quartzite. Specifically, two different brine types were prepared, one containing monovalent Na⁺ of different concentrations and the other containing values of divalent Ca²⁺ of varying concentrations. Figure 7.30 show the effect of different salt compositions and concentrations on polymer adsorption. Figure 7.30a shows polymer adsorption as function of different concentrations of NaCl solution. The figure shows that as the

salt concentration increases, the intra-and intermolecular repulsion forces between the anionic groups reduce; thus the hydrodynamic volume in brine of the individual polymer polyions become smaller (Szabo, 1979). This means that a polymer density in its hydrodynamic volume in the adsorbed layer is high; hence, as the salt salinity (or concentration) increases, adsorption also increases for these cases.

Figure 7.30b shows the effect of increasing calcium divalent ions on polymer adsorption. As the data of Figure 7.30b shows, the adsorption at TDS1 brine containing 0.69% Ca^{2+} is higher than that for TDS1 brine containing 0.043% Ca^{2+} for both samples of 750ppm FP3630 S and FP3330 S. This is because the divalent ions in the brine compress the molecular sizes of the flexible HPAMs and reduces the static repulsion between the silica surface and polymer carboxyl group. This result is consistent with previous study such as Chiappa et al. (1999) as illustrated in Figure 7.31. Additionally, sample FP3630 S shows a higher adsorption than FP3330 S in both the TDS1 and TDS2 brines due to its higher molecular weight. These results generally show that electrostatic interactions between charged groups at the rock-brine and polymer-brine interfaces dominate in polymer adsorption; and from a practical point of view, these results demonstrate that brines with low-salinity comprising monovalent ion would be preferable in order to reduce polymer adsorption onto rock surfaces.



(a)



(b)

Figure 7.30 - Effect of salinity/hardness and polymer type on polymer adsorption on silica sand (0.043% Ca^{2+} in TDS1 and 0.69% Ca^{2+} in TDS1).

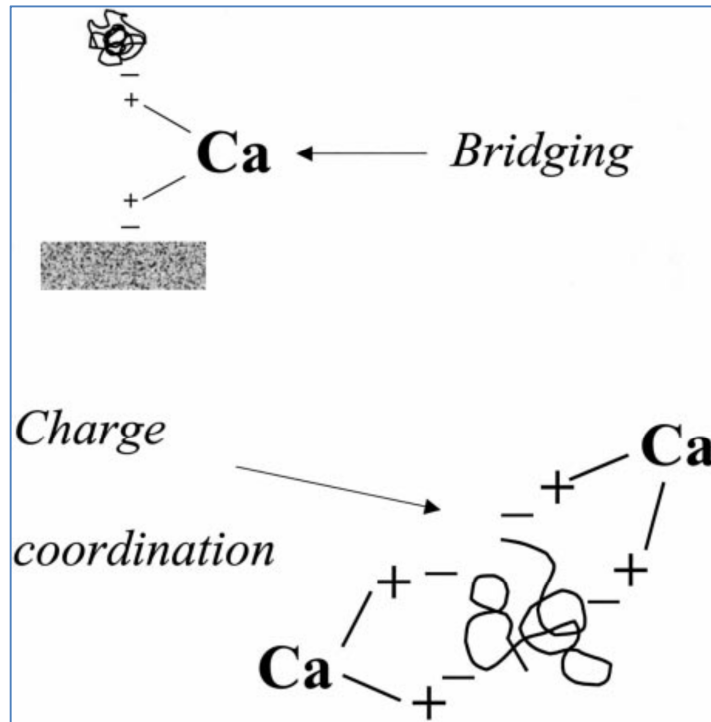


Figure 7.31 - Shows that presence of divalent calcium ions in brine enhances adsorption of negatively charged polymer molecules onto quartzite by two probable mechanisms: (1) Bridging:- Ca^{2+} ions create a link between the negatively charged polymer molecules and the negatively charged quartz surface, (2) Charge coordination:- Ca^{2+} ions neutralizes part of the negative sites and reduces the electrostatic repulsion (Chiappa et al., 1999).

7.7.5 Experiment E: Effect of permeability and pore size distributions.

The flow behaviour and the effect of 500 ppm of sample FP3330 S in two clashach cores are shown in the data of [Figure 7.32](#) to [Figure 7.35](#). As shown in [Figure 7.32](#) and [Figure 7.33](#), a higher permeability and mobility reductions is observed to occur in the low-permeability core than the high-permeability core. The results support the fact that cores with smaller openings are more vulnerable to flow restrictions caused by polymers. The data of [Figure 7.34](#) shows that core 7A induced an equilibrium adsorbed layer thickness greater than core 2A in the ratio of about 10:1. However, these figures also show retention-related permeability reduction attributable to rate or velocity variation.

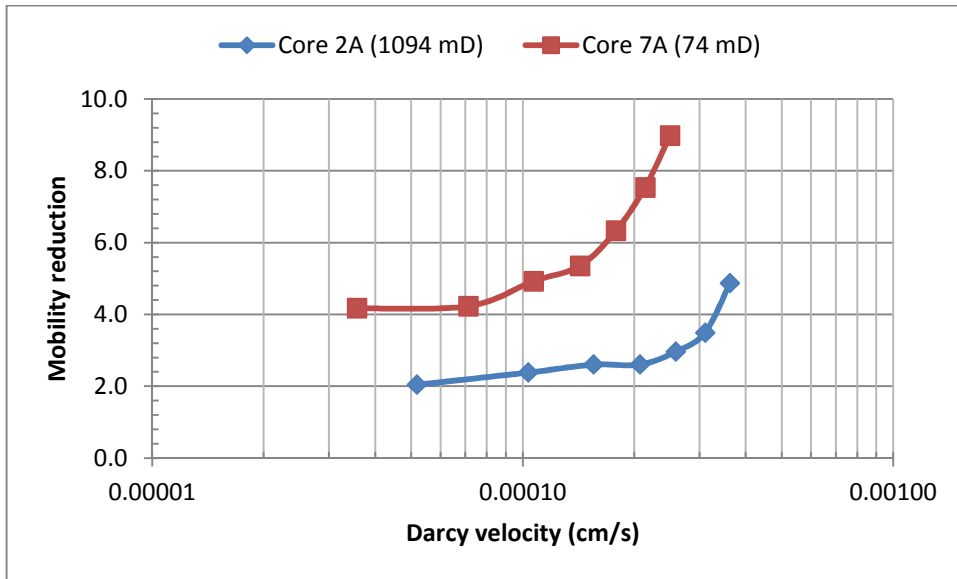


Figure 7.32 - Pore size distribution effect on flow of 500 ppm of polymer FP3330 S through clashach in TDS1.

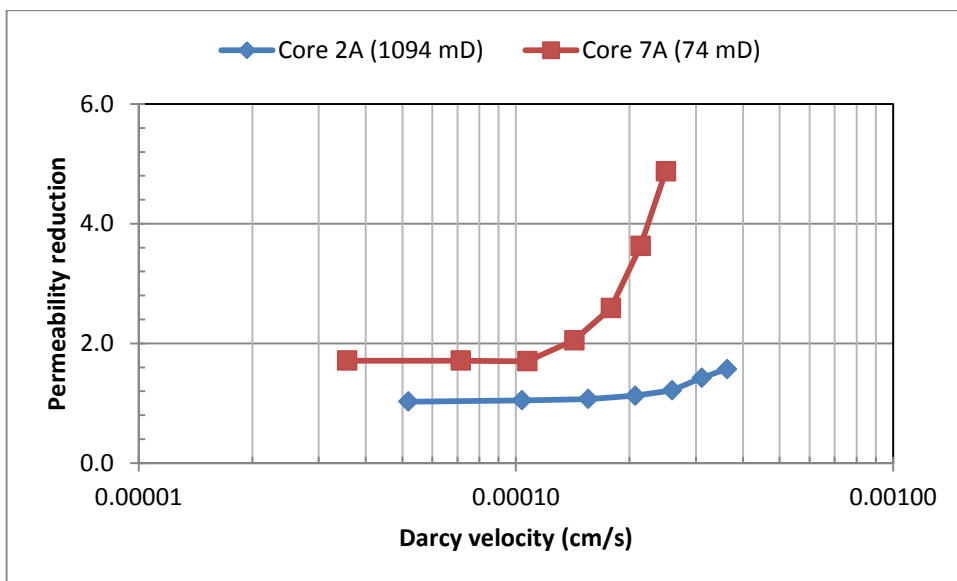


Figure 7.33 - Pore size distribution effect on reduction of clashach permeability after flowing 500 ppm of polymer FP3330 S in TDS1.

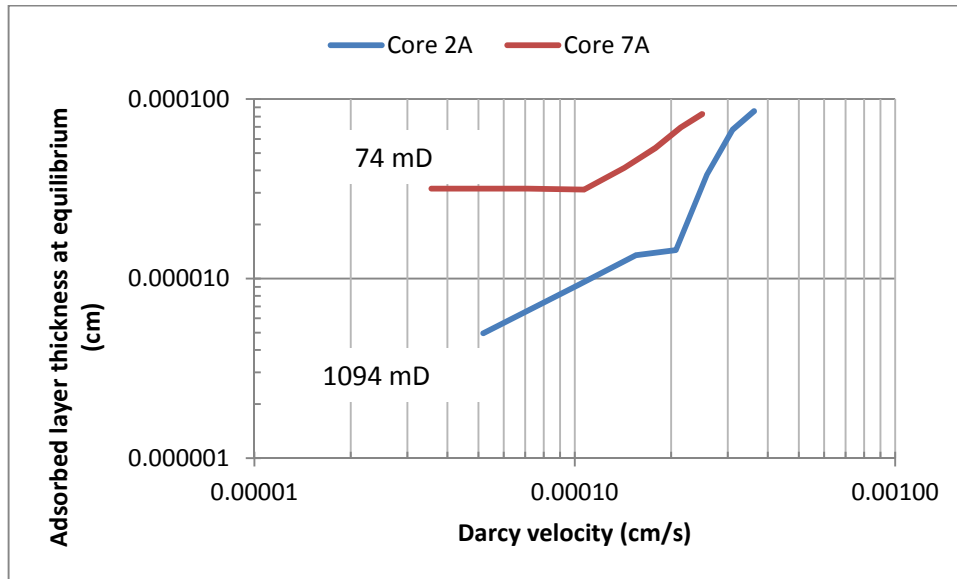


Figure 7.34 - Effect of pore size distributions on adsorbed layer regime after flowing 500 ppm of polymer FP3330 S through clashach in TDS1.

7.8 Permeability Reduction Mechanism

The mechanism of permeability reduction in porous media is complex and involves polymer-rock-brine interactions. Laboratory displacement experiments were performed in which polymer was used to saturate the cores at constant flow rate until pressure stabilised across the core. Solution concentrations were measured before entering and after leaving the core using the turbidity method. The experimental result shown in Figure 7.35 describes HPAM FP3330 S effluent behaviour in two clashach cores. Typically, in each case, no polymer appeared until after an approximate 1 pore volume (PV) of solution was injected; during which time the original water in the core was displaced by the polymer solution. Polymer effluent stream concentration continually increased from the injection of about 1 to 3 PVs; indicating that some polymer was being retained in each core. As expected, and due to the higher permeability of core 2A, the polymer front reaches its injected concentration after injection of about 1 PV; indicating probably, an insignificant adsorption. This core stabilized to polymer after injecting roughly 2 PVs. Having attained stabilization at constant flow rate, the drop in pressure across the core equally remained constant as additional pore PVs was injected. Consequently, viscosities and concentrations of the effluent polymer

stream then become equal to those of the solution entering the core after stabilisation.

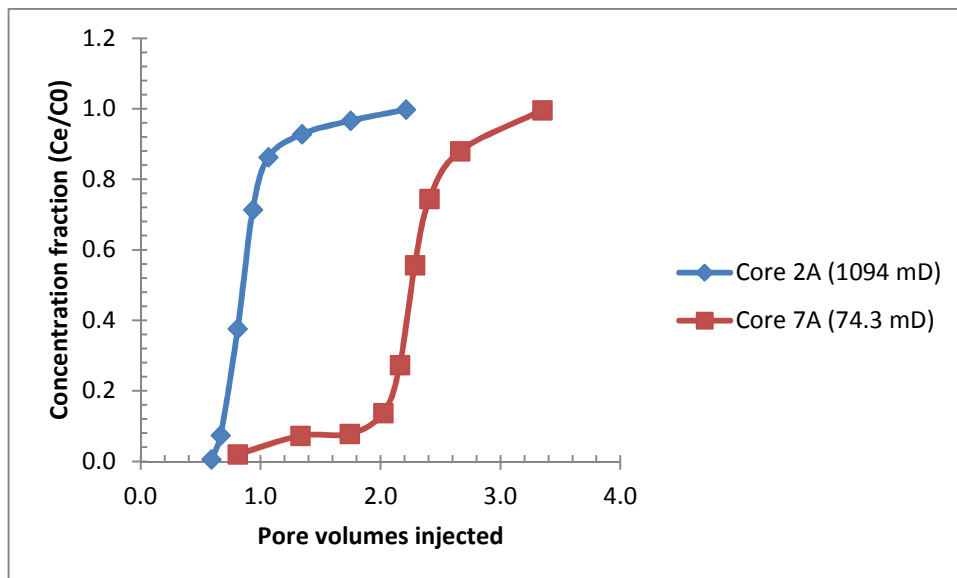


Figure 7.35 - Effect of permeability on retention of 500 ppm 3330 S HPAM on clashach cores in brine TDS1.

In the low permeability core 7A (Figure 7.35), a further shift to higher pore volumes injected in breakthrough is observed; indicating a very high retention in the accessible pore volume requiring around over 3 PVs to reach its injected concentration in the effluent. It is probably due to entrapment in smaller openings between pores and adsorption in the entire core that resulted in higher polymer loss in this case. Furthermore, mass separations between polymer molecules (i.e., smaller molecules have penetrated the pores and were retained) and adsorption kinetics are perhaps, responsible for the spread-out aspect of the polymer front in this low-perm core. Therefore, the data of Figure 7.35 suggests the following generalisation: a) throughout stabilisation, the flow that takes place between pores in larger openings allows polymer solution to pass the core unaltered, b) following stabilisation, a combined effect of adsorption and mechanical entrapment occurs in smaller openings between pores during polymer retention, c) as the polymer solution stops flowing between pores in the smaller openings, permeability is consequently reduced significantly.

7.8.1 Impact of Polymer Retention

The impact of polymer retention is illustrated in [Figure 7.36](#) and [Figure 7.37](#) generated by Eqns. 7.1 (given earlier) and 7.11 respectively (Manichand and Seright (2014):

$$\Gamma_{PV} = [\rho_{g_rock}(1-\phi)/\phi][\Gamma_p/C_p] \quad (7.1)$$

and

$$\Gamma_p = \frac{(C_i - C_f) \cdot W_p}{W_s} \quad (7.11)$$

where, Γ_{PV} = fractional pore volume (PV) retained; ρ_{g_rock} = rock density, g/cm³; C_p = polymer concentration, ppm; ϕ = porosity, fraction; Γ_p = polymer adsorption, microgram adsorption per gram of solid ($\mu\text{g/g}$) as function of time; W_p = weight of polymer solution, g; W_s = weight of solid, g; C_i = initial concentration of polymer solution, ppm; C_f = final equilibrium concentration of polymer solution, ppm.

Using Eqns. 7.1 and 7.11 above and the data given below, [Figure 7.36](#) shows delay factors for different concentrations of HPAM FP3630 S. Assuming the absence of inaccessible pore volume (IAPV), polymer retention of 20 $\mu\text{g/g}$ at 1000 ppm would represent a delay factor of about 0.025 (2.5%) of 1 pore volume (PV) of reservoir. For higher polymer retention of 40 $\mu\text{g/g}$ at 750ppm this would represent 0.7 (70%) of 1 PV. This analogy means that to reach a given target in the formation, 70% more polymers must be injected if compared with the case of no retention. By similar illustration, [Figure 7.37](#) shows that polymer FP3630 S retained more pore volume per pore volume compared to sample FP3330 S for the same set of conditions. From this simple illustration, it is clear that polymer adsorption can have detrimental effect on oil

recovery as well as the economics of the project; therefore the need to evaluate polymer-induced formation damage cannot be overemphasized.

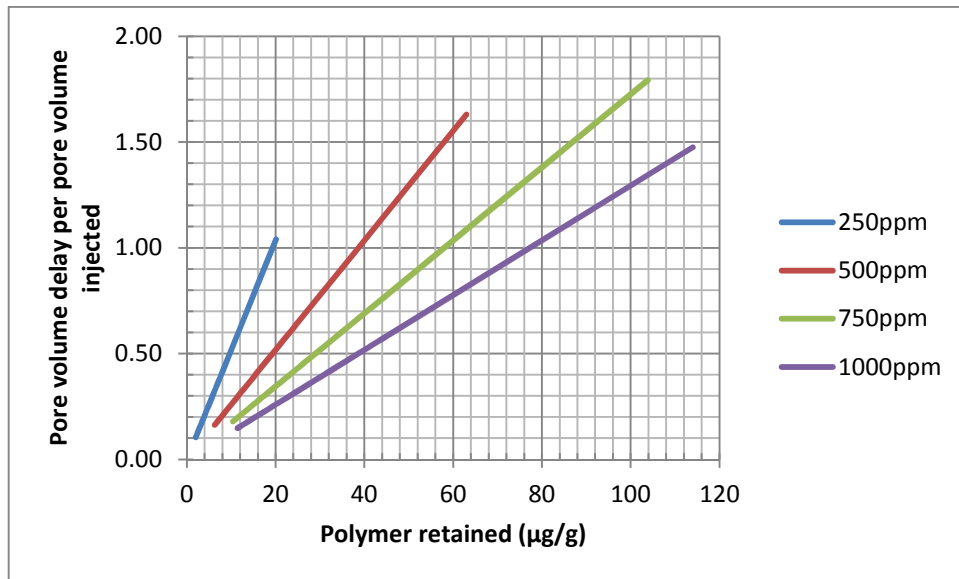


Figure 7.36 - Impact of adsorption on polymer bank injection.

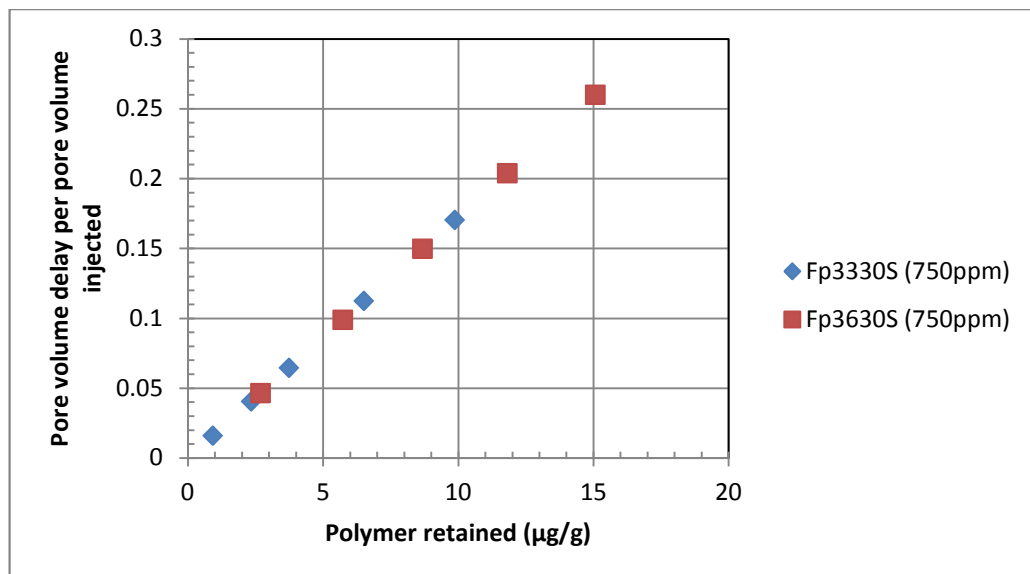


Figure 7.37 - Impact of adsorption on polymer bank injection for two different polymer products.

7.8.2 Polymer-Induced Formation Damage

The computation of formation damage induced by polymer was done in a separate experiment by measuring brine permeability (K_b) before and after polymer flow test from flowrate-pressure drop data. Brine TDS1 was flowed through core sample 1A. The flowrate and pressure drop data

were recorded after steady state was attained for each rate selected. These data were then used to calculate the sample brine permeability (K_b) using Darcy's law. The change in brine transmissibility after about 10ml of polymer solution was flowed through the core is shown in Figure 7.38. The increase in flow resistance (consequently causing increase in pressure drop) could possibly be the result of polymer molecules retained on the rock surfaces. Figure 7.39 shows SEM image after polymer flow with polymer draping grains and restricting pores. Both brine and polymer flows follow the same rate.

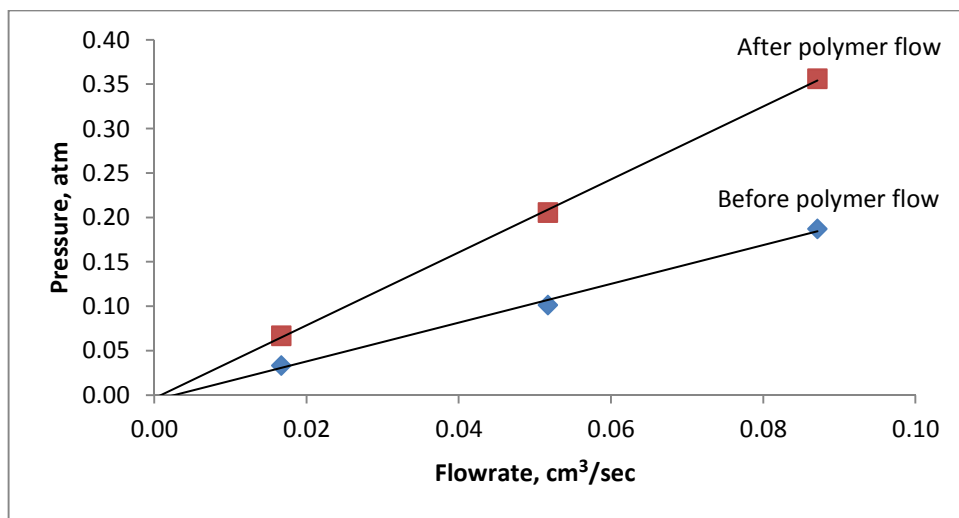


Figure 7.38 - Characteristic flowrate-pressure drop behaviour for brine before and after flow of polymer FP3330 S through Core sample 1A

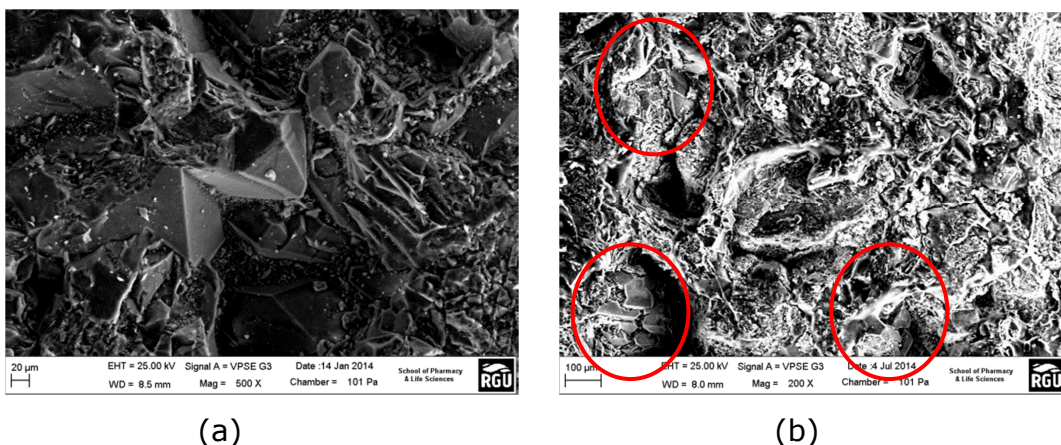


Figure 7.39 - SEM image: (a) before (b) after polymer flow on core 1A. NB: Fig. 7.39b shows SEM image after polymer flow with polymer draping grains and restricting pores as indicated by red circles.

7.9 Polymer-induced Formation Damage Modelling

The study of formation damage is the study of permeability impairment as porosity decreases. Porous media permeability damage can be predicted by an exponential decay function of the effective fractional bulk volume occupied by adsorbed polymer in a non-linear form as Eqn. (7.12):

$$\frac{k_d}{k_0} = A * e^{-B * \Gamma_p} = A * \exp(-B * \Gamma_p) \quad (7.12)$$

where A and B are empirical fitting coefficients. These coefficients together with the experimentally measured retained polymer on rock surface (Γ_p) enables the prediction of k_d/k_0 or the permeability damage ratio (PDR) in terms of field operational parameters such as brine salinity and hardness, polymer concentration, reservoir permeability, etc. By measuring the permeability versus the amount of polymer adsorbed at certain time intervals during core flow experiments, the estimation of the non-linear model parameters in Eqn. (7.12) lends itself to a direct solution approach using the method of least squares.

Among the phenomenon related to polymer adsorption and filtration, permeability is possibly considered to be the most important. The amount of mass polymer adsorbed can be related to the pore volume blocking that causes damage to the porous media on the assumption that permeability damage is caused by porosity loss, and that polymer retention is by adsorption rather than entrapment. In the literature, different relationship between permeability and porosity have been proposed and discussed by different researchers (e.g., Kozeny, 1927; Carmen, 1937; Frank et al., 1991). Let k_0 and ϕ_0 correspond to the original or initial undamaged permeability and porosity of the porous medium, and k_d and ϕ_d represent the instantaneous, local formation properties once it has been invaded and damaged by adsorbed polymer molecules. The instantaneous, local porosity is the difference between the

initial porosity and damaged fraction of the pore spaces (i.e. the fraction of adsorbed polymers that occupied the total porous medium bulk volume). The initial and instantaneous permeability is expressed as function of altered porosity using the Kozeny (1927) and Carmen (1937) equation:

$$\frac{k_d}{k_0} = \left(\frac{\phi_d}{\phi_0} \right)^3 \left(\frac{1 - \phi_0}{1 - \phi_d} \right)^2 \quad (7.13)$$

During adsorption process, porosity is reduced by the equivalent amount of fractional pore volume occupied by the adsorbed polymer. Hence, instantaneous, local porosity is given by Eqn. (7.14):

$$\phi_d = \phi_0 - \Gamma_{pv} \quad (7.14)$$

The definition of porosity gives Eqn. 7.15:

$$\phi_d = \phi_0 - \frac{\text{amount of polymer adsorbed}}{\text{bulk volume of porous media elements}} \quad (7.15)$$

From the definition of porosity, the core initial pore space or volume (V_{p0}) and the damaged pore space due to adsorbed polymer (V_{dp}) (i.e., the fractional reduction in porosity; or the percentage of connected pore-volume rendered impermeable by adsorbed polymer ('Coating')) are related by Eqn. (7.16):

$$\frac{V_{dp}}{V_{p0}} = \left(1 - \frac{\phi_d}{\phi_0} \right) \quad (7.16)$$

where, $\Gamma_{PV} = \left[\rho_{g_rock} (1 - \phi_0) / \phi_0 \right] \left[\Gamma_P / C_P \right]$ as earlier given by Eqn. (7.11),

$$\text{and } \Gamma_p = \frac{(C_i - C_f) \cdot W_p}{W_s} \quad (7.17)$$

where; Γ_{pv} is the volume fraction of polymer adsorbed in the pores. A numerical approach was used to rigorously determine the value of ϕ_d using Eqns. 7.14 through 7.17. The calculated value of ϕ_d was then used to calculate k_d/k_0 in Eqn. (7.13). If not mentioned in the text, the laboratory experimental adsorption data input values and the model results used in the model construction are given in [Table 7.5](#) (polymer and porous media), [Table 7.6](#) (parameters for 0.043% Ca^{2+} concentrations in brine TDS1), and [Table 7.7](#) (parameters for 0.69% Ca^{2+} concentrations in brine TDS1).

Table 7.5 - Polymer and porous media properties used in calculating models parameters.

	Polymer	Porous Media
C_0 (ppm)	300	-
ϕ_0	-	0.373
K_0 (mD)	-	348.8
W_{sg} (g)	-	57.55
ρ (g/cm ³)	-	2.65

Table 7.6 - Input values and model results used in the models construction for 0.043% Ca^{2+} concentrations in brine TDS1.

Parameter	Model Input Value					
	0	2	4	6	8	10
PV_{inj} (ml)	0	2	4	6	8	10
$(\Gamma_p)_i$ ($\mu\text{g/g}$)	0	1.1537	4.2265	7.2905	11.4488	12.8024
Model Results						
$(\phi_d)_i$	0.373	0.3665	0.3493	0.3325	0.3166	0.3025
$(k_d/k_0)_i$	1.0	0.9295	0.7626	0.6249	0.5149	0.4309

Table 7.7 - Input values and model results used in the models construction for 0.69% Ca²⁺ concentrations in brine TDS1.

Parameter	Model Input Value					
	0	2	4	6	8	10
PV _{inj} (ml)	0	2	4	6	8	10
(r _p) _i (μg/g)	0	2.6436	7.0647	11.6224	16.2173	20.5389
Model Results						
(φ _d) _i	0.373	0.3584	0.3339	0.3086	0.2832	0.2592
(k _d /k ₀) _i	1.0	0.8486	0.6354	0.4659	0.3348	0.2405

Figure 7.40 and Figure 7.41 fitted with Eqn. 7.12 illustrate the models correlation between k_d/k_0 and the amount of polymer adsorbed at different salinities/Ca²⁺ concentrations. The exponential function coefficients and the model errors from Eqn. 7.12 are shown in Table 7.8. The model errors are within engineering accuracy.

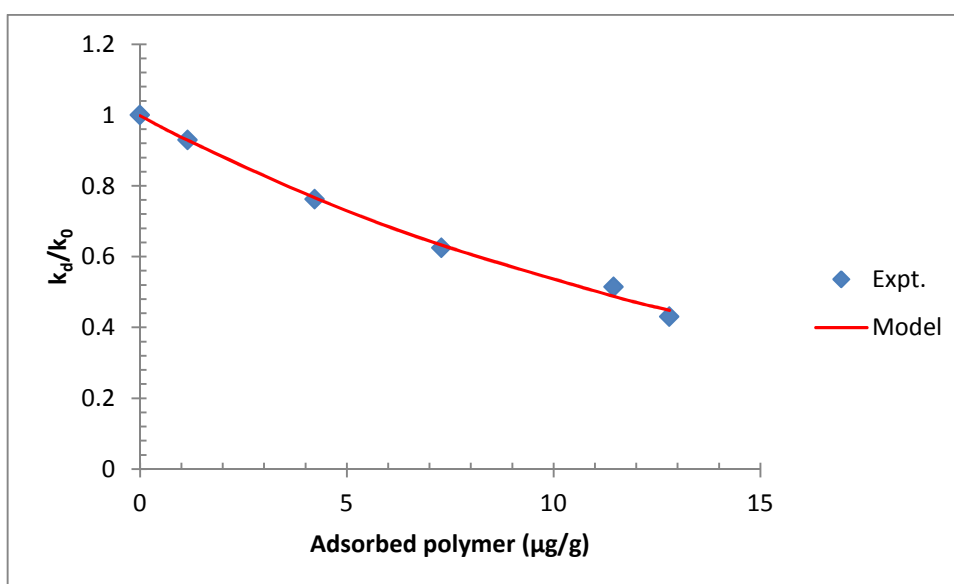


Figure 7.40 - Measured and calibrated permeability damage variation as function of adsorbed polymer, showing the effect of salinity (300 ppm of FP3630 S with 0.043% Ca²⁺ in TDS1 brine).

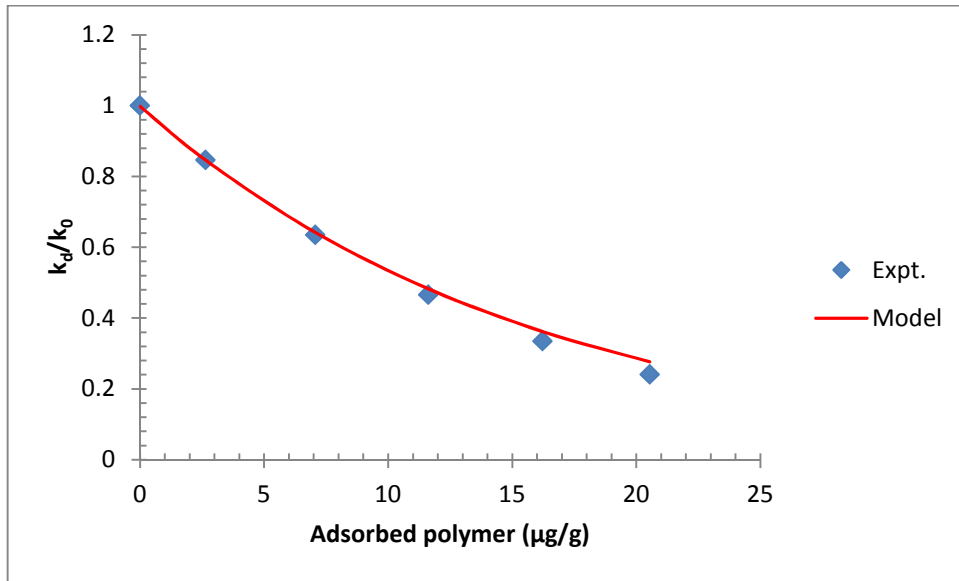


Figure 7.41 - Measured and calibrated permeability damage variation as function of adsorbed polymer, showing the effect of salinity (300 ppm of FP3630 S with 0.69% Ca^{2+} in TDS1 brine).

Table 7.8 - Showing model fitting parameters and errors from Eqn. (7.12).

Salinity	Constant A	Constant B	Model Error
0.043% Ca^{2+} in TDS1	0.9979	-0.0625	1.8%
0.69% Ca^{2+} in TDS1	1.0193	-0.0700	4.6%

Using the calculated constants in Table 7.8 for the two salinity cases, the final models become Eqns. 7.18 (0.043% Ca^{2+} in TDS1) and 7.19 (0.69% Ca^{2+} in TDS1) respectively.

$$\frac{k_d}{k_0} = 0.9979 * e^{-0.0625 * \Gamma_p} = 0.9979 * \exp(-0.0625 * \Gamma_p) \quad (7.18)$$

$$\frac{k_d}{k_0} = 1.0193 * e^{-0.0700 * \Gamma_p} = 1.0193 * \exp(-0.0700 * \Gamma_p) \quad (7.19)$$

In order to check the results taken from the model, the percent average arithmetic deviation was calculated using Eqn. (7.20):

$$PAAD = \frac{1}{n_d} \sum_{i=1}^{n_d} \left(\frac{|y_{\text{exp}t.} - y_{\text{mod}el}|}{y_{\text{exp}t.}} \times 100 \right) \quad (7.20)$$

where; n_d is the number of data points, i is an index, $y_{\text{exp}t.}$ is the experimentally measured polymer adsorption, and $y_{\text{mod}el}$ is the predicted polymer adsorption.

The Kozeny-Carmen equation coupled with adsorbed polymer mass balance was effectively used to model salinity-dependent polymer formation damage in silica sand with minimal error (see [Table 7.8](#)). With knowledge of adsorption profiles for different parameters, the model can also be used to predict polymer-induced formation damage based on concentration, permeability, polymer type, formation lithology, etc for similar high salinity conditions. In developing the models the following general assumptions were made:

- Homogenous formation
- Linear geometry of flow
- Laminar flow
- No other retention mechanism than adsorption occurs

7.9.1 Model Validation using different Initial Polymer Concentration and Adsorption Datasets

In order to test the predictive ability of the calibrated polymer-induced formation damage models, additional Ca^{2+} effect experiments using the same sand and 500 ppm initial concentration of HPAM FP3630 S was conducted. The calibrated model was used to make independent predictions for the 500 ppm polymer solution at different Ca^{2+} concentrations. The results for these separate predictions are shown in [Figure 7.42](#) and [Figure 7.43](#) respectively. From the figures, the 0.69% Ca^{2+} concentration in brine TDS1 induces greater polymer adsorption unto the silica sand because the divalent calcium ions in the brine compress the molecular sizes of the flexible HPAMs and reduces the static repulsion between the silica surface and polymer carboxyl group. This

greater adsorption due to the 0.69% Ca^{2+} concentration consequently induces greater permeability damage as shown in Figure 7.43. In general, the data of these two figures show that the models are able to predict the polymer adsorption for the two Ca^{2+} (i.e., 0.043% Ca^{2+} and 0.69% Ca^{2+}) concentrations in brine TDS1.

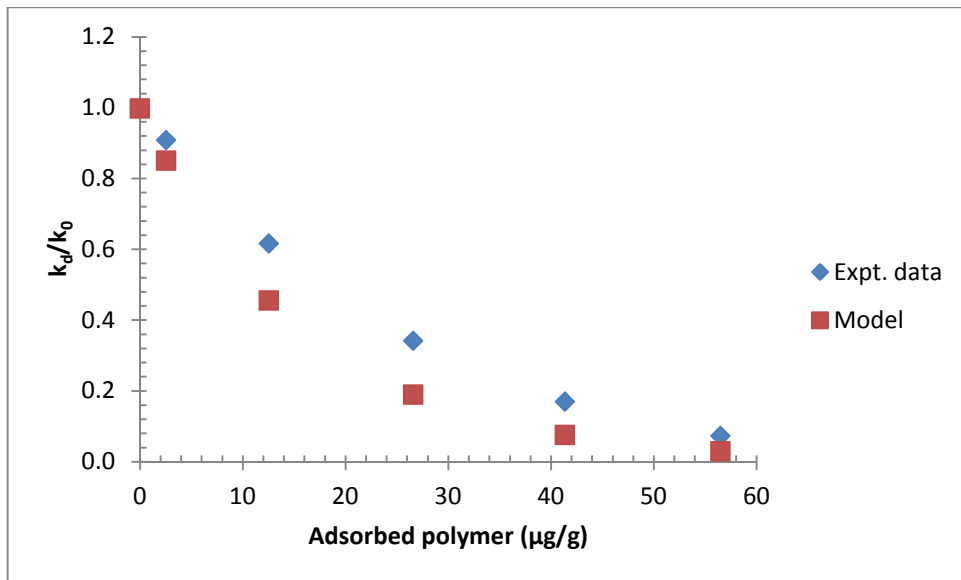


Figure 7.42 - Measured and predicted permeability damage variation as function of adsorbed polymer, showing the effect of salinity (500 ppm of FP3630 S with 0.043% Ca^{2+} in TDS1 brine).

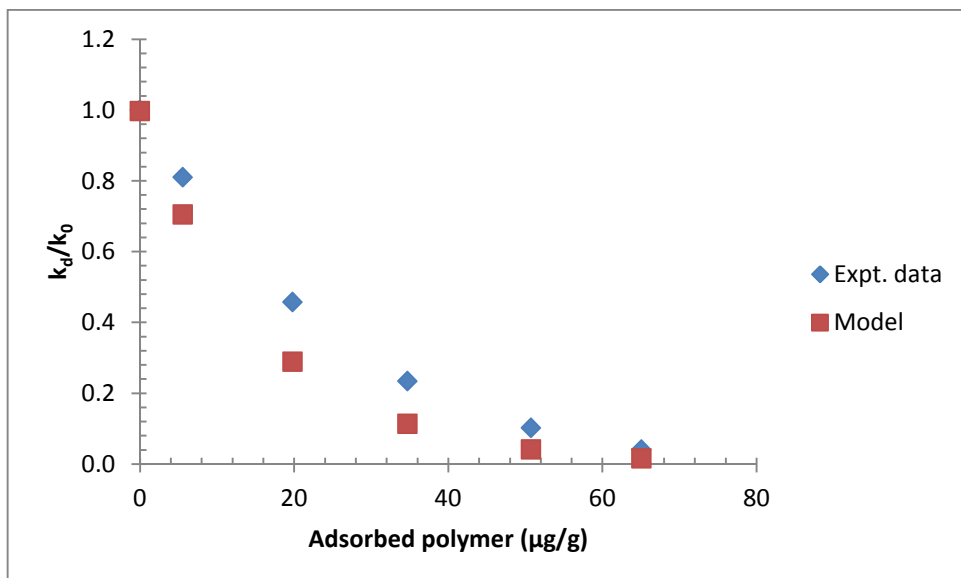


Figure 7.43 - Measured and predicted permeability damage variation as function of adsorbed polymer, showing the effect of salinity (500 ppm of FP3630 S with 0.69% Ca^{2+} in TDS1 brine).

7.10 Polymer Selection model for Flood Design

There are a lot of factors that influence polymer adsorption process (such as cost, rock type, polymer type, molecular weight, salinity, concentration, pH, porous media structure, chemistry of the aqueous phase, porous media surface area, porosity and permeability of the porous media, pore-size distribution, grain-size distribution, flow rate, clay content, quantity of fluid injected, amongst others) during EOR flooding. In practice, the products used in each one of these applications are not the same. Also, correlation from one reservoir formation would not probably hold for another because of the likelihood of different factors mentioned earlier.

Furthermore, mathematical model studies provide a reliable means of evaluating potential benefits of polymer pre-injection. However, such studies require input data that permit the model to simulate the physical processes that may occur in the reservoir. From the above, a simple economic model is proposed that would aid polymer screening prior to field operations using a combination of experimental data obtained from this flow experiments. The most important parameters affecting polymer flooding considered in the model include: 1) adsorption (as highest resistance factors with lowest retention is preferred), 2) cost (affects the economics), 3) resistance factors (linked with volumetric sweep and mobility reduction) and 4) surface area (affects the amount of adsorbed polymer). From these combinations, by incorporating rock surface area (A_s) into Szabo (1979) merit index formula, a modified screening index (SI) is formulated as follows:

$$SI = \frac{\left[\left(\frac{F_{r-p} + F_{r-bf}}{2} \right) + A_s \right] [1 - \Gamma_{pv}]}{\$/lb} ; \text{lb}/\$ \quad (7.21)$$

in which the lumped rock surface area parameter is defined by Eqn. 7.22 (Kozeny-Carman, 1937):

$$A_s = \frac{31.8\phi}{\rho_{gr}(1-\phi)} \sqrt{\frac{\phi}{\alpha_t k}} ; \text{ m}^2/\text{g} \quad (7.22)$$

Where, F_{r-p} =polymer resistance factors, F_{r-bf} =brine flushed resistance factors, Γ_{pv} =fractional retention (see Eqn. 1.1), k =permeability, mD; ϕ =fractional porosity; ρ_{gr} =rock grain density, g/cm³; α_t =non-dimensional textural factor taken as 11.3 for the clashach cores (Brooks and Purcel, 1952). F_{r-p} , F_{r-bf} , and Γ_{pv} are experimentally determined using polymer dynamic flow method.

The data applied in the model (Eqn. (7.21)) and the eventual ranking of two polymer products based on their flow characteristics and other parameters considered are shown in [Figure 7.44](#) and [Table 7.9](#) respectively. [Figure 7.44](#) shows that the resistance factors due to the two polymer types stabilised at 100% water saturation. However, the observed differences in the flow-resistance factors in these two experiments could be attributed to the differences in their molecular weights. Technically, this means that the bigger molecules of sample FP3630 S caused greater flow restriction (i.e., higher polymer-induced damage) to the rock compared to sample FP3330 S as evidenced in the calculated F_{r-bf} ([Figure 7.44](#) and [Table 7.9](#)). This result is in agreement with that obtained for the static test involving these two polymer products earlier discussed in the static experiment section.

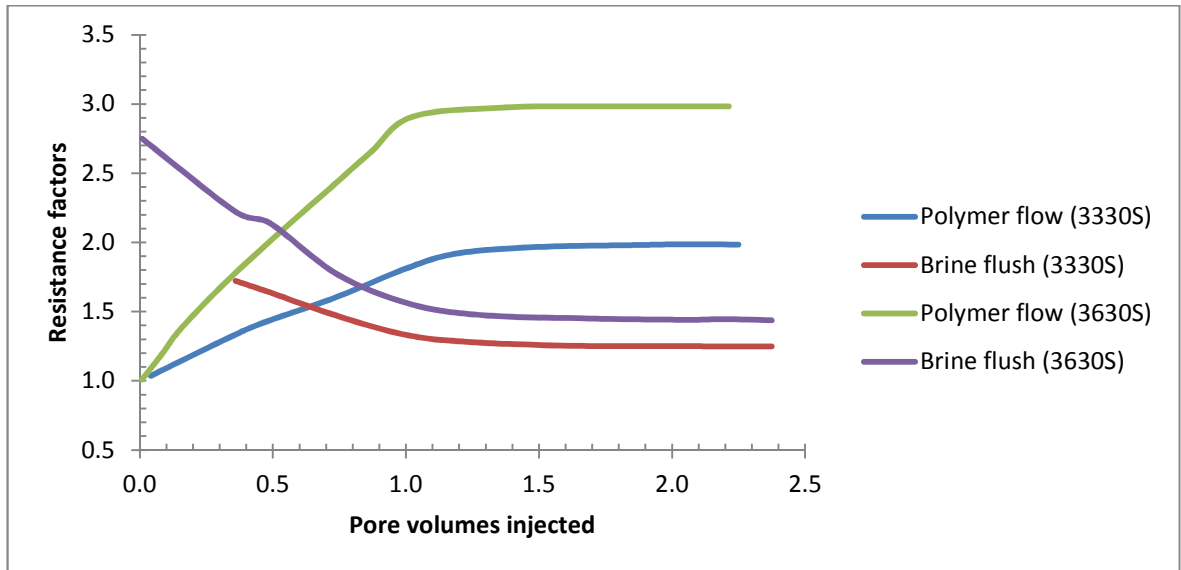


Figure 7.44 - Polymer flow and brine flushed resistance factors for 500 ppm of FP3330 S and FP3630 S in TDS1 during flow in core 2A.

Equation 7.21 rates polymers of low cost, high resistance factors and low retentions; while it eliminates polymers of high price and high retention. Polymers with higher SI values are preferred. As Table 7.9 shows, even though sample FP3630 S has higher resistance factor, it doubles sample FP3330 S in terms of retention and cost resulting in low SI fraction (0.561). For this scenario therefore, sample FP3330 S would be the preferred flooding candidate.

Table 7.9 - Screening Index for polymers (Eqn. 7.21).

No.	Product type	F_{r_p} (@ 1PV)	$F_{r_{bf}}$ (@2PV)	\$/lb	Γ_{pv}	SI (lb/\$)
1	3330 S	1.82	1.24	*1.45	0.11	1.009
2	3630 S	2.90	1.44	* 2.90	0.25	0.561

*These values are based on the product viscosity, and may not be current (See SPE-6601-PA, Part 1).

The next section provides a discussion on the research conclusions and recommendations for future work.

8

Chapter 8 – Conclusion and Recommendations for Future Work

8.1 Conclusion

Loss of additive and loss of viscosity arising from polymer adsorption and retention leads to decrease in final oil recovery as well as increase in operational costs. Retention is therefore, one of the many factors that will continually influence the success or failure of polymer flooding projects. A review of previous knowledge on polymer-induced formation damage indicates that few models available for polymer risk assessments appear to be used for all scenarios with unsatisfying results. Specifically, some of current industry challenges in this regard are finding effective polymers for high salinity environments. Also, the effect of polymer charge, as well as charges at the brine-rock interface are issues that require deeper understanding in order to address the role polymer play in formation damage. Furthermore, no much recognition has been given to polymer rheological behaviour in complex porous media, etc. Quite unfortunately, the oil and gas industry (OGI) still faces the challenge of the inability to correctly predict HPAM viscosity under shear degradation; and consequently have not been able to meet the needs of OGI production

predictions. The effect of the above mentioned factors, etc have not been fully integrated into the polymer formation damage modelling; and this research was conducted to proffer solutions to some of these many problems. However, this work is limited to reservoir single-phase flow application. Although the concluding statements presented apply to porous media and HPAM products used in the experiments (as polymers that are not chemically similar may perform differently) the results and models presented can also act as guide to other polymer applications.

In this research, series of monophasic (i.e., no oil phase) laboratory core flood studies (both in cores and sandpacks) using two HPAM products were conducted to study the effect of polymer retention on oil recovery in relation to adsorption and desorption kinetics. Also, a special method was used to study the formation damage potential of polymers in different clashach cores having extreme permeability differences. In all experiments, the following variables were considered in the research: 1) polymer type, 2) effect of concentration, 3) effect of salinity/hardness, 4) effect of permeability and pore size distributions, 5) effect of inaccessible pore volume (IAPV) on retention, 6) effect of flow rate (where a special method was established to quantify the effect of flow rate on polymer adsorption); and analytical models suitable for the prediction of polymer-related formation damage in oil and gas-bearing formations were developed and validated. The formation damage models were based on the assumption that adsorption was the only mechanism causing polymer retention on the surface of the rock investigated.

In summary, experimental results and findings show that:

- Although adsorption is concentration-dependent, it did not generally obey Langmuir law contrary to most previous studies; it is worthy to note here that Dawson and Lantz (1972) first suggested the use of Langmuir isotherm for polymer adsorption without any experimental justification where they apparently presumed polymers would follow similar adsorption behaviour as surfactants.

- By first flooding a low-concentration front, polymer adsorption may be reduced during polymer injection. In other words, it could be reasonable to first inject a low-concentration polymer solution bank before the main flood bank in order to reduce polymer retention and thereby maximise use of chemicals, and thus reduce project cost.
- Most polymer retention were observed to be irreversible; this finding also shows that Langmuir law was probably always not logically correct since Langmuir isotherm was customarily used for the description of reversible adsorption of small gas and surfactant molecules.
- Polymer retention is influenced by flow rate. A better method was used to quantify total incremental retention (both reversible and irreversible) due to flow rate variation different from previous studies. Specifically, as flow rate was increased from 0.8, to 6.0 ml/min, incremental reversible adsorption also increased from 0.04 to 0.17 PVs; while incremental irreversible adsorption increased from 0.047 to 0.134 PVs.
- Inaccessible pore volume (IAPV) decreases with flow rate which consequently increases polymer adsorption. As flow rate increased through 0.8, 3.0 and 6.0 ml/min, IAPV decreased from 32% and 28% to 15% respectively.
- Dynamic method used for retention measurements shows that over 50% of polymer adsorption takes place prior to the polymer front reaching the core outlet.
- Experimental results generally show that electrostatic interactions between charged groups at the rock-brine and polymer-brine interfaces dominate in polymer adsorption; hence, higher concentrations of Ca^{2+} in brine induces greater polymer adsorption onto the silica sand because the divalent ions in the brine compress the molecular sizes of the flexible HPAMs and reduces the static repulsion between the silica surface and polymer carboxyl group. Therefore, from a practical point of view, these results demonstrate that brines with low-salinity comprising monovalent ion would be preferable in order to reduce polymer adsorption onto rock surfaces.

These observations were also effectively modelled; and the validated models matched experimental data.

- Other experimental results show that polymer rheological behaviour is affected by factors such as shear rate, concentration, salinity/hardness, temperature, polymer type, etc. For example, in the experiment to study the impact of salt on polymer viscosity, FloComb C3525 exhibited higher resistance to Ca^{2+} ion in brine; confirming the manufacturer's claim that FloComb C3525 is calcium tolerant.
- It was also shown by simulation that pore size distributions, in particular greatly affect polymer viscosity in complex porous media.
- In some dynamic flow experiments, stabilisation was not attained as pressure continually increased probably due to mechanical entrapment; and because reliable adsorption information was impossible with these experiments, they were terminated.

8.2 Recommendations for future work

1) In this work, two HPAM polymers having medium to high anionic charge were tested. However, there are polymers of different charges such as cationic, anionic, or weakly anionic. It is recommended to conduct salinity tests with polymers of different charges with different lithologies while considering the effect of pH, because electrostatic determines polymer adsorption on negative quartz surface at pH larger than 2.

2) The results presented here were based on the use of sandpacks and clashach rock outcrops. Due to the importance of polymer adsorption, sand from polymer-flooded intervals from actual reservoir formation should be used for polymer damage quantification. In so doing, polymer retention values can be derived from real field results thereby enhancing design of field projects.

3) The use of Langmuir isotherm was probably always not correct mechanistically since the law was based on the assumption that polymer retention proceeds towards zero and is reversible. Ironically, many

chemical flooding simulators apply Langmuir isotherm to report polymer retention, and have very often, been seen to make grossly incorrect prediction of polymer retention. It is therefore recommended that more experimental work is needed to further validate those presented here to enable Langmuir-law reformulation for polymer retention in conventional simulators.

4) Because different correlations would be expected for different rock types it is therefore recommended that further laboratory experimental measurements on a particular reservoir rock would be required to develop correlations that are comparable to those presented in this research.

References

References

ABU-KHAMSIN, D.S.A., 2004. Basic Properties of Reservoir Rocks. King Fahd University of Petroleum & Minerals, Dhahran, Saudi Arabia.

AFSHARPOOR, A., BALHOFF, M.T., BONNECAZE, R. and HUH, C., 2012. CFD modeling of the effect of polymer elasticity on residual oil saturation at the pore-scale. *Journal of Petroleum Science and Engineering*, 94-95, pp. 79-88.

AGNEW, H.J., 1972. Here's how 56 polymer oil-recovery projects shape up. *Oil and Gas J.* 70: 109-112.

AGUAYO, J., TAMADDON-JAHROMI, H. and WEBSTER, M., 2008. Excess pressure-drop estimation in contraction and expansion flows for constant shear-viscosity, extension strain-hardening fluids. *Journal of Non-Newtonian Fluid Mechanics*, 153(2), pp. 157-176.

AIT-KADI, A., CARREAU, P. and CHAUVETEAU, G., 1987. Rheological properties of partially hydrolyzed polyacrylamide solutions. *Journal of Rheology*, 31(7), pp. 537-561.

AL-BAHAR, M.A., MERRILL, R., PEAKE, W., JUMAA, M. and OSKUI, R., 2004. Evaluation of IOR Potential within Kuwait. Paper SPE 88716-MS presented at the SPE Abu Dhabi International Conference and Exhibition, Abu Dhabi, United Arab Emirates, 10-13 October.

ALBAUGH, F.W., 1950. Water drive. U.S. Patent No. 2,533,546, December 12.

AL-HASHMI, A. and LUCKHAM, P., 2010. Characterization of the adsorption of high molecular weight non-ionic and cationic polyacrylamide on glass from aqueous solutions using modified atomic force microscopy. *Colloids and Surfaces A: Physicochemical and Engineering Aspects*, 358(1), pp. 142-148.

ALI, L. and BARRUFET, M., 2001. Using centrifuge data to investigate the effects of polymer treatment on relative permeability. *Journal of Petroleum Science and Engineering*, 29(1), pp. 1-16.

AL-SHARJI, H.H., GRATTONI, C.A., DAWE, R.A. and ZIMMERMAN, R.W., 2001. Flow of oil and water through elastic polymer gels. *Oil & Gas Science and Technology*, 56(2), pp. 145-152.

ALSOFI, A. and BLUNT, M., 2010. Streamline-based simulation of non-Newtonian polymer flooding. *SPE Journal*, 15(4), pp. 895-905.

AL-SOFI, A., LA FORCE, T. and BLUNT, M., 2009. Sweep Impairment Due to Polymers Shear Thinning. Paper SPE 120321 presented at the SPE Middle East Oil and Gas Show and Conference, Bahrain, 15-18 March.

ALVARADO, V. and MANRIQUE, E., 2010. Enhanced Oil Recovery: An Update Review. *Energies*, 3(9), pp. 1529-1575.

ALVES, M.A., OLIVEIRA, P.J. and PINHO, F.T., 2003. Benchmark solutions for the flow of Oldroyd-B and PTT fluids in planar contractions. *Journal of Non-Newtonian Fluid Mechanics*, 110(1), pp. 45-75.

AMAEFULE, J.O., KERSEY, D.G., NORMAN, D.K. and SHANNON, P.M., 1988. Advances in Formation Damage Assessment and Control Strategies. Paper PETSOC-88-39-65 presented at the 39th Annual Technical Meeting of the Petroleum Society of CIM, Calgary, Canada, 12-16 June.

ANNIE, A., JEAN-FRANCOIS, A., LADVA, H.K.J., WAY, P.W. and HOVE, A.O., 1999. Role of Polymers on Formation Damage. Paper SPE 54767 presented at the SPE European Formation Damage Conference. The Hague, Netherlands, 31 May-1 June.

API. 1990. API RP 63 Recommended Practices for Evaluation of Polymers Used in Enhanced Oil Recovery Operations. American Petroleum Institute, Washington, D.C.: API, June 1990.

API. 2009. API RP 13I Recommended Practice Standard Procedure for Laboratory Testing of Drilling Fluids.

AUBERT, J. and TIRRELL, M., 1980. Flows of dilute polymer solutions through packed porous chromatographic columns. *Rheologica Acta*, 19(4), pp. 452-461.

BALESTRINI, A., MAAS, A., SEHEULT, M. and MORTON, E., 2009. Advances in API/ISO Standard Grade Purified Poly-Anionic Cellulose (PAC) and Drilling Grade Xanthan Gum (XG) Test Procedure and Specifications Definition. Paper SPE/IADC 119973 presented at the SPE/IADC Drilling Conference and Exhibition, Amsterdam, The Netherlands, 17-19 March.

BARREAU, P., LASSEUX, D., BERTIN, H., GLENAT, P. and ZAITOUN, A., 1999. An experimental and numerical study of polymer action on relative permeability and capillary pressure. *Petroleum Geoscience*, 5(2), pp. 201-206.

BARRUFET, M.A. and ALI, L., 1994. Modification of relative permeability curves by polymer adsorption. *Society of Petroleum Engineers Journal*, Volume1, pp. 175-186.

BENNION, D., 2002. An overview of formation damage mechanisms causing a reduction in the productivity and injectivity of oil and gas producing formations. *Journal of Canadian Petroleum Technology*, 41(11), pp. 29-36.

BERNARD, G.G., 1960. Water flooding process. U.S. Patent No. 2,950,760, August 30.

BERNARDI, C., DAUGE, M., MADAY, Y., and AZAIEZ, M., 1999. *Spectral Methods for Axisymmetric Domains*, Series in Applied Mathematics 3. Gauthier-Villars & North-Holland, Elsevier, Paris.

BINDER, J.G.G., WEST, R.C. and ANDRESEN, K.H., 1956. Water flooding secondary recovery method. U.S. Patent No. 2,731,414, January 17.

BINDING, D.M., PHILLIPS, P. and PHILLIPS, T., 2006. Contraction/expansion flows: The pressure drop and related issues. *Journal of Non-Newtonian Fluid Mechanics*, 137(1), pp. 31-38.

BIRD, R., STEWART, W.E., and LIGHTFOOT, E.N., 1960. *Transport phenomena*, John Wiley & Sons, New York City.

BIRD, R.B., ARMSTRONG, R.C. and HASSAGER, O., 1977. *Dynamics of polymeric liquids*. John Wiley & Sons, New York City.

BIRD, R.B., ARMSTRONG, R.C. and HASSAGER, O., 1987a. Dynamics of polymeric liquids. Vol. 1. Fluid mechanics, John Wiley & Sons, New York City.

BIRD, R.B., STEWART, W.E., and LIGHTFOOT, E.N., 2002. Transport Phenomena, John Wiley & Sons, New York City.

BORTHAKUR, A., RAHMAN, M., SARMAH, A., and SUBRAHMANYAM, B., 1995. Partially Hydrolysed Polyacrylamide for Enhanced Oil-Recovery. *Research and Industry*, 40(2), pp. 90-94.

BROOKS, C.S., and PURCELL, W.R., 1952. Surface area measurements on sedimentary rocks. Fall Meeting of the Petroleum Branch of AIME. Society of Petroleum Engineers.

CANNELLA, W., HUH, C. and SERIGHT, R., 1988. Prediction of xanthan rheology in porous media. Paper SPE 18089 presented at SPE Annual Technical Conference and Exhibition, 63rd Annual Technical Conference, Houston, Texas, 2-5 October.

CARCOANA, A.N., 1982. Enhanced Oil Recovery in Rumania. SPE Enhanced Oil Recovery Symposium. Paper SPE-10699-MS presented at the SPE/DOE 3rd joint Symposium on Enhanced Oil Recovery of the Society of Petroleum Engineers, Tulsa, Oklahoma, 4-7 April.

CARMAN, P., 1937. Fluid flow through granular beds. *Transactions-Institution of Chemical Engineers*, 15, pp. 150-166.

CARPITA, M., MARCOLINI, M. and BATTISTELLI, A., 2006. Simulation of the effects of hydrophilic polymer adsorption on two-phase flow of oil-water mixtures. Proceedings of the TOUGH Symposium, Berkeley, CA. May 15-17.

CARREAU, P.J., 1972. Rheological equations from molecular network theories. *Transactions of the Society of Rheology*, 16(1), pp. 99-127.

CASTAGNO, R.E., SHUPE, R.D. and GREGORY, M.D., 1987. Method for laboratory and field evaluation of a proposed polymer flood. *SPE Reservoir Engineering*, 2(04), pp. 452-460.

CHANG, H., 1978. Polymer Flooding Technology Yesterday, Today, and Tomorrow. *Journal of Petroleum Technology*, 30(8), pp. 1113-1128.

CHAUVETEAU, G., 1981. Molecular interpretation of several different properties of flow of coiled polymer solutions through porous media in oil recovery conditions. Paper SPE-10060-MS presented at the 56th SPE Annual Technical Conference and Exhibition of the Society of Petroleum Engineers of AIME, San Antonio, Texas, USA, 5-7 October.

CHAUVETEAU, G., 1982. Rodlike polymer solution flow through fine pores: influence of pore size on rheological behaviour. *Journal of Rheology (1978-present)*, 26(2), pp. 111-142.

CHAUVETEAU, G., 2002. The Grain and Pore Throat Model: A Tool to Predict Mass Transport and Formation Damage. Paper SPE 73736 presented at the SPE International Symposium on Formation Damage Control, Lafayette, Louisiana, USA, 20 February, pp. 20-21.

CHAUVETEAU, G., DENYS, K. and ZAITOUN, A., 2002. New Insight on Polymer Adsorption under High Flow Rates. Paper SPE-75183-MS presented at the SPE/DOE Symposium on Improved Oil Recovery of the Society of Petroleum Engineers, Tulsa, OK, USA, 13-17 April.

CHAUVETEAU, G., TIRRELL, M. and OMARI, A., 1984. Concentration dependence of the effective viscosity of polymer solutions in small pores with repulsive or attractive walls. *Journal of colloid and interface science*, 100(1), pp. 41-54.

CHENG, L. and CAO, R., 2010. Constitutive model of viscous-elastic polymer solution in porous media. *Petroleum Science and Technology*, 28(11), pp. 1170-1177.

CHENG, L., LIAN, P. and CAO, R., 2013. A Viscoelastic Polymer Flooding Model Considering the Effects of Shear Rate on Viscosity and Permeability. *Petroleum Science and Technology*, 31(1), pp. 101-111.

CHHABRA, R., COMITI, J. and MACHAC, I., 2001. Flow of non-Newtonian Fluids in Fixed and Fluidised Beds. *Chemical Engineering Science*, 56(1), pp. 1-27.

CHIAPPA, L., MENNELLA, A., LOCKHART, T.P., and BURRAFATO, G., 1999. Polymer adsorption at the brine/rock interface: the role of electrostatic interactions and wettability. *Journal of Petroleum Science & Engineering*, 24(2-4), pp. 113-122.

CHRISTOPHER, R.H. and MIDDLEMAN, S., 1965. Power-law flow through a packed tube. *Industrial & Engineering Chemistry Fundamentals*, 4(4), pp. 422-426.

CIVAN, F., 2007. Reservoir formation damage. Gulf Professional Publishing.

CIVAN, F., 2011. Reservoir formation damage. Gulf Professional Publishing.

CLARK, P.E., 2010. Analysis of fluid loss data II: Models for dynamic fluid loss. *Journal of Petroleum Science and Engineering*, 70(3), pp. 191-197.

COHEN, Y. and CHRIST, F., 1986. Polymer retention and adsorption in the flow of polymer solutions through porous media. *SPE Reservoir Engineering*, 1(02), pp. 113-118.

COHEN, Y., 1988. Hydrodynamic thickness of adsorbed polymers in steady shear flow. *Macromolecules*, 21(2), pp. 494-499.

CRAVEN, T.J., REES, J.M. and ZIMMERMAN, W.B., 2006. Stabilised finite element modelling of Oldroyd-B viscoelastic flows: In COMSOL Conference; Birmingham.

DA SILVA, I., LUCAS, E. and DE FRANCA, F., 2010. Study of Conditions for Polyacrylamide Use in Petroleum Reservoirs: Physical Flow Simulation in Porous Media. *Chemical Technology*, 4(1).

DABBOUS, M.K., 1977. Displacement of Polymers in Waterflooded Porous Media and Its Effects on a Subsequent Micellar Flood. *Society of Petroleum Engineers Journal*, 17(05), pp. 358-368.

DANG, C., CHEN, Z.J., NGUYEN, N., BAE, W., and PHUNG, T.H., 2011. Development of Isotherm Polymer/Surfactant Adsorption Models in Chemical Flooding. Paper SPE 147872 presented at the SPE Asia Pacific Oil and Gas Conference and Exhibition, Jakarta, Indonesia, 20-22 September. pp. 1562-1571.

DANG, C., CHEN, Z.J., NGUYEN, N., NGUYEN, T.B.N., and BAE, W., 2014. Investigation of Isotherm Polymer Adsorption in Porous Media. *Petroleum Science and Technology*, 32(13), pp. 1626-1640.

DARCY, H.P.G., 1856. *Les fontaines publiques de la ville de Dijon: Exposition et Application des principes a Suivre et des Formules a Employer dans les Questions de Distribution d'Eau*, Victor Dalmont, Paris.

DAWSON, R. and LANTZ, R.B., 1972. Inaccessible pore volume in polymer flooding. *Society of Petroleum Engineers Journal*, 12(05), pp. 448-452. SPE-3522-PA.

DELAMAIDE, E., ZAITOUN, A., RENARD, G., and TABARY, R., (2014). Pelican Lake Field: First Successful Application of Polymer Flooding In a Heavy-Oil Reservoir. *SPE Reservoir Evaluation & Engineering*, 17(03), 340-354.

DENG, Y., DIXON, J.B. and WHITE, G.N., 2006. Adsorption of polyacrylamide on smectite, illite, and kaolinite. *Soil Science Society of America Journal*, 70(1), pp. 297-304.

DETLING, K.D., 1944. Process of recovering oil from oil sands. U.S. Patent No. 2,341,500, February 8.

DICKSON, J.L., LEAHY-DIOS, A. and WYLIE, P.L., 2010. Development of Improved Hydrocarbon Recovery Screening Methodologies. Paper SPE 129768 presented at the SPE Improved Oil Recovery Symposium, Tulsa, Oklahoma, 24-28 April.

DIJT, J.C., STUART, M.A.C. and FLEER, G.J., 1992. Kinetics of polymer adsorption and desorption in capillary flow. *Macromolecules*, 25(20), pp. 5416-5423.

DOMINGUEZ, J. and WILLHITE, G., 1977. Retention and Flow Characteristics of Polymer Solutions in Porous Media. *Society of Petroleum Engineers Journal*, 17(02), pp. 111-121.

DU, Y. and GUAN, L., 2004. Field-scale polymer flooding: Lessons learnt and experiences gained during past 40 years. Paper SPE 91787 presented at the SPE International Petroleum Conference in Mexico, Puebla Pue., 7-9 November.

EINSTEIN, A., 1955. *The Meaning of Relativity*, Princeton (1953).

ESCUDIER, M.P., GOULDSON, I.W., PEREIRA, A.S., PINHO, F.T., and POOLE, R.J., 2001. On the reproducibility of the rheology of shear-thinning liquids. *Journal of Non-Newtonian Fluid Mechanics*, 97(2), pp. 99-124.

EZELL, R., EZZAT, D., TURNER, J. and WU, J., 2010. New Filtration-Control Polymer for Improved Brine-Based Reservoir Drilling-Fluids Performance at Temperatures in Excess of 400⁰F and High Pressure. SPE International Symposium and Exhibition on Formation Damage Control.

FAN, Y., TANNER, R. and PHAN-THIEN, N., 1999. Galerkin/least-square finite-element methods for steady viscoelastic flows. *Journal of Non-Newtonian Fluid Mechanics*, 84(2), pp. 233-256.

FLORY, P.J. and FLORY, P., 1956. Statistical thermodynamics of semi-flexible chain molecules. *Proceedings of the Royal Society of London. Series A. Mathematical and Physical Sciences*, 234(1196), pp. 60-73.

FLORY, P.J., 1953. *Principles of polymer chemistry*. Cornell University Press.

FOSHEE, W., JENNINGS, R. and WEST, T., 1976. Preparation and testing of partially hydrolyzed polyacrylamide solutions. Paper SPE 6102 presented at the 51st SPE Annual Fall Technical Conference and Exhibition, New Orleans, LA, 3-6 October.

FRIEDMANN, F., 1986. Surfactant and polymer losses during flow through porous media. *SPE Reservoir Engineering*, 1(03), pp. 261-271. SPE-11779-PA.

GARCÍA-OCHOA, F., SANTOS, V.E., CASAS, J.A., and GOMEZ, E., 2000. Xanthan gum: production, recovery, and properties. *Biotechnology Advances*, 18(7), pp. 549-579.

GLEASURE, R.W., 1990. An experimental study of non-Newtonian polymer rheology effects on oil recovery and injectivity. SPE Reservoir Engineering, 5(04), pp. 481-486. SPE-17648-PA.

GOGARTY, W.B, 1967. Mobility control with polymer solutions. Soc. Pet. Eng. J. 7(2): 161-173. SPE-1566-B.

GRATTONI, C.A., AL-SHARJI, H.H., DAWE, R.A., and ZIMMERMAN, R.W., 2002. Segregated pathways mechanism for oil and water flow through an oil-based gelant. Journal of Petroleum Science and Engineering, 35(3), pp. 183-190.

GRATTONI, C.A., LUCKHAM, P.F., JING, X.D., NORMAN, L., and ZIMMERMAN, R.W., 2004. Polymers as relative permeability modifiers: adsorption and the dynamic formation of thick polyacrylamide layers. Journal of petroleum science and engineering, 45(3), pp. 233-245.

GREEN, D.W. and WILLHITE, G.P., 1998. Enhanced oil recovery. Vol. 6, 100-185, Richardson, Texas: Henry L. Doherty Memorial Fund of AIME, Textbook Series, Society of Petroleum Engineers.

GUPTA, S. and TRUSHENSKI, S., 1978. Micellar Flooding—The Propagation of the Polymer Mobility Buffer Bank. Soc.Pet.Eng.J. 18(1): 5-12. SPE-6204-PA.

HILL, H.J., BREW, J.R., CLARIDGE, E.L., HITE, J.R., and POPE, G.A., 1974. The Behaviour of Polymers in Porous Media. Paper SPE 4748 presented at the SPE Improved Oil Recovery Symposium, Tulsa, Oklahoma, 22-24 April.

HIRASAKI, G. and POPE, G., 1974. Analysis of factors influencing mobility and adsorption in the flow of polymer solution through porous media. SPE Journal 14(4), pp. 337-346.SPE-4026-PA.

HOAGLAND, D.A., LARSON, K.A, PRUD'HOMME, R.K., and BARTH, H.G., 1984. Hydrodynamic chromatography of high molecular weight water-soluble polymers. *Modern Methods of Particle Size Analysis*, Wiley-Interscience, pp. 277.

HU, Y., WANG, S. and JAMIESON, A., 1995. Rheological and rheoptical studies of shear-thickening polyacrylamide solutions. *Macromolecules*, 28(6), pp. 1847-1853.

HUANG, Y. and SORBIE, K., 1993. Scleroglucan Behaviour in Flow through Porous Media: Comparison of Adsorption and In-Situ Rheology with Xanthan. Presented at the SPE International Symposium on Oilfield Chemistry, New Orleans, Louisiana, 2-5 March. SPE-25173-MS.

HUGHES, D.S., TEEW, D., COTTRELL, C.W. and TOLLAS, J.M., 1990. Appraisal of the use of polymer injection to suppress aquifer influx and to improve volumetric sweep in a viscous oil reservoir. *SPE Res Eng*, 5(1), pp. 33-40. SPE-17400-PA.

HUH, C., LANGE, E. and CANNELLA, W., 1990. Polymer retention in porous media. SPE/DOE Enhanced Oil Recovery Symposium, Tulsa, Oklahoma, 22-25 April. SPE-20235-PA.

HUI PU, S. and XU, Q., 2009. An update and perspective on field-scale chemical floods in Daqing oilfield. Paper SPE 118746 presented at the SPE Middle East Oil & Gas Show and Conference, Bahrain, 15-18 March.

ISCAN, A.G., CIVAN, F. and KOK, M.V., 2007. Alteration of permeability by drilling fluid invasion and flow reversal. *Journal of Petroleum Science and Engineering*, 58(1), pp. 227-244.

JENNINGS, R., ROGERS, J. and WEST, T., 1971. Factors influencing mobility control by polymer solutions. *J. Pet Tech* 23(3):391-401. SPE-2867-PA.

JONES, M., 1966. Waterflood Mobility Control: A Case History. *Journal of Petroleum Technology*, 18(9), pp. 1151-1156.

KAMINSKY, R., WATTENBARGER, R., SZAFRANSKI, R., and COUTEE, A., 2007. Guidelines for polymer flooding evaluation and development. Paper IPTC 11200 presented at the SPE International Petroleum Technology Conference, Dubai, U.A.E., 4-6 December.

KAZEMPOUR, M., SUNDSTROM, E. and ALVARADO, V., 2011. Geochemical modeling and experimental evaluation of high pH floods: Impact of water-rock interactions in sandstone. Paper SPE 143479 presented at the SPE EUROPEC. EAGE Annual Conference and Exhibition. pp. 23-26.

KAZEMPOUR, M., SUNDSTROM, E.A. and ALVARADO, V., 2012. Effect of alkalinity on oil recovery during polymer floods in sandstone. *SPE Reservoir Evaluation & Engineering*, 15(02), pp. 195-209.

KOHLER, N. and CHAUVETEAU, G., 1981. Xanthan Polysaccharide Plugging Behaviour in Porous Media-Preferential Use of Fermentation Broth. *Journal of Petroleum Technology*, 33(02), pp. 349-358.

KOŁODZIEJ, E.J., 1988. Transport Mechanisms of Xanthan Biopolymer Solutions in Porous Media. Paper SPE presented at the SPE 63rd Annual Technical Conference and Exhibition, Houston, Texas, 2-5 October. SPE-18090-MS.

KOZENY, J., 1927. Über kapillare Leitung des Wassers im Boden: (Aufstieg, Versickerung und Anwendung auf die Bewässerung). Hölder-Pichler-Tempsky.

KOZICKI, W., HANNA, M. and TIU, C., 1988. Polymer adsorption in packed bed flow. *Journal of Rheology* (1978-present), 32(6), pp. 593-619.

KOZICKI, W., HSU, C. and PASARI, S., 1987. Evaluation of polymer adsorption-gel formation and slip in polymer solution flows. *Chemical Engineering Communications*, 59(1-6), pp. 137-160.

KOZICKI, W., KUANG, P.Q., ARAGAKI, T. and YIM, S.P., 1993. Surface phenomena in capillary flow of polymer solutions. *The Canadian Journal of Chemical Engineering*, 71(3), pp. 347-357.

KRUEGER, R., 1988. An overview of formation damage and well productivity in oilfield operations: An update. SPE California Regional Meeting.

LAGANA, K., DUBINI, G., MIGLIAVACCA, F., PIETRABISSA, R., PENNATI, G., VENEZIANI, A., and QUARTERONI, A., 2002. Multiscale modelling as a tool to prescribe realistic boundary conditions for the study of surgical procedures. *Biorheology*, 39(3), pp. 359-364.

LAKATOS, I., LAKATOS-SZABO, J. and TOTH, J., 1981. Factors influencing polyacrylamide adsorption in porous media and their effect on flow behaviour. *Surface Phenomena in Enhanced Oil Recovery*. Springer. pp. 821-842.

LAKATOS, I., LAKATOS-SZABO, J., KOSZTIN, B., PALASTHY, G., and KRISTOF, P., 2000. Application of Iron-Hydroxide-Based Well Treatment Techniques at the Hungarian Oil Fields. Paper SPE 75185 presented at the SPE/DOE Improved Oil Recovery Symposium, Tulsa, Oklahoma, USA, 13-17 April.

LAKATOS, I., LAKATOS-SZABO, J., TISZAI, G., PALASTHY, G., KRISTOF, P., TROMBOCZKY, S., BODOLA, M., and PATTERMAN-FARKAS, G., 1999. Application of Silicate-Based Well Treatment Techniques at the Hungarian Oil Fields. Paper presented at the SPE Annual Technical Conference and Exhibition, Texas, USA, 3-6 October.

LAKE, L.W., 1989. Enhanced oil recovery, Prentice-Hall Inc., Eaglewood Cliffs, NJ.

LANGE, E.A., and HUH, C., 1994. A polymer thermal decomposition model and its application in chemical EOR process simulation. Paper SPE 27822 presented at the 9th SPE/DOE Improved Oil Recovery Symposium, Tulsa, Oklahoma, USA, 17-20 April.

LEE, K.S., 2010. Effects of polymer adsorption on the oil recovery during polymer flooding processes. *Petroleum Science and Technology*, 28(4), pp. 351-359.

LEVERETT, M., 1941. Capillary Behaviour in Porous Solids. *Transactions of the AIME*, 142(01), pp. 152-169.

LEWANDOWSKA, K., 2007. Comparative studies of rheological properties of polyacrylamide and partially hydrolyzed polyacrylamide solutions. *Journal of Applied Polymer Science*, 103(4), pp. 2235-2241.

LIANG, J. and SERIGHT, R., 1997. Further investigations of why gels reduce water permeability more than oil permeability. *SPE Production & Facilities*, 12(04), pp. 225-230.

LIANG, J. and SERIGHT, R., 2001. Wall-effect/gel-droplet model of disproportionate permeability reduction. *SPE Journal*, 6(03), pp. 268-272.

LIU, B., SUN, X.S., WANG, K., XU, H., LIU, Q., LIU, X., and SONG, S., 2007. Flooded by high concentration polymer doubled oil recovery of common polymer on field test with 20% closed to the result of laboratory test in Daqing. Paper SPE 108684 presented at the International Oil Conference and Exhibition in Veracruz, Mexico, 27-30 June.

LIU, S.Q., ZHANG, J.C. and XU, J.C., 2013. Investigation on polymer adsorption and retention in a polymer flooded reservoir. 2013 2nd International Conference on Energy and Environmental Protection, ICEEP 2013, April 19, 2013 - April 21, 2013. Guilin, China: Trans Tech Publications Ltd. pp. 1200-1203

LOTSCH, T., MULLER, T. and PUSCH, G., 1985. The effect of inaccessible pore volume on polymer coreflood experiments. Paper SPE 13590 presented at the SPE Oilfield and Geothermal Chemistry Symposium, Phoenix, Arizona, 9-11 April.

MAERKER, J., 1973. Dependence of polymer retention on flow rate. J. Pet. Technology. 25(11): 1307-1308. SPE-4423-PA.

MANICHAND, R.N. and SERIGHT, R., 2014. Field vs. Laboratory Polymer-Retention Values for a Polymer Flood in the Tambaredjo Field. SPE Reservoir Evaluation & Engineering, 17(03), pp. 314-325.

MARSHALL, D., GRAY, R. and BYRNE, M., 1997. Development of a recommended practice for formation damage testing. Paper SPE 38154 presented at the SPE European Formation Damage Conference, The Hague, Netherlands, 2-3 June.

MARSHALL, R. and METZNER, A., 1967. Flow of viscoelastic fluids through porous media. Industrial & Engineering Chemistry Fundamentals, 6(3), pp. 393-400.

MARTIN, F., HATCH, M., SHEPITKA, J. and WARD, J., 1983. Improved Water-Soluble Polymers for Enhanced Recovery of Oil. Paper SPE 11786 presented at the SPE Oilfield and Geothermal Chemistry Symposium, Denver, Colorado, USA, 1-3 June. SPE-11786-MS.

Mathematical Reviews (MathSciNet): MR53649 Zentralblatt MATH, 50.

MEADORS, V.G., 1960. Waterflooding Method of Secondary Recovery. U.S. Patent No. 2,920,041, January 5.

MENNELLA, A., CHIAPPA, L., BRYANT, S. and BURRAFATO, G., 1998. Pore-scale mechanism for selective permeability reduction by polymer injection. Paper SPE 39634 presented at the SPE/DOE Improved Oil Recovery Symposium, Tulsa, Oklahoma, USA, 19-22 April.

MEZZOMO, R.F., MOCZYDLOWER, P., SANMARTIN, A.N., and ARAUJO, C.H.V., 2002. A new approach to the determination of polymer concentration in reservoir rock adsorption tests. Paper SPE 75204 presented at the SPE/DOE Improved Oil Recovery Symposium, Tulsa, Oklahoma, USA, 13-17 April.

MORITIS, G., 2000. EOR weathers low oil prices. Oil and Gas Journal, 98(12), pp. 39-44.

MUNGAN, N., 1969. Rheology and Adsorption of Aqueous Polymer Solutions. Journal of Canadian Petroleum Technology, 8(2), pp. 45-50.

NAVARRETE, R.C., DEARING, H.L., CONSTIEN, V.G., MARSAGLIA, K.M., SEHEULT, J.M., and RODGERS, P.E., 2000. Experiments in Fluid Loss and Formation Damage with Xanthan-Based Fluids While Drilling. IADC/SPE Asia Pacific Drilling Technology, Kuala Lumpur, Malaysia, 11-13 September.

NAVARRETE, R.C., HIMES, R.E. and SEHEULT, J.M., 2000. Applications of Xanthan Gum in Fluid-Loss Control and Related Formation Damage, paper SPE 59535 presented at the SPE Permian Basin Oil and Gas Recovery Conference. Midland, Texas, 21-23 March.

NEEDHAM, R.B. and DOE, P.H., 1987. Polymer flooding review. *Journal of Petroleum Technology*, 39(12): 1503-1507.

OSTERLOH, W. and LAW, E., 1998. Polymer transport and rheological properties for polymer flooding in the North Sea Captain field. Paper SPE 39694 presented at the SPE/DOE Improved Oil Recovery Symposium, Tulsa, Oklahoma, USA, 19-22 April.

PANCHAROEN, M., THIELE, M. and KOVSCEK, A., 2010. Inaccessible Pore Volume of Associative Polymer Floods. Paper SPE presented at the SPE Improved Oil Recovery Symposium, Tulsa, Oklahoma, USA, 24-28 April. SPE-129910-MS.

PATTON, J.T., COATS, K.H., and COLEGROVE, G.T., 1971. Prediction of polymer flood performance. *Society of Petroleum Engineers Journal*, 11(01), pp. 72-84.

POPE, D.S., LEUNG, L.K.W., GULBIS, J. and CONSTIEN, V.G., 1996. Effects of Viscous Fingering on Fracture Conductivity. *SPE Production & Facilities*, 11(4), pp. 230-237.

PORTER, K., 1989. An Overview of Formation Damage (includes associated paper 20014). *Journal of Petroleum Technology*, 41(8), pp. 780-786.

PURCELL, W.R., 1949. Capillary pressures-their measurement using mercury and the calculation of permeability therefrom. *Journal of Petroleum Technology*, 1(02), pp. 39-48.

PYE, D.J., GOGARTHY, W. and PYE, D., 1964. Improved secondary recovery by control of water mobility. *J. Pet. Technology* 16(8):911-916. SPE-845-PA.

RANJBAR, M., RUPP, J. and PRUSCH, G., 1991. Influence of pore radi distribution on polymer retention in natural sandstones. Oral presentation at the 6th European Symposium on Improved Oil Recovery, Stavanger, Norway, 21-23 May.

REID, P., SANTOS, H., LABENSKI, F., SABINS, F. and WATTERS, L., 2004. Associative polymers for invasion control in water-and oil-based muds and in cementing spacers: laboratory and field case histories. Paper AADE-04-DF-HO-33 presented at the American Association of Drilling Engineers (AADE) 2004 Drilling Fluids Conference, Houston, Texas, 6-7 April.

RHO, T. Park, J., Kim, C., YOON, H-K. and SUH, H-S., 1996. Degradation of polyacrylamide in dilute solution. *Polymer Degradation and Stability*, 51(3), pp. 287-293.

ROMERO-ZERÓN, L.B., ONQSURAKUL, S., LI, L. and BALCOM, B., 2009. Visualization of mobility-control by polymer waterflooding through unconsolidated porous media using magnetic resonance imaging. *Petroleum Science and Technology*, 27(17), pp. 2046-2062.

SALEH, L.D., WEI, M. and BAI, B., 2014. Data Analysis and Updated Screening Criteria for Polymer Flooding Based on Oilfield Data. *SPE Reservoir Evaluation & Engineering*, 17(01), pp. 15-25.

SAMUELSON, M. and CONSTIEN, V., 1996. Effects of high temperature on polymer degradation and cleanup. Paper SPE 36495 presented at the Annual Technical Conference and Exhibition, Denver, Colorado, USA, 6-9 October.

SANDIFORD, B., 1964. Laboratory and field studies of water floods using polymer solutions to increase oil recoveries. *Journal of Petroleum Technology*, 16(08), pp. 917-922. SPE-844-PA.

SANDVIK, E. and MAERKER, J., 1977. Application of xanthan gum for enhanced oil recovery. *ACS Symp. Ser.* pp. 242-264.

SAVINS, J., 1969. Non-Newtonian flow through porous media. *Industrial & Engineering Chemistry*, 61(10), pp. 18-47.

SERIGHT, R.S., FAN, T., WAVRIK, K. and BALABAN, R., 2011. New insights into polymer rheology in porous media. *SPE Journal*, 16(1), pp. 35-42. SPE-129200-PA.

SERIGHT, R.S., SEHEULT, J.M. and TALASHEK, T., 2009. Injectivity characteristics of EOR polymers. *SPE Reservoir Evaluation & Engineering*, 12(05), pp. 783-792. SPE-115142-PA.

SEYBOLD, C., 1994. Polyacrylamide review: soil conditioning and environmental fate. *Communications in Soil Science and Plant Analysis*, 25(11-12), pp. 2171-2185.

SHAH, B.N., LAWRENCE, G., WILLHITE, P. and GREEN, D.W., 1978. The effect of inaccessible pore volume on the flow of polymer and solvent through porous media. Paper SPE 7586 presented at the SPE Annual Fall Technical Conference and Exhibition, Houston, Texas, 1-3 October.

SHIYI, Y., DONG, H., QIANG, W. and HUA, Y., 2000. Numerical simulator for the combination process of profile control and polymer flooding. Paper SPE 64792 presented at the SPE International Oil and Gas Conference and Exhibition, Beijing, China. pp. 7-10.

SINGLETON, M., SORBIE, K. and SHIELDS, R., 2002. Further Development of the Pore Scale Mechanism of Relative Permeability Modification by Partially Hydrolysed Polyacrylamide. Paper SPE 75184 presented at the SPE/DOE Improved Oil Recovery Symposium, Tulsa, Oklahoma, USA.

SLOAT, B., 1969. Polymer treatment boosts production on four floods. *World Oil* 168, 44-47.

SLOAT, B., 1972. How six polymer floods are faring. *Oil and Gas Journal* 70, 101-103.

SMITH, F., 1970. The behaviour of partially hydrolyzed polyacrylamide solutions in porous media. *Journal of Petroleum Technology*, 22(2): 148-156.

SORBIE, K.S., MACKEY, E.J., COLLINS, I.R., and WAT., R., 2007. Placement Using Viscosified Non Newtonian Scale Inhibitor Slugs: The Effect of Shear-Thinning. *SPE Production & Operations*, 22(04), pp. 434-441.

SORBIE, K.S., 1991. *Polymer-Improved Oil Recovery*. Blackie and Son Ltd. Glasgow and London.

STANDNES, D.C. and SKJEVRAK, I., 2014. Literature review of implemented polymer field projects. *Journal of Petroleum Science and Engineering*, 122, pp. 761-775.

STAVLAND, A. and NILSSON, S., 2001. Segregated Flow is the Governing Mechanism of Disproportionate Permeability Reduction in Water and Gas Shutoff. Paper SPE 71510 presented at the SPE Annual Technical Conference and Exhibition, New Orleans, LA, 30 September-3 October.

STAVLAND, A., JONSBRAATEN, H., LOHNE, A., MOEN, A., and GISKE, N., 2010. Polymer Flooding–Flow Properties in Porous Media versus Rheological Parameters. Paper SPE 131103 presented at the 72nd SPE EUROPEC/EAGE Annual Conference and Exhibition, Barcelona, Spain, 14-17 June.

STOSUR, G., 2003. EOR: Past, Present and What the Next 25 Years May Bring. Paper SPE 84864 presented at the SPE International Improved Oil Recovery Conference in Asia Pacific, Kuala Lumpur, Malaysia, 20-21 October.

STOSUR, G., HITE, J., CARNAHAN, N. and KARL, M., 2003. The Alphabet Soup of IOR, EOR and AOR: Effective Communication Requires a Definition of Terms. Paper SPE 84908 presented at the SPE International Improved Oil Recovery Conference in Asia Pacific, Kuala Lumpur, Malaysia, 20-21 October.

STUTZMANN, T. and SIFFERT, B., 1977. Contribution to the adsorption mechanism of acetamide and polyacrylamide on to clays. *Clays and Clay Minerals*, 25(6), pp. 392-406.

SZABO, M.T., 1972. Molecular and microscopic interpretation of the flow of hydrolyzed polyacrylamide solution through porous media. Paper SPE 4028 presented at the 47th Annual SPE Fall Meeting, San Antonio, Texas, USA, 8-11 October.

SZABO, M.T., 1975a. Laboratory investigations of factors influencing polymer flood performance. *Society of Petroleum Engineers Journal*, 15(4), pp. 338-346.

SZABO, M.T., 1975b. Some aspects of polymer retention in porous media using a C14-tagged hydrolyzed polyacrylamide. *Society of Petroleum Engineers Journal*, 15(4), pp. 323-337. SPE-4468-PA.

SZABO, M.T., 1979. An Evaluation of Water-Soluble Polymers for Secondary Oil Recovery–Part 1. *J. Pet. Tech*, 31(5), pp. 553-560. SPE-6601-PA.

SZABO, M.T., 1979. An Evaluation of Water-Soluble Polymers for Secondary Oil Recovery–Part 2. *J. Pet. Tech*, 31(5), pp. 561-570. SPE-6601-PA.

TAYLOR, K. and NASR-EL-DIN, H., 2002. Coreflood evaluation of in-situ gelled acids. *International Symposium and Exhibition on Formation Damage Control*.

THOMAS, C., 1976. The Mechanism of Reduction of Water Mobility by Polymers in Glass Capillary Arrays. *Society of Petroleum Engineers Journal*, 16(03), pp. 130-136.

URBISSINOVA, T., TRIVEDI, J. and KURU, E., 2010. Effect of elasticity during viscoelastic polymer flooding: a possible mechanism of increasing the sweep efficiency. *Journal of Canadian Petroleum Technology*, 49(12), pp. 49-56.

VELA, S., PEACEMAN, D. and SANDVIK, E.I., 1976. Evaluation of polymer flooding in a layered reservoir with crossflow, retention, and degradation. *Society of Petroleum Engineers Journal*, 16(02), pp. 82-96. SPE-5102-PA.

WANG, D., CHENG, J. and WU, J., 2002. Producing by Polymer Flooding more than 300 Million Barrels of Oil, What Experiences Have Been Learnt?" paper SPE 77872 presented at the 2002 SPE Asia Pacific Oil and Gas Conference and Exhibition, Melbourne, Australia, 8-10 October.

WANG, D., WANG, G., XIA, H., YANG, S. and WU, W., 2011. Incremental recoveries in the field of large scale high viscous-elastic fluid flooding are double that of conventional polymer flooding. Paper SPE 146473 presented at the SPE Annual Technical Conference and Exhibition, Denver, USA, 30 October - 2 November.

WANG, J. and DONG, M., 2009. Optimum effective viscosity of polymer solution for improving heavy oil recovery. *Journal of Petroleum Science and Engineering*, 67(3), pp. 155-158.

WEVER, D.A.Z, PICCHIONI, F. and BROEKHUIS, A.A., 2011. Polymers for Enhanced Oil Recovery: A Paradigm for Structure-Property Relationship in Aqueous Solution. *Progress in Polymer Science*, 36(11): 1558-1626.

WISSELER, E.H., 1971. Viscoelastic effects in the flow of non-Newtonian fluids through a porous medium. *Industrial & Engineering Chemistry Fundamentals*, 10(3), pp. 411-417.

XUE, L., AGARWAL, U.S., ZHANG, M., STAAL, B.B.P., MULLER, A.H.E., BAILLY, C.M.E., and LEMSTRA, P.J., 2005. Synthesis and direct topology visualization of high-molecular-weight star PMMA. *Macromolecules*, 38(6), pp. 2093-2100.

YANG, F., WANG, D., YANG, X., SUI, X., CHEN, Q. and ZHANG, L., 2004. High concentration polymer flooding is successful. Paper SPE 88454 presented at the SPE Asia Pacific Oil and Gas Conference and Exhibition, Perth, Australia, 18-20 October.

YE, Z., GOU, G., GOU, S., JIANG, W. and LIU, T., 2013. Synthesis and characterization of a water-soluble sulfonates copolymer of acrylamide and N-allylbenzamide as enhanced oil recovery chemical. *Journal of Applied Polymer Science*, 128(3), pp. 2003-2011.

YUAN, S., HAN, D., WANG, Q. and YANG, H., 2000. Numerical simulator for the combination process of profile control and polymer flooding. Paper SPE 64792 presented at the SPE International Oil and Gas Conference and Exhibition, Beijing, China, 7-10 November.

ZAITOUN, A. and KOHLER, N., 1987. The role of adsorption in polymer propagation through reservoir rocks. Paper SPE 16274 presented at the SPE International Symposium on Oilfield Chemistry, San Antonio, Texas, 4-6 February.

ZAITOUN, A. and KOHLER, N., 1988. Two-phase flow through porous media: effect of an adsorbed polymer layer. Paper SPE 18085 presented at the SPE Annual Technical Conference and Exhibition, Houston, Texas, 2-5 October.

ZAITOUN, A., BERTIN, H. and LASSEUX, D., 1998. Two-phase flow property modifications by polymer adsorption. Paper SPE 39631 presented at the SPE Symposium on improved oil recovery, Tulsa, Oklahoma, pp. 285-292.

ZAITOUN, A., BERTIN, H. and LASSEUX, D., 1998. Two-phase flow property modifications by polymer adsorption. Part 2 (of 2), April 19, 1998 - April 22, 1998. Tulsa, OK, USA: Soc Pet Eng. (SPE). pp. 285-292.

ZHANG, H., XU, K., AI, H., CHEN, D., XV, L. and CHEN, M., 2008. Synthesis, characterization and solution properties of hydrophobically modified polyelectrolyte poly (AA-co-TMSPMA). *Journal of Solution Chemistry*, 37(8), pp. 1137-1148.

ZHANG, L., DENG, S. and HUANG, M., 2002. Cationized polyacrylamides AEE for use as clay stabilizer/sand controller. *Oilfield Chem*, 19, pp. 208-209.

ZHANG, P., WANG, Y., YANG, Y., ZHANG, J., CAO, X., CHEN, W., and LI, K., 2012. One Factor Influencing the Oil-displacement Ability of Polymer Flooding: Apparent Viscosity or Effective Viscosity in Porous Media? *Petroleum Science and Technology*, 30(14), pp. 1424-1432.

ZHANG, R., YE, Z., PENG, L., QIN, N., SHU, Z., and LUO, P., 2013. The shearing effect on hydrophobically associative water-soluble polymer and partially hydrolyzed polyacrylamide passing through wellbore simulation device. *Journal of Applied Polymer Science*, 127(1), pp. 682-689.

ZHENG, C.G., GALL, B.L., GAO, H.W., MILLER, A.E. and BRYANT, R.S., 2000. Effects of polymer adsorption and flow behaviour on two-phase flow in porous media. *SPE Reservoir Evaluation & Engineering*, 3(03), pp. 216-223.

ZITHA, P., 1995. Effects of Bridging-Adsorption of Macromolecules on the Flow of Linear Flexible Polymer-Solutions in Porous-Media. *Comptes Rendus De L Academie Des Sciences Serie II*, 320(9), pp. 447-453.

ZITHA, P., 2001. Prediction of Polymer Viscosity Reduction in Pores Using an Exact Depletion Profile. Paper SPE 68981 presented at the SPE European Formation Damage Conference, The Hague, Netherlands, 21-22 May.

ZITHA, P., CHAUVETEAU, G. and ZAITOUN, A., 1995. Permeability-dependent propagation of polyacrylamides under near-wellbore flow conditions. *International symposium on oilfield chemistry*. pp. 101-116.

ZITHA, P., DANIEL, M., FRED, V. and DARWISH, M.I.M., 2003. Modelling of polymer adsorption under near-wellbore flow conditions. Paper SPE 82256 presented at the SPE European Formation Damage Conference, The Hague, Netherlands, 13-14 May.

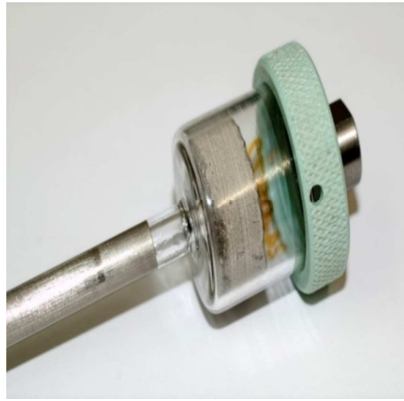
Appendices

Appendices

Appendix A

Experimental High Mercury Injection Capillary Pressure Procedure (MICP)

- 1) The clean dry core samples were weighed and each placed in the bulb of a penetrometer (Figure A-1) selected so that the pore volume of the sample was approximately 70-80% of the volume of the penetrometer stem.
- 2) The sample and penetrometer were weighed together.
- 3) The penetrometer containing the sample was loaded into the low-pressure chamber of a Micromeritics Autopore II 9220 porosimeter (Figure A-2).
- 4) The penetrometer was evacuated to a pressure of less than 50 μ m of mercury, and then filled with mercury at a pressure of 0.5 psia. The bulk volume of the sample was determined at this point.



A1: Rock sample in penetrometer chamber.



A2: Autopore 9505

- 5) For drainage, mercury (non-wetting phase) saturation increasing, mercury was injected into the core plug at increasing incremental pressures from 0.5 to 25.0 psia.
- 6) At each pressure point, mercury intrusion was monitored while the pressure was held constant. Equilibrium was identified when the rate of intrusion dropped below $0.001 \mu\text{L/g-sec}$. The pressure and the total volume for that point were recorded.
- 7) The injection pressure was reduced to atmospheric and the penetrometer was removed and weighed with the sample and mercury in place.
- 8) It was then loaded into a high-pressure chamber of the Autopore system.
- 9) For drainage only, and calculation of pore size distribution, the cumulative volume of mercury injected is increased by incremental pressure changes up to a maximum of approximately 60,000 psia (4144 bar) with data being recorded at each pressure as described in paragraph 6 above.

Calculation of Mercury Injection Data

- I. Sample weight, sample and penetrometer weight with and without mercury were used to calculate grain density and bulk density.

- II. Volumes of mercury injected at each injection pressure were recorded.
- III. Initial apparent intrusion at low pressures may be the result of mercury conforming to the surface irregularities of the core sample. These irregularities are not representative of the pore structure. The threshold pressure, where mercury injection into the pore structure begins, is identified at the pressure where the rate of mercury injection increases rapidly. Cumulative apparent injection up to this threshold pressure was subtracted as surface porosity from measured data before subsequent calculations were made.
- IV. Cumulative volumes of mercury injected are expressed as a fraction of the total pore volume of the sample.
- V. At any mercury displacement pressure the minimum radius of pore throat which can be penetrated by mercury is given by:

$$r = \frac{2\sigma \cdot \cos \theta \cdot C}{P_c} \quad (A-1)$$

where:

r = pore throat radius, μm

σ = interfacial tension between air and mercury, dynes/cm
(485)

θ = contact angle between air and mercury, degrees (140)

P_c = capillary pressure, psia

C = conversion constant (0.145)

Using this relationship, a graph of fraction of pore volume injected (PV) versus pore throat radius was constructed. The differential of this gives a pore throat size distribution (PSD) function:

$$PSD = \frac{dv}{d(\log(r))} \quad (A-2)$$

PSD is smoothed using 1 - 2 - 1 smoothing:

$$PSD_i = \frac{(PSD_{i-1} + 2PSD_i + PSD_{i+1})}{4} \quad (A-3)$$

PSD is then normalised to 1 as follows:

$$PSD_{normalised\ i} = \frac{PSD_i}{PSD_{max.}} \quad (A-4)$$

Normalised PSD was presented in graphical form along with saturation against pore throat radius and permeability distribution function against pore throat radius. The normalised pore throat size distribution function displayed graphically was used to identify pore throat size groupings and the relative proportions of pore volume controlled by Macro pore throats (>1.5µm), Meso pores throats (1.5 to 0.5 µm) and Micro pore throats (<0.5 µm).

VI. Oil-brine capillary pressure (reservoir) data was obtained from air-mercury data by the following conversion:

$$PC_{o-b} = PC_{a-Hg} \cdot \frac{\sigma_2 \cdot \cos \theta_2}{\sigma_1 \cdot \cos \theta_1} \quad (A-5)$$

where, P_{co-b} = oil-brine capillary pressure (reservoir), psia

P_{ca-Hg} = air-mercury capillary pressure, psia

σ_2 = interfacial tension between oil and brine (reservoir), dynes/cm (30)

θ_2 = contact angle between oil and brine (reservoir), degrees (30)

σ_1 = interfacial tension between air and mercury, dynes/cm (485)

θ_1 = contact angle between air and mercury, degrees (140)

VII. The mean hydraulic radius (MHR), is the average pore throat size of the sample and is given by:

$$MHR = \frac{\sum_{i=0}^n (r_i^2 \cdot (S_i - S_{i-1}))}{2 \cdot \sum_{i=0}^n (r_i \cdot (S_i - S_{i-1}))} \quad (A-6)$$

S = mercury saturation, fraction of pore volume

VIII. A method for averaging capillary pressure data from various systems is the use of the Leverett J-function (Leverett, 1940). The J-function is a dimensionless capillary pressure function expressed as,

$$J = \frac{0.2166 P_c \cdot \sqrt{\left(\frac{k}{\phi}\right)}}{\sigma \cdot \cos \theta} \quad (A-7)$$

where, J = Leverett capillary pressure function, dimensionless

P_c = Capillary pressure, psia

σ = Air-mercury interfacial tension, dynes/cm (485)

θ = Air-mercury contact angle, degrees (140)

k = Permeability, mD

φ = Porosity, fraction

(Leverett, M.C. (1940). Capillary Behaviour in Porous Solids. Trans. AIME 142, pp 151 – 169).

IX. The theoretical cumulative permeability (k_{ti}) of a sample with a given pore size distribution, (r_0 to r_i), can be expressed as Eqn. (A-8) (Purcell, 1949):

$$k_{ti} = \sum_{i=0}^n r_i^2 \cdot \Delta S_i \quad (A-8)$$

Where S_i = mercury saturation, fraction of pore volume (i.e., the volume of each capillary expressed as percentage).

X. The k_{ti} in Eqn. (A-8) is then normalized such that the maximum is 1.0. Then a cumulative Permeability Distribution Function (PDF) is given by Eqn. (A-9) (Purcell, 1949):

$$PDF_{normalised\ i} = \frac{k_{ti}}{k_{t\max.}} \quad (A-9)$$

Appendix B:

Procedure for Experimental X-ray diffraction (XRD) and Analysis

Sample Preparation

Whole Rock XRD Analysis

1. For whole rock XRD analysis, the cleaned sample is gently disaggregated with a pestle and mortar, and then 'micronised' using a McCrone Micronising Mill to obtain an x-ray diffraction 'powder' with a mean particle diameter between 5-10 microns.
2. The slurry is then dried and packed into an aluminium cavity mount, producing a randomly orientated sample for presentation to the x-ray beam.

Clay Fraction XRD Analysis

1. For clay fraction analysis, the <2 micron fraction is separated from the sample by ultrasound, shaking and centrifugation.
2. The total weight of clay extracted is obtained by removing 20ml of clay suspension and evaporating to dryness.
3. Size fractions other than <2 micron (e.g. 2-16 micron) are obtained by varying the centrifuge speed and time.
4. The XRD mount is obtained by filtering the clay suspension through a Millipore filter and drying the filtrate on the filter paper.
5. The samples are analysed as untreated clay, after 'glycolation' overnight and following 'heating' at 380°C for 2 hours and 550°C for one hour.

Analysis Procedures

Whole Rock XRD Analysis

Each whole rock sample is analysed between 5-60 degrees 2 theta at a step size of 0.05 degrees/sec. Samples are exposed to x-ray radiation from a copper anode at 40kV, 30mA. Peak heights are measured for each mineral phase present. The counts (peak height) for each mineral are compared to a standard count for a pure sample of that mineral and a percentage calculated. The final results are presented as a normalised percentage for each mineral identified.

Clay Fraction XRD Analysis

The initial scan for the treatments is between 3-35 degrees 2 theta at a step size of 0.05 degrees/sec. Samples are exposed to X-Ray radiation from a copper anode at 40kV, 30mA. The untreated sample is also analysed between 24-27 degrees 2 theta at a step size of 0.02 degrees/2 sec to further define kaolinite/chlorite peaks. Traces obtained from the four clay treatments are studied to assess the clay mineral assemblages present. Peak height measurements are taken and incorporated in a formula to indicate the relative amounts of clay minerals present. The data is then used to quantify the clay minerals with respect to the whole rock by reference to the amount of <2 micron clay fraction which has been previously extracted. An indication of the clay mineral crystallinities can be given by assessment of the peak width for each component. Where applicable the relative intensities of the chlorite 001 and 003 peaks can be used to measure the total heavy metal (predominantly Fe) content of the mineral.

Appendix C

Porosity and Grain Density Determination Procedure

- 1) The grain volumes of the samples were measured using a calibrated helium gas volume expansion meter. Prior to each set of data (20 samples maximum) the porosimeter was checked for potential leaks. This was done by performing a 'dummy' expansion with a steel blank in the matrix cup. The apparatus was then calibrated using five stainless steel discs of known volumes and the relationship between pressure and volume (which is ideally linear) was calculated. A calibration of 0.99999 (1=linear) or better is acceptable.
- 2) The plug samples were weighed and the weight recorded prior to the grain volume measurement. The samples were loaded into the matrix cup. If the cup was not filled a stainless steel disc of known volume was added in order to minimise the dead volume. Helium was then expanded into the matrix cup and the pressure was allowed to stabilise for a minimum of five minutes per sample before being recorded.
- 3) In order to check the repeatability of the results, two stainless steel blanks of known volume were run prior to, and after, each set of results. The results had to fall within 0.02 cc of their known volume for the data produced to be acceptable. The equipment was kept at a constant temperature throughout.
- 4) Bulk volumes were measured by mercury displacement using Archimedes principle. The samples were then placed in a mercury oven.
- 5) This data used in combination with the weights of the samples, gave porosity, and grain density values. On completion of the analysis, 10% of the samples were re-analysed as a quality control check.

$$\text{Pore Volume (ccs)} = \text{Bulk Volume (ccs)} - \text{Grain Volume (ccs)} \quad (\text{C-1})$$

$$\text{Porosity (\%)} = \frac{\text{Pore Volume}}{\text{Bulk Volume}} \times 100 \quad (\text{C-2})$$

$$\text{Grain Density (g.cc}^{-1}\text{)} = \frac{\text{Sample Dry Weight (g)}}{\text{Grain Volume (ccs)}} \quad (\text{C-3})$$

Appendix D

Procedure for the Determination of Sand Particle Size

1. The cleaned, dried, weighed and disaggregated sample was placed in the topmost (coarsest mesh) of a stack of sieves with decreasing mesh size.
2. A lid was placed on the topmost sieve.
3. The bottom-most sieve was mounted on a receiver pan.
4. Prior to stacking, the sieves were cleaned, dried, weighed and properly checked for possible rupture.
5. A mechanical sieve shaker was used to vibrate the stack such that given particle sizes remain in each of the sieves after travelling downward through the stack screens until retained on a screen having a mesh size smaller than the minimum grain dimensions.
6. Sufficient time (60 minutes for this work) was allowed in vibrating the screens to ensure that each size fraction has completely settled.
7. The weight fractions retained on each of the sieves used in the test and in the pan (if any) were recorded and converted to percentages of the original test sample weight (i.e., by dividing weight of particles remaining on each screen by the initial total weight of sand particles used in the sieve analysis).
8. In order to estimate the percentages of material larger or smaller than a certain mesh size, the cumulative percentage weight of these remains were calculated and plotted against the mesh size of the sieves, resulting in a distribution curve.
9. Generally, the largest percentage determines the size of particles of the sand. Hence, the largest percentage was therefore taken as the particle size of the sand used in the flow experiments.
10. The sample was then either recombined or maintained in separate size fractions for additional static and dynamic adsorption/desorption testing.

Appendix E

Procedure for Gas Permeability Determination

- I. Gas permeability was measured using a calibrated steady state permeameter with air as the flowing medium. The flow was allowed to stabilise before the readings were taken.
- II. To check the performance of the permeameter a full set of check plugs of known permeability was run at the beginning of every day (one check plug for each orifice of the permeameter). After every set of samples analysed (20 samples maximum), check plugs were again tested - one check plug specific to each orifice used in the analysis.
- III. Gas Permeability measurements were then made on the clean and dry samples in a Hassler core holder with an applied overburden pressure of 400 psig. Nitrogen gas was flowed through each sample and the differential pressure (across the sample) was measured using a transducer. The permeability value was calculated by application of Darcy's law.

$$K_g = \frac{Q_b \times \mu \times P_b \times L \times 2000}{A \times [(P_1 + P_b)^2 - (P_2 + P_b)^2]}$$

(E-1)

- where, K_g = Permeability to gas (mD)
 L = Length of sample (cm)
 A = Cross sectional area of sample (cm²)
 μ = Viscosity of gas (cP)
 P_b = Atmospheric pressure (atm)
 P_1 = Corrected upstream pressure (atm)
 P_2 = Corrected downstream pressure in (atm)
 Q_b = Flow rate (ccs.sec⁻¹)

(Darcy, H. 1856. Les Fontaines Publiques de la Ville de Dijon. Victor Dalmont, Paris.)

IV. When the analysis was complete, 10% of the samples were reanalysed as a quality control check.

Appendix F

Procedure for the Turbidity (Bleach) Method for Polymer Concentration Determination

F.1 General: Bleach method for use with all samples free of oil and coloured contaminants.

F.2 Reagents.

1. Acetic acid, glacial.
2. Sodium chloride, reagent grade.
3. Sodium hypochlorite, aqueous solution, 3.50 wt% weight percent (fresh commercial-grade Clorox®).

F.3 Apparatus.

1. UV-Spectrophotometer and matched cuvettes.
2. Standard laboratory balance, sensitivity, 0.0001 g.
3. 5, 8 and 10-micron membrane filters.
4. Stopwatch or timer.

F.4 Procedure for Sample Preparation for Measurement of Turbidity.

1. Solution containing 6 weight percent acetic acid and 30 weight percent of 3.50 weight percent sodium hypochlorite solution was prepared in distilled water. Shelf life of this solution is approximately two days.

NB: Components were added to water and all operations were performed in a fume hood to prevent accumulation of hazardous vapours.

2. Polymer samples more concentrated than 500 ppm were diluted to required concentration with brine of the same composition.

Dilution factors were recorded.

$$\text{Dilution Factor} = \frac{\text{weight of diluted sample}(g)}{\text{weight of initial sample}(g)} \quad (\text{F-1})$$

3. 10g of polymer solution was filtered through 8 micron filter membranes.
4. 5.0g of the filtered polymer solution from Step 3 was weighed into a clean small vial and capped.

NOTE: Steps 2 through 4 were completed for all samples to be analysed before beginning Step 5.

5. The sodium hypochlorite plus acetic acid solution from Step 1 was added to the vials to obtain a total weight (sample plus solution) of 9.5g.
6. The container was capped and mixed by inverting several times. There was no shaking as shaking can result in flocculation of the reaction product.
7. The mixture was transferred to a sample cuvette and the percent transmittance was measure at a wavelength of 470nm. For each sample, Steps 6 and 7 were completed within a maximum of five minutes after completion of Step 5. A standing time of three minutes is recommended. Standing time was kept as constant as possible.

F.5 Procedure for Measuring Transmittance.

1. About 15 minutes was allowed as warm-up time for the UV-Spectrophotometer.
2. Wavelength was set to 470 nm.

3. The reference cuvette was filled with distilled water (or brine as nearly identical in composition to the sample as possible).
4. The instrument was set to zero percent transmittance.
5. The reference cuvette was inserted and the instrument set to 100 percent transmittance.
6. The cuvette containing the sample was therefore inserted and the percent transmittance was recorded. Following the measurement, the instrument was continuously checked with reference solution to ensure against drift.

F.6 Preparation of the Standard Curve.

1. 250 ppm stock solution of the appropriate polymer in brine that is identical in composition to that present in the unknowns was prepared. Recommended standard solution preparation procedures were followed.
2. From the above stock solution, standard solutions were prepared by diluting with brine to obtain concentrations of 0 to 250 ppm in 50 ppm increments.
3. Steps 3 through 7 of section F.4 were performed for the set of standard solutions and transmittances were recorded. A standard calibration curve of percent transmittance versus polymer concentration was then Prepared.

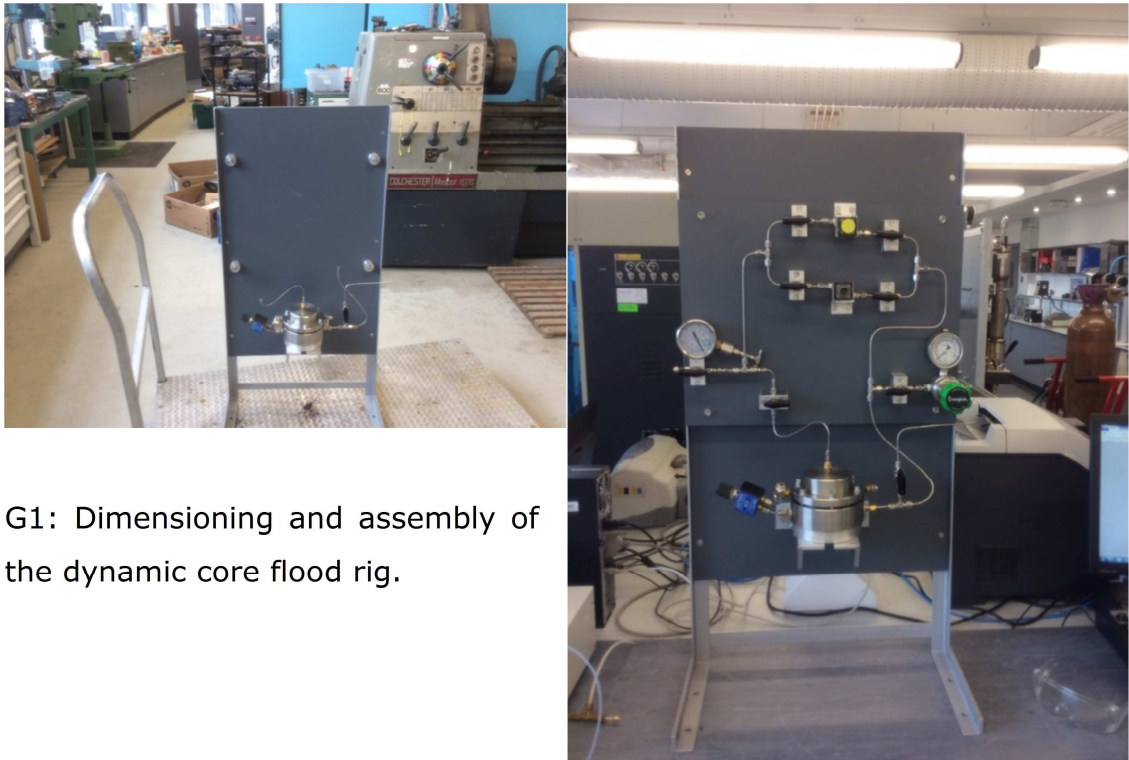
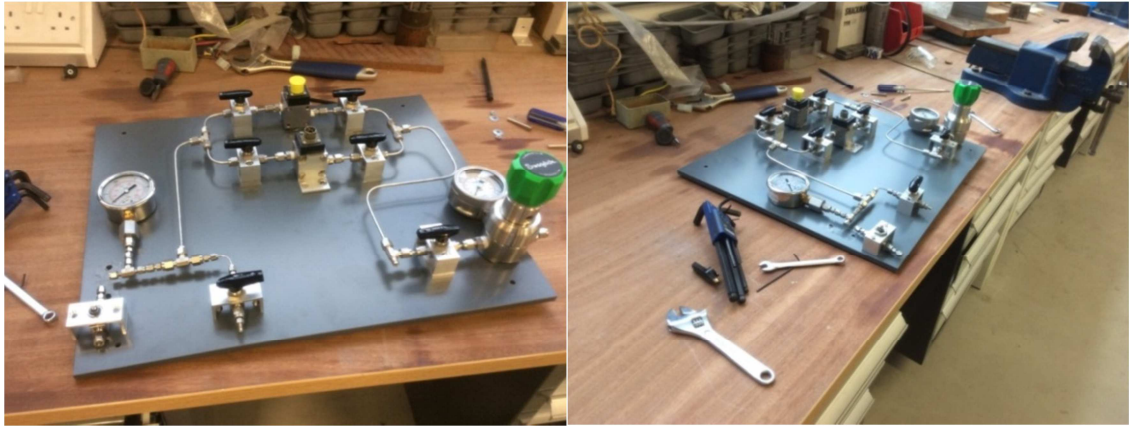
F.7 Determination of Sample Concentrations.

Sample concentrations were found by direct comparisons of sample transmittances with the standard calibration curve. These comparisons were taken into account of any dilution that was made using Eqn. (F-2):

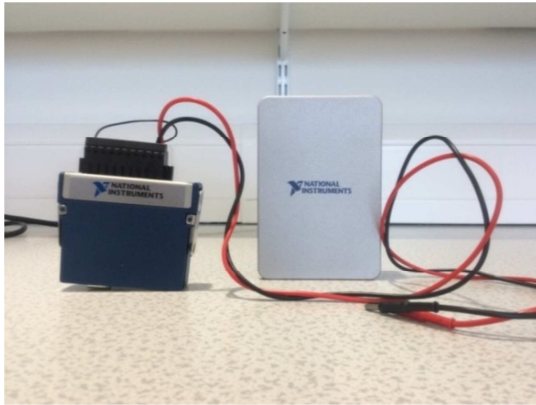
$$\text{Polymer conc.} = \text{polymer conc. read from the curve} \times \text{dilution factor} \quad (\text{F-2})$$

Appendix G

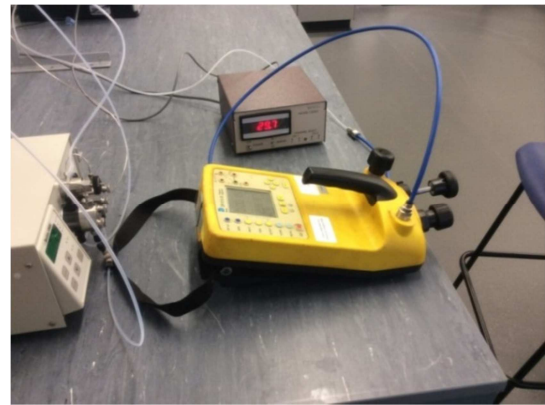
Photographs Showing Construction Stages of the Set-up used for the Implementation of the Polymer Dynamic Core flood Experiments.



G1: Dimensioning and assembly of the dynamic core flood rig.



(a)



(b)

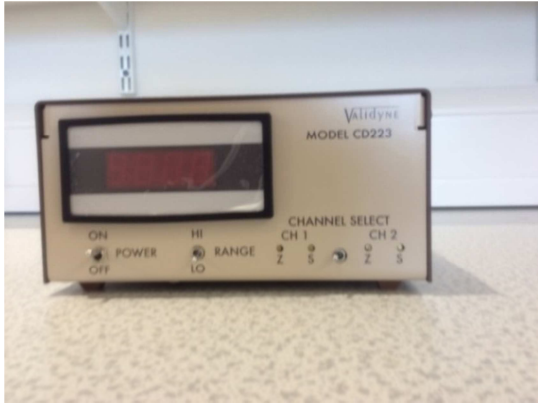
G2: (a) High-speed National Instruments Data Acquisition system (NIDAQ), (b) Druck DPI 615 IS pressure calibrator used for transducers calibration and to perform rig leakage test.



G3: Helium gas regulator



G4: Gas cylinders

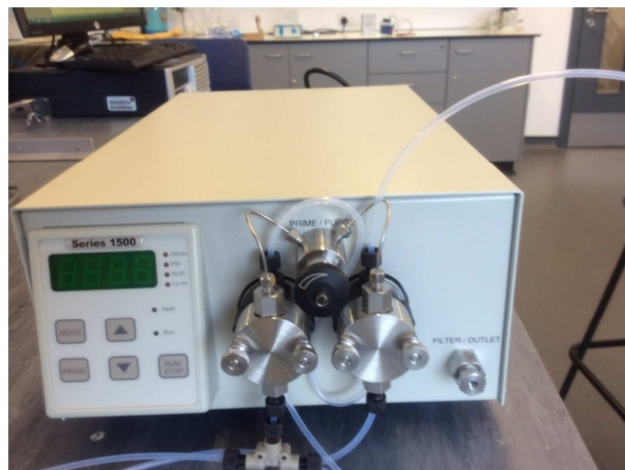


(a)



(b)

G5: Model CD 223 Validyne Engineering DC Output Digital Transducer Demodulator: (a) Front view (b) Rear view.



G6: Model 1500 Digital Dual Piston HPLC Pump

Appendix H

Publications

Journal Papers:

P.E.G. Idahosa⁹¹, G.F. Oluyemi², M. B. Oyeneyin², and R. Prabhu².

¹ IDEAS Research Institute, Robert Gordon University, Riverside East, Garthdee Road, Aberdeen, AB10 7GJ, United Kingdom.

² School of Engineering, Robert Gordon University, Riverside East, Garthdee Road, Aberdeen, AB10 7GJ, United Kingdom.

1. Formation Damage Induced by Polymer Adsorption.

Journal of Petroleum Science and Engineering – Elsevier (Under Review).

2. Rate-Dependent Polymer Adsorption in Porous Media.

Journal of Petroleum Science and Engineering – Elsevier (Under Review).

3. Prediction of Rheological Behaviour of Partially Hydrolysed Polyacrylamide (HPAM) Polymer Solution.

Journal of Petroleum Science and Engineering – Elsevier (Under Review).

4. Polymer-Brine-Rock Interactions: A Possible Mechanism for Formation Damage.

In preparation for: Journal of Transport in Porous Media – Springer.

5. Laboratory Investigation of the Effect of Inaccessible Pore Volume on Polymer Retention.

In preparation for: Journal of Energy Resources Technology - ASME.

⁹ Address all correspondence to: P.E.G. Idahosa, IDEAS Research Institute, Robert Gordon University, Riverside East, Garthdee Road, Aberdeen, AB10 7GJ, United Kingdom. Tel: +44(0)1224262451, E-mail: p.e.g.idahosa@rgu.ac.uk

Conference presentation:

- P.E.G. Idahosa, G.F. Oluyemi, M. B. Oyenehin, and R. Prabhu, 2013. Modelling Formation Damage Induced by Propagation of Single-Phase Non-Newtonian Polymer Solution in Porous Media. Paper presented at the 37th SPE Nigeria Annual International Conference and Exhibition, Lagos, Nigeria, 5–7 August.
- P.E.G. Idahosa, G.F. Oluyemi, M. B. Oyenehin, and R. Prabhu, 2014. Rheological Behaviour of Single-phase nonNewtonian Polymer Solution in Complex Pore Geometry: A Simulation Approach. Proceedings of the 2014 COMSOL Conference, Cambridge, United Kingdom, 17-19 September.

Presentation only:

Conceptual Formation Damage Mechanism of Oilfield Polymers. Presented at the Northern Research Partnership (NRP) Graduate Symposium, University of Dundee, United Kingdom, January 2011.

Poster presentation:

P.E.G. Idahosa, G.F. Oluyemi, M. B. Oyenehin, and R. Prabhu, 2013. Modelling Formation Damage Induced by Propagation of Single-Phase Non-Newtonian Polymer Solution in Porous Media, IDEAS Research Students Symposium, Robert Gordon University, Riverside, East, Aberdeen, UK, 2013.